A study of SNARE-mediated autophagosome clearance using fluorescence lifetime microscopy

Rebecca Saleeb

Thesis submitted for the degree of Doctor of Philosophy

The Institute of Biological Chemistry, Biophysics and Bioengineering

Heriot Watt University

February 2017

Abstract

Cell survival requires the turnover of toxic cellular material and recycling of biomolecules in low nutrient conditions. An efficient degradation system is therefore essential for disease prevention and its dysfunction has been linked to both neurodegeneration and oncogenesis. Bulk degradation is accomplished through the collection of cytoplasmic material in a unique sequestration vesicle, which forms *de novo* and subsequently deposits cargo in the lysosome for degradation. This process, known as autophagy, therefore requires membrane fusion between the autophagosomal vesicle and the lysosome. SNARE proteins mediate membrane fusion events and therefore their careful regulation ensures the proper organisation of the membrane trafficking network. The SNARE proteins governing autophagosome clearance have been identified as syntaxin 17, SNAP29 and VAMP8 and SNARE assembly appears to be positively regulated by VPS33A. This well established model of SNARE-mediated autophagosome clearance has not, however, been demonstrated within the spatiotemporal framework of the cell and little is known about how VPS33A modulates SNARE function. The research presented in this thesis therefore aims to determine the applicability of the proposed SNARE model within the cellular environment and to investigate the regulatory mechanisms controlling syntaxin 17 function. To accomplish this, carefully validated fluorescence colocalisation and time-resolved fluorescence lifetime imaging techniques were primarily employed. The limitations of these techniques were also considered for data interpretation and a novel prototype SPAD array technology, designed for high-speed time-correlated single photon counting, was trialled for widefield FLIM-FRET. FLIM-FRET revealed that VAMP8 has been incorrectly assigned as the dominant autophagosomal R-SNARE and VPS33A studies evidence a multi-modal regulation of Stx17 that diverges from other studied syntaxin family modulation mechanisms. A new model of SNARE-mediated autophagosome clearance is therefore proposed, where syntaxin 17 engages with SNAP29 and VAMP7 to drive membrane fusion with the endolysosome in a manner governed by VPS33A and dependent on the phosphorylation status of syntaxin 17.

Acknowledgements

First of all, I would like to thank Paul and Rory for this opportunity. Their constant belief in my capabilities was a huge encouragement through the varied challenges of PhD research. I would also like to thank Colin, who contributed more than he may be aware; his insightful questions during data presentations provided inspiration on more than one occasion. The contribution of Deirdre cannot be overstated, her guidance in the lab and data discussions have been invaluable and her generosity of time has not only astounded me, but also shaped the type of scientist I hope to be. Thanks to Deirdre, Ali and Alicja who took me under their wing from day one and whose friendship kept me sane through the laughter and tears, with Ali always on hand for a motivational speech. Thank you to Laura, Amy and Sophie for their shared resolve that tea and chocolate solves all difficulties, to Werther for his help and understanding with the various plumbing problems over the last year, to Philipp for his efforts to keep me healthy through the write up and to Wilson whose support would extend to picking me up from the lab in the early hours of the morning. And finally, my family, to whom I dedicate this thesis. They inspire me daily with their hard work, generosity and wisdom. Thank you for your unwavering faith and your friendship. You are the giants on whose shoulders I stand.

Declaration

I declare that this thesis embodies the results of my own work and is of my own composition. Work carried out by persons other than myself is clearly indicated by reference to the researcher or their published work.

Signed: _____ Date:

Rebecca Saleeb

Table of Contents

List of Figures

List of Tables

Abbreviations

ADC	Analog-to-digital converter
ADP	Adenosine diphosphate
ALR	Autophagic lysosome reformation
ATP	Adenosine triphosphate
Baf A_1	Bafilomycin A_1
BiFC	Bimolecular fluorescence complementation
CCD	Charge coupled device
CFD	Constant fraction discriminator
CLSM	Confocal laser scanning microscopy
CMA	Chaperone-mediated autophagy
CMOS	Complimentary metal oxide semiconductor
CORVET	Class C core vacuole/endosome tethering
CW	Continuous wave
DNA	Deoxyribonucleic acid
EGFP	Enhanced green fluorescent protein
EMCCD	Electron multiplying charge coupled device
ER	Endoplasmic reticulum
ERES	Endoplasmic reticulum exit site
ERGIC	ER to Golgi intermediate compartment
FCS	Fluorescence correlation spectroscopy
FCCS	Fluorescence cross-correlation spectroscopy
FLIM	Fluorescence lifetime imaging microscopy
FPGA	Field-programmable gate array
FRET	Förster resonance energy transfer
FWHM	Full width at half-maximum
GDI	Guanine displacement inhibitor
GDP	Guanine diphosphate
GEF	Guanine exchange factor
GTP	Guanine triphosphate
HOPS	Homotypic fusion and vacuole protein sorting
IRF	Instrumental response function
LED	Light emitting diode
LIR	LC3-interacting region
LMP	Lysosomal membrane protein
MCC	Manders correlation coefficient
MCP	Microchannel plate
MTC	Multi-subunit tethering complex
NA	Numerical aperture
NSF	N-ethylmaleimide sensitive factor
PALM	Photoactivated localisation microscopy
PAS	Pre-autophagosomal structure
PBS	Phosphate-buffered saline
PCC	Pearson's correlation coefficient
PCR	Polymerase chain reaction
PE	Phosphatidylethanolamine
PI	Phosphatidylinositol
PI3K	Phosphoinositide 3-kinase
PI3P	Phosphatidylinositol-3-phosphate
PMT	Photomultiplier tube

PSF	Point spread function
sCMOS	Scientific-grade complimentary metal-oxide semiconductor
SDM	Site-directed mutagenesis
SDS	Sodium dodecyl sulfate
SEM	Standard error of the mean
SIM	Structured illumination microscopy
siRNA	small inhibitory ribonucleic acid
SM	Sec1/Munc18-like
SMLM	Single molecule localisation microscopy
SNARE	Soluble N-ethylmaleimide sensitive attachment protein receptor
SNR	Signal to noise ratio
SPAD	Single photon avalanche diode
SPIM	Selective plane illumination microscopy
STED	Stimulated emission depletion
STORM	Stochastic optical reconstruction microscope
TAC	Time-to-amplitude converter
TCSPC	Time-correlated single photon counting
TGN	Trans Golgi network
TIRFM	Total internal reflection fluorescence microscopy
TIR	Total internal reflection
T_m	DNA melting temperature
TMD	Transmembrane domain
TTS	Transit time spread
UV	Ultraviolet
WLL	White light laser
WT	Wild-type

Publications

Xu, F., Dongeek, S., Utzat, H., Li. DU., **Saleeb, RS.,** Chen, Y., Coropceanu, I., Dalgarno, PA. and Wong, FNC. Computational fluorescence-lifetime imaging using a small number of photons. *Nature photonics*. [under review].

Mackenzie, MD., Cialowicz, KI., Hamilton, C., Martin, K., **Saleeb, RS**., Paterson L., Duncan RR. And Kar AK. Femtosecond pumped biological laser for use in fluorescence studies. *Scientific Reports*. [under review].

Qiu, Z., Wilson, RS., Liu, Y., Dun, AR., **Saleeb, RS.,** Liu, D., Rickman, C., Frame, M., Duncan, R.R. and Lu, W. Translation Microscopy (TRAM) for super-resolution imaging. *Scientific Reports* **6**, 1-10 (2016).

Yu, H., **Saleeb, RS.,** Dalgarno, PA. and Li, D. Estimation of Fluorescence Lifetimes via Rotational Invariance Techniques. *IEEE Trans. Biomed. Eng.* **63**, 1292-1300 (2016).

CHAPTER ONE:

Introduction

The diverse workings of the cell depend on the proper spatial and temporal organisation of the biological macromolecules contained within[1]. By segregating molecules into functionally distinct organelles, eukaryotic cells can enrich these compartments with the molecular factors and environmental conditions required to execute their functions. This organisation is sustained by shuttling molecules between different organelles or the extracellular environment in small membrane-bound vesicles[2]. In this way, membrane trafficking forms the basis of sub-cellular organisation; its careful regulation is critical to cell health by appropriately targeting proteins across the cell, exchanging cargo with the external environment for inter-cellular communication and maintaining the structural integrity of organelles. Such regulation relies largely on protein interactions to ensure the high flux of cargo is delivered to precise locations at the appropriate time.

As a dynamic process, membrane trafficking can be challenging to study on a molecular level and consequently the published literature is fraught with compelling yet conflicting results. Without a means to directly observe *in vivo* the interactions of non-modified proteins, *in vitro* assays and cell imaging are employed to decipher protein function, but they cannot replicate with certainty the *in vivo* function. As a result, there remain many gaps in our understanding of the membrane trafficking network. I am particularly interested in the membrane fusion events of autophagy, the cell's bulk degradation pathway[3]. Autophagy has great therapeutic potential, with evidence suggesting roles in ageing, oncogenesis, neurodegeneration and immunity[4], however much of the pathway remains incompletely understood, precluding clinical applications. My thesis therefore explores the use, development and limitations of advanced fluorescence microscopy techniques to dissect how proteins coordinate membrane fusion in the final stages of autophagy.

1.1 Membrane trafficking

Proteins are targeted to their cellular residence through encoded signal peptides or structural information[5]. In some cases this can be achieved by direct translocation of cytosolic proteins across an organelle membrane[5]; in all other

cases it is directed by vesicular distribution, and these proteins are transferred to the endoplasmic reticulum (ER) lumen during synthesis[6]. The ER is therefore the entry organelle into the membrane trafficking network, but it also functions as the main source of new membrane synthesis and the site of *N*-linked protein glycosylation[5]. Vesicles are dispatched from ER exit sites (ERES)[7] to the Golgi complex where their cargo is sorted, modified and either returned to the ER, shipped to another organelle or secreted by dispatch in a secretory vesicle that fuses with the plasma membrane in a process called exocytosis[6]. Material can also be acquired from the extracellular environment by the inward budding of the plasma membrane in the process of endocytosis[5]. Just as internally synthesised material is organised by the early secretory pathway, endocytic cargo is organised by the endosomal pathway[5]. Unlike endocytosis and exocytosis, which depend on membrane budding for vesicle formation, autophagy is a seemingly unique membrane trafficking pathway in forming sequestering vesicles *de novo*[8]. This allows cytoplasmic material, including organelles, to be captured and routed to endolysosomes for degradation[5].

Vesicles are dispatched from an organelle by the local deformation of the membrane into a highly curved bud with a constricted neck[5]. Both the distortion of the membrane and cargo selection is usually accomplished by the recruitment of cytosolic coat proteins and their accessory factors[9, 10]. As highlighted in figure 1.1, distinct coat proteins are involved in different trafficking routes through the cell: most notably, COPII coated vesicles assist cargo transport anterograde between the ER, ER-Golgi intermediate compartment (ERGIC) and the Golgi complex[11], COPI assists in retrograde transport between the ER and Golgi complex as well as between Golgi cisternae[12], and clathrin is the main endosomal and post-Golgi complex coat protein[13]. These coat proteins dissociate shortly following budding[14] and the vesicles attach to specific microtubule motor proteins, for directed active transport to their target membrane[15]. Tethering proteins aid membrane recognition and hold the vesicular and target membranes in a docked, closely apposed state[16], readied for site-specific SNARE (soluble N-ethylmaleimide sensitive attachment protein receptor) complex driven membrane fusion[17, 18].

Membrane fusion most commonly results in the complete collapse of the vesicular membrane with the target membrane, forming a continuous bilayer of the two[19].

However, the apparent endocytosis-independent recovery of partially emptied synaptic vesicles[20, 21] has prompted researchers to suggest a second mode of transient fusion, termed kiss-and-run[22]. This controversial theory suggests that secretory vesicles bind transiently to the plasma membrane, creating a pore through which the vesicle contents may pass before the vesicle dissociates from the membrane[21]. However, little is known about how and when this fusion mode is designated.

Though each membrane trafficking pathway is often studied in isolation, the various pathways are heavily interconnected creating the complex network summarised in figure 1.1. For example, endocytosed material can be routed back into the secretory pathway[23], proteins destined for the endolysosome can be delivered by vesicles dispatched from the early secretory pathway[24], other endosomal proteins may reach their target compartment *via* secretion and subsequent endocytosis[24], both secretory and endosomal compartments may donate membrane for *de novo* vesicle synthesis in autophagy[25-27], and autophagic membranes ultimately fuse with the endolysosomal compartment[28]. The integrity of this network, and therefore both organelle function and inter-cellular communication, depends on efficient vesicle targeting, a means of selective cargo incorporation, membrane recognition and regulated membrane fusion. The molecular mechanisms underlying these processes remain to be fully clarified despite extensive research, highlighting the need for tools to detect protein dynamics *in situ*.

1.2 Membrane fusion

1.2.1 Membrane recognition

Membranes are composed of a fluid lipid and protein bilayer of approximately 5 nm width[29] held together by non-covalent hydrophobic and van der Waals interactions[30]. The contributing lipids are predominantly – though not exclusively – phospholipids, which have a hydrophilic phosphate and glycerol head group and two hydrophobic fatty acid tails[5] as depicted in figure 1.2. Covalently bound additions to the phosphate head provide further variation and the resultant

phospholipid composition contributes to a membrane's unique identity[31]. The five major phospholipid variations are sphingomyelin, phosphatidylcholine, phosphatidylserine, phosphatidylethanolamine and phosphatidylinositol (PI)[30]. The latter offers further variation by the reversible phosphorylation of the inositol group in any of the 3, 4 or 5 positions, thereby providing a means to define organelle identity[31]. Controlled phospholipid modifications also enable signal transduction in a wide range of signalling pathways[31] due to the selective binding of effector proteins[32].

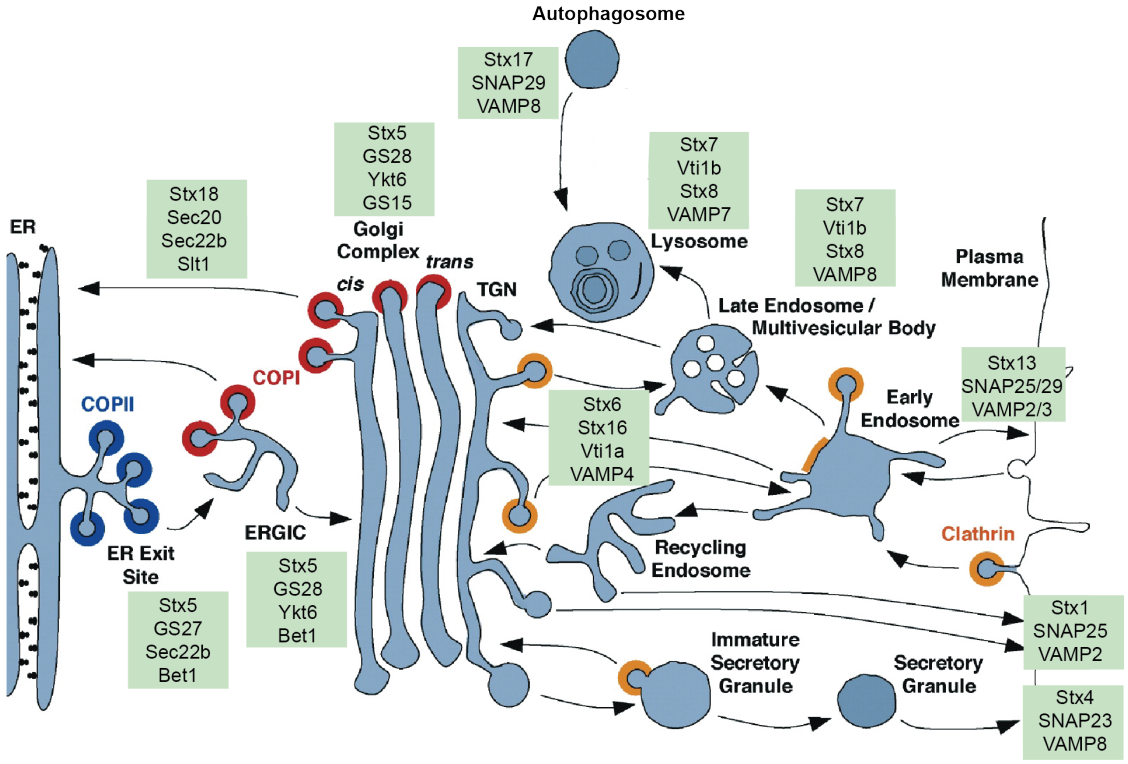

Figure 1.1 The membrane trafficking network in higher eukaryotes Vesicles transport cargo between membrane organelles in a highly specific manner. Depicted are three major membrane trafficking pathways: the secretory pathway (transporting material between the ER and Golgi as well as exocytosis of secretory vesicles), the endosomal pathway (plasma membrane derived vesicles are sorted in the early endosome and transported to the recycling endosome, plasma membrane or lysosome) and autophagy (a sequestration vesicle, the autophagosome, forms *de novo* and fuses with the endolysosome). Different coat proteins mediate budding and cargo recruitment in different parts of the pathway as indicated, COPII in blue, COPI in red and clathrin in yellow. Distinct complexes of SNARE proteins mediate membrane fusion as noted in the green boxes. Figure adapted from Bonifacino and Glick, 2004[33] with information from Hong and Lev, 2014[34].

In addition to its lipid content, the proteins associated with a membrane also contribute to its unique identity. As figure 1.2 shows, proteins may be permanently integrated into the lipid bilayer by insertion of a hydrophobic transmembrane domain during translation or by post-translational covalent attachment to a lipid anchor[30]. Additionally, soluble proteins can transiently associate with the lipid bilayer as peripheral membrane proteins, forming ionic interactions with integral membrane proteins or phospholipids[30]. The topology of a cellular membrane is not therefore fixed upon formation, but can be remodelled by dynamic peripheral protein associations and the lateral diffusion of integral proteins[29].

Members of the Rab and Arf/Arl small GTPase protein families are considered to be molecular landmarks of compartment identity[35]. Indeed, Rab5 and Rab7 consistently identify early and late endosomes respectively[36]. As vesicle trafficking is dependent on successful membrane recognition, the efficient targeting of Rab proteins to the correct membrane is critical[37]. Rabs can associate with membranes *via* a co- or post-translationally linked C-terminal geranylgernayl group for lipid anchoring in the cytosolic leaflet of a membrane[38]. Based on the finding that active GTP-bound Rab has greater stability in the membrane than the inactive GDP-bound form[39], it has been proposed that the distribution of the Rab's cognate GEF (guanine exchange factor) dictates its membrane recruitment by catalysing the replacement of GDP for GTP[39]. A model of rapid membrane sampling mediated by GDI-assisted (guanine displacement inhibitor) membrane dissociation has been proposed, which would enable trial-and-error targeting of a Rab to identify membranes where its cognate GEF resides[35]. In agreement with this model, GEFs have been shown to be the minimal machinery required for Rab targeting to a specific membrane and experimentally re-distributing GEFs correlates with a re-distribution of Rab GTPases[40]. GEFs, in turn, target membranes based on the unique composition of phosphoinositols and membrane-associated proteins[35].

Rab and Arf/Arl GTPases aid membrane recognition during vesicle docking by the recruitment of tethering factors that can bridge partner membranes and aid efficient *trans*-SNARE complex formation[16]. Three types of membrane tethering factors have been identified: long homodimeric coiled-coil proteins that can span up to 200 nm for long-range membrane recognition, multi-subunit tethering

complexes (MTCs) that enable shorter range recognition up to 30 nm, and TRAPP (transport protein particle) complexes, which are MTCs with an intrinsic GEF activity[16]. Indicative of their importance, all types of membrane tethers are found in the secretory pathway, the endocytic pathway and the autophagy pathway[16].

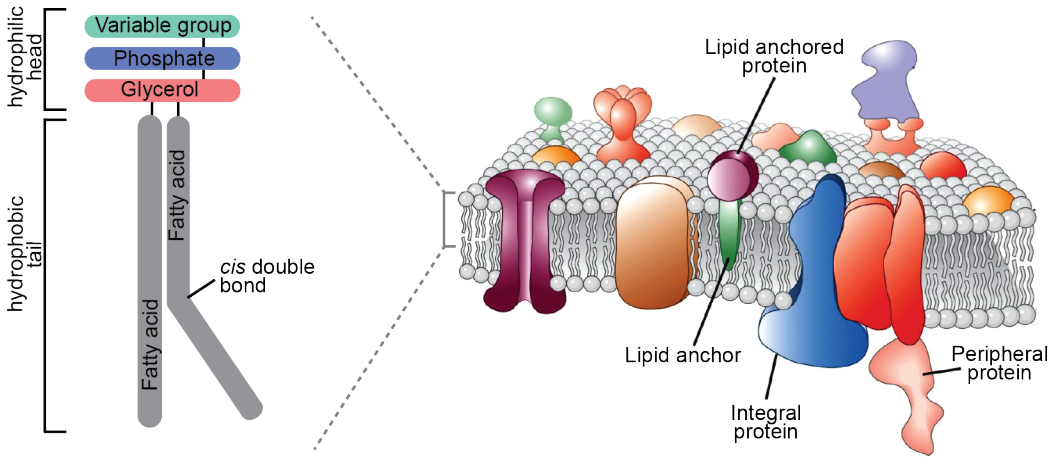

Figure 1.2 Biological membranes Biological membranes are largely composed of a bilayer of amphipathic phospholipids and membrane proteins (right); proteins associate by covalent attachment to membrane lipids (lipid anchor), by insertion into the membrane (integral protein) or by non-covalent association with integral proteins or phospholipids (peripheral protein). Shown left is an enlarged glycerophospholipid. These have two hydrophobic fatty acid tails and a hydrophilic head group containing glycerol, a phosphate group and either choline, serine, inositol or ethanolamine; *cis* double bonds in the fatty acid tail cause kinks that promote membrane fluidity. (Representative phospholipid adapted from Alberts *et al.*[5] and lipid bilayer cartoon taken from Lodish *et al.*[41])

1.2.2 SNARE proteins

Membrane fusion must overcome the electrostatic repulsion between incident membranes and the steric hindrance of membrane associated proteins[42]. The molecular driving force underlying intracellular fusion is highly conserved from yeast to mammals[43, 44] and depends on SNARE proteins, a superfamily of fusogenic proteins[45]. As suggested by their evolutionary conservation, *in vitro* liposome reconstitution assays have identified SNARE proteins as the minimal machinery required for membrane fusion[17]. Since the first SNAREs were identified more than twenty years ago[45], 38 different mammalian family members have now been

reported[34]; these mediate fusion at different sites within the cell via distinct SNARE complexes[45] as noted in figure 1.1. Figure 1.3 indicates the structural diversity of proteins within this family. As can be seen, with the exception of SNAP29[46], they are all integral membrane proteins or anchored by palmitoylation, and they all encode a large cytosolic domain containing at least one SNARE motif[34]. A number of them also encode N-terminal Habc or longin domains, which have a known regulatory function[47-50]. Detailed mechanistic insights on SNARE function have been attained primarily through studies of the exocytic SNARE complex, composed of Syntaxin 1A (Syx1A), SNAP25 and VAMP2[45].

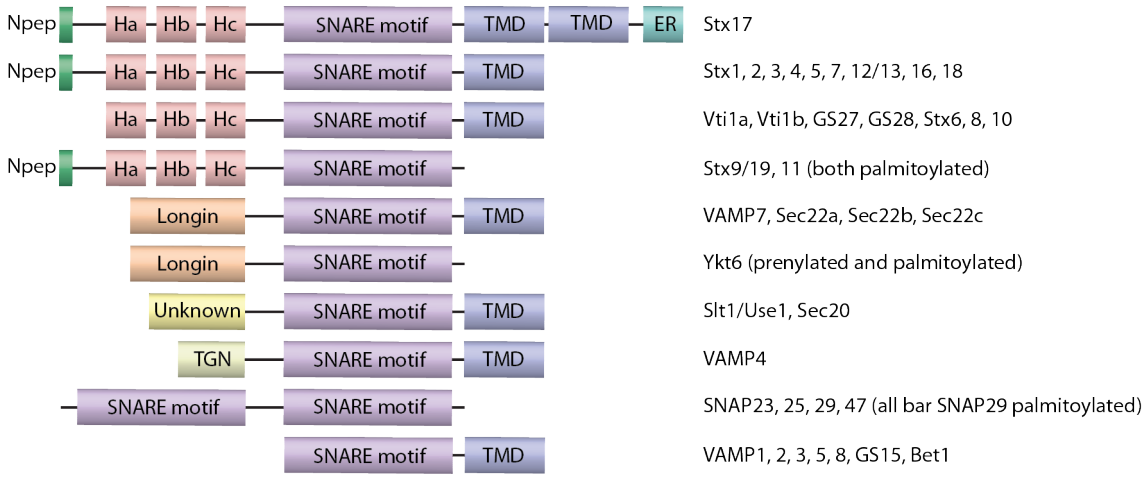

Figure 1.3 The structural diversity of the SNARE family SNARE proteins are defined by their α-helical SNARE motif but can otherwise differ in their size and structure. Many encode putative regulatory domains including the three α-helical Habc domain, the profilin-like longin domain and a variable N-peptide motif (Npep). VAMP4 and Stx17 encode targeting signals for the trans Golgi network (TGN) and endoplasmic reticulum (ER) respectively. With the exception of SNAP29, all contain at least one transmembrane domain (TMD) or a palmitoylation site (noted right). Figure compiled based on the information in Hong and Lev 2014[34] and Steegmaier *et al*. 1998[46].

SNARE theory dictates that a SNARE complex, often referred to as a 'SNAREpin', forms between a SNARE protein resident on the vesicle membrane (v-SNARE) and those resident on the target membrane (t-SNARE)[45], as demonstrated in figure 1.4. SNARE proteins are defined by their SNARE motif, a conserved stretch of 60-70 amino acids in heptad repeats of hydrophobic residues[51, 52]. The significance of this motif for membrane fusion has prompted mimicry of the heptad pattern in

microorganisms to aid pathogenesis by manipulating eukaryotic fusion[53]. The SNARE motifs of monomeric SNARE proteins are largely unstructured, allowing them to mediate complex formation by assembling into an organised quaternary structure[54]. Early work originally hypothesised that they form an anti-parallel link bridging the two membranes[45]. However, it has since been shown in three independent studies, using electron microscopy[55], circular dichroism spectroscopy[56] or spin-labelling[57], that the four SNARE motifs of the exocytic complex actually assemble into a parallel coiled coil α-helical structure. Indeed, crystallisation of the post-fusion exocytic complex, shown in figure 1.4, confirmed this structure[58] and later crystallisation of the post-fusion endosomal complex demonstrated high structural conservation[59]. The coiled coil is reliant on 15 layers of conserved hydrophobic amino acid side chain interactions positioned perpendicular to the helix and centred around a highly polar ionic layer[58]. Furthermore, sequence analyses noted that this central layer, termed the zero-layer, is consistently composed of three glutamine residues and one arginine, each contributed by a different SNARE motif[60]. The conservation of this attribute led to the reclassification of SNAREs into Q-SNAREs and R-SNAREs, which contribute a zero-layer glutamine or arginine respectively[60]. All known functional SNARE complexes are composed of a single R-SNARE and three Q-SNAREs termed Qa, Qb and Qc dependent on their position in the coiled coil[60].

SNARE complex formation appears to be a multi-stage process requiring the step-wise assembly of the binary complex[61, 62], in a manner coordinated by underlying lipid patterning[62], creating a platform for R-SNARE engagement[63]. Subsequent zippering of the four helical coiled coil is apparent from the membrane distal N-terminal towards the membrane proximal C-terminal[64]; this has long been speculated to provide the free energy required to drive membrane fusion[65], likely requiring multiple complexes per fusion event[66]. Precisely how this energy is coupled to membrane fusion remains under investigation, though a recent study demonstrating extension of the coiled coil into the lipid bilayer suggests that straining of the surrounding lipids may make fusion energetically more favourable[67]. Recent observations indicate that zippering is also a multi-step process, involving formation of a partially zippered intermediate that hinges at the zero-layer[68] and may dictate assembly direction[69]. Though still poorly understood,

the completion of zippering is hypothesised to be temporally governed by final-stage regulatory proteins[70]. This would be consistent with vesicle priming, where secretory vesicles are maintained in a readily releasable state by accessory proteins[71, 72]. Further research is needed to confirm these hypotheses centred on the exocytic machinery and determine whether such models are applicable in other cellular membrane fusion events.

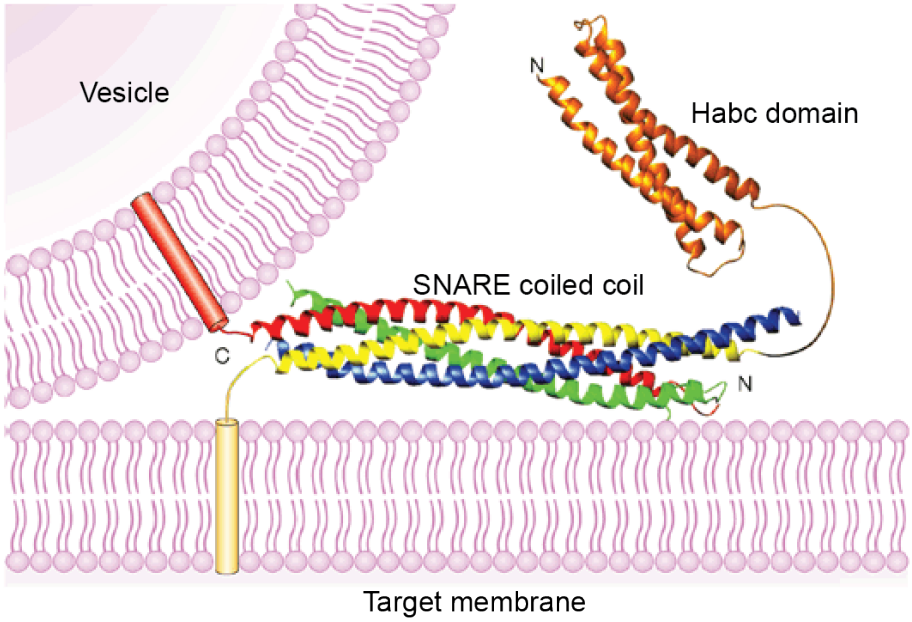

Figure 1.4 The structure of the exocytic SNARE complex A ribbon model created from the crystal structure of the exocytic core *cis*-SNARE complex[58] and the NMR structure of the Habc domain of Syx1A[73] (Syx1A in orange/yellow, VAMP2 in red, SNAP25 N-terminal motif in blue and SNAP25 C-terminal motif in green). Cylinders indicate the transmembrane domains of VAMP2 on the vesicle membrane and Stx1A on the plasma (target) membrane. SNAP25 is also associated with the plasma membrane via palmitoylation (not depicted). The four SNARE motifs assemble into a four helical coiled coil, which drives membrane fusion by 'zipping up' from the N-terminal to the C-terminal. The Habc domain of Stx1A demonstrates a three helical structure. Figure adapted from Rizo and Südhof[74].

Unlike the pre-fusion *trans*-SNARE complex, the post-fusion *cis*-SNARE complex is highly stable, demonstrating resistance to proteolysis, high temperatures and sodium dodecyl sulfate (SDS) dissolution[75]. Indeed, SDS-insensitivity is considered an *in vitro* readout of complex formation[75]. Given the high stability of the fully formed *cis*-SNARE complex, it must be actively disassembled to recycle the proteins for further rounds of fusion[76]. This disassembly, as well as the

deconstruction of incorrect SNARE complexes, is accomplished by the type II AAA+ ATPase, NSF (N-ethylmaleimide sensitive factor)[76]. NSF was identified as an essential protein for vesicular transport in early *in vitro* reconstitution studies; its inhibition by N-ethylmaleimide arrested membrane fusion[77], indicative of the importance of SNARE disassembly. NSF activity requires an adaptor protein, SNAP, that enables SNARE binding[78]. In fact, it was immunoprecipitation with α-SNAP that identified the first SNARE proteins[45]. Both SNAP and NSF are evolutionarily conserved, identified in yeast studies as Sec17 and Sec18 respectively[2]. Unlike SNARE proteins, which show specificity to certain fusion reactions, NSF and SNAP are universally employed within the cell[79, 80].

NSF monomers encode two ATP-binding domains and an N-terminal SNAP-interacting domain[78]. These assemble into a homohexameric cylindrical structure that, when in the ATP-bound state[81], binds SNAP-associated SNARE complexes to form a large 20S complex[82]. Subsequent ATP hydrolysis by the SNARE-proximal domain[83] instigates a conformational change[55] that drives SNARE disassembly. Recent work suggests that this is an efficient process requiring only a single round of ATP hydrolysis to disassemble the complex by a suspected unwinding mechanism[84]. To protect useful *trans*-SNARE complexes from NSF/SNAP disassembly, regulatory proteins are essential to deter formation of the 20S complex[85].

1.2.3 Regulation of fusion

SNARE complex formation must be precisely localised and timed to prevent ectopic fusion events. However, SNARE proteins can bind promiscuously[46, 86-88] within the restrictions of the Qabc- and R-SNARE model[60], indicating that SNARE pairing alone cannot dictate fusion specificity. Both enrichment of SNAREs at the docking site[88] and Sec1/Munc18-like (SM) regulatory protein interactions have been shown to orchestrate this control[89]. There are four major subclasses of SM protein, Munc18 (including Munc18-1, Munc18-2 and Munc18-3), VPS33 (including VPS33A and VPS33B), VPS45 and Sly1[34]. Each protein is approximately 600 amino acids in length and specifically interacts with certain SNARE complexes

to modulate distinct membrane fusion events[34]. For example Munc18-1 is perhaps the most heavily studied SM protein, governing synaptic vesicle fusion with the plasma membrane during neurotransmission[90], while VPS33, VPS45 and Sly1 coordinate fusion events in the endolysosomal system[91], retrograde endosome to trans Golgi network (TGN)[92] and ER to Golgi complex[93] respectively.

Early research attempting to dissect the role of these proteins in membrane fusion produced conflicting results, alluding to the complexity of SM regulation. Munc18-1 or its homologs were found to be essential for neurotransmitter secretion *in vivo*[2, 90, 94], tendering the model that Munc18-1 promotes fusion, which later *in vitro* studies supported[95]. To accomplish this, Munc18-1 appeared to preferentially bind the SNARE bundle, stabilising the complex[96]. However, this model directly conflicted with interaction studies that detected an association between Munc18-1 with a 'closed' conformation of Syx1A, where the N-terminal Habc domain folds back onto the SNARE motif, creating a four-helical structure that precludes SNARE complex formation[47, 97, 98]. Indeed, crystallisation of Syx1A or its yeast homolog demonstrated a closed conformation both when free and when in complex with Munc18-1[48, 49].

Tandem investigations into the regulation of other membrane fusion events failed to reconcile this conflict, instead reporting a different SM binding mechanism altogether. SM protein association with monomeric syntaxin was found to be contingent upon a peptide at the extreme N-terminal of the SNARE[92, 93], distinct from the N-terminal Habc domain. Indeed, despite encoding a Habc domain, no closed conformation has been detected for Syntaxin 4, T1g2p and Syntaxin 8[92, 99, 100], indicating that SM interactions *via* closed conformation binding are not the exclusive means of interaction.

Crystallisation of different SM proteins demonstrated similar overall structure and provided the first hint of the multi-modal binding model that now prevails[89]. The crystal structure of Munc18-1, Sly1 and VPS33A all demonstrate an arch-like structure with a major groove that can encircle the four helical structure of either closed syntaxin or a SNARE bundle, and a separate minor groove that is required for N-peptide associations[49, 101, 102]. This raised the possibility that at least some SM

proteins are capable of binding in multiple modes, which was later experimentally demonstrated[103].

Exactly how these different binding modes contribute to SNARE regulation still remains a matter of debate. As free Syx1A has been shown to fluctuate rapidly between open and closed conformations[104], the SM protein likely shifts the equilibrium to stabilise the required configuration dependent on its binding mechanism[105]. Current models propose that the closed conformation interaction may provide a chaperone function to prevent ectopic complex formation during protein targeting[106-108]. Subsequent transition to SNARE complex binding may then aid zippering by stabilising the binary complex[109]. The N-peptide association is seemingly unnecessary for this role in complex formation[110], yet Syx1A remains associated with the N-peptide of Munc18-1 throughout the SNARE reaction cycle[111]. Indeed, the N-peptide is essential for fusion[112], seemingly by providing a physical tether during binding mode transitions as recent reports suggest[99, 111, 113]. If transition of syntaxin between closed and open states regulates fusogenicity, there should be a trigger for this conversion. In the case of Munc18-1, the domain 3a loop has been implicated in catalysing conversion[114], thereby offering a direct means by which the SM proteins may control SNARE complex assembly. Alternative hypotheses that have been evidenced include serine-14 phosphorylation of Syx1A[115], Munc13-mediated transition[116] and Sec17-regulated loading of the SM protein onto the SNARE complex[85]. It is speculated that this latter mechanism may provide a proofreading step that can alternatively trigger disassembly by the recruitment of NSF[85].

SM modulation of SNARE complex formation focuses largely on the regulation of the syntaxin Qa-SNARE. As a syntaxin family member contributes to every identified mammalian SNARE complex[34], this control mechanism may be sufficient. However, five non-syntaxin SNAREs, namely VAMP7, Ykt6, Sec22a, Sec22b and Sec22c, encode a regulatory longin domain in addition to their SNARE motif[34]. Notably, these are predominantly R-SNAREs (Sec22a and Sec22c are unclassified)[117], suggesting that another level of regulation is provided by the availability of the R-SNARE on the target membrane. Indeed, association of the VAMP7 longin domain with the Rab effector, Varp, has been shown to sandwich the SNARE motif such that it cannot contribute to SNARE assembly[50].

As SM proteins and longin domain interactions preside over SNARE complex assembly, they can therefore ensure the correct location of complex initiation. Neurotransmission additionally requires fine temporal precision of synaptic vesicle fusion with the pre-synaptic membrane. Additional proteins have been implicated in the coupling of this process with calcium signalling[118]. Essentially, complexin stabilises the primed *trans*-SNARE complex, preventing fusion, until it is displaced by a calcium induced conformational change in synaptotagmin-1[118]. Similar timing regulators have not been identified for non-exocytic complexes, which may, or may not, require the same level of timing precision.

1.3 Sub-cellular clearance mechanisms

In order to function, a cell must be able to recognise and respond to damaging stressors. This is partly carried out by its degradation machinery, which selectively destroys harmful cellular components and provides a source of recycled particles when stores are low[3]. To accomplish this, the cell has two known degradation pathways, centred around the lysosome and the proteasome[5]. The proteasome specifically recognises and degrades ubiquitinated proteins, whereas the lysosome catabolises, in bulk, biological macromolecules[5].

The lysosome is a membrane-bound organelle of 0.1 – 0.8 μm in diameter[119]. It has a characteristically low pH of less than 5, where its collection of approximately 50 soluble acid hydrolases function optimally[5]. The inner leaflet of the lysosomal membrane has a thick glycoprotein coat to protect it from hydrolysis[120]. These qualities allow the lysosome to accumulate a pool of non-specific hydrolytic enzymes that are non-functional at the higher pH outwith the lysosome. This therefore enables safe transport of the enzymes through the cell and causes minimal damage if the lysosome is ruptured[5].

The lysosome matures from a late endosome by the vesicular delivery of acid hydrolases from the TGN[24]. Proteins are targeted to the lysosome by the addition of a mannose-6-phosphate (M6P) tag[121], which is recognised by M6P receptors in the TGN, prompting clathrin-mediated transport to the lysosome[122]. Lysosomal-associated membrane proteins (LAMPs) that are essential for the acidification of

the lumen and the export of proteolytic products, can also be delivered via this pathway or transported to the plasma membrane for endocytic transport to the lysosomal compartment[123]. The LAMP vacuolar H^+-ATPase (V-ATPase) drives acidification, generating a proton motive force that also facilitates small molecule export[124], for example, through coupling with the SLC36 family of amino acid transporters[125].

As depicted in figure 1.5, extracellular and intracellular material is directed to the lysosome via endocytosis and autophagy respectively. Autophagy commonly and henceforth refers to macroautophagy, but two other types exist – chaperone-mediated autophagy (CMA) and microautophagy[126]. (Macro)autophagy is unique in requiring the formation of a sequestration vesicle called an autophagosome that subsequently fuses with the lysosome to deliver its contents[126]. CMA and microautophagy instead deliver material directly to the lysosome; CMA is a LAMP2-dependent process that translocates single proteins, delivered by the chaperone protein hsc70, across the lysosomal membrane[127], while microautophagy describes the engulfment of cytoplasmic material by invagination of the lysosomal membrane[128].

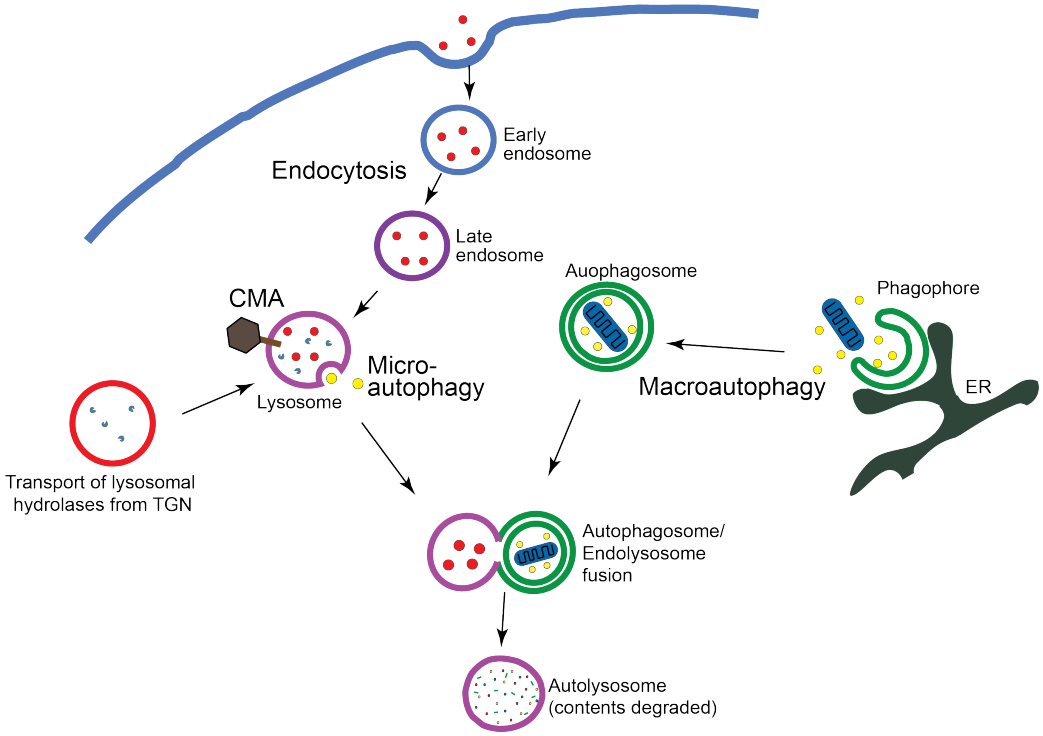

Figure 1.5 Delivery of cargo to the lysosome Multiple membrane trafficking pathways converge on the lysosome to deliver material for degradation. The

lysosome is the cell's degradative organelle and matures from the late endosome by the delivery of lysosomal proteins from TGN-derived vesicles. Endocytosed extracellular material collected by invagination and budding of the plasma membrane is sorted in early endosomes, material destined for degradation is routed to the lysosome *via* the late endosome. Macroautophagy delivers cytoplasmic material to the lysosome in a sequestration vesicle that forms *de novo* by the nucleation and growth of a phagophore that closes to become a double-membrane autophagosome. The lysosome can also directly sequester material by the invagination of its membrane (microautophagy) or LAMP2-assisted (black hexagon) translocation of proteins across the membrane in chaperone-mediated autophagy (CMA).

1.4 The importance of autophagy

The connections between autophagy and diverse disease states[4] have highlighted its importance beyond a simple waste disposal function. However, despite its importance for cell health, the intricacies of the pathway remain poorly understood. Autophagy therefore remains an intensively studied field for its therapeutic potential more than sixty years after it was identified[129]. Both basal and selective autophagy are important for cell health, aiding protein and organelle turnover, energy production during metabolic stress, protection against pathogenesis and unconventional routes to secretion.

1.4.1 Turnover of cellular components

A basal level of autophagy recycles organelles and toxic protein aggregates too large for the single-protein capacity of the proteasome, providing both quality and quantity control[3]. Dysfunction of autophagy is therefore tied to the pathology of various human diseases, including oncogenesis and neurodegeneration, as well as cellular and organismal ageing[4]. Autophagy has been shown to aid the clearance of polyglutamine-based and mutant α-synuclein protein aggregates, which cause Huntington's disease and familial Parkinson's disease respectively[4]. Indeed, the upregulation of autophagy protects against neurodegeneration in fly and mouse models of Huntington's disease[130]. Autophagy similarly protects against oncogenesis by removing malfunctioning mitochondria that cause chromosomal instability through the overproduction of reactive oxygen species (ROS)[131]. An

inability to carry out autophagy due to the monoallelic deletion of the essential autophagy protein, Beclin-1, contributed to 40-75% of breast, ovarian and prostate cancers tested[4]. Conversely, functional autophagy can also promote tumour development where established cancer cells hi-jack autophagy to overcome the hypoxic and low nutrient conditions of pre-angiogenic tumours[132]. There are therefore varied therapeutic applications of autophagy modulation for human disease.

1.4.2 Metabolic stress

Amino acids dissipate metabolic stress by supporting the synthesis of survival proteins[133] and the production of chemical energy in the form of ATP[134] (adenosine triphosphate). Autophagy is therefore upregulated during nitrogen starvation to provide an amino acid reserve from protein hydrolysis[133]. This is exemplified in neonates that depend on autophagy for survival upon the loss of the transplacental blood supply[135].

As shown in figure 1.6, ATP is produced mainly by the oxidative phosphorylation of adenosine diphosphate (ADP) by ATP synthase, driven by a proton gradient across the mitochondrial membrane[134]. For this process to occur, NADH must first be produced by the Krebs Cycle, which in turn requires acetyl-CoA[134]. Acetyl-CoA can be produced by glucose catabolism, lipid catabolism or it can be directly synthesised from the backbone of amino acids[134], as outlined in figure 1.6. As hepatic cells can additionally use alanine to produce pyruvate, which can be converted to glucose by gluconeogenesis for distribution through the body (the glucose-alanine cycle)[134], amino acids assist glucose-derived acetyl-CoA generation, as such they are a valuable store for ATP production during starvation. Indeed, autophagy-incompetent cells can be rescued from starvation with methylpryuvate, a cell permeable substrate for acetyl CoA production[136]. Moreover, it has been shown that both an ATP-sensor, AMPK, and hypoxia play a role in initiating autophagy, providing an alternative means of energy generation where insufficient oxygen is available for oxidative phosphorylation[137, 138].

1.4.3 Protection against infection

A selective form of autophagy, called xenophagy, can be upregulated upon pathogenesis to target polyubiquitinated pathogens for lysosomal degradation[139]. Evidence has been presented linking the upregulation of autophagy to every step of the infection pathway. Prior to host cell invasion, autophagy can be pre-emptively activated by ROS signaling[140], cytokine signaling[141] or pattern recognition receptors (PRRs), which respond directly to pathogen associated molecular patterns (PAMPs) and damage associated molecular patterns (DAMPs)[142]. Upon cell invasion, signals such as galectin-8 identification of plasma membrane damage, can also trigger autophagy[143]. Microorganisms have evolved diverse countermeasures against autophagy, such as the inhibition of autophagosome-lysosome fusion[144], highlighting its importance in impeding pathogenesis.

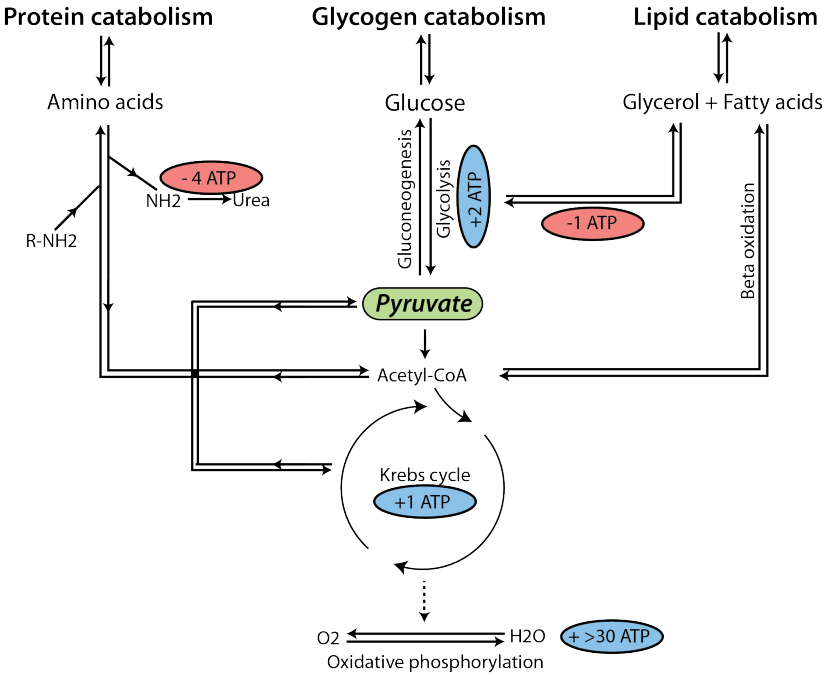

Figure 1.6 Lysosomal catabolites feed into energy production A simplified model of how lysosomal catabolites (amino acids, glucose, glycerol and fatty acids) can feed into cellular metabolism. Net ATP generation (blue) or depletion (red) is indicated for each pathway. ATP is the energy currency of the cell and oxidative phosphorylation produces at least 30 molecules of it per molecule of glucose metabolised. During starvation, amino acids can feed into energy production by the direct synthesis of acetyl-CoA from their backbone or the synthesis of pyruvate *via* glycolysis of glucose produced in the glucose-alanine cycle. Breakdown of fatty acids to generate acetyl-CoA is achieved by beta-oxidation. This figure was compiled with reference to Matthews *et al.*, 1999[134].

In addition to the removal of invading microorganisms, autophagy also plays a role in alerting the immune system to infections *via* major histocompatibility (MHC) class II antigen presentation[145]. MHC class II molecules recruit antigens in a specialised late endosome-like compartment called the MHC class II loading compartment, which can be reached via direct fusion of the autophagosome[145]. Moreover, the assimilation of proteins by the lysosome, is essential for the turnover of MHC class II bound peptides[146, 147]. Such wide-ranging involvement of autophagy in both innate and adaptive immunity has prompted research into novel antimicrobial drugs that initiate the pathway[148].

1.4.4 Unconventional protein secretion

Conventional protein secretion requires a peptide leader sequence that targets the protein to the ER to begin its journey through the secretory pathway[149]. However, a number of cytoplasmic proteins lacking this leader sequence are known to be secreted through different pathways that do not require the ER or Golgi complex[149]. Unconventional secretion by direct protein translocation across the plasma membrane has been described, as well as vesicular delivery that bypasses the ER and Golgi complex[149]. A number of compartments have been identified for the latter mode, including secretory lysosomes, intermediate autophagosomes and a novel compartment termed CUPS (compartment for unconventional protein secretion), all of which contain core autophagy proteins[150-152].

1.5 The coordination of autophagy

Upon initiation of autophagy, a flattened sac-like membrane is nucleated and subsequently expands into a pre-autophagosomal structure called the phagophore[8]. The phagophore membrane curves as it elongates to create an open-ended vesicle that sequesters cargo before closing in on itself and sealing, forming the double-membrane autophagosome[8]. The autophagosome can then fuse with the endolysosome to deposit its contents for hydrolytic degradation[8].

Early studies used the strength of yeast genetics and the conservation of autophagy in yeast and mammals to identify the molecules coordinating autophagy. Ohsumi's Nobel Prize-winning work to develop and use nitrogen starvation-resistant mutant strains of *Saccharomyces cerevisiae* identified many of the autophagy-related (Atg) genes[153]. With refined techniques, more than 30 autophagy genes have now been identified in yeast[154]. However, as autophagy in yeast is centred on the vacuole, there are marked differences between yeast and mammalian autophagy and as a result, not all autophagy proteins are conserved between the two[154]; table 1.1 provides a complete list of the known mammalian autophagy proteins. As further discussed below, despite these insights into the molecules underlying autophagy, much remains to be discovered with regard to how they coordinate it.

1.5.1 Nucleation of the phagophore

The site of nucleation is one of the key differences between autophagy in yeast and mammals. In yeast, it occurs at a single site on the vacuolar membrane referred to as the pre-autophagosomal structure (PAS)[155], whereas in higher eukaryotes it occurs at multiple sites throughout the cell[156]. The position of these sites in higher eukaryotes are reportedly associated with endoplasmic reticulum (ER) membrane convolutions named omegasomes[157], which frequently coincide with ER-mitochondrial contact sites[158]. The most temporally upstream indicator of nucleation is the presence of VMP1[159] (figure 1.7(i)), the aberrant expression of which is sufficient to induce autophagy in nutrient-replete cells[160]. Direct evidence is still sought to determine whether the omegasome is a pre-existing structure that VMP1 is localised to or is formed consequent to VMP1 localisation. However, as omegasomes are reportedly rich in phosphatidylinositol-3-phosphate (PI3P)[157], a compelling model suggests the latter, due to the downstream enrichment of PI3P following a cascade of autophagy protein recruitments to the site of VMP1 localisation[159], as shown in figure 1.7.

Table 1.1 The core mammalian autophagy proteins A list of all mammalian autophagy proteins identified to date and a brief description of their putative functions in autophagy, compiled based on the review of Feng *et al*[154].

Human	Yeast	Complex	Suggested role
UL1/2	Atg1	ULK1/2 complex	Serine-threonine protein kinase
Atg13	Atg13	ULK1/2 complex	Regulates ULK1/2 activity
FIP200	Atg17	ULK1/2 complex	Scaffold protein and most upstream autophagy protein
Atg101	-	ULK1/2 complex	Interacts with Atg13 to stabilise the complex
Beclin-1	Atg6	PI3K complex	Regulates the activity of the complex
Vps34	Vps34	PI3K complex	Catalyses the conversion of PI to PI(3)P
p150	Vps15	PI3K complex	Membrane anchor
Atg14/Barkor	-	PI3K complex	Targets the complex to the ER
UVRAG	Vps38	PI3K complex	Negative and positive feedback regulation of Vps34 activity
Atg5	Atg5	Atg16L complex	Conjugates with Atg12 in first steps of Atg16L complex formation
Atg16L	Atg16	Atg16L complex	Complexes with Atg12-Atg5 forming multimeric E3-ligase for LC3 lipidation
Atg12	Atg12	Atg16L complex	Conjugates with Atg5 C-terminal in first steps of Atg16L complex formation
mAtg9	Atg9	-	Uniquely membrane-bound under normal conditions with unknown function
Atg7	Atg7	-	E1-like enzyme prepares Atg12 and LC3 for their conjugations
Atg10	Atg10	-	E2-like enzyme that conjugates Atg12 with Atg5
Atg4	Atg4	-	Cysteine protease prepares pro-LC3 for lipidation and cleaves PE-conjugated LC3-II
WIPI2	Atg18	-	Positively regulates LC3 lipidation
Atg3	Atg3	-	E2-like enzyme that conjugates LC3 with PE
LC3	Atg8	-	Diverse roles in cargo recruitment, transport and possibly phagophore closure
WIPI1	Atg2	-	WD-40 repeat-containing protein that interacts with PI(3)P

An exhaustive study by the Ohsumi laboratory dissected the hierarchy of Atg protein recruitment in yeast to ascertain the proteins behind the nucleation event[161]. Together with complementary studies in starved mammalian cells[162], these propose that the ULK1/2 complex (or Atg1 complex in yeast) is the first autophagy machinery to translocate to the nucleation site. This complex was first characterised using yeast two-hybrid screens, identifying its constituents as Atg1, Atg13 and Atg17[163]. Atg1 or ULK1/2 in higher eukaryotes, confer the name to the complexes and contribute the essential kinase function required for membrane nucleation[154, 163]. Atg13 activates Atg1 in yeast[164] and enables inter-complex linkages that are essential for PAS organisation[165]. The role of Atg13 is less apparent in mammalian cells, where regulatory mTOR phosphorylation of ULK1/2 queries the need for Atg13 in regulation[166], however, Atg13 is required for autophagy in higher eukaryotes[166] and its expression is stabilised by the presence of an additional complex constituent not found in yeast called Atg101[167]. The final

component of the complex is Atg17 in yeast or the heterologous FIP200 in mammalian cells[168], which both provide a scaffold function essential for the localisation of other autophagy proteins to the nucleation site[161].

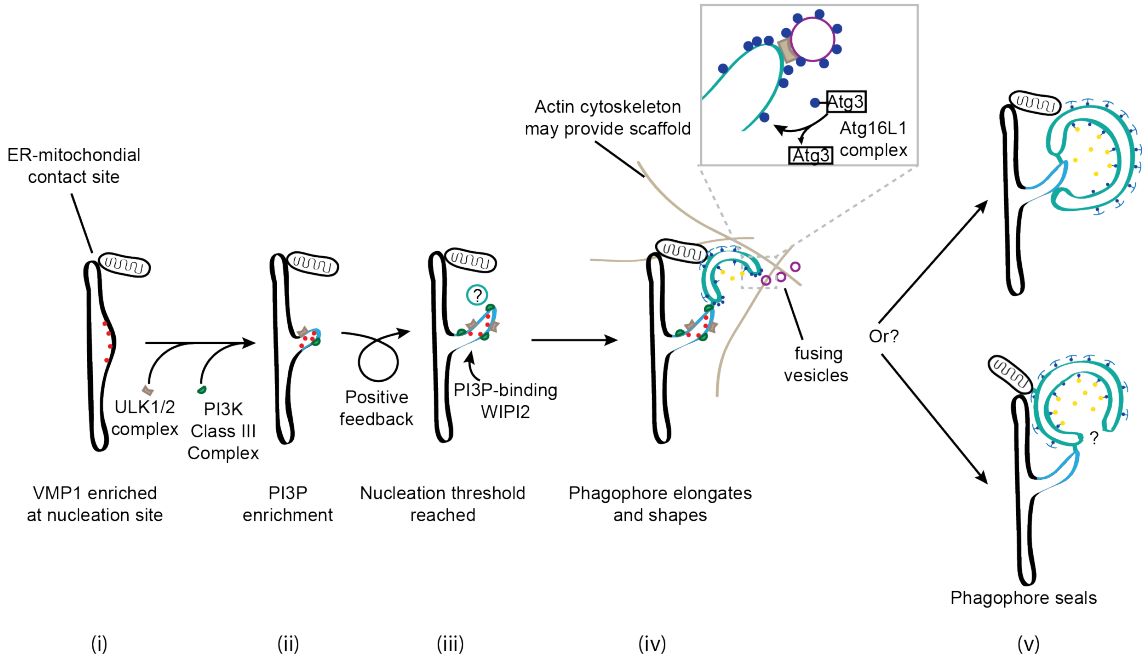

Figure 1.7 A summary of phagophore development A cartoon overview combining the suggested mechanisms underlying phagophore nucleation and growth. As indicated with question marks, some aspects are still poorly understood. (i) VMP1 (red dots) is the first molecule to target the nucleation site, commonly found at ER-mitochondrial contact sites. (ii) Sequentially recruited core autophagy complexes promote PI3P enrichment (blue membrane), which further enhances protein recruitment in a positive feedback loop. (iii) PI3P-binding effectors translocate, such as WIPI2, causing membrane nucleation by an unknown manner. (iv) The phagophore elongates using lipid likely donated from incoming vesicles and direct links to organelles; enriched LC3 (blue dots) at the phagophore tips may control growth. Outer membrane LC3-binding proteins and the actin cytoskeleton may assist shaping, though inner-membrane LC3 alternately binds cargo and it is unclear how LC3 recognises its position. Inset demonstrates the suggested tethering of incoming vesicles by the ULK1/2 complex and the LC3 lipidation reaction catalysed by the WIPI2-recruited Atg16L1 complex. (v) The phagophore seals by an unknown mechanism. It remains unclear whether the omegasome forms part of the autophagosome or not.

The PI3K (phosphoinositide 3-kinase) class III complex colocalises following translocation of the Atg1 or ULK1/2 kinase complex to the nucleation site[161].

Though the PI3K and ULK1/2 complexes can be regulated by separate mechanisms discussed further in section 1.5.2, this consistent hierarchy in their recruitment suggests that the ULK1/2 complex promotes recruitment of the PI3K complex. Indeed, ULK1 phosphorylation of Ambra1 has been shown to trigger the release of microtubule-associated PI3K complexes to allow their translocation to the nucleation site[169]. Moreover, the HORMA domain of yeast Atg13 has been shown to bind Atg14, a subunit of the PI3K complex, thereby aiding complex recruitment[170].

The mammalian PI3K core complex consists of Beclin-1, VPS34 and p150, which are homologous to the yeast Atg6, Vps34 and Vps15 respectively[154]. Due to the activity of the lipid kinase PI3K, this complex causes local enrichment of PI3P[157] (phosphatidylinositol-3-phosphate) by catalysing its conversion from PI (phosphatidylinositol)[171]. p150 enables membrane anchoring via N-terminal myristoylation[172], and the complex is stabilised and activated at the nucleation site by an interaction between Beclin-1 and VMP1[173]. Beclin-1 also enables variants of the PI3K complex to be formed by mutually exclusive interaction with either Atg14 or UVRAG (Vps38 in yeast)[174], which participate in phagophore nucleation[175] and autophagosome maturation[176] respectively, though contrary studies contest the latter[177].

The local enrichment of PI3P enables progression from nucleation to phagophore growth by recruiting essential effectors with PI3P-binding WD-40 repeat domains, such as WIPI2[178] and DFCP1[157] (refer to figure 1.7(iii-iv)). The structure of PI3P has also been postulated to encourage ER membrane budding in PI3P-rich regions, causing the characteristic deformation of the omegasome[8] shown in figure 1.7. Such membrane curvature triggers a positive feedback loop for further PI3P enrichment that augments membrane remodelling by promoting further binding of curvature-sensitive autophagy proteins including mammalian Atg14[179] and yeast Atg1[180]. Moreover, the reported association of Atg13 with PI3P also drives this positive feedback[181].

Despite having clear importance in the nucleation of the phagophore, the role of the omegasome in later stages of autophagy is less clear. It is now widely agreed that the omegasome and phagophore are physically connected, based on 3D electron microscopy tomography studies observations[182, 183]. However, whether

the omegasome feeds phagophore growth or detaches to become part of the phagophore is yet to be determined (see figure 1.7(v)).

1.5.2 Phagophore nucleation control mechanisms

Phagophore nucleation must be sensitive to a wide range of signals both internal and external to the cell and central to this regulation is the mammalian target of rapamycin (mTOR)[163]. TOR is an evolutionarily conserved protein kinase of the phosphatidylinositol kinase-related kinase (PIKK) family[184]. It constitutes part of two distinct complexes, TORC1 and TORC2[185]. These two complexes have very different functions; TORC1 is a nutrient-sensor that governs autophagy induction[186] and cell cycle progression[187], while TORC2 plays an important role in the organisation of the actin cytoskeleton[188]. As a specific TORC1 antagonist, rapamycin is a useful tool for the stimulation of autophagy in non-starved cells[189].

mTORC1 is a potent inhibitor of autophagy and it must therefore be itself inhibited under stress conditions[163]. This is achieved by the TSC complex, which integrates various stress signals as overviewed in figure 1.8, and accordingly terminates the activity of the mTORC1 activator, Rheb[184]. In this way, mTORC1 is responsive to growth factor signalling, nutrient status, energy homeostasis, hypoxia, DNA damage and redox imbalances[184]. Conversely, in nutrient replete conditions, mTORC1 represses autophagy via two modes. Firstly, it inhibits by phosphorylation the core phagophore nucleation proteins ULK1/2 and Atg14[163, 190]. Secondly, it phosphorylates the transcription factor, TFEB, preventing its nuclear translocation[191], consequently reducing the expression of more than 400 genes of the coordinated gene expression and regulation (CLEAR) network, including lysosomal genes and autophagy regulators[192]. Efficient autophagy termination is reliant on a negative feedback loop on mTORC1 activity provided by the changing lysosomal nutrient status, which triggers translocation of mTORC1 to the lysosomal membrane where Rheb can reactivate it[193].

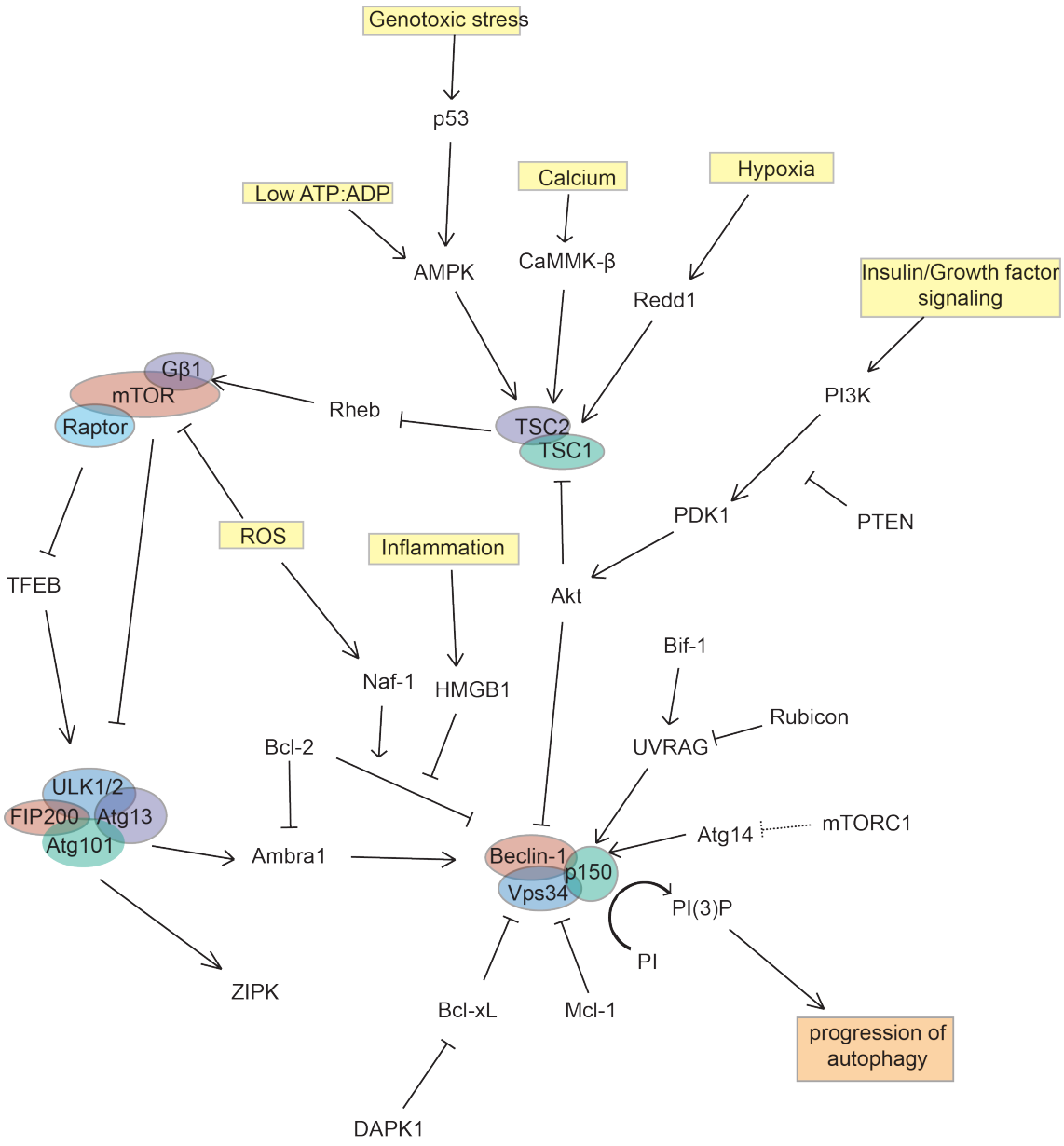

Figure 1.8 The initiation of autophagy A summary of the signalling network that controls the initiation of phagophore nucleation, compiled based on the reviews of Wullschleger *et al.*[184] and Kang *et al.*[194] Arrows indicate a promotory effect or interaction, while T-bars indicate an inhibitory one. The TSC complex integrates various stress signals to activate autophagy through the inhibition of the mTORC1 complex (mTOR, Raptor and GβL). The resulting enrichment of PI3P (phosphatidylinositol-3-phosphate) by the sequential recruitment of the ULK1/2 complex (ULK1/2, Atg13, Atg101 and FIP200) and the PI3K Class III complex (Vps34, Beclin-1 and p150) causes phagophore nucleation.

mTORC1-mediated inhibition of autophagy is complemented by other mechanisms to suppress membrane nucleation, which are largely centred around Beclin-1 regulation[194]. As a core component of the PI3K class III complex, Beclin-1 is essential for phagophore nucleation[154]. The activity of both Beclin-1 and the

proteins that regulate it are determined by their ubiquitination and phosphorylation status, offering several layers of control[194]. Sequestration of Beclin-1 to prevent PI3K class III complex formation is a key mechanism for its regulation. For example, the anti-apoptotic proteins Bcl-2 and Bcl-X_L[195] bind Beclin-1, unless starvation signals its dissociation[196, 197]. Similarly, Akt phosphorylation of Beclin-1 in response to normal growth factor signalling, promotes its sequestration by vimentin[198].

This simplified overview of autophagy initiation alludes to the multi-level regulation over phagophore nucleation that enables single stress signals to efficiently trigger autophagy. Redox signalling alone, for example, can affect mTOR activity[199], NAF-1 promotion of the Bcl-1/Beclin-1 interaction[200] and NF-κB transcriptional control over Beclin-1[138].

1.5.3 Phagophore development and cargo recruitment

During phagophore development, the double-membrane structure must be lengthened, shaped and closed, in order to accommodate recruited cargo. The lipid source for phagophore elongation has long been sought and though various cellular structures have been implicated, as discussed below, no single consensus over the primary lipid source has been attained[154]. Lipid redistribution is dependent on either vesicle carriers fusing to the growing phagophore or direct physical connections between the donor organelle and the phagophore, both of which have been evidenced[25, 26, 201].

The 3D electron microscopy tomography studies that first described the tubular connections between the ER omegasome and phagophore[182, 183] have recently been extended, demonstrating physical connections between the phagophore and ER exit sites, Golgi complexes, mitochondria, late endosomes and lysosomes[201]. All of these organelles are therefore well placed to donate lipid, supporting earlier evidence that mitochondria[202], ER exit sites[203, 204] and Golgi complexes[205, 206] may be involved. It is likely that an assortment of organelles contribute lipid and it has been suggested that the membrane source may in fact vary dependent on the initiation signal[202].

In addition to direct lipid transfer, vesicular lipid transfer is also well evidenced. Early work to identify a membrane source by tracking the origin of Atg9, the only autophagy transmembrane protein, implicated its redistribution from the TGN and late endosomes[25] via Atg9-positive vesicles[207, 208]. Moreover, plasma membrane-derived Atg16L1-positive vesicles and Atg9-positive vesicles, produced via clathrin-mediated endocytosis, have been detected in higher eukaryotes[26, 27]. Such vesicles reportedly aid phagophore elongation by SNARE-mediated membrane fusion with the growing membrane[209, 210]. It is speculated that the recycling endosome may be a hub of autophagy precursor vesicle coordination; the plasma membrane derived vesicles are first routed here[27] and sorting nexin 18 (SNX18) has demonstrated a key role in mediating this[211]. Moreover, precursor vesicles originating from the recycling endosome contain the autophagy marker, LC3[211]. The presence of LC3 on fusing vesicles may promote docking at the phagophore membrane via LIR-motif (LC3 interacting region) dependent interactions with ULK1/2, Atg13 and FIP200[212]. This docking mechanism may be assisted by structural complementation of the incoming vesicle with the Atg1/ULK1 complex[180], as depicted in figure 1.7(iv).

The expanding phagophore membrane is organised into a cup-shaped sequestration vesicle (figure 1.7(iv)), requiring a means of directing elongation in the absence of any detected coat proteins[8]. Though the mechanism remains a matter of debate, the yeast Atg8 protein appears to play a key role[213], carried out in higher eukaryotes by LC3[214]. The suspected recruitment of LC3 to the leading edge of the phagophore, directed by the curvature-sensing Atg3, may offer a basis for elongation regulation[215]. Reconstituted Atg8 conjugation on artificial membranes indicates that it may shape the vesicle[216]. Atg8 appears to form a stiff coat-like structure on the convex outer membrane, requiring components of the Atg16L1 complex, which is out-competed by binding cargo on the concave inner membrane[216] (depicted in figure 1.7(iv)). Perhaps functioning in conjunction with this, evidence has also been presented that an actin-based scaffold forms to shape phagophore growth in a PI3P- and LC3-dependent manner[217, 218], explaining earlier reports that actin depolymerisation abolishes new autophagosomal vesicle development in starved cells[219].

LC3 is transferred from Atg3 to the phagophore by conjugation to phosphatidylethanolamine (PE)[220]. This follows an ubiquitin-like conjugation reaction catalysed by the Atg16L1 complex[156, 221], which is recruited by the PI3P-binding effector WIPI2[178, 222], thereby coupling this process to phagophore nucleation. LC3 is pre-processed for conjugation by an Atg4 cysteine protease cleavage at the carboxyl-terminal to expose a glycine residue that will form an amino bond with the PE head group[223, 224]. Atg4 later recycles LC3 by cleaving it from the outer autophagosomal membrane[223]. However, as LC3 is also present on the inner membrane, it remains associated with the compartment throughout its lifecycle, therefore offering a useful marker of autophagy[225].

As the phagophore develops, cargo must be recruited requiring either selective autophagy to target pathogens, protein aggregates and damaged organelles, or bulk autophagy to recycle cytosolic material randomly sequestered upon nutrient depletion[154]. Known as the cytoplasm to vacuole targeting (Cvt) pathway in yeast, selective autophagy in higher eukaryotes is named according to the target material, such as mitophagy[226] and xenophagy[227] for mitochondria and pathogens respectively. LC3 or Atg8 can directly sequester cargo via a conserved LC3-interacting region (LIR) or Atg8-family interacting motif (AIM) on the targeted cargo[228], encoded for example by the mitochondrial outer membrane proteins Nix and FUNDC1[229, 230]. Where the cargo lacks such a motif, adaptor proteins encoding it facilitate cargo recruitment. For example, p62 and NBR1 recognise protein aggregates[228, 231], while NDP52 and optineurin sequester pathogens[139, 232]. Notably, an Atg5-binding protein called Tecpr1 has recently been shown to facilitate xenophagy[233], implying that LC3-independent cargo recruitment mechanisms exist.

Once the phagophore has grown sufficiently to enclose its cargo, early autophagy proteins dissociate and the phagophore closes in upon itself, sealing to form the complete autophagosome[8]. As Atg8/LC3 is the only remaining autophagy protein, it is speculated to be involved in the closure, where its tendency towards self-association *in vitro* has prompted theories that LC3-driven hemi-fusion makes membrane fusion thermodynamically feasible[234]. However, the occurrence of this under physiological conditions remains controversial[209]. Membrane fusion events are generally facilitated by SNARE (soluble NSF attachment protein receptor)

proteins and indeed, silencing of the SNARE protein syntaxin 13 causes an accumulation of phagophores[235]. However, sealing of the phagophore is an unusual membrane fusion event and is perhaps topologically more similar to fission in vesicle budding. As ESCRT (endosomal sorting complex required for transport) complexes enable such budding events, they are attractive candidates to facilitate phagophore closure[8]. Moreover, both ESCRT-0 and ESCRT-II have PI3P-binding subunits[236] that could assist phagophore targeting, and mutant ESCRT complex phenotypes indicate an accumulation of autophagosomal structures[237]. As no single model has yet garnered consensus, further research is still required to elucidate the poorly understood mechanism by which the open phagophore transitions to the closed autophagosome.

1.5.4 Autophagosome fusion with the endolysosome

Once formed, the autophagosome is transported to the peri-nuclear region where lysosomes cluster upon nutrient starvation[238]. This reportedly occurs in a microtubule-dependent manner via an association with autophagosomal LC3[239]. Though it is unclear how autophagosomes are recognised, only complete autophagosomes and not open phagophores are targeted, indicating that spatial separation may help to prevent ectopic fusion of the phagophore with the lysosome[240].

The terminal compartment responsible for autophagic cargo degradation differs between yeast and higher eukaryotes, fulfilled by the vacuole or lysosome respectively[154]. The existence of an autophagosome-endosome fusion intermediate, termed an amphisome, was demonstrated by the ability of endocytosed β-galactosidase to degrade autophagy-sequestered [^{14}C]lactose upon lysosome fusion inhibition[241]. Amphisomes acquire some lysosomal characteristics such as reduced pH[242] and it is unclear whether or not they can mature into lysosomes or must undergo a second fusion step. However, as mannose-6-phosphate receptors (M6PRs) are commonly used to differentiate late endosomes from lysosomes[243], they have been used to demonstrate that amphisome formation is not a prerequisite for lysosomal targeting[244], though conflicting work[245] has left the dominant target compartment under debate.

As with any membrane fusion event in the cell, autophagosome-endolysosome fusion is facilitated by the formation of a SNARE protein complex that bridges the apposing membranes and mechanically drives their amalgamation[89]. As described in section 1.2.2, distinct SNARE complexes mediate different membrane fusion events. The SNARE proteins governing endosomal fusion events are syntaxin 7, syntaxin 8, Vti1b and VAMP8[59]; while the replacement of VAMP8 for VAMP7 has been reported to instead specify late endosome to lysosome fusion[246]. These findings offered a number of possible endolysosome-resident SNAREs that may also be implicated in autophagy, however, the lack of clarity over the dominant phagophore lipid source long defied attempts to identify a corresponding autophagosomal SNARE protein with which they may complex.

Knockdown studies of the endosomal SNARE complex components indicate that syntaxins 7 and 8 are not required for autophagy completion[247], suggesting that the autophagosome may contribute the syntaxin family protein, thereby narrowing the search. Indeed, recent studies into ER-derived syntaxins in higher eukaryotes finally elucidated the autophagosomal SNARE as Stx17[248, 249]. The identification of Stx17 prompted immunoprecipitation-based determination of its binding partners, required to untangle the conflicting studies that had hitherto proposed VAMP7, VAMP8 and Vti1b to be involved[247, 250]. Based on this work, Stx17 in complex with SNAP29 and VAMP8 is the SNARE model widely agreed to facilitate autophagosome-endolysosome fusion in mammalian cells[248], complexed as shown in figure 1.9.

Stx17 is ER-resident in nutrient replete cells[46] and has been controversially reported to associate with the phagophore upon autophagy induction[158], implying that a regulatory mechanism must be at play to prevent ectopic fusion events. Indeed, it has been proposed both that trafficking of VAMP8 is nutrient-sensitive[251] and that glycosylation of SNAP29 reduces SNARE complex formation[252], tying autophagosome clearance to cellular nutrient status, but not clarifying how fusion is restricted to the closed autophagosome. Furthermore, the known promiscuity of SNAP29 interaction with syntaxins[46] is at odds with this protein providing a regulatory function. Aberrant fusion can also be minimised by the specific targeting of tethering factors and SM proteins that promote SNARE complex assembly[34]. Indeed, the endolysosomal SM protein VPS33A has been shown to

interact with Stx17[177] and facilitate autophagosome-endolysosome fusion[176]. Furthermore, VPS33A resides on the HOPS complex, which in addition to Atg14 has been proposed to promote fusion *via* membrane tethering[177, 179, 253].

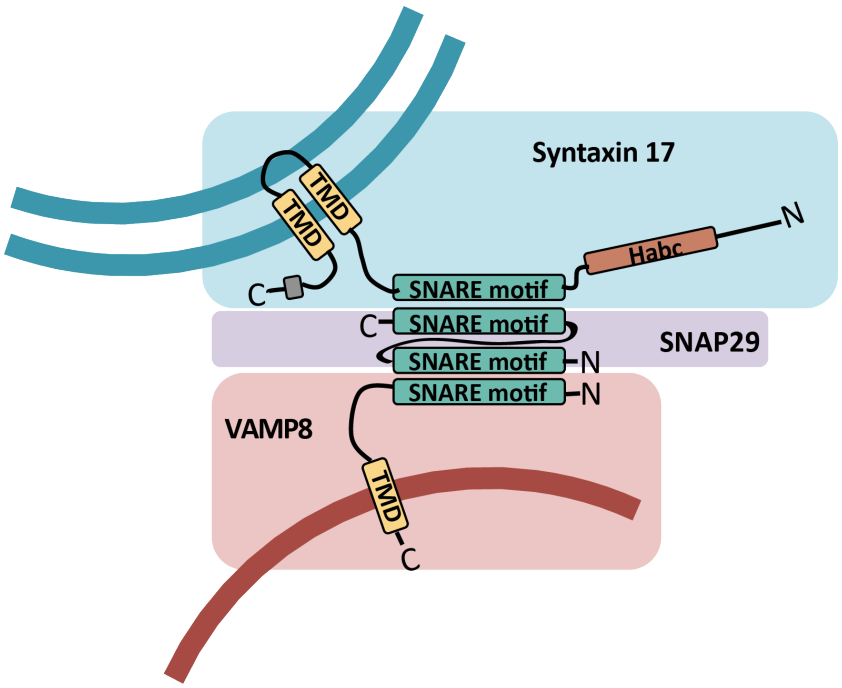

Figure 1.9 The autophagosomal SNARE model A cartoon depicting the established model of SNARE-mediated fusion between the autophagosome (blue) and the endolysosome (red), the diagram is not to scale. The two transmembrane domains of syntaxin 17 are proposed to integrate into the autophagosomal membrane in a hairpin conformation, recruited from the cytosol. Stx17 mediates fusion with the endolysosome by interaction with the two SNARE motifs of SNAP29 (recruited from the cytosol) and the SNARE motif of VAMP8, an endolysosome-resident SNARE. This model is based on the research of Itakura *et al*., 2012[248].

1.5.5 Lysosome clearance and recycling

As multiple lysosomes fuse with each autophagosome, lysosomes are quickly depleted in the process of autophagy[254]. Without a mechanism for lysosomal homeostasis, the lysosomal compartments become fewer and larger structures[254]. Lysosomes are therefore regenerated from healthy autolysosomes by a process of autophagic lysosome reformation (ALR)[254], while damaged lysosomes are removed by lysophagy[255], a selective form of autophagy. ALR is triggered in response to

mTOR reactivation following the autophagic replenishment of needed nutrients[256]. However, if mTOR inhibition is chemically maintained with rapamycin, the lysosome is unable to undergo reformation[254]. Upon the initiation of ALR, autophagy is attenuated and tubular extrusions extend from the autolysosome from which lysosomal vesicles bud[254]. Interestingly, these extrusions have little content, near-neutral pH and membranes absent in LC3, prompting them to be labelled as proto-lysosomes that mature upon delivery of vesicle-trafficked membrane proteins and soluble hydrolases[254]. Separation of the autolysosome and proto-lysosome must be intricately controlled, however little is known about how this is accomplished beyond a dependence on the microtubule network, Vps34, clathrin and phosphatidylinositol-4,5-bisphosphate[257, 258].

1.6 Aims

The key proteins underlying autophagosome-endolysosome fusion have been established and it is widely accepted that Stx17, SNAP29 and VAMP8 form the autophagosomal SNARE complex[248] facilitated by the SM protein, VPS33A[177]. However, this model is based solely on *in vitro* co-immunoprecipitation alongside knockdown and fluorescence colocalisation microscopy studies. To date, no method has been employed to detect protein interactions within the spatiotemporal control of the cell. My thesis therefore uses the most robust microscopy tools available to determine both the applicability and the mechanistic details of this model *in situ*. In particular, I sought to address a number of outstanding questions concerning the mechanism of autophagosome-endolysosome fusion: do Stx17, SNAP29 and VAMP8 interact at the autophagosome-lysosome fusion site *in situ*? How and when is Stx17 recruited to the autophagosome? And how is the assembly of the autophagosomal SNARE complex regulated?

As autophagy is dependent on functioning endosomal and secretory systems[28, 122, 259], its interconnected nature necessitates that caution is used when interpreting protein function from techniques that cannot detect protein interaction, such as fluorescence colocalisation and siRNA knockdown. For example, non-functional

colocalisation with autophagic proteins may result from the completion of an upstream function elsewhere in membrane trafficking. Similarly, protein knockdown may disrupt a membrane trafficking event that has a knock-on impact on autophagy. Techniques such as fluorescence colocalisation and siRNA knockdown can be insightful in combination with *in vitro* protein biochemistry to ascertain the capacity for protein interactions; however, SNARE proteins are known to promiscuously form non-functional SNARE complexes both *in vitro* and *in vivo*[46, 86-88] and they may have more than one role within the cell[34], complicating the interpretation of function. These limitations highlight the need to confirm SNARE protein interactions within the spatiotemporal framework of the cell.

In order to study protein interactions *in situ*, carefully validated advanced microscopy techniques have been applied to the study of autophagosome-endolysosome fusion. Most notably, the detection of Förster resonance energy transfer (FRET) between interacting proteins *in situ*, using fluorescence lifetime imaging microscopy (FLIM) as described in chapter two. FLIM-FRET offers a useful tool to extend the information that can be obtained by fluorescence microscopy, however it is infrequently used in the standard biology laboratory. As FLIM-FRET cannot achieve real-time detection of protein interactions, I speculate that many consider the advantages of its use to be outweighed by its complexity, expense and slow speed. I therefore explore in chapter six the applicability of a new technology to mainstream FLIM-FRET.

CHAPTER TWO:

Microscopy theory and method validation

While the field of optics can be traced back as far as ancient Greece, its application to microscopy was not until the 16-17th century[260]. Records suggest that the first compound microscope, combining an eyepiece and an objective lens, was designed by Hans Jensen and his son Zacharias in the late 16th century[260], though the term 'microscope' was not yet in use. The Italian Academia Dei Lincei coined the term microscope in the early 17th century and the use of microscopy for scientific research began with Robert Hooke and Antony van Leeuwenhoek in the same century[260].

Once early challenges in producing high quality lenses was overcome and high magnification microscopes were established, the study of cellular structure was impeded by the lack of contrast. Different routes were taken in the late 19th and early 20th centuries to achieve the required contrast. These included, altering the light absorption properties of cellular structures with stains[261], translating the phase shift of light as it passes through the sample into signal contrast[262], and detecting the autofluorescence of cells (their intrinsic fluorescence) using the first fluorescence microscopes[263]. The evolution and refinement of these methods enabled the study of sub-cellular structures. Key among this progress has been the development of specific fluorescent probes for targeted labelling using antibody-conjugated fluorescent dyes[264] and, later, encodable fluorescent proteins[265]. With the advances of microscopy technologies in modern science, microscopes can now be used to resolve structures that are physically separated by as little as 20 nm in the most advanced techniques.

2.1 The principles of fluorescence

As defined by Stokes, fluorescence is the molecular emission of lower energy light upon absorption of higher energy light[266]. For excitation to occur, the fluorescent molecule, or fluorophore, must acquire at least the difference in energy between its ground state and lowest excited state ($S_{1,0}$), which can be achieved by absorbing a photon of sufficient energy[267]. As demonstrated in figure 2.1a, which shows a Jablonski diagram of the energy transitions of a hypothetical fluorophore, photonic energy is typically absorbed by the fluorescent molecule on a femtosecond

timescale and subsequently released by a slower two-step process[267]. The first stage in shedding the excess energy is relaxation of the excited electron to the lowest energy state, $S_{1,0}$, by the non-radiative processes of internal conversion and vibrational relaxation; this occurs within picoseconds of light absorption[267]. Relaxation from this point back to the ground state usually favours radiative emission occurring over a nanosecond timescale and resulting in the emission of light. It is, however, also possible for the excited fluorophore to undergo a 'forbidden' transition, termed intersystem crossing, to a triplet state[267] as indicated in figure 2.1a. Relaxation following intersystem crossing is much slower, as another forbidden transition is first required; the subsequent release of radiative energy is phosphorescence[267].

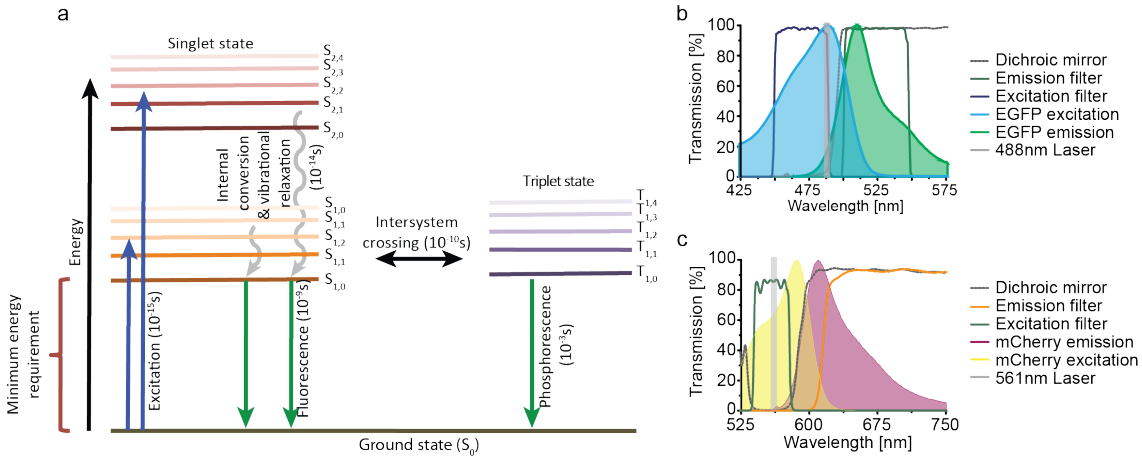

Figure 2.1 Fluorescence excitation and emission (**a**) Jablonski diagram schematising the process and timescales of fluorescence. The vertical axis represents energy and the horizontal lines represent different energy levels and vibrational states. High energy light (blue arrows) is absorbed and this energy is shed by non-radiative processes (grey curling arrows) to the lowest excited state and radiative energy release (green arrows) to the ground state. This release usually occurs very quickly as fluorescence, but forbidden transitions to the triplet state create a more stable excited state that must transition back before releasing energy as phosphorescence. (**b-c**) The excitation and emission spectra of EGFP (b) and mCherry (c), provided by the Tsien laboratory, with the filters and lasers used for the Olympus IX81 in this thesis; the filter sets shown are from Chroma Technology, product 49002 in (b) and 11010V2 in (c).

Fluorophores can absorb and emit light of varying energy, dependent on the fluorophore's energy levels and vibrational states. As photonic energy (E) is linked to wavelength (λ) by the relationship[268]

$$E = hc/\lambda \quad [2.1]$$

where h is Plank's constant and c is the speed of light, the unique absorption and emission properties of a fluorophore can be described as a spectral response, as shown for EGFP and mCherry in figure 2.1b-c. The shift between the excitation spectrum and the emission spectrum, Stokes shift, allows the separation of excitation and emission wavelengths in microscopy, while still efficiently exciting the fluorophore. Optical filters are typically used to achieve this separation; as shown in figure 2.1b-c for the Olympus IX81 used in my work, a dichroic mirror, which transmits only lower energy emitted light to the detector, is commonly paired with excitation and emission filters to select the required wavelengths.

2.1.1 Useful properties of fluorescence

Fluorescence intensity is a measure of the quantity of fluorescence signal under steady state conditions. This can provide both an indication of the concentration and targeting of a single protein of interest and an indication of the co-distribution of two proteins; the latter by using a technique called colocalisation, which determines the spatial correlation of probe intensities[269]. Fluorescence intensity can alternatively be used to gather information about protein mobility, for example using FRAP (fluorescence recovery after photobleaching)[270] or FCS (fluorescence correlation spectroscopy)[271, 272], and to probe for protein interactions, using BiFC (bimolecular fluorescence complementation)[273] or FCCS (fluorescence cross-correlation spectroscopy)[274].

FRAP uses the known sensitivity of fluorophores to excessive and high-energy light to irreversibly bleach a small sub-cellular region, enabling the diffusion of surrounding fluorophores into the ablated region to be monitored[270]. BiFC probes protein interaction by conjugating the proteins of interest to purpose-designed non-fluorescent fragments of a fluorophore, which fluoresce upon protein interaction-driven complementation[273]. Finally, single molecule spectroscopies,

namely FCS and FCCS, can be used to observe fluorophores over time as they traverse a fixed imaging volume. In these techniques, the diffusion kinetics of the labelled molecules can be extracted from detailed correlation analysis of the time traces obtained[271, 274]. In FCCS, this can be extended to unravelling protein interactions by the cross-correlation of two-channel fluorescent signal[274].

In addition to studies based on fluorescence intensity measurements, it is also possible to derive information about a fluorophore's local environment and dynamics using other quantifiable properties of fluorescence that are sensitive to environmental changes, such as fluorescence lifetime. Every fluorophore has a characteristic fluorescence lifetime, defined as the time required to emit a photon following energy absorption[267]. This is typically on the order of nanoseconds and is dominated by the relaxation time from the lowest excited state to the ground state by fluorescence[267]. Deviations away from a fluorophore's characteristic lifetime can indicate changes in its local environment that either quench radiative emission or stabilise the excited state[275]. Fluorescence lifetime imaging microscopy (FLIM) is therefore a powerful technique that is independent of fluorophore concentration and enables, for example, the differentiation of fluorophores with similar spectral properties[276], the detection of changes to the local environment such as pH or ion concentration[277] and the robust detection of protein interactions via Förster resonance energy transfer (FRET)[278]. The latter application, FRET, forms a core part of my research and is discussed further in section 2.4.

2.1.2 Fluorophores

The outer orbital electrons of fluorescent molecules have a sufficiently small energy difference between their ground state and lowest excited state to enable excitation in the visible electromagnetic range[279]. This is advantageous for microscopy as silicon-based detectors, which dominate microscope detector technology, are most sensitive to visible and near-infrared wavelengths[268]. As a rule, the more conjugated bonds a molecule has, the more widely the outer orbital electrons are distributed across it and the lower the energy required to excite it[279]. For this reason, common fluorophores often contain a chromophore of aromatic ring structures[279]. The fluorescence characteristics of a fluorophore can be

quantified by the amount of light it absorbs at its excitation maxima, known as its extinction coefficient, and its photonic output per photon absorbed, known as its quantum yield[267]. Desirable fluorophores for fluorescence microscopy therefore have a high fluorescence output, the product of its extinction coefficient and its quantum yield, and well separated excitation and emission spectra.

To study proteins of interest by fluorescence microscopy requires a means to fluorescently label certain molecules with high specificity. This is commonly accomplished by introducing recombinant DNA encoding the protein fused to a fluorescent protein[265]. This approach offers specific labelling of the protein with known 1:1 stoichiometry in live cells. However, the expression of exogenous DNA independent of the cell's regulation, commonly accomplished using a CMV promoter to drive expression, results in abnormally high protein levels[280]. This may disrupt normal behaviour and must be considered when interpreting data. To overcome this it is possible to express the recombinant gene under a crippled promoter to minimise expression[281] or to use genome-editing techniques such as CRISPR/Cas9 to replace the endogenous gene with the recombinant gene construct[282]. This latter approach is quickly becoming the preferred method of exogenous DNA expression, but requires a lengthy process to establish each cell line and may result in protein levels too low to be compatible with some imaging techniques.

An alternative to expressing recombinant fusion proteins is to specifically immuno-label endogenous protein with fluorescently-tagged antibodies[264]. This bypasses the risk that encoded probes may alter tertiary and quaternary protein structure and allows the use of fluorophores with superior quantum yield. However, antibodies are approximately 150 kDa[5] and therefore labelling of intracellular targets typically requires permeabilisation of the plasma membrane to enable antibody access, therefore largely restricting immunofluorescence to fixed cell work. As proteins of interest are generally labelled by an indirect two-step process and there is no control over the target to antibody ratio, the fluorescent probe is both far from the protein of interest and not stoichiometrically equal, which has particular implications on single molecule imaging[283]. Immuno-labelling also suffers the disadvantage that it requires highly sensitive and specific antibodies that can be difficult to procure and time-consuming to raise.

2.2 High-resolution fluorescence microscopy

Presented here is a summary of the state of the art of imaging technologies. Alongside this, experimental calibration and verification of the imaging techniques employed in this thesis are presented in section 2.5, along with validated analytical approaches for data analysis.

2.2.1 The diffraction limit

The resolution of an imaging system defines how far apart two distinct points must be for them to be spatially separated. Due to the wave-like properties of light, a single point of emitted light is diffracted by the aperture of the objective lens[284]. The resulting diffraction of the wavefront results in the production of an image broader than the true point source, known as the point spread function (PSF). As shown in figure 2.2, the lateral PSF consists of a central bright disk contained within numerous diffraction rings of deteriorating intensity, an Airy function[285]. This is produced by the constructive and destructive interference of light as the wavefronts arrive at the image plane in or out of phase with each other[285].

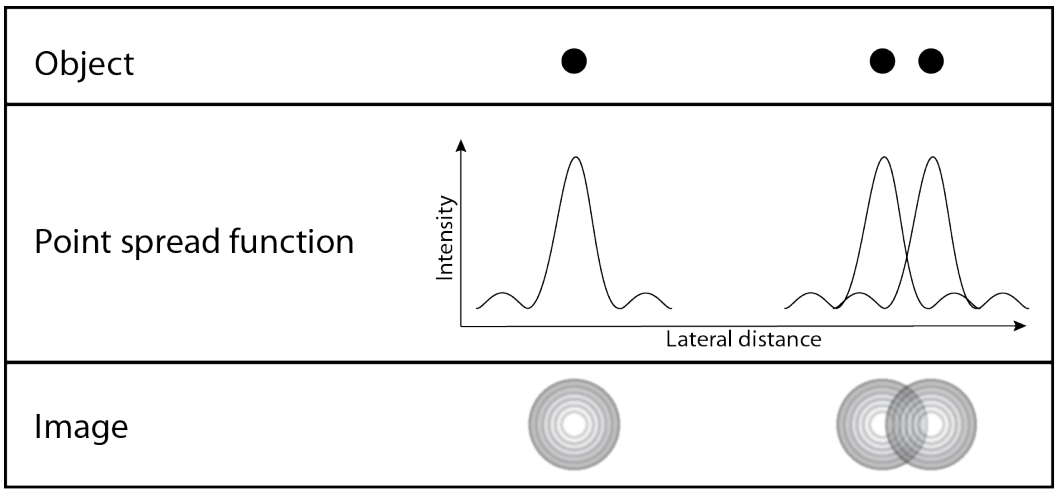

Figure 2.2 Diffraction-limited imaging A single point source (top row) is diffracted by the aperture of the objective lens resulting in a point spread function (middle row) that has interference peaks at the edges. This is imaged as a bright central disk surrounded by rings of lower fluorescence, known as an Airy disk

(bottom row). The width of the PSF defines the resolution of the microscope as overlapping PSFs preclude the separation of individual objects.

The physical proximity of two point sources will result in an overlap of their PSFs as seen in figure 2.2, thereby preventing resolution of the two points in the observed image. The theoretical lateral resolution of an imaging system is dependent on the wavelength of light (λ) and the numerical aperture (NA) of the lens. It was originally defined by Ernst Abbe[286] as

$$\text{resolution}_{xy} = \frac{\lambda}{2\text{NA}} \qquad [2.2]$$

and later adapted by Rayleigh[287] and Sparrow[288], though it is commonly measured experimentally as the full-width at half maximum (FWHM) of the Gaussian fit of the central peak of the PSF[268].

Logically, both reducing the incident wavelength and increasing the NA of the objective lens will improve the resolution of a microscope. However, glass lenses poorly transmit low wavelength ultra-violet light[289], and though quartz may enable this, the lower wavelength light is more susceptible to optical aberrations (distortion of the light path) than longer wavelengths[268], deteriorating image quality. Furthermore, high-energy light is poorly suited to bioimaging as it enhances photodamage to the cell and photobleaching of the fluorophore[279]. These limitations on wavelength restrict improvements in resolution to the NA of the objective lens. Numerical aperture describes the widest angle of light that can be captured by the lens, defined mathematically by Ernst Abbe[284] as

$$\text{NA} = n \sin \alpha \qquad [2.3]$$

where n is the refractive index of the medium between the lens and the sample, and α is the half aperture angle of the objective lens. As demonstrated in figure 2.3, the collection angle cannot exceed 90° and therefore the NA is constrained to 1 in air (which has a refractive index of 1). The use of immersion media with higher refractive indices can improve the NA, for example, immersion oil has a refractive index of 1.518[268]. However, numerical apertures greater than 1.5 are rarely attained. High-resolution imaging is referred to as being 'diffraction limited' as it

cannot achieve resolutions superior to 200-250 nm[279]. As this resolution is insufficient to observe cellular processes on a molecular level, the field of super-resolution microscopy has developed to circumvent the diffraction-limit, which is described further in section 2.3.

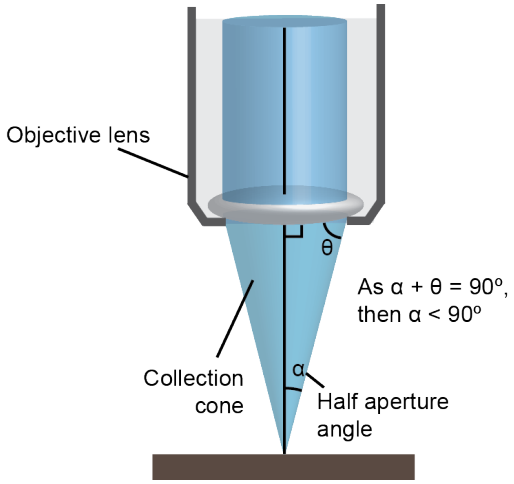

Figure 2.3 The maximum half aperture angle of an objective lens The objective lens can collect light from a limited angle range. This collection cone (blue) is quantified using the half aperture angle (α), which is physically limited to 90° as indicated.

2.2.2 Diffraction-limited microscopy techniques

Epifluorescence microscopes use the same objective lens to both focus excitation light onto the sample and emission light onto the detector, requiring optical filters to separate the different wavelengths. Illumination and detection can be carried out over the whole field by widefield microscopy, or through point-by-point scanning, as for confocal microscopy[290]. Though scanning techniques are much slower and ill-suited to imaging fast-changing cellular dynamics, confocal microscopy can offer superior resolution by excluding out-of-focus background signal that lowers the SNR in the focal plane[290]. Figure 2.4 schematises the optical paths of both widefield and confocal modalities for comparison. As shown in figure 2.4, confocal microscopy excludes out-of-focus emission by using a physical pinhole placed conjugate to the focal plane; the pinhole allows fluorescence emission originating from the focal point to pass through, but not emission from above or below this plane[290]. Reducing the diameter of the pinhole therefore improves the SNR of the image, however, this is at the cost of signal intensity[291].

Experimentally, the pinhole is therefore often set to the width of the theoretical Airy disk, referred to as 1 Airy unit[291]. To focus the excitation light to a fine point as required for confocal microscopy, laser illumination is required for its coherent and monochromatic nature[292].

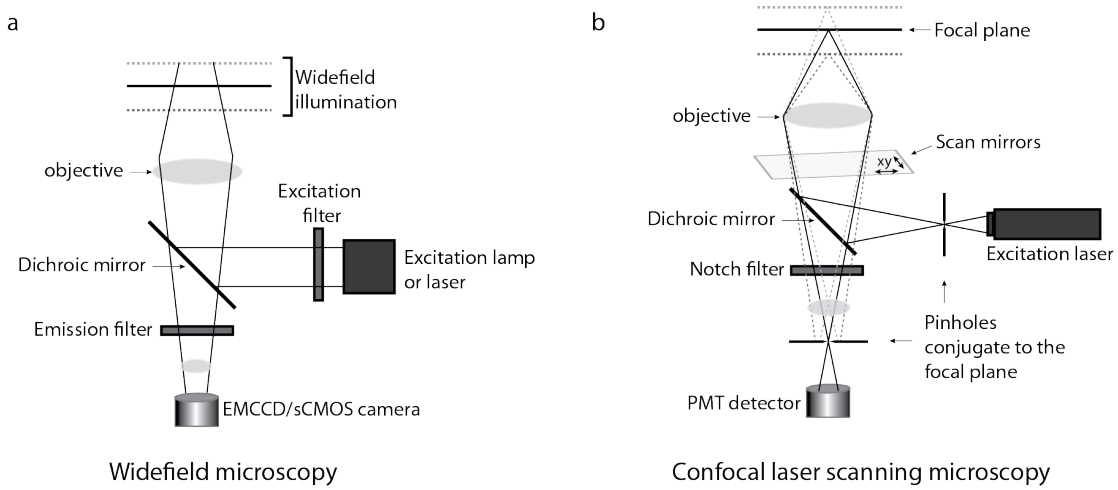

Figure 2.4 A comparison of widefield and confocal optical pathways (**a**) Simplified schematic of a widefield microscope, which illuminates the full field with lamp or laser light and simultaneously detects signal across the field with a pixel-array camera such as an EMCCD or sCMOS. (**b**) A simplified schematic of a confocal laser scanning microscope, which using laser illumination to focus the excitation light to a fine point which is raster scanned by mirrors across the field. Light emitted outside the focal plane is excluded from detection with pinholes conjugate to the focal plane.

The different illumination strategies of widefield and confocal microscopy require matching full-field or point scanning detection, respectively. Widefield detectors, such as sCMOS or EMCCD cameras, consist of an array of individual pixels that simultaneously capture the entire field of view in a single frame[268]. This is favourable for dynamic processes, as imaging speed is limited only by frame-to-frame exposure and readout times, and can reach over 1000 frames per second in commercial systems[293]. On the other hand, confocal microscopy utilises single-channel devices, such as PMTs and SPADs. In addition to integrating more advanced timing and counting options, these detectors can achieve single photon detection and are therefore significantly more sensitive than widefield cameras[294].

The SNR of widefield microscopy can be improved when observing structures close to the coverslip by employing total internal reflection fluorescence

microscopy (TIRFM). TIR occurs when the incident light impinges on an interface to a lower refractive index medium at an angle sufficient to cause at least 90° refraction[295] (the critical angle), as determined by Snell's law[295],

$$n_i \sin(\theta_i) = n_r \sin(\theta_r) \qquad [2.4]$$

where *i* and *r* refer to the incident and refracted light respectively, *n* is the refractive index of the medium and θ is the angle of incidence from the normal.

TIR generates an electromagnetic field known as an evanescent wave at the interface of the two media, which has the same energy as the reflected light, but decays exponentially with distance from the interface[295]. By achieving TIR between the coverslip and the sample mountant, the evanescent wave will therefore efficiently excite only the fluorophores within approximately 100 nm of the coverslip surface[296]. This improves the SNR by excluding emission from out-of-focus light. This optical arrangement is schematised in figure 2.5, which compares standard widefield illumination, panel a, with TIR illumination, panel b. TIR can be attained by focussing the laser to a peripheral region of the back focal plane of a high NA objective so that it propagates at an angle, the steepness of which is dependent on the radial position of the focal point[297]. Alternatively, the excitation laser can be introduced directly from above the sample, without using an objective lens, by guiding the light path with a prism to attain an incident angle greater than the critical angle[296].

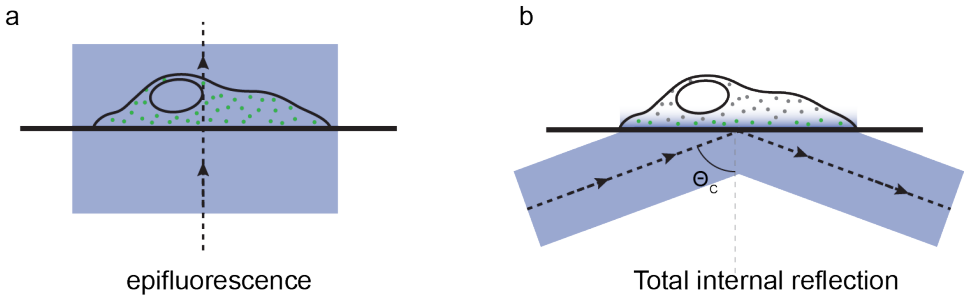

Figure 2.5 Total internal reflection fluorescence microscopy (**a**) Full-field illumination using standard widefield microscopy excites all fluorophores (green dots) in the field of interest. (**b**) Total internal reflection is achieved when the incident light is at or above the critical angle (θ_c). This type of illumination creates a rapidly decaying evanescent wave at the coverslip to mountant interface with the same energy as the illumination light. This results in excitation of fluorophores close to the coverslip (green dots) but not in the rest of the cell (grey dots).

2.2.3 Optimising the imaging set up

In practice, attaining diffraction-limited images requires, in addition to a high NA objective, an imaging system with a sufficiently high signal-to-noise ratio (SNR)[268]. The SNR provides a measure of the contrast in an image. It can logically be improved by maximising the amount of emitted light from the focal plane that reaches the detector while minimising the amount of background signal. The use of confocal and TIRF microscopies both aim to do this by minimising out-of-focus blur[290, 296]. It can additionally be improved by using fluorophores with a high extinction coefficient and quantum yield, where available, as they require lower excitation power[298], thus minimising the contribution of autofluorescence and excitation light that may be detected. The latter can also be reduced with high efficiency filters and the use of lasers, which provide a monochromatic light source[292] that can therefore be more cleanly filtered.

As image brightness, and therefore SNR, is diminished in a manner inversely proportional to the square of the magnification factor[268], an objective with the minimum magnification required to sample the field of interest should be used. The Nyquist-Shannon sampling theorem dictates that to appropriately sample for maximum resolution, the sampling frequency should be at least twice the bandwidth of the microscope's PSF[299]. In the case of widefield microscopy, the magnification must be matched to the fixed pixel dimensions of the camera, or *vice versa*, such that the pixels provide a lateral sampling interval (Δ_{xy}) of[300]

$$\Delta_{xy} = \frac{\lambda_{em}}{4n\sin(\alpha)} \qquad [2.5]$$

where λ_{em} is the emission wavelength, n is the refractive index of the objective lens immersion and α is the half aperture angle of the objective lens. The single channel detector of the confocal laser scanning microscope, on the other hand, can be scanned with differing sampling intervals, thus enabling pairing with objective lenses of different magnifications. The lateral sampling interval (Δ_{xy}) of the confocal microscope is[300]

$$\Delta_{xy} = \frac{\lambda_{ex}}{8n\sin(\alpha)}$$

[2.6]

where λ_{ex} is the excitation wavelength, n is the refractive index of the objective lens immersion and α is the half aperture angle of the objective lens.

Objective lenses are also prone to distortions of the light path or 'optical aberrations', which are typically corrected to some extent by design[289]. However, incorrect use can exacerbate these aberrations[289]. Spherical aberration is a common distortion where light focused by the edge of the lens has a different axial focal point to that focussed by the centre[289], reducing both the axial resolution and the contrast of the image. As spherical aberration is worsened by refractive index mismatches, the impact can be minimised by using corrected lenses paired with their specified coverslip thickness (typically 0.17mm) and mounting medium refractive index for which the lens was designed[289].

In addition to the aforementioned contributions to background signal, image SNR is also reduced by both photon shot noise and camera noise. Photon shot noise refers to the intrinsic fluctuations in signal resulting from the quantum nature of light and therefore can only be reduced with increased photon statistics[268]. Camera noise, on the other hand, is produced by fluctuations in both the thermal generation of electrons in the absence of signal and in signal read out accuracy[268], both of which can be minimised to an extent. Thermally generated electrons can be minimised in cooled detectors and the contribution by read out noise is reduced in detectors that amplify the signal prior to read out, such as EMCCD cameras and PMT detectors[268].

2.2.4 Image deconvolution

An imaged object represents a three dimensional convolution of the true object with the PSF of the microscope[301]. With knowledge of the PSF and therefore the optical convolution of the emission signal, it is possible to mathematically reverse its effect after acquisition. Deconvolution routines aim primarily to remove image

blur caused by out-of-focus signal, either by subtraction or preferably by pixel reassignment to avoid loss of photonic information[301]. In this way, diffraction-limited information can be recovered in post-processing. Indeed, deconvolved widefield data has a resolution comparable to confocal microscopy[302]. Deconvolution of widefield data is therefore a viable alternative for high-speed imaging or working with fluorophores with a poor quantum yield, for which confocal microscopy is ill-suited. Deconvolution is undoubtedly worthwhile, but software can be costly and image processing can be slow, requiring high processing power. Furthermore, image information may be lost or noise artificially added if the PSF used for deconvolution does not accurately represent the system.

2.3 Super-resolution fluorescence microscopy

Over recent years, methods have been proposed to resolve beyond the diffraction-limit, giving rise to the field of 'super-resolution' fluorescence microscopy. Figure 2.6 provides a comparison of the axial and lateral resolving power of some of the most commonly employed super-resolution techniques, which fall into two categories: single molecule localisation microscopy such as PALM and STORM or PSF reshaping such as STED and SIM.

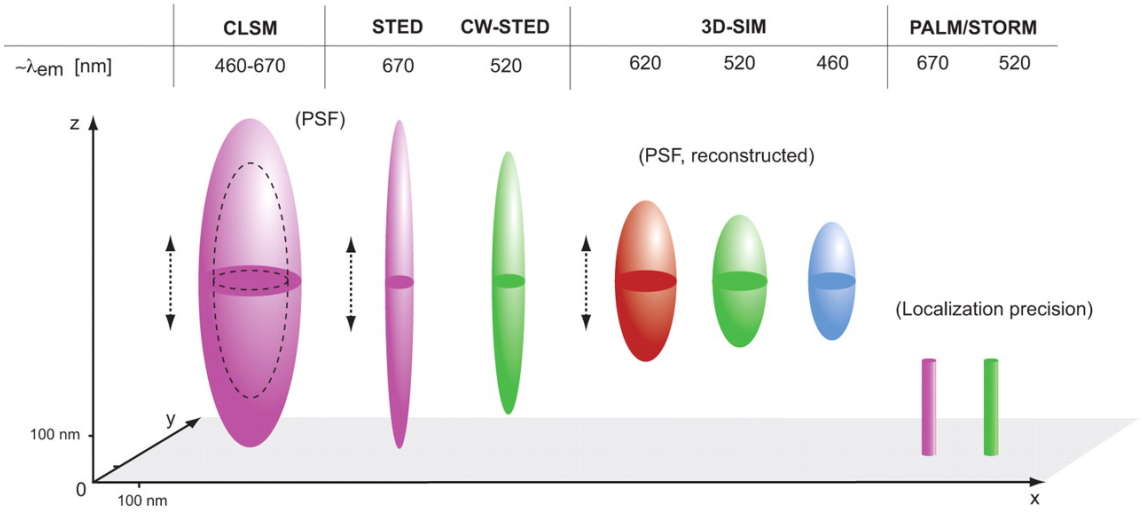

Figure 2.6 A comparison of the focal volumes of different imaging techniques
Image taken from Schermelleh et al., 2010[303] compares the approximate lateral (D_{xy}) and axial (D_z) resolution at different wavelengths of the most commonly used super-resolution techniques with values listed below along with focal volume (V_{xyz}).

2.3.1 Single molecule localisation techniques

Single molecule localisation microscopy (SMLM) techniques offer the highest lateral resolution available in fluorescence microscopy[268]. These techniques separate overlapping fluorophore emission events in time to pinpoint single molecules and construct an image of precise molecular locations[304-306]. The symmetrical nature of a PSF from a diffraction-limited source allows for single molecule position to be determined. This is accomplished using a localisation algorithm based on Gaussian fitting[307] or centre-of-mass measurements[308], the accuracy and precision of which limits resolution[309]. SMLM is carried out with widefield microscopy but as the localisation precision is inversely proportional to the square root of the number of photons emitted[307], it often requires a higher SNR than traditional epifluorescence provides. TIRFM is therefore typically employed, but this restricts SMLM to the basal membrane. More recently, selective plane illumination microscopy (SPIM) using light sheet illumination to allow SMLM at any focal plane has been realised[310].

Three research groups independently developed and published different approaches to achieve sparse activation of a subset of fluorophores at the same time. Photoactivated localisation microscopy (PALM) and fluorescence photoactivation localisation microscopy (FPALM) use photoactivatable or photoswitchable fluorescent proteins to repeatedly and randomly activate a subset of proteins for imaging[304, 305]. As PALM relies on probes with appropriate quantum yield and photoactivation characteristics, this can be quite restrictive for the design of multi-channel experiments, however, the development of new probes is beginning to alleviate this limitation[311, 312]. A key advantage of PALM is its compatibility with live cell imaging, enabling single-particle tracking[313]. Furthermore, 3D PALM based on interferometry has also been demonstrated[314].

An alternative approach to SMLM is offered by stochastic optical reconstruction microscopy or STORM[306]. This method uses antibodies conjugated to a reporter dye paired with an activator that switches the dye from a dark to a visible state upon irradiation[306]. Spontaneous return of a reporter dye from an induced dark triplet state can also be used to remove the requirement for an activator in direct or dSTORM[315]. As STORM requires antibody labelling, it is restricted to fixed cell imaging and suffers reduced labelling specificity. Moreover, 1:1 stoichiometry of the protein and label cannot be guaranteed, resulting in multiple signal events for the same protein. However, multi-colour reporter dyes can be used[316] and 3D multi-colour STORM based on astigmatism has been realised[317]. A similar approach to dSTORM called ground state depletion followed by individual molecule return (GSDIM) has demonstrated use of fluorescent proteins in a similar manner[318].

2.3.2 PSF re-shaping techniques

Stimulated emission depletion microscopy (STED) is a super-resolution technique used with confocal laser scanning microscopy. STED reduces the size of the PSF by overlaying an additional ring-shaped depletion laser over the excitation beam to inhibit fluorescence around the periphery of the PSF[319], as depicted in figure 2.7. The depletion laser accomplishes this by inducing direct transition of the fluorophores from the excited state to the ground state by stimulated emission before fluorescence can take place[319]. This attenuates fluorescence where the beams are overlaid, thereby reducing the full width at half maximum (FWHM) of the PSF. For ideal samples, resolutions down to 20 nm have been reported[320]. To quantify the resolution limits of the STED microscope used in my thesis, figure 2.8 presents a direct comparison between the ability of confocal laser scanning microscope to resolve 20 nm fluorescent beads with and without stimulated emission depletion. This figure demonstrates that STED can separate closely neighbouring beads where standard confocal cannot (panels a-b), achieving resolutions below 50 nm with a consistent FWHM that is 4.6 fold smaller than for confocal microscopy (panel c).

STED can be carried out with pulsed or continuous wave (CW) lasers. Pulsed excitation has the advantage of requiring four times lower depletion power over an equivalent timescale to achieve the same resolution as CW-STED[321]. This is advantageous because the efficiency of the depletion increases with power of the laser[319], a concept that is demonstrated in figure 2.8e, which shows the narrowing intensity profiles through a bead under increasing depletion power. However, the use of pulsed lasers requires a more complex set up to ensure their temporal alignment. CW-STED is therefore often preferred and can be used in conjunction with time gating to exclude fluorescence emitted prior to depletion, thereby improving the apparent depletion efficiency at lower powers[322]. The effect of time gating is demonstrated in figure 2.8d, which shows the narrowing intensity profiles through a bead under constant depletion power as the delay prior to detection is increased.

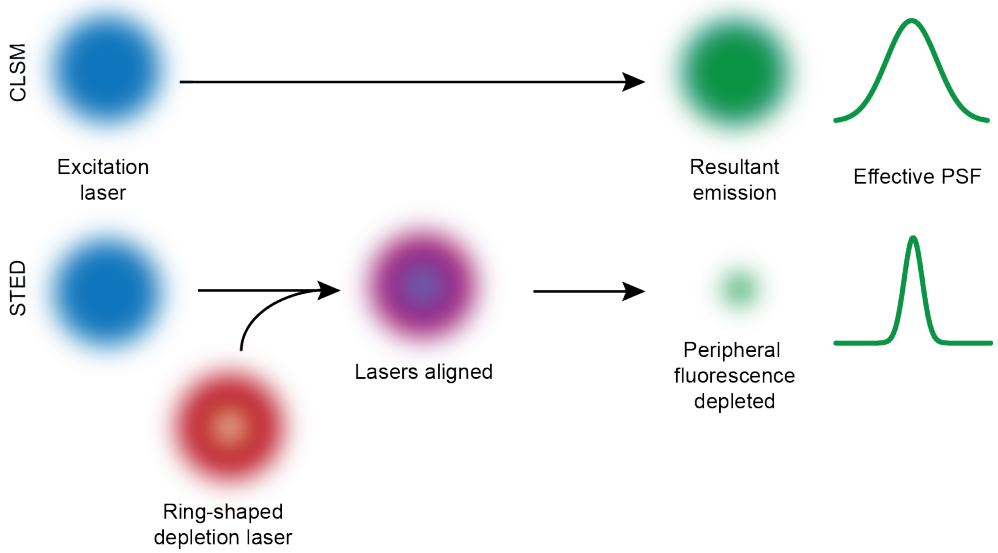

Figure 2.7 Stimulated emission depletion can reshape the PSF The excitation of a point source produces a diffraction-limited spot with a broad PSF in confocal microscopy (top row). In STED microscopy (bottom row), the addition of a ring-shaped depletion laser (red) aligned to the excitation laser (blue) will deplete the peripheral fluorescent emission of a compatible fluorophore (green), thereby narrowing the PSF.

STED was originally constrained to lateral improvements in resolution until three-dimensional STED was achieved by using two STED beams to reduce the PSF in both the axial and lateral directions[323]. Multi-colour STED has also been realised for super-resolution colocalisation studies[324, 325], however compatible probes are severely restricted by the depletion wavelength, which must overlap with the tail of the fluorophore's emission spectrum. For two probes to be spectrally resolved in STED, either a second excitation and depletion laser pair that occupies a distinct spectral region can be used[324] or two probes with different Stokes-shift that can be separated by excitation wavelength and depleted by the same wavelength[325]. STED remains, however, a harsh technique due to the high-power lasers involved. The photobleaching and phototoxicity largely restricts STED to fixed sample imaging, though live STED on a fluorescent protein has been demonstrated[326].

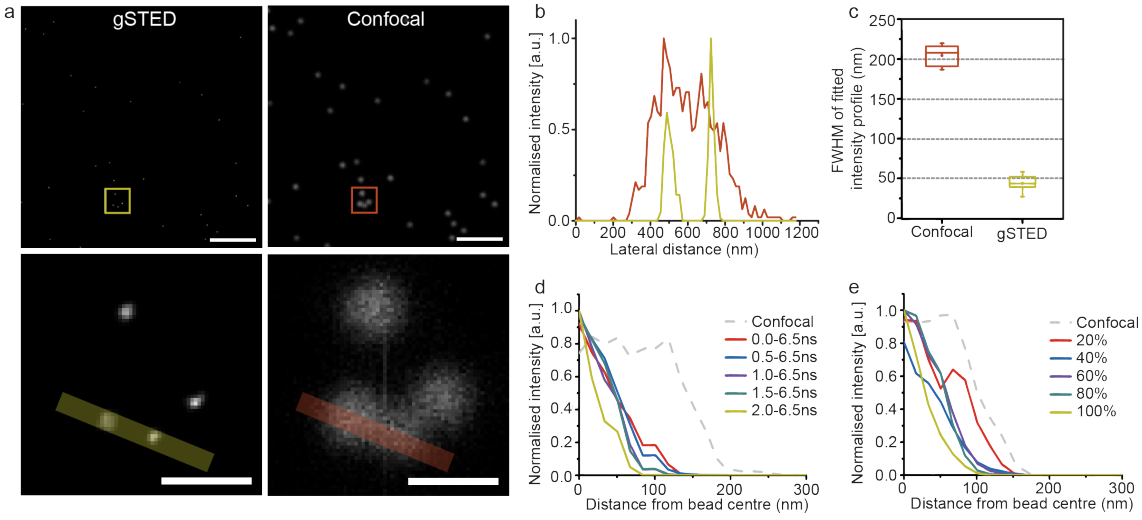

Figure 2.8 Characterisation of achievable CW-STED resolution (**a**) Top row: confocal and deconvolved CW gSTED images (acquired with 100% depletion power and 2-6.5 ns time gating) of 0.02 µm microspheres (505/515), scale bar 5 µm. Bottom row: Zoomed area of boxed regions above showing improved resolution of SW gSTED, scale 1 µm. (**b**) Intensity profile over the line indicated in (a) resolving two distinct peaks with STED (yellow) and only one broad peak in confocal (red) and (**c**) box-and-whisker plots of the FWHM values through n=7 line profiles to quantify this improvement in resolution, the box represents 25th to 75th quartiles with line and dot indicating median and mean respectively, whiskers represent minimum and maximum values. (**d**) Representative line profiles through beads showing improved resolution with increased gating at 100% depletion laser power and (**e**) with increased laser depletion power with 2-6.5 ns gating.

As STED microscopy is a scanned technique, its benefits cannot be translated to widefield microscopy. However, an alternative patterned illumination technique, called structured illumination microscopy (SIM), is commonly used to improve widefield resolutions. Instead of illuminating the full field, SIM uses known striped illumination patterns to create interference patterns, called Moiré fringes, with the unknown fluorophore distribution pattern[327]. These Moiré fringes contain higher spatial resolution signals than conventional imaging. By acquiring phase shifted patterns in different directions, it is possible to mathematically reconstruct the image from the information contained[327]. 2D-SIM uses two interfering light beams to create the illumination pattern and this has been developed into 3D-SIM by the addition of a third light beam to provide axial patterning[328]. Though SIM cannot achieve the resolution improvements of other super-resolution techniques, it requires no specialist sample preparation and is compatible with all standard fluorophores. The disadvantage of this technique is its reliance on complex optics and non-trivial reconstruction procedures provided commercially, precluding the implementation of this technique at low budget. Recently, however, an open-source reconstruction plugin called fairSIM has been released[329], which may make SIM accessible to more users. An assessment of the achievable resolution on a Nikon SIM is presented in figure 2.9. This demonstrates that neighbouring 20 nm beads can be resolved with SIM but not standard widefield, as shown in panel a. The improvement in both axial and lateral resolution is highlighted by intensity plots in panels b and c, respectively, which demonstrate a 1.4 fold improvement in axial resolution and a 2.4 fold improvement in lateral resolution, which is highly consistent as panel d indicates.

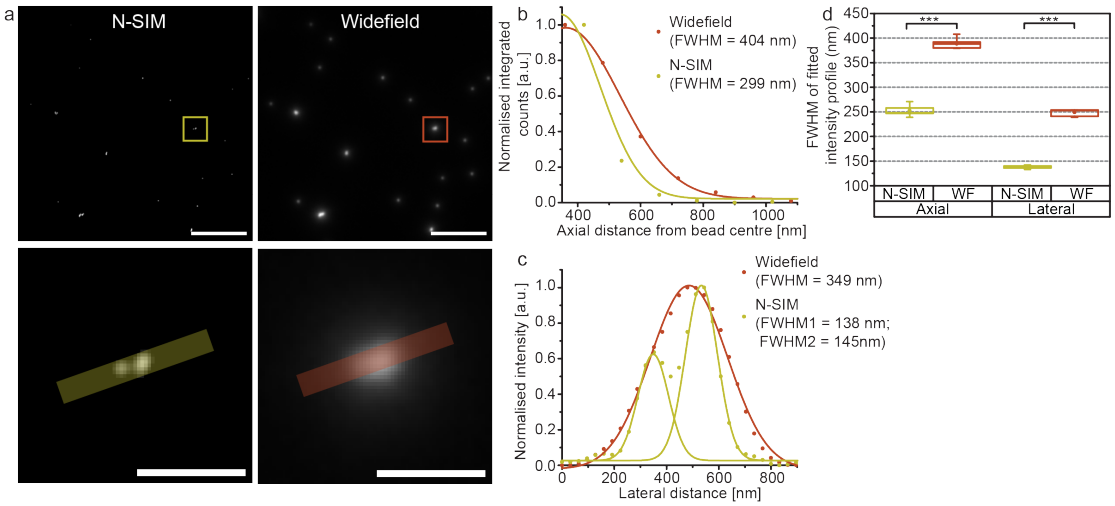

Figure 2.9 Characterisation of achievable N-SIM resolution (**a**) 0.02 µm microspheres (505/515) were imaged in widefield mode and by SIM, a zoomed region demonstrates separation of two beads that could not be resolved by widefield, scale bars 5 µm (top) and 1 µm (bottom). (**b**) Intensity profile of a single bead through Z and (**c**) XY line profile of beads as highlighted in (a) demonstrating an improvement in both lateral and axial resolution. (**d**) Box-and-whisker plots of the FWHM values through n=7 line profiles to quantify the improvement in resolution, the box represents 25th to 75th quartiles with line and dot indicating median and mean respectively, whiskers represent minimum and maximum values, significance tested with paired sample t-test.

2.4 Förster resonance energy transfer

Probe colocalisation is often improperly used to evidence protein interaction *in situ*. While colocalisation can provide a useful readout of protein proximity within the spatial and temporal control of the cell, this information is limited to the resolution of the technique. Protein interactions occur on a nanometer scale and therefore their detection even at super-resolution is not possible. Förster resonance energy transfer (FRET), however, offers an indirect and robust approach to the detection of protein interactions.

FRET is the non-radiative transfer of energy between two fluorophores, a so-called donor in the excited state and an acceptor in the ground state[330]. Fluorophores are optical dipoles and alignment of two compatible fluorophore dipole moments in close proximity enables resonant energy transfer *via* long-range dipole-dipole coupling[330]. This phenomenon is of interest to fluorescence microscopists because its dependence on fluorophore proximity is on the same scale as protein

interactions[278]. The separation distance at which FRET occurs with 50% efficiency is known as the Förster radius (R_0), after Theodor Förster, who defined it as[331]

$$R_0 = \left[2.8 \times 10^{17} \cdot \kappa^2 \cdot Q_D \cdot \varepsilon_A \cdot J(\lambda)\right]^{\frac{1}{6}} \quad [2.7]$$

where κ^2 is the dipole orientation factor, Q_D is the quantum yield of the donor, ε_A is the peak extinction coefficient of the acceptor and $J(\lambda)$ is the spectral overlap integral between donor emission and acceptor excitation. Knowledge of the Förster radius of a FRET pair enables calculation of the separation range over which FRET can occur. The relationship between FRET efficiency (E_{FRET}) and separation distance (r) is[331]

$$E_{FRET} = \frac{1}{1 + \left(\frac{r}{R_0}\right)^6} \quad [2.8]$$

.

This can been used to determine the FRET efficiency for EGFP and mCherry as a function of separation distance, which is shown graphically in figure 2.10a, based on the published Förster radius of 5.24 nm[332]. This graph indicates that the two probes must be within at least 8 nm proximity for FRET to be detected. Generally, calculated FRET efficiencies cannot, however, be a metric of separation distance and instead only provide an indication of close proximity. The reason for this is that although spectral overlap, donor quantum yield and acceptor extinction coefficient can be calculated with some certainty, the dipole orientation factor used to calculate the Förster radius will inherently fluctuate. Indeed, it is often approximated as 2/3 to calculate R_0, which is the average orientation factor under randomising conditions[333]. Therefore changes to FRET efficiency are influenced by both fluorophore separation distance and dipole alignment.

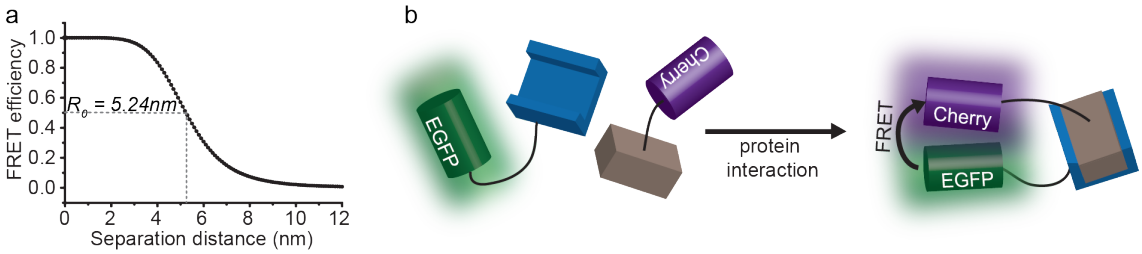

Figure 2.10 FRET efficiency is dependent on fluorophore proximity (**a**) The theoretical relationship between FRET efficiency and separation distance for EGFP and mCherry, calculated using equation 2.8, demonstrating the sensitivity of FRET to protein proximity (based on a Forster radius of 5.24 nm calculated by Akrap et al., 2010[332]). (**b**) A schematic demonstrating how FRET reports protein interactions. In the absence of interaction, the protein-fluorophore conjugates are freely diffusible. Upon protein interaction, the fluorophores are held in sustained sub-10 nm proximity, allowing FRET to occur between the donor (EGFP in this case) and the acceptor (mCherry in this case).

As protein interactions commonly occur within a 10 nm scale, their interaction can drive FRET between a donor and acceptor conjugated to each of the proteins of interest, therefore providing an indirect readout of protein interaction[278]. This is schematised in figure 2.10b, which shows FRET occurring only upon protein interaction. To benefit from the phenomenon of FRET in this way, a means of experimentally measuring it within the cellular environment is required. The occurrence of FRET causes a decrease in the donor fluorescence lifetime and onset of fluorescence emission from the acceptor, which would otherwise remain dark[331]. Sensitised emission of the acceptor and the donor fluorescence lifetime can therefore both be experimentally measured, enabling the detection of FRET through either fluorescence intensity or fluorescence lifetime imaging. It is important, however, to carefully consider the fluorophore pair to be used to maximise FRET detection and to shrewdly design constructs to ensure fluorescent probes are within 10 nm upon interaction without sterically hindering complex formation.

2.4.1 Intensity FRET

Intensity measurements can be used to detect FRET based on both the sensitised emission of the acceptor and reduced emission of the donor. Sensitised emission detects acceptor fluorescence upon donor excitation, requiring corrections for donor bleed-through into the acceptor channel[334]. To accomplish this, a donor only, acceptor only and donor-acceptor sample must all be imaged in both channels and for sensitised emission to determine the contribution of FRET[331]. Uncertainty arises with this method, however, when measuring FRET between proteins with different and varying concentrations[267]. To overcome this, acceptor photobleaching can be employed independently or following sensitised emission experiments. In this case, the donor emission is measured both before and after the acceptor is bleached to provide a FRET and non-FRET measurement from the same sample[335]. However, the dependence of this technique on bleaching restricts its use to fixed samples to avoid acceptor fluorescence recovery and requires that corrections for incomplete acceptor bleaching and inadvertent donor bleaching be applied[336].

2.4.2 FLIM-FRET

Fluorescence lifetime imaging (FLIM) provides the most robust measure of FRET because, unlike intensity imaging, fluorescence lifetime is independent of both laser intensity and fluorophore concentration[331]. As FRET causes a reduction in the donor fluorescence lifetime, FRET efficiency (E_{FRET}) can be derived from the change in the donor lifetime in the presence (τ_{DA}) and absence (τ_D) of the acceptor as follows[331]:

$$E_{FRET} = 1 - \frac{\tau_{DA}}{\tau_D} . \qquad [2.9]$$

This requires that either a donor-only control sample is imaged alongside the donor-acceptor sample, or that fluorescence lifetime measurements are taken before and after acceptor photobleaching.

Fluorescence lifetime can be measured in the time-domain (TD) or frequency-domain (FD), both of which require specialist equipment and non-trivial data analysis. FD FLIM-FRET uses camera-based detection, allowing relatively high frame-rate acquisition by widefield microscopy, but is disadvantaged by poor handling of multi-exponential decays, less accurate lifetime measurements and detectors that are amenable to lifetime drift[267]. FD FLIM applies a phase-modulated light source to excite the fluorophore and measures the relative phase delay (Φ) and modulation ratio (*m*) of the emitted light[267]. These measurements can be used to determine either the phase fluorescence lifetime (τ_Φ) using the relationship[267]

$$\tau_\phi = \omega^{-1} \tan \phi \qquad [2.10]$$

where ω is the modulation frequency, or the modulation fluorescence lifetime using the relationship[267]

$$\tau_m = \frac{1}{\omega} \left[\frac{1}{m^2} - 1 \right]^{\frac{1}{2}}. \qquad [2.11]$$

Differences between the phase fluorescence lifetime and the modulation fluorescence lifetime are indicative of a multi-exponential decay[267]. As the different lifetime components of a multi-exponential decay cannot be derived, FD FLIM is largely restricted to donor fluorophores that decay mono-exponentially. This is a troublesome obstacle for the detection of FRET, as variations in protein interactions typically cause a donor with a mono-exponential decay to adopt a second lifetime component upon FRET[337].

TD FLIM-FRET can produce full fluorescence decays per pixel for accurate and reproducible lifetime derivation and is therefore considered the gold-standard approach. TD FLIM-FRET data acquisition is still, however, largely based on single-channel detectors that must be coupled with scanned techniques such as confocal microscopy. Recent technological developments have laid the foundations for widefield time-domain FRET[338, 339], which is explored further in chapter six. Time-domain FLIM uses a pulsed excitation source correlated to a time measure of photon arrival to quantify photon arrival times. This can be achieved coarsely using time-gated detection, the precision of which is dependent on the number and

width of time gates acquired, originating from studies with just two channels[340]. Alternatively, precise single photon arrival times can be measured by time-correlated single photon counting (TCSPC) to build a complete fluorescence decay of histogrammed arrival times[341]. The fluorescence lifetime can then be accurately derived from the fit of this decay. To detect the changes in fluorescence lifetime caused by FRET, the histogram must provide a reliable representation of photon arrival times requiring both high temporal resolution of the electronics and sufficient photon statistics.

2.5 Techniques used and their validation

My research uses some of the techniques outlined here to investigate the SNARE protein dynamics involved in autophagy, which are reported in chapters four and five. Mammalian autophagosomes are typically 0.5 to 1.5 μm in diameter[342] and therefore diffraction-limited microscopy provides sufficient resolution to assess the co-occurrence of different proteins on these structures. Indeed, CW-gSTED detects no reduction in the size of autophagosomal structures, as will be demonstrated in section 4.3.2. Diffraction-limited multi-channel confocal laser scanning microscopy has therefore been used throughout for the assessment of protein colocalisation.

To detect protein interaction, TCSPC FLIM-FRET and FCCS are the most robust approaches. Though the occurrence of FRET suggests interaction, the absence of FRET cannot reliably conclude the absence of one because interactions can span a greater distance than the 10 nm limits of FRET. FCCS is therefore unique in being able to evidence the absence of an interaction, however it cannot provide the spatial information reported by FLIM-FRET. Furthermore, as FCS requires that the confocal volume is parked at a point of interest it is suited to exploring only the dynamics of freely diffusible proteins or proteins that are associated with stationary membranes. As my research investigates protein dynamics on mobile vesicles, FCS could not therefore be used. TCSPC FLIM-FRET has instead been employed to detect protein interactions *in situ*.

In order to interpret colocalisation and FLIM-FRET data with confidence, the techniques were carefully validated and methods to quantify the results were explored.

2.5.1 Colocalisation

As previously discussed, colocalisation is a method to assess the degree to which fluorescent probes co-distribute. The encodable fluorescent proteins, EGFP and mCherry, were used throughout my work for this purpose, labelling proteins of interest specifically and with known 1:1 stoichiometry. Multi-channel images were acquired sequentially to minimise the contribution of channel bleed-through, an artefact of imaging where spectral overlap may lead to the detection of the shorter wavelength emitter (EGFP in this case) under parameters reserved for the longer wavelength emitter (mCherry in this case)[268].

For colocalisation to accurately be assessed, it is crucial that when two probes are in the same location, the image produced reflects this. This, however, requires perfect alignment of the optical paths in both channels. Lateral displacement of one channel relative to another is often an indicator of misaligned filters[268]. Additionally, due to chromatic aberrations caused by the objective lens, different wavelengths are refracted to different degrees, and therefore focussed at different points, resulting in axial shifts between channels[289]. The channel alignment of the confocal laser scanning microscope (CLSM) used in my research (refer to section 3.5.1 for CLSM specifications) was assessed using 100 nm TetraSpeck microspheres (ThermoFisher Scientific, T7279), which emit at multiple wavelengths. Shown in figure 2.11 is the merged image of detected emission with peaks at 515 nm and 580 nm, the most relevant wavelengths to EGFP and mCherry, for a single bead and both lateral and axial intensity profiles of both wavelengths. These demonstrate high lateral correlation in the signal (figure 2.11a-b) but a strong axial shift in focus (panel c) despite the use of an apochromatic lens (Leica HC PL APO 63X 1.4 NA oil immersion lens), which has chromatic aberration correction. Colocalisation studies were therefore restricted to 2D images.

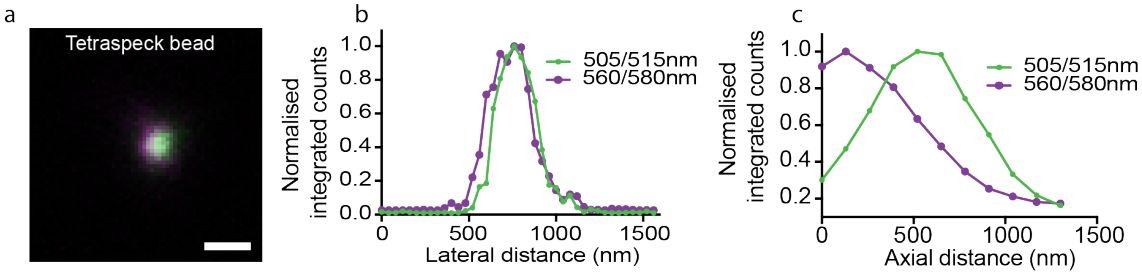

Figure 2.11 Characterisation of confocal channel alignment (**a**) A merged image of a single TetraSpeck bead with peak excitation and emission at 505 nm and 515 nm (green) or 560 nm and 580 nm (purple), scale bar 500 nm. (**b**) Lateral and (**c**) axial intensity profiles of the bead in (a). These indicate good lateral colocalisation but strong axial chromatic aberration.

To quantify probe colocalisation, Pearson's and Manders correlation coefficients (PCC and MCC) are both commonly used[269]. PCC applies the following equation[343], which notably includes a mean signal subtraction, negating the need for image pre-processing,

$$\mathrm{PCC} = \frac{\sum_i (R_i - \overline{R}) \times (G_i - \overline{G})}{\sqrt{\sum_i (R_i - \overline{R})^2 \times \sum_i (G_i - \overline{G})^2}} \qquad [2.12]$$

where R_i and G_i refer to the intensity values of the mCherry and EGFP channels respectively and $\overline{R}$ and $\overline{G}$ to their mean values. As PCC quantifies how the signal intensities vary with each other, it therefore assumes co-occurrence in fixed proportion[269]. This is well-suited to proteins that interact at all times, but less so for proteins that are proposed to interact transiently within sub-populations. For the latter scenario, MCC is better suited[344]. MCC uses the following equations to quantify the fractional overlap between channels,

$$\mathrm{M}_1 = \frac{\sum_i R_{i,colocal}}{\sum_i R_i} \qquad [2.13]$$

and

$$M_2 = \frac{\sum_i G_{i,colocal}}{\sum_i G_i} \quad [2.14]$$

where $R_{i,colocal}$ is the value of the mCherry channel if the equivalent EGFP signal is greater than 0, otherwise it is 0, and R_i is the value of the mCherry pixel. The reverse channels apply for $G_{i,colocal}$ and G_i. MCC therefore produces two values, denoting the fraction of channel one pixels also containing channel two signal (M1) and *vice versa* (M2). MCC can therefore highlight when one protein is consistently co-occurring with a second, but the second only partially co-distributes with the first. These algorithms are sensitive to the background signal common in most images and therefore, unlike PCC, require that background signal is removed and colocalisation is restricted to the structures of interest alone[269].

The differences between these two algorithms mean they are better suited to different colocalisation tasks: PCC for the quantitation of signal intensity co-variance for probes that follow a linear regression relationship, MCC for the determination of co-occurrence between channels for probes suspected to only partially colocalise[269]. To verify this, the colocalisation of EGFP and mCherry fused to the same autophagosomal protein, LC3, in autophagic HeLa cells was assessed (refer to sections 3.4 and 3.5.7 for sample preparation and colocalisation methodology). As shown by figure 2.12, in the presence of bafilomycin A_1, which inhibits lysosomal degradation of EGFP[345] (discussed further in section 4.3.1), the colocalisation of the probes is visually apparent (panel a) and their signal intensities vary with respect to each other in a linear manner (panel d); in this case, PCC, M1 and M2 all produce high values of 0.93, 0.897 and 0.931 respectively. If, however, lysosomal degradation is not inhibited, EGFP alone is sensitive to the lysosomal environment and is therefore degraded[346]. This produces a split population of vesicles: those with both EGFP and mCherry and those with mCherry alone (panel b). In this case, the signal intensities no longer vary linearly and PCC is heavily reduced to 0.53 despite the known colocalisation in a subset of vesicles (panel d). MCC, however, indicates the high colocalisation of EGFP with mCherry vesicles with an M2 value of 0.754, but the lower correlation of mCherry with EGFP vesicles with an M1 value of 0.369. Based on this assessment, the colocalisation

algorithm implemented in my research was determined based on the expected and apparent signal distributions and the frequency scatter plots of signal intensities.

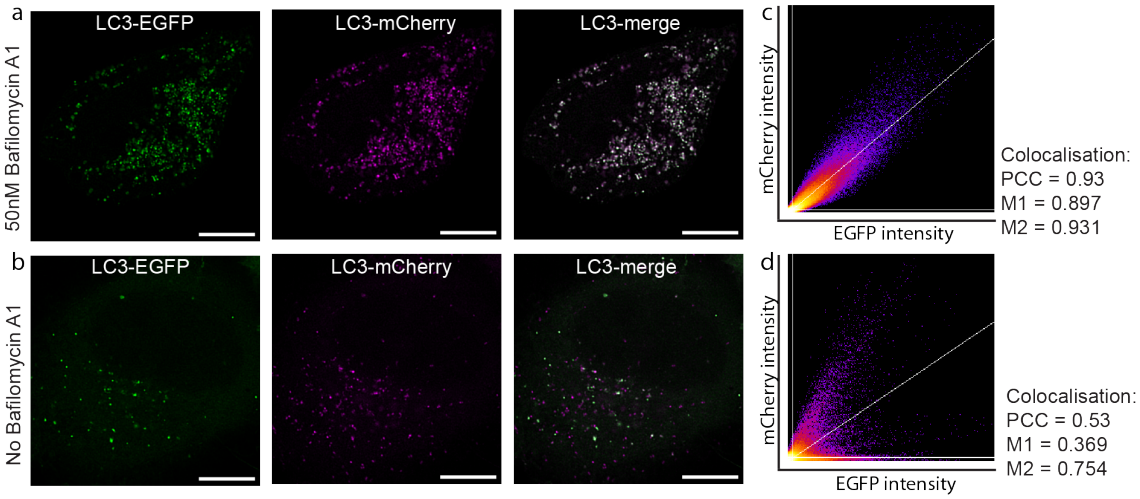

Figure 2.12 Selecting the most appropriate colocalisation test (**a**) Intensity images of autophagic HeLa cells expressing tandem labelled LC3-EGFP-mCherry in the presence of bafilomycin A1 to prevent lysosomal degradation of EGFP and (**b**) in the absence of bafilomycin A1. (**c**) A frequency scatter plot of the pixel intensities in (a), showing a linear relationship and (**d**) the same for (b), showing a non-linear relationship. PCC clearly reports colocalisation for (c) but is more difficult to interpret for (d) where MCC demonstrates that as expected, only a subset of mCherry vesicles now colocalise with EGFP (M1) while almost all EGFP vesicles still colocalise with mCherry (M2). Scale bars 10 µm.

2.5.2 FLIM-FRET

TCSPC FLIM-FRET has been used throughout my work to robustly detect sub-10 nm protein proximity, which can be considered an indirect read out of protein interactions. An overview of the optical configuration and electronics I used for FLIM-FRET is provided in figure 2.13 and described fully in section 3.5.5. As shown in this diagram, a pulsed white light laser provided the excitation source. This laser produces a supercontinuum light source covering a broad spectral range, from which bandlets of the desired wavelength can be isolated[347, 348]. To excite the donor fluorophore, EGFP, the laser was tuned to 488 nm and set to a pulse frequency of 40 MHz, therefore pulsing every 25 ns, which was found to be a sufficient window for EGFP fluorescence to completely decay prior to the next

pulse. As indicated in figure 2.13, following excitation, emitted fluorescence is filtered using a notch filter to selectively remove the 488 nm excitation light and a dichroic mirror to direct wavelengths below approximately 550 nm to a SPAD detector with optimal sensitivity at these wavelengths. The SPAD has single photon sensitivity and triggers a timing mechanism upon photodetection that is halted by the next laser pulse, thus tagging the photon with a time relative to the laser pulse. Timing is synchronised to excitation and photodetection by the PicoHarp 300 TCSPC module. This type of TCSPC FLIM is referred to as reverse-mode because the detection event and not the laser pulse initiates the timing mechanism[267].

To acquire sufficient photon counts for accurate decay fitting, measurements were integrated to reach a maximum count per pixel of approximately 10,000 photons, usually requiring 8-12 minute acquisitions. The acquisition rate can be enhanced at the cost of spatial resolution by under-sampling; large pixel sizes of 0.16 μm were found to balance the need for spatial information with the risk of excessive photobleaching over longer acquisitions. The acquisition speed is also limited by a maximum useful count rate, dictated by the 'dead time' of the detector, which is a period of insensitivity that follows a photodetection event such that additional photons cannot be detected[349]. If multiple photons arrive at the detector within the same pulse cycle, the decay will be biased to early arrivals and will therefore report an artefactually low lifetime[349], an issue referred to as 'pulse pile-up'. To avoid this, it is typically recommended that the photon count rate is maintained at 1% of the laser repetition rate[267] and therefore to avoid pile-up, the laser power was adjusted such that the count rate did not exceed 10^5 counts per second as recommended by the manufacturer.

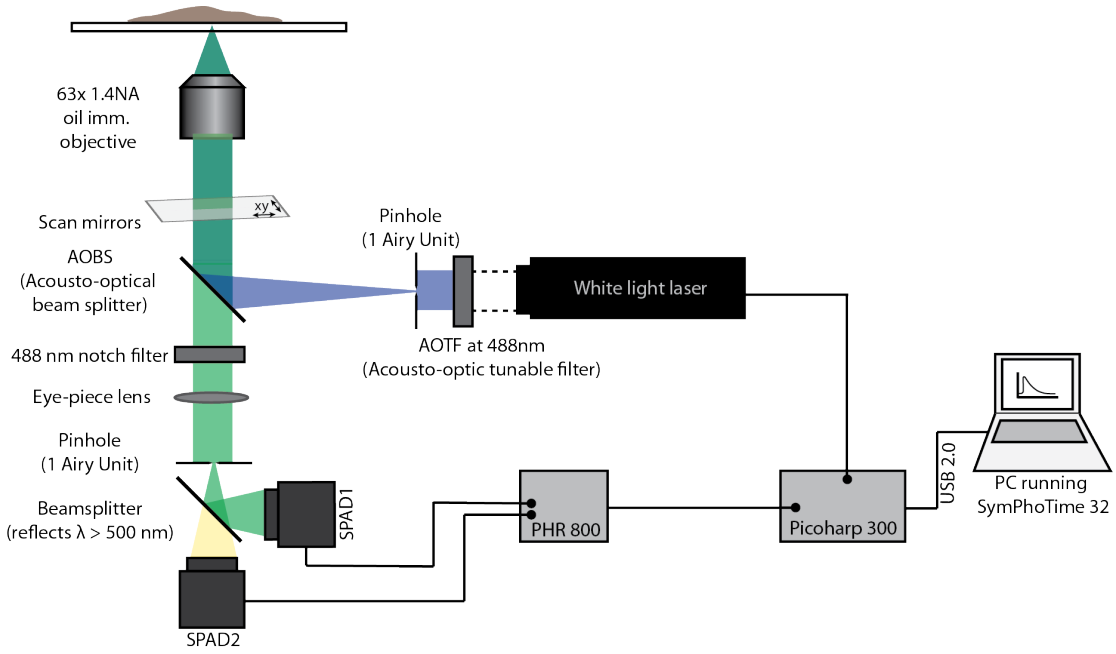

Figure 2.13 TCSPC FLIM-FRET acquisition FLIM was carried out using the set up schematised. Time-correlated single photon counting was achieved using a PicoHarp 300 TCSPC module synchronised with a pulsed white light laser (WLL) and SPAD detectors with single-photon detection efficiency. For the FLIM-FRET experiments carried out with the EGFP and mCherry FRET pair, the WLL was tuned to 488 nm to excite the EGFP donor and fluorescence emission was filtered and directed to SPAD1.

32-bit SymPhoTime v5.4.4 (PicoQuant) software was used to acquire and process FLIM data. During acquisition, this software automatically organises the time-tagged photon counts into 1600 histogram time bins. The fluorescence lifetime can then be derived by fitting a global decay of summed counts across all pixels or by sequentially fitting single pixel histograms. As demonstrated in figure 2.14, which shows both global and single pixel tail-fitted decays, global decay fitting is advantaged by stronger photon statistics. However, as pixel-by-pixel analysis provides spatial fluorescence lifetime information, it has been used exclusively in my thesis. Fitting of a model decay generated from all photon counts across a manual region of interest (ROI) identified the fit parameters to guide single pixel analysis for more reliable fitting. This was also used to identify the number of exponents and the fitting window, which spanned from as close to the peak as accurate fitting would allow to the end of the tail. Mono-exponential fits

consistently failed to fully converge with the EGFP decay, requiring instead a bi-exponential fit with the equation

$$y = y_0 + A_1 e^{-\frac{x}{\tau_1}} + A_2 e^{-\frac{x}{\tau_2}} \quad [2.15]$$

where y_0 is the Y offset, A is the amplitude and τ is the lifetime. Fitting was carried out by maximum-likelihood estimation (MLE), which is better suited to poissonian photon statistics than the least squares method sometimes employed and therefore better handles low count data, reportedly able to fit mono-exponential decays with as few as 100 counts[350].

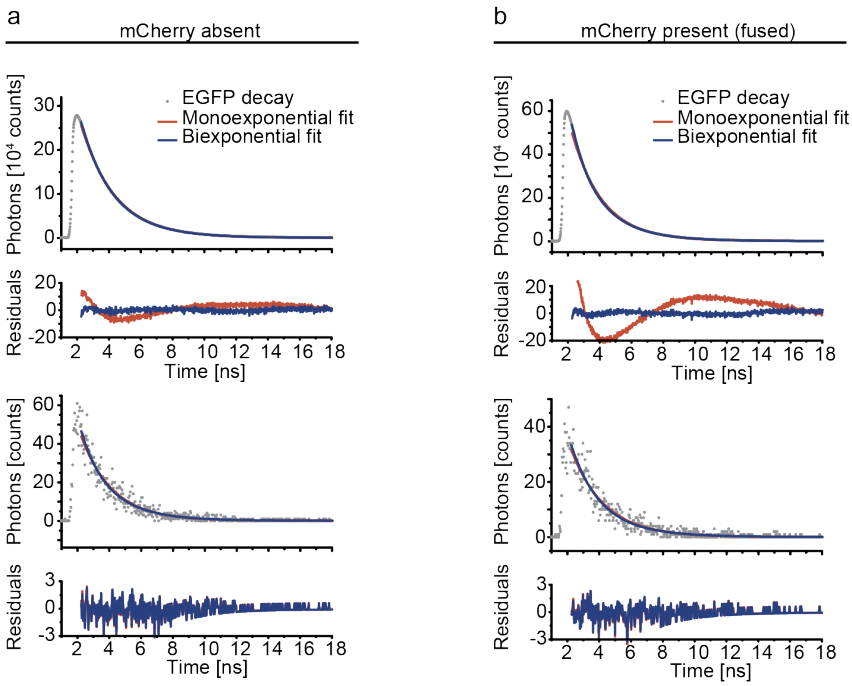

Figure 2.14 Representative EGFP fitted decays (**a**) Whole cell (top) and single pixel (bottom) fluorescence decays for EGFP expressed alone in HeLa cells. Mono-exponential (red) and bi-exponential (blue) fits are shown with their corresponding weighted residuals below, indicating improved fit statistics with a bi-exponential equation. (**b**) Presents the same as in (a) for EGFP fused to mCherry expressed in HeLa cells.

Following pixel-by-pixel analysis, the lifetime and amplitude fit parameters per pixel were exported and processed using a custom-designed Microsoft Excel VBA script. This script calculates the single-pixel amplitude-weighted average fluorescence lifetimes (τ_{amp}) using the equation

$$\tau_{amp} = \frac{A_1\tau_1 + A_2\tau_2}{A_1 + A_2}. \quad [2.16]$$

It then determines the pixel FRET efficiencies for the donor-acceptor sample based on equation 2.9 by using the median donor-only amplitude-weighted fluorescence lifetime, exports image maps of each parameter and compiles all non-zero values for graphical analysis in OriginPro.

FLIM-FRET data is presented throughout my thesis as representative intensity and amplitude-weighted average lifetime maps, alongside box-and-whisker plots of single pixel lifetimes accumulated from multiple images. FRET efficiency histograms were additionally used to compare the differences in FRET between samples, with a shift away from zero indicative of protein proximity. To validate the acquisition, fitting and analysis routines described, a control study was carried out to compare the fluorescence lifetimes and FRET efficiencies reported for co-expressed but separate EGFP and mCherry and fused EGFP-mCherry. The resulting data is presented in figure 2.15, and as expected, a drop in fluorescence lifetime is visually apparent in the fluorescence lifetime map of the fused construct (figure 2.15a), which equates to a 17.2% decrease in median fluorescence lifetime compared to the donor only sample, from 2.09 ns to 1.73 ns (figure 2.15b). By comparison, the EGFP lifetime in the presence of free mCherry is 2.04 ns, which is just 2.4% lower than the donor-only median value. These differences are reflected in the FRET efficiency histograms, where free EGFP and mCherry has a distribution centred around zero, but fused EGFP-mCherry is strongly shifted (figure 2.15c).

There is currently no typical approach to the presentation and quantitation of FRET data and this may be one of the reasons that it has not become a mainstream technique. Careful consideration was therefore given to the statistical analysis of FRET. As the mathematical relationship between FRET efficiency and separation distance (figure 2.10) indicates that values below 0.1 are poor indicators of FRET and the FRET efficiency curves for freely diffusible and fused EGFP/mCherry (figure 2.15c) intersect at this value, it has been used as a lower threshold value. FRET efficiencies greater than 0.1 (right of the red line in figure 2.15c) were integrated and differences between samples assessed using an unpaired one-tailed student *t*-test. In the case of EGFP and mCherry, integration reported values of 0.04 and 0.15 for the free fluorophores and fused fluorophores, respectively.

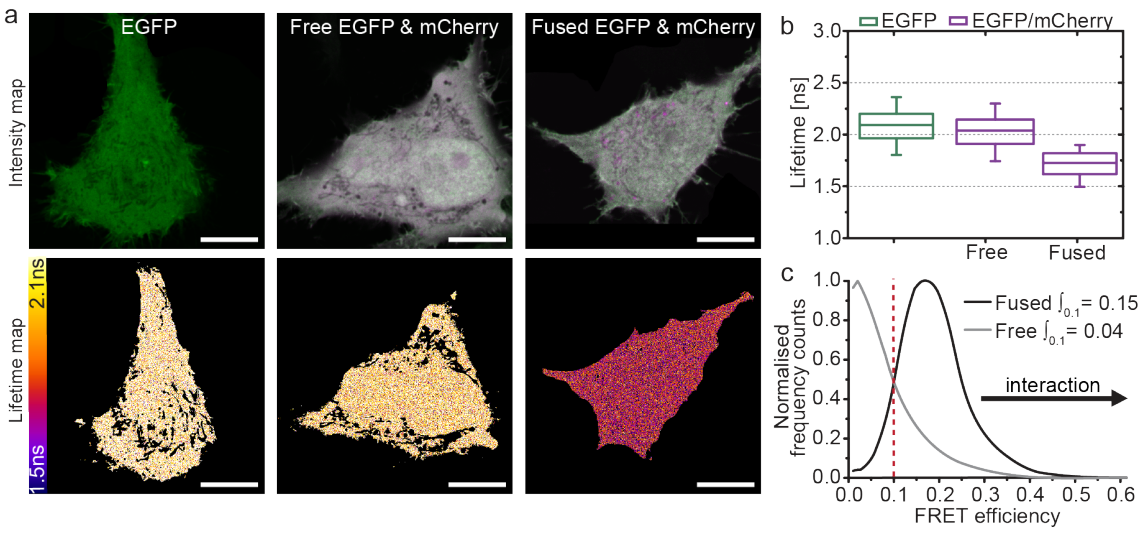

Figure 2.15 Demonstrative FLIM-FRET with fused EGFP and mCherry (**a**) Intensity images (top) and amplitude-weighted lifetime maps (bottom) of EGFP along, co-expressed with freely diffusible mCherry or fused with mCherry. Scale bars are 10 µm (**b**) Box-and-whisker plots of amplitude-weighted lifetime representing the median (central line), 25th and 75th quartiles (box) and 1st and 99th quartiles (10 µm) (**c**) FRET efficiency histogram demonstrated FRET only occurs when the fluorophores are fused, the integral of values above 0.1 provides a useful metric for comparison of histograms.

It must also be noted that during data processing a 1,000 photon count threshold was applied to exclude unreliable fits from low-count pixels. This threshold was determined based on experimental analysis, presented in figure 2.16, which demonstrates successful fitting across the 1,000-10,000 photon count range. Intensity images (panel a) were acquired from HeLa cells expressing either EGFP or the EGFP-mCherry fusion protein. Additionally, four fluorescence lifetime measurements were carried out such that acquisition was terminated when a pixel reached either 500, 1000, 5000 or 10000 counts. As demonstrated in panel b, the uneven fluorophore distribution ensures that each image has a spread of data below these maximum values. It is apparent from the fluorescence lifetime maps in panel c that the expected differences in lifetime between these two samples are strongly diminished when the counts are capped at 1,000 photons, which is reflected in the improved photon statistics of the corresponding single pixel decays, panels d-g, and the assessment of their fits, panel m. Furthermore, this does not appear to be a consequence of EGFP self-quenching at high concentration

because the fluorescence lifetime does not reduce with signal intensity, instead high count data reduces the variation in lifetime values, panels d-g. Calculations of FRET efficiency between EGFP-only and EGFP-mCherry image pairs, highlights the need for photon counts greater than 1,000 as both of the datasets acquired below this threshold produced nonsensical FRET efficiency histograms (panel l). These findings align with theoretical expectations[351] and provide a strong argument for the use of a minimum count threshold of 1,000.

2.6 Summary

Modern biology now has a vast array of techniques to investigate protein structure, function and interaction; this chapter has explored some of the techniques offered by fluorescence microscopy. Microscopy allows valuable insight into protein function *in situ* but even with the advent of super-resolution microscopy, the direct detection of protein interactions in living cells remains elusive. FLIM-FRET, however, can probe protein proximity at the scale of protein interactions and provides a robust technique to confirm, *in situ*, suspected interactions. I have presented here the validation of the two cornerstone techniques of this thesis, quantified fluorescence colocalisation and TCSPC FLIM-FRET. This validation allows conclusions to be confidently drawn from these techniques.

FLIM-FRET remains a side-line technique not in mainstream use and I speculate that this may stem from the expense of the specialist equipment, the complexity of the analysis and the slow acquisition of the most robust TCSPC methods. Therefore, a novel standardised approach to the visualisation and statistical analysis of FLIM-FRET data has been proposed here, which could be broadly applied to other FLIM-FRET studies and may alleviate the apparent complexity of analysis. Furthermore, to address the requirement for specialist equipment and lengthy acquisition times, chapter six characterises a novel non-commercial detector that has both photon counting and TCSPC acquisition modes for intensity and fluorescence lifetime imaging respectively. This was assessed for its applicability as a 'plug-and-play' camera for the real-time acquisition of widefield TCSPC FLIM-FRET data.

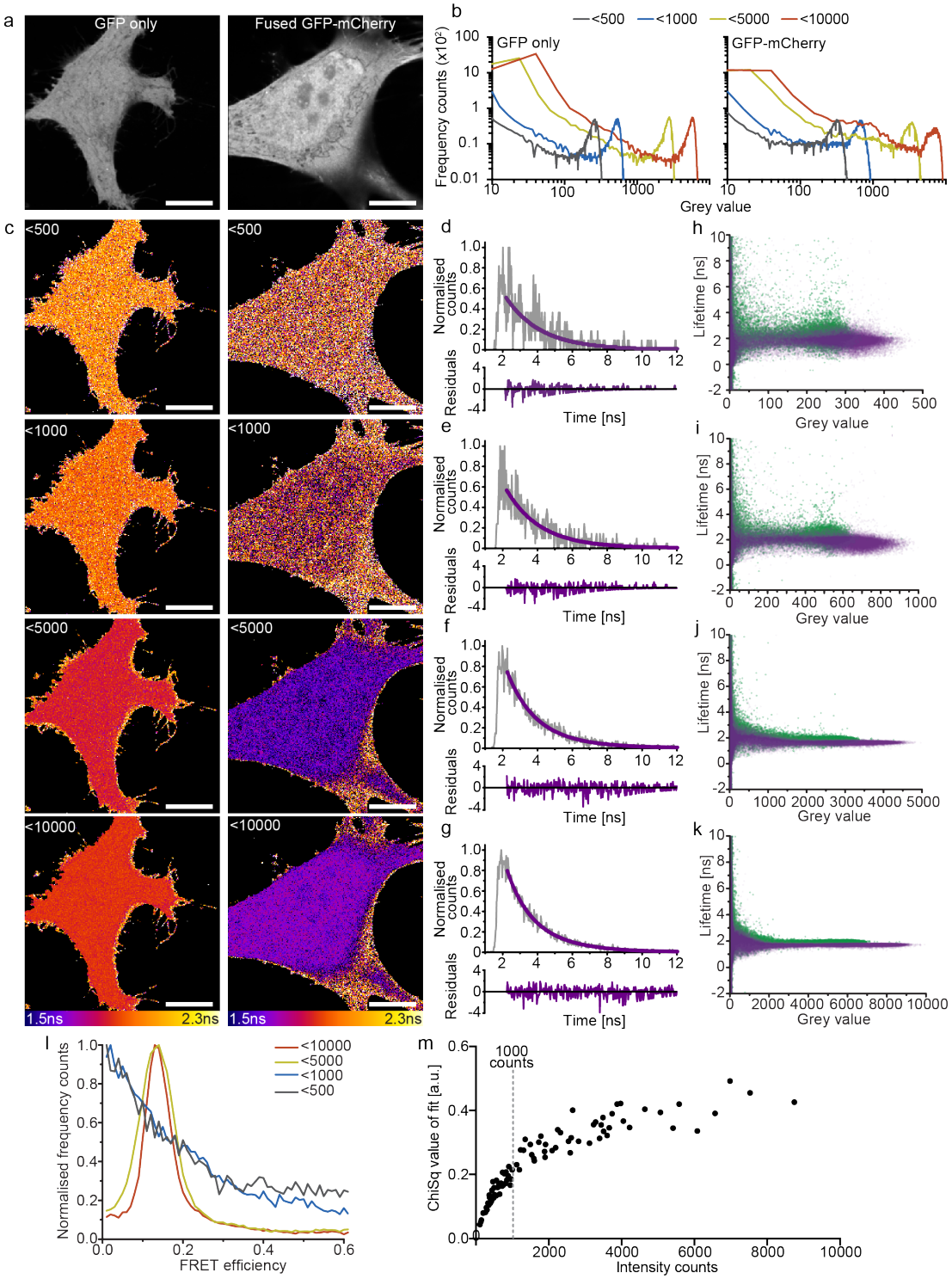

Figure 2.16 Minimum photon count analysis for decay fitting (**a**) Photon count images of EGFP or fused EGFP-mCherry with (**b**) intensity histograms showing the spread of counts per pixel. (**c**) Fluorescence lifetime maps for EGFP only (left) and fused EGFP-mCherry (right) when acquiring to a maximum of 500, 1000, 5000 or 10000 pixel counts as indicated and demonstrating poor lifetime differentiation when the counts are below 1000. (**d-g**) demonstrative single pixel fits corresponding to the adjacent images in (c). (**h-k**) The distribution of average lifetimes as a function of photon counts and (**i**) FRET efficiency histograms for each image pair in (c). (**m**) Single pixel fit χ^2 values demonstrating improved fit with increased photon counts. Scale bars are 10 μm.

CHAPTER THREE:

Materials and Methods

3.1 Molecular biology

The work presented in this thesis required the generation of a variety of genetic constructs for the transfection of mammalian cells as listed in table 3.1 overleaf. A number of the constructs used were kindly gifted from other labs and the remaining I engineered using the molecular techniques described in this section. All constructs used the discontinued Clontech vector backbone that encodes a fluorescent protein tag. The gene of interest was inserted in-frame with the fluorescent protein separated by a flexible linker either upstream of the tag (N-vector) or downstream (C-vector) as demonstrated in figure 3.1. The only construct used that has a different vector backbone was pCDNA3.1_EGFP-mCherry, which is also depicted in figure 3.1.

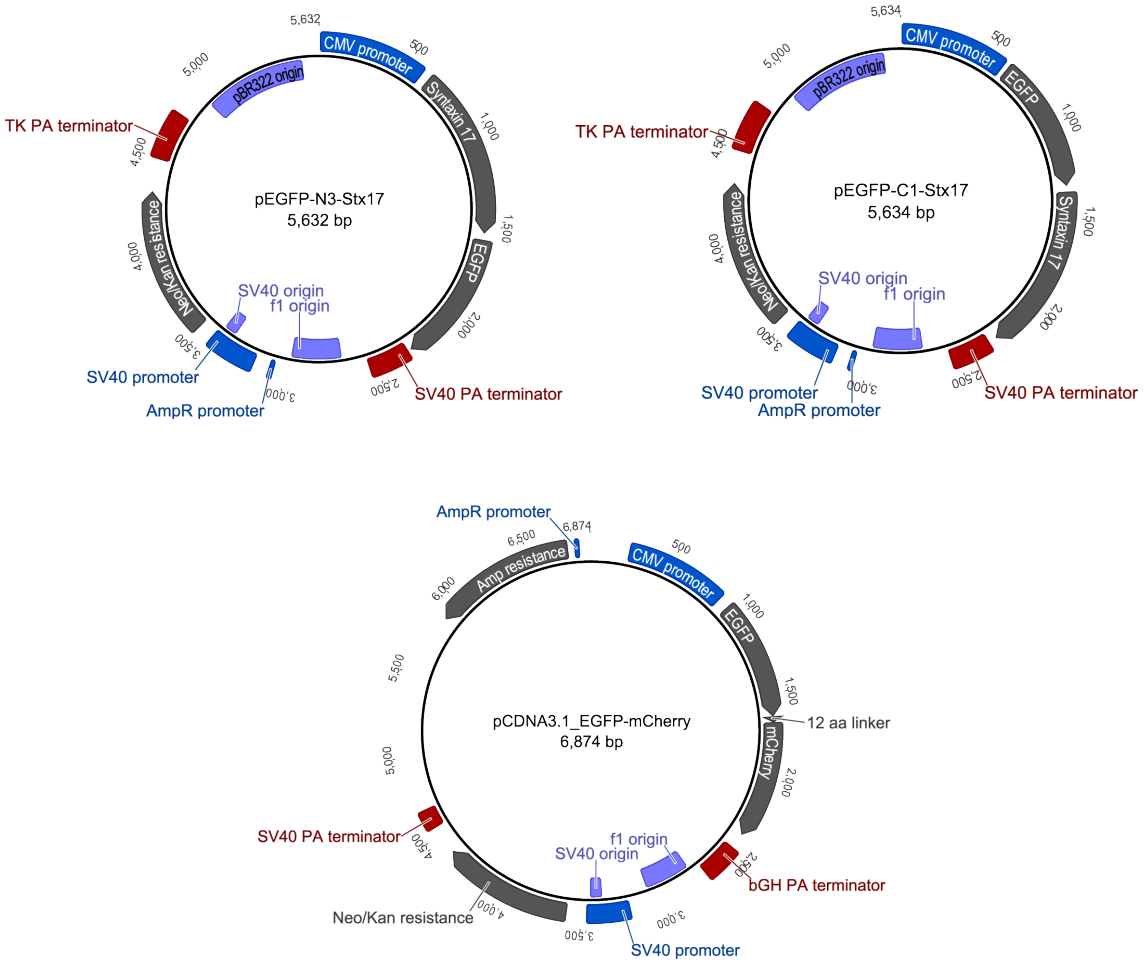

Figure 3.1 Demonstrative plasmid maps of fluorescent constructs Clontech pEGFP vectors with Stx17 inserted upstream of EGFP (top left) or downstream of EGFP (top right). The pCDNA3.1 vector was also used to express the EGFP-mCherry fusion protein (bottom).

Table 3.1 List of plasmids used in this thesis

Gene of interest	Vector	Source
LC3	pmCherry-C2-LC3B	Addgene 24920 – Toren Finkel's lab
	pEGFP-C2-LC3B	Cloned by R.Saleeb
	pEGFP-mCherry-C2-LC3B	Cloned by R.Saleeb
Syntaxin 17	pMRXIP-GFP-Stx17	Addgene 45909 – Noboru Mizushima's lab
	Non-labelled Stx17 (Stx17[inv])	SDM of pEGFP-N3-Stx17 to introduce stop codon
	pEGFP-N3-Stx17	Cloned by R.Saleeb
	pEGFP-C1-Stx17	Cloned by R.Saleeb
	pmCherry-N3-Stx17	Cloned by R.Saleeb
	pmCherry-C1-Stx17	Cloned by R.Saleeb
	R-GECO-N3-Stx17	Cloned by R.Saleeb
	G-GECO-N3-Stx17	Cloned by R.Saleeb
	pmCherry-Stx17-EGFP	Cloned by R.Saleeb
	pEGFP-Stx17-mCherry	Cloned by R.Saleeb
	pmCherry-Stx17[TMD]-EGFP	Cloned by R.Saleeb
	pmCherry-C1-Stx17[Q196G]	SDM of pmCherry-C1-Stx17
	pmCherry-C1-Stx17[ED3-6K]	SDM of pmCherry-C1-Stx17
	pmCherry-C1-Stx17[S2A]	SDM of pmCherry-C1-Stx17
	pmCherry-C1-Stx17[S2E]	SDM of pmCherry-C1-Stx17
SNAP29	pMRXIP-GFP-SNAP29	Addgene 45923 – Noboru Mizushima's lab
	pEGFP-N3-SNAP29	Cloned by R.Saleeb
	pEGFP-C1-SNAP29	Cloned by R.Saleeb
	pmCherry-N3-SNAP29	Cloned by R.Saleeb
	pmCherry-C1-SNAP29	Cloned by R.Saleeb
VAMP8	pMRXIP-GFP-VAMP8	Addgene 45919 – Noboru Mizushima's lab
	pEGFP-C1-VAMP8	Cloned by R.Saleeb
	pmCherry-C1-VAMP8	Cloned by R.Saleeb
VAMP7	pEGFP-C3-VAMP7	Addgene 42316 – Thierry Galli's lab
VPS33A	pMXsIP-GFP-VPS33A	Addgene 67022 – Noboru Mizushima's lab
	pEGFP-C1-VPS33A	Cloned by R.Saleeb
	pmCherry-C1-VPS33A	Cloned by R.Saleeb
Vti1b	pmCherry-C1-Vti1b	Gift from Atsuo Amano's lab
Atg14	pEGFP-C2-Atg14L	Addgene 21635 – Tamotsu Yoshimori's lab
LAMP1	pmGFP-N3-LAMP1	Addgene 34831 – Esteban Dell'Angelica's

		lab
	pmCherry-N3-LAMP1	Cloned by R.Saleeb
Rab5a	pmCherry-C-Rab5a-7	Addgene 55126 – Michael Davidson's lab
Rab7a	pmCherry-C-Rab7a-7	Addgene 55127 – Michael Davidson's lab
Golgi marker construct	pmCherry-Golgi-7	Addgene 55052 – Michael Davidson's lab
Calreticulin	pmCherry-N1-Calreticulin-16	Addgene 55006 – Michael Davidson's lab
EGFP	pEGFP-N3	Clontech vector
mCherry	pmCherry-N1	Clontech vector
EGFP-mCherry fusion	pCDNA3.1_EGFP-mCherry	Cloned by D.Kavanagh

3.1.1 Standard buffers and media

The standard buffers and media used for molecular biology were prepared as outlined in table 3.2.

Table 3.2 Media and buffers for molecular biology

Buffer	Concentration	Reagent
LB (Lennox method)		
pH adjusted to 7.4 and heat sterilised	10 g/L	Tryptone
	5 g/L	Yeast extract
	5 g/L	Sodium chloride
LB Agar		
pH adjusted to 7.4 and heat sterilised	1X	LB
	1.5% (w/v)	Agar
TBE (10X)		
	1 M	Tris-base
	1 M	Boric acid
	20 mM	EDTA
TFB1		
pH adjusted to 5.8 and filter sterilised	30 mM	Potassium acetate
	10 mM	Calcium chloride
	50 mM	Manganese chloride
	100 mM	Rubidium chloride
	15% (v/v)	Glycerol
TFB2		
pH adjusted to 6.5 and filter sterilised	10 mM	MOPs
	75 mM	Calcium chloride
	10 mM	Rubidium chloride
	15% (v/v)	Glycerol

3.1.2 Polymerase chain reaction

Polymerase chain reaction (PCR) amplifies DNA fragment number by repeated cycles of DNA polymerase-mediated replication[352]. This process is controlled by thermocycling to separate double-stranded DNA, anneal primers and finally promote primer extension[352]. Forward and reverse primers are designed to flank the amplification region and can introduce additional bases such as restriction sites for cloning[353]. The high fidelity polymerase, PfuUltra (Agilent, 600380), was selected for its 3'-5' exonuclease proofreading capacity to minimise the generation of mutant sequences[354].

The reaction mix was prepared to 50 µl containing 0.2 mM dNTPs, 125 ng of each primer, 10 ng of plasmid DNA template, 1X PfuUltra buffer and 2.5 U PfuUltra (added last). These were mixed gently and centrifuged to collect before thermocyling in a Techne 5PrimeG Thermal Cycler as described in table 3.3.

Table 3.3 PCR thermocycling conditions

Step	Time	Temperature (°C)	Cycles
Initial denature	2mins	95	1
Denature	30s	95	5
Anneal	30s	T_m – 5 (complimentary primer sequence)	
Elongate	1min/kb	72	
Denature	30s	95	25
Anneal	30s	T_m – 5 (full primer sequence)	
Elongate	1min/kb	72	
Final elongate	7mins	72	1
Hold	-	10	

3.1.3 Site-directed mutagenesis

Site-directed mutagenesis (SDM) is a PCR-based technique to engineer specific mutations into a sequence of interest[355]. SDM uses forward and reverse primers that both bind to the mutation site and contain the desired mutation flanked by 15-20 bases on each side[353]. Following amplification, the non-mutant template is selectively digested with the methylation-sensitive restriction enzyme, dpnI[353]. To

ensure the template DNA is methylated, it was purified from dam+ XL10-Gold *E. coli*.

The reaction mix was prepared to 50 µl using the Quikchange II Site-Directed Mutagenesis kit (Agilent, 200524). It contained 0.2 mM dNTPs, 125 ng of each primer, 5 ng of plasmid DNA template, 1X PfuUltra buffer, 3 µl Quik solution and 2.5 U PfuUltra (added last). Reactions were mixed gently and centrifuged to collect before thermocyling as described in table 3.4.

Table 3.4 Site-directed mutagenesis thermocycling conditions

Step	Time	Temperature	Cycle
Initial denaturation	1 min	95°C	1
Denature	50 s	95°C	18
Anneal	50 s	60°C	
Elongate	1 min/kb	68°C	
Final elongation	7 min	68°C	1
Hold	-	10°C	

Following thermocycling, methylated template DNA was digested by 60 minute incubation of each sample at 37 °C with 1 µl DpnI. The digestion product was used to transform competent bacteria as outlined in section 3.1.12 with the exception that all transformation mix was grown on LB agar, split across two plates, due to the low yield of SDM transformants.

3.1.4 Agarose gel electrophoresis

Agarose gel electrophoresis is a standard technique used to separate nucleic acids by length. It applies an electric field that drives DNA migration through the agarose gel from the cathode to the anode due to the negative charge of the phosphate backbone[353]. The agarose forms a 3D matrix of helical agarose molecules in supercoiled bundles forming a porous structure that impedes DNA migration dependent on size[353].

The gels were prepared by heating 1-2% (w/v) agarose in TBE buffer until dissolved. 1:10,000 SYBR Safe DNA gel stain (Life Technologies, S33102) was added after cooling, which intercalates with DNA and fluoresces upon UV exposure to visualise DNA bands. The gel was poured into a cast and allowed to set before

submerging in TBE within the electrophoresis chamber and removing the comb. Orange G loading dye (Sigma Aldrich, O3756) in 50% (v/v) glycerol was added to each sample to a final concentration of 500 μg/ml. Samples were transferred to individual wells alongside the MassRuler Express Reverse DNA ladder Mix (Thermo Scientific, SM1293), which contains a mix of DNA of known size for fragment size analysis. A constant voltage of 100 V was applied for approximately 40 minutes and the gel was imaged under UV using the Fusion FX7 Imaging System.

3.1.5 DNA purification from agarose

DNA bands requiring purification were excised from the agarose gel using a UV transilluminator box for visualisation. Bands were purified using the GeneJET Gel Extraction kit (ThermoFisher Scientific, K0692) as per the manufacturer's instructions. This kit uses a chaotropic agent to disrupt the structure of the agarose gel and thereby dissolve it. The DNA is adsorbed onto a silica column and macromolecular contaminants are solubilised and eluted through the column using 70-75% ethanol before eluting the purified DNA with deionised water.

3.1.6 Quantitation of DNA concentration

DNA concentration and quality was measured using a ThermoFisher Scientific NanoDrop 2000c UV-Vis Spectrophotometer blanked with the DNA carrier solution (deionised water). 2 μl of the sample is transferred to the measurement pedestal where the device uses surface tension to create a liquid column between two optical fibres. The light transmitted through the sample across the 220-350 nm spectral range is measured and used in combination with the reference sample to determine the absorbance spectrum using the following relationship:

$$\text{absorbance} = -\log\left[\frac{\text{Intensity}_{\text{sample}}}{\text{Intensity}_{\text{Reference}}}\right]. \qquad [3.1]$$

The concentration of DNA is automatically calculated based on Beer-Lamberts law,

$$\text{Absorbance} = \varepsilon bc \qquad [3.2]$$

where absorbance is 260 nm (the absorption maxima for DNA), e is the extinction coefficient, b is the path length and c is the analyte concentration. The quality of the sample is determined by the ratio of absorbance at 260 nm and 280 nm. Contaminants such as protein absorb strongly at 280 nm and therefore a low 260/280 value suggests contamination. A pure DNA sample has a 260/280 value of approximately 1.8.

3.1.7 DNA restriction digestion

Restriction enzymes are endonucleases that recognise and cleave a specific DNA sequence often leaving behind an overhang, allowing two DNA fragments digested with the same enzyme to be joined by cohesive-end ligation[353]. Optimal reaction conditions vary dependent on the enzyme. Throughout my work, the ThermoFisher Scientific fast-digest restriction enzymes were used.

The reaction mix was prepared as per table 3.5. The reactions were gently mixed and centrifuged to collect before incubating as recommended per enzyme. In order to avoid star activity (non-specific cleavage), the enzyme volume never exceeded one tenth of the total volume as insufficient dilution of the storage buffer can interfere with enzyme activity[356].

Table 3.5 Restriction digest reaction preparation

Component	Volume for analysis	Volume for product purification
10X fast digest green buffer	2 µl	3 µl
Plasmid DNA	200 ng	3 µg
Restriction enzyme 1	1 µl	1 µl
Restriction enzyme 2	1 µl	1 µl
dH_2O	To 20 µl	To 30 µl

3.1.8 DNA ligation

T4 DNA ligase (ThermoFisher Scientific, EL0011) was used to facilitate cohesive-end ligation, which joins two DNA fragments with complimentary overhangs[353]. The DNA ligase is derived from bacteriophage T4 where its role in DNA nick repair allows it to catalyse the formation of phosphodiester bonds between adjacent 5'-phosphate and 3'-hydroxyl termini of nucleic acid fragments for DNA ligation[353].

20-100 ng vector DNA was ligated to the insert DNA with either a 1:1, 1:3 or 3:1 ratio of the insert:vector molarity of available ligation sites. This was calculated based on the quantity (ng) and size (Kb) of the insert (I) and vector (V) as per the following equation:

$$I_{ng} = \frac{(V_{ng} \times I_{Kb})}{V_{Kb}} \times \text{ratio}. \qquad [3.3]$$

To carry out the ligation, a reaction mix was prepared to 20 µl containing 1X ligation buffer and 1 U T4 DNA ligase as well as the vector and insert DNA. This mix was incubated at room temperature for 10 minutes. The ligation product was then used for bacterial transformation.

3.1.9 TA Cloning

TA cloning is the ligation of a gene of interest into a T-vector, which is a linearised double-stranded vector with a 3' unpaired thymine overhang[353]. The trivial addition of an adenosine overhang (A-tail) to the insert DNA allows any fragment to be ligated into the intermediate T-vector, with an efficiency 50 times greater than blunt-end ligation would allow[353]. The flanking restriction sites on the T-vector backbone subsequently enable easy transfer of the gene into other vectors.

Agarose gel-purified PCR product was A-tailed using DreamTaq (ThermoFisher Scientific, EP0701) by the preparation of a 50 µl reaction mix containing the purified PCR product, 1X DreamTaq buffer with $MgCl_2$, 0.2 mM dATP and 5 U DreamTaq polymerase. This reaction was incubated for 30 minutes at 72°C and TA cloning was completed by DNA ligation of the A-tail product into the pre-linearised pGEM-T Easy vector.

3.1.10 Bacterial culture

All bacterial work was carried out with XL10-Gold *E. coli* (Agilent Technologies, 200315) cultured in LB medium or on LB agar at 37°C and with agitation in the case of liquid culture. These cells are deficient in all known restriction systems, RecA and endonuclease to enhance insert stability and high plasmid purification yield[357]. As XL10-Gold cells are tetracycline and chloramphenicol resistant, all bacterial transformations were carried out with plasmids encoding either ampicillin or kanamycin resistance and cultured in the presence of 100 μg/ml ampicillin or 50 μg/ml kanamycin as required. All bacterial work was carried out close to an open flame to prevent contamination and large-scale cultures were derived from a single colony.

3.1.11 Preparation of chemically competent bacteria

Chemically competent *E. coli* are amenable to heat shock transformation with exogenous DNA[353]. To prepare chemically competent bacteria, the rubidium chloride method was used. XL10-Gold *E. coli* were grown in the presence of 20 mM $MgSO_4$ and harvested during the log growth phase (optical density of 0.4-0.6) by five minute centrifugation at 4,500 xg and 4°C. The cells were resuspended to two fifths of the original culture volume with ice-cold TFB1 and incubated for five minutes on ice. The cells were then centrifuged under the same conditions as previously and resuspended to one tenth the original culture volume with ice-cold TFB2 and incubated for one hour on ice. Aliquots of bacteria were prepared, snap frozen in liquid nitrogen and stored at -80°C.

3.1.12 Transformation of competent bacteria

Chemically competent cells are able to take up exogenous DNA upon heat shock[353]. As the heat shock procedure is optimised for the material and thickness of the container, this protocol uses 1.5 ml Eppendorf tubes (Fisher Scientific, 10451043).

50 µl of chemically competent XL10-Gold *E. coli* thawed on ice were transferred to a pre-chilled 5 µl aliquot of the ligation product. The DNA and bacteria mixture were incubated for ten minutes on ice prior to a precise 30 second heat shock by transfer to a 42°C waterbath. They were subsequently returned to ice for a further two minutes.

Following heat shock, the bacterial suspension was supplemented with 500 µl of antibiotic-free LB media and cultured at 37°C with agitation for 45 minutes to allow expression of the plasmid-encoded antibiotic resistance gene prior to antibiotic exposure. 50 µl of the transformed bacteria was then spread on agar supplemented with 100 µg/ml ampicillin or 50 µg/ml kanamycin as appropriate and grown overnight at 37°C.

3.1.13 Plasmid DNA purification from bacteria

Plasmid DNA was purified from bacteria using either the GeneJET plasmid Miniprep kit (ThermoFisher Scientific, K0503) for low yield or the PureLink HiPure Plasmid Maxiprep kit (ThermoFisher Scientific, 210007) for high-yield by following the manufacturer's instructions. These kits are based on the alkaline lysis method for plasmid purification, using SDS to disrupt bacterial membranes and DNA-protein complexes and high pH to denature DNA. Plasmid DNA can subsequently be isolated following neutralisation, where it re-anneals more easily than genomic DNA allowing it to resist precipitation under high salt conditions, unlike single-stranded genomic DNA. Bacteria were grown for purification, from a single colony to stationary phase, in 5 ml or 200 ml LB for miniprep and maxiprep purification, respectively.

3.2 Cell culture

Both HEK293T cells and HeLa cells were used to develop the assays to study autophagy (see section 4.3.1), however HeLa cells were found to induce autophagy more consistently and were therefore subsequently used throughout my research. Both of these are well-established adherent mammalian cells. HeLa cells are highly resilient cervical adenocarcinoma cells that were the first cell line to be established in culture[358], and HEK293T cells are human embryonic kidney cells that have been immortalised by transformation with sheared adenovirus 5 DNA[359].

3.2.1 Standard buffers and media

The standard media used for cell culture were prepared as per table 3.6.

Table 3.6 Cell culture medium

Reagent	Concentration	Supplier
DMEM with 4.5 g/L D-glucose	1X	Gibco, 31053-044
Penicillin	100 U/ml	Gibco, 15140-122
Streptomycin	100 µg/ml	Gibco, 15140-122
Glutamax	1X	Gibco, 35050
Sodium pyruvate	1 mM	Gibco, 11360-039
Heat-inactivated foetal bovine serum	10% (v/v)	Gibco, 10500-064

3.2.2 Cell freezing and reuse

Cell stocks were frozen at a concentration of $1x10^6$ cells per aliquot (determined by haemocytometry) in culture medium supplemented with 5% (v/v) dimethyl sulfoxide (DMSO). Aliquots were frozen to -80°C at a rate of approximately -1°C/minute by using a Mr. Frosty Freezing Container (Thermo Scientific, 5100-0001). Stocks frozen to -80°C were transferred to liquid nitrogen for long-term storage.

All experimental work was carried out with cells that had been passaged no more than 25 times after thawing. To establish a new aliquot in culture, cells were thawed as quickly as possible by warming at 37°C and transferred to a T75 cm^3 culture flask containing 15-20 ml pre-warmed medium. Cells were incubated overnight at 37°C and 5% CO_2 (v/v) to allow adherence before changing the

culture medium to remove all DMSO that was present in the freezing medium. Cells were subsequently maintained as normal.

3.2.3 Cell line maintenance

Both HeLa and HEK293T cells were maintained at 37°C and 5% CO_2 (v/v) in the culture medium outlined in section 3.2.1. They were cultured in 75 cm^3 flasks and passaged twice weekly upon reaching 80% confluence; this requires 72 hours when a flask is seeded with $1.5x10^6$ HeLa cells or $2x10^6$ HEK293T cells.

Cell passaging was carried out by removing media, rinsing cells with Versene (Gibco, 15040-033) and incubating for 2 minutes with 2 ml 0.05% Trypsin-EDTA (Gibco, 25300) at 37°C. Further trypsinisation was inhibited by the addition of culture medium due to the protease inhibitors present in the FBS. The cell suspension was collected, pelleted by centrifugation and resuspended at the desired concentration as determined by haemocytometry. The required amount of cell suspension was added to 15-20 ml warmed culture medium in a fresh T75 cm^3 flask.

3.2.4 Transient transfection of cells

Exogenous DNA can be efficiently introduced into both HeLa and HEK293T cells by cationic lipid or polymer mediated transfection. This was carried out using Turbofect Transfection reagent (Thermo Scientific, R0531) optimised for each cell line. Turbofect reportedly contains a cationic polymer that forms a stable positively-charged complex with DNA that facilitates its cell uptake[360].

For transient transfection of cells, $0.3x10^6$ HeLa cells or $0.4x10^6$ HEK293T cells were plated in 6-well format and cultured at 37°C and 5% CO_2 (v/v) overnight. For each well, 400 µl non-supplemented DMEM (Gibco, 31053-044) was combined with 2 µg of total plasmid DNA and 8 µl Turbofect for HeLa cells or 4 µg DNA and 6 µl Turbofect for HEK293T cells. The transfection mix was equilibrated at room

temperature for 20 minutes before drop-wise addition to wells. The media was changed after 6-7 hours of exposure to the transfection reagent to minimise cationic lipid or polymer-mediated toxicity[361].

3.2.5 siRNA knockdown in HeLa cells

Custom-designed double-stranded small interfering RNA (siRNA) can specifically bind endogenous mRNA and target it for degradation by the RNA-induced silencing complex (RISC) thereby significantly reducing expression of a gene of interest[362, 363]. Knockdown studies were used in this project to suppress the translation of both SNAP29 and VPS33A using the siRNA duplexes listed in table 3.7.

Table 3.7 Details of siRNA duplexes used in knockdown studies

Knockdown target	siRNA	Antisense sequence
SNAP29	SMARTpool siGENOME siRNA (Dharmacon, M-011935-00-0005)	Not published
VPS33A	Stealth siRNA ThermoFisher Scientific, HSS127975	5′-AUGAGAUCUAAGC UGUACUCCUCCC-3′
Non-targeting negative control	siGENOME Non-Targeting siRNA #2 (Dharmacon, D-001210-02)	Not published

Cells for knockdown studies were plated onto coverslips in 6-well format. $0.1x10^6$ cells in 2.5 ml culture medium were seeded per well and incubated overnight at 37°C and 5% CO_2 (v/v). siRNA was introduced by cationic lipid mediated transfection using the Lipofectamine RNAiMAX Transfection Reagent (ThermoFisher Scientific, 13778030). 250 µl of non-supplemented DMEM was separately added to 1.5 µl 20 µM siRNA or 3 µl Lipofectamine and incubated at room temperature for five minutes before combining both and allowing to equilibrate for a further 20 minutes. 500 µl of the transfection mix was added drop-wise to each well and the cells were cultured for 48 hours prior to DNA transfection or lysate preparation. After the first 6-7 hours following siRNA transfection, the cells were washed with Versene and fresh medium applied.

3.3 Protein biochemistry

3.3.1 Standard buffers and media

The standard buffers and media used for protein biochemistry were prepared as outlined in table 3.8.

Table 3.8 Buffers for protein biochemistry

Buffer	Concentration	Reagent
Lysis buffer		
	25 mM	Tris-HCl pH 7.4
	150 mM	sodium chloride
	1 mM	EGTA
	1 mM	EDTA
	5 mM	sodium pyrophosphate
	10 mM	b-glycerophosphate
	0.1% (v/v)	β-mercaptoethanol
	1% (v/v)	NP-40
	1 per 200 ml	EDTA-free protease inhibitor tablet (Sigma Aldrich, #4693132001)
SDS running buffer		
	25 mM	Tris base
	200 mM	Glycine
	1% (w/v)	Sodium dodecyl sulfate
2X LSB		
	65.8 mM	Tris-HCl pH 6.8
	26.3% (v/v)	Glycerol
	2.1% (w/v)	Sodium dodecyl sulfate
	0.01% (w/v)	Bromophenol blue
	355 mM	β-mercaptoethanol (added per use)
PBS-T		
	19 mM	Sodium phosphate monobasic monohydrate
	16 mM	Sodium phosphate dibasic
	150 mM	Sodium chloride
	0.05% (v/v)	Tween-20

3.3.2 Cell lysate preparation

Cell lysis aims to isolate the total cellular protein. As protein is unstable at room temperature, all steps were carried out on ice using chilled consumables. Cells cultured in 6-well format were transferred to ice and washed with cold 1X filter-sterilised PBS (Fisher Scientific, 10388739). After removal of all residual PBS, 100 µl lysis buffer was applied and cells were scraped into suspension. The suspension

was transferred to a tube and incubated on ice for 30 minutes to allow complete lysis. The lysate was clarified by a 30 minute 14,000 xg centrifugation at 4°C, the total protein in the supernatant was separated and the pellet disposed of.

3.3.3 Protein concentration determination

Protein concentration was determined in triplicate per sample using the Bradford assay. This is a Coomassie G-250 dye-based colorimetric assay that detects total protein concentration based on a colour-shift of the dye upon protein binding[364]. This assay was selected for its compatibility with β-mercaptoethanol in the lysis buffer, however it suffers the disadvantage of sensitivity to detergents. To overcome this limitation, samples were diluted with detergent-free lysis buffer to bring the final NP-40 concentration within the maximum 0.5% concentration compatible with the assay[365].

Each protein sample was diluted 1:5 and 1:50 in detergent-free lysis buffer to bring them into the working range of the Bradford reagent. For standard curve generation, five bovine serum albumin (BSA) protein standards of known concentration were also prepared in detergent-free lysis buffer ranging from 0 - 1.5 mg/ml. 5 µl of each sample was combined in a 24-well plate with 250 µl Bradford reagent that had been warmed to room temperature and gently mixed to uniformly disperse the dye. The plate was gently vortexed for 30 seconds before measuring absorbance at 595 nm using a ThermoFisher Scientific NanoDrop 2000c UV-Vis Spectrophotometer. The known BSA standards were used to generate a standard curve and the concentrations of the unknown protein samples were derived from the best fit of this curve. Total protein concentrations were subsequently adjusted to 2 mg/ml.

3.3.4 SDS-PAGE

Sodium dodecyl sulfate polyacrylamide gel electrophoresis (SDS-PAGE) is a standard technique to separate denatured protein by molecular weight. In

similarity to agarose gel electrophoresis, the polyacrylamide gel consists of a crosslinked porous structure that hinders the migration of proteins dependent on their size[366]. Anionic SDS denatures and coats the protein, driving their migration to the anode when an electric field is applied[366].

SDS-PAGE was carried out using the Bio-Rad Laemmli-like Tris-Glycine gels with compatible Laemmli sample buffer (LSB) and SDS-running buffer, prepared as described in section 3.3.1. This method uses a discontinuous buffer system to concentrate the proteins prior to separation by trapping them between a moving boundary, which is encased between the fast-migrating leading chloride ions contained in the gel and the slow-migrating glycinate ions in the buffer[367]. Such protein stacking results in sharper bands upon separation.

Pre-cast 4-20% or Any kD Mini-PROTEAN TGX gels (Bio-Rad, 45690333) were set up in the Mini-PROTEAN Tetra Cell chamber before filling the chamber with SDS running buffer. Laemmli sample buffer (LSB) supplemented with 355 mM β-mercaptoethanol was added to protein samples to a final concentration of 1X and samples were incubated for 10 minutes at 70°C to assist protein denaturation before gel-loading 10-40 µg protein as indicated. Gels were run under constant voltage with 100 V for approximately 15 minutes to enhance protein stacking followed by 150 V for approximately 35 minutes for protein separation.

3.3.5 Protein transfer from SDS-PAGE to PVDF membrane

Protein bands were transferred from the Mini-PROTEAN TGX Precast protein gel (Bio-Rad, 4569033) to PVDF membrane using the Bio-Rad Trans-Blot Turbo Transfer System in combination with the Trans-Blot Turbo Mini PVDF Transfer Packs (Bio-Rad, 1704156). Proteins were transferred by a 7 minute application of 1.3 A constant current and fluctuating voltage up to 25 V.

3.3.6 Western blotting

Western blotting uses immuno-detection to identify the presence of a protein of interest on PVDF or nitrocellulose membrane. An indirect labelling technique was used in this work, whereby the primary antibody raised against the protein of interest is detected using a secondary enzyme-bound antibody raised against the species of the primary antibody. Chemiluminescence detection was carried out using horseradish peroxidase (HRP)-conjugated secondary antibodies detected with an enhanced luminol-based substrate that chemiluminesces upon oxidation by HRP. The precise conditions of the western blot are dependent on the protein of interest and the antibody used. The conditions used in this work are summarised in table 3.9.

Table 3.9 Details of antibodies used in western blots

Protein of interest	Lysate	Primary antibody	Secondary antibody
SNAP29	20 µg HeLa	1:1000 rabbit mAb anti-SNAP29 (Abcam, ab138500)	1:2000 goat anti-rabbit pAb IgG(H+L) HRP-conjugate (Thermo Fisher Scientific, 31460)
GAPDH	10 µg HeLa	1:3000 mouse mAb (6C5) anti-GAPDH (EMD Millipore, CB1001)	1:2000 goat anti-mouse pAb IgG(H+L) HRP-conjugate (Thermo Fisher Scientific, 31430)

Following protein transfer, PVDF membranes were air-dried for 30 minutes before blocking by rocking in 5% (w/v) BSA for 60 minutes at room temperature. Membranes were washed four times (ten minutes each with rocking motion) in PBS-T and then incubated overnight with rocking at 4°C with the primary antibody diluted in 5% BSA. The next day, the primary antibody was removed and the membrane washed as before with PBS-T before applying the secondary antibody diluted in 5% BSA and incubating with rocking for one hour at room temperature. The membrane was washed a further four times with PBS-T and the bands of interest were visualised using Clarity Western ECL substrate (Bio-Rad, 1705061) as per the manufacturer's protocol and imaged with a Fusion FX7 Imaging System.

3.4 Sample preparation

3.4.1 Preparation of coverslips for cell culture

Prior to growing cells on coverslips, the coverslips were cleaned by 30 second sonication in 0.1 M sodium hydroxide supplemented with 0.1% (v/v) Decon-90. Residual sonication buffer was removed by three wash steps in deionised water, followed by washes in absolute ethanol, absolute acetone and finally deionised water. This routine removes contaminants and thereby reduces background signal upon imaging, caused by the autofluorescence of debris.

The coverslips were coated with poly-D-lysine by one hour incubation, with rocking, in 0.05 mg/ml poly-D-lysine hydrobromide (Sigma Aldrich, P6407). Coverslips were then rinsed in deionised water and dried and sterilised by 60 minute UV irradiation. Poly-D-lysine is a positively charged synthetic amino acid chain that promotes cell adherence to the glass surface by electrostatic interactions[368].

3.4.2 Chemical cell fixation

Cell fixation provides a temporal snapshot of cell behaviour by irreversibly holding the cell in its state upon fixation. To achieve this, proteins can be chemically fixed in place using formaldehyde and glutaraldehyde by forming covalent crosslinks between inter- and intra-molecular amino groups[369]. Formaldehyde fixation is less efficient than that of glutaraldehyde; glutaraldehyde, however, cannot be used at high concentrations for fluorescence microscopy samples because any non-reacted amine groups fluoresce upon excitation within the visible spectrum, resulting in a high background signal[369].

To circumvent the limitations of each fixative, a solution containing 4% (v/v) methanol-free formaldehyde (TAAB, F017) and 0.1% (v/v) glutaraldehyde (TAAB, G010) was used. Cells were rinsed with ice-cold filter-sterilised PBS prior to application of 1 ml fixative solution per well. The cells were incubated at 4°C for 20 minutes in the fixative to minimise cell dynamics during fixation and this was

followed by a further 15 minute incubation at room temperature to ensure complete fixation. Following fixation, the cells were rinsed thoroughly by three wash steps with PBS. Cells were then incubated for 15 minutes with PBS supplemented with 50 mM ammonium chloride to bind any free glutaraldehyde amine groups, thereby reducing autofluorescence. Cells were rinsed in PBS and partially air dried before mounting.

3.4.3 Sample mounting

Samples were mounted on slides with Mowiol 4-88. This mountant cures to a solid with a refractive index ranging from 1.41-1.49, dependent on batch preparation, which closely matches the refractive index of immersion oil (1.515) and is therefore well suited to imaging with an oil immersion objective lens. To mount, a drop of Mowiol 4-88 is applied to the slide and the coverslip placed on top. The samples were allowed to cure at room temperature for 24 hours before transferring to 4°C.

Mowiol 4-88 stocks were prepared in bulk to avoid batch-to-batch variation and aliquots of frozen stocks were used as required. 2.4 g Mowiol 4-88 was combined with 6 g glycerol and 6 ml dH_2O and stirred for three hours at room temperature. 12 ml of 0.2 M Tris-HCl pH 8.5 was added and the mixture was heated to 50°C until fully dissolved. Non-solubilised particles were removed by a 15 minute 5000 xg centrifugation. The supernatant was aliquoted and stored at -20°C.

3.4.4 Quantum dot & bead sample preparation

Samples for microscopy characterisation work were prepared by adhering dilutions of commercial quantum dots or beads to coverslips. For this, 0.02 µm FluoSpheres carboxylate-modified yellow-green Microspheres (ThermoFisher Scientific, #F8787), Qdot 525 carboxyl quantum dots (ThermoFisher Scientific, #Q21341MP) and 0.01 µm TetraSpeck Microspheres (ThermoFisher Scientific, #T7279) were used. The quantum dots or beads were sonicated for 10 minutes to

disrupt aggregates and promote an even suspension. Any remaining aggregates were pelleted by centrifugation and dilutions were prepared in deionised water from the supernatant. 10,000-100,000 fold dilutions were prepared for the FluoSphere beads, 1,000-3,000 for TetraSpeck beads and 10-100 fold the QDot 525 quantum dots.

Coverslips were coated with 20 µl Cell-Tak neutralised with the addition of 0.1 M sodium hydrogen carbonate pH 8.0 and allowed to adsorb for 20-30 minutes. The manufacturer identifies Cell-Tak as a natural adhesive of polyphenolic proteins extracted from *Mytilus edulis*, a marine mussel that uses it to attach itself to structures[370]. Cell-Tak is stored in 5% acetic acid and is non-adhesive under low pH, however, it becomes highly adhesive upon neutralisation. Excess Cell-Tak was removed by washing with deionised water and replaced with the bead or quantum dot dilution, which was allowed to incubate for 20-30 minutes before washing non-bound material with deionised water. The samples were slide mounted with Mowiol 4-88.

3.4.5 Live cell imaging

To maintain healthy cells during live cell imaging, coverslips were transferred to a POC chamber system and maintained in Krebs buffer prepared as described in table 3.10. Both the Leica SP5 confocal laser scanning microscope and the Olympus IX81 widefield microscope used an external forced air heating device to maintain the microscope housing at 37°C after pre-warming overnight. A stage enclosure allowed the imaging chamber alone to be maintained at 5% (v/v) humidified CO_2. The CO_2 conditions fluctuate due to the feedback requirement and changes in CO_2 are buffered by HEPEs in the Krebs buffer. To ensure cells were healthy during live imaging, they were replaced after 30 minutes.

Table 3.10 Live cell imaging buffer composition

Buffer	Concentration	Reagent
Krebs buffer		
pH adjusted to 7.4 and osmolarity to 290 mOsmol/kg	115 mM	Sodium chloride
	5 mM	Potassium chloride
	24 mM	Sodium bicarbonate
	2.5 mM	Calcium chloride
	1 mM	Magnesium chloride
	10 mM	HEPEs
	0.1% (w/v)	Bovine serum albumin

3.4.6 Induction and inhibition of autophagy

Unless otherwise stated, autophagy was chemically induced in cells by a 60 minute incubation with 160 nM rapamycin (Thermo Fisher Scientific, PHZ1235). Rapamycin treatment is a standard approach to induce autophagy[371]; it is an mTORC1 antagonist that blocks mTORC1 inhibition of the initiation of autophagy[225]. Live cell imaging used cells exposed to 160 nM rapamycin for 60-90 minutes and rapamycin was included in the Krebs buffer to maintain induction conditions.

To ascertain autophagic flux, autophagosome-lysosome fusion was inhibited using 50 nM bafilomycin A_1 (Sigma Aldrich, B1793)[225]. Bafilomycin A_1 specifically inhibits Vacuolar-type H^+-ATPase activity and therefore the acidification of the lysosome[372]. Its effect on autophagosome-lysosome fusion is not fully understood but is believed to be a secondary effect of disrupted lysosomal acidification and function.

3.5 Microscopy and image processing

3.5.1 Confocal Microscopy

Confocal microscopy was carried out with a Leica SP5 SMD confocal laser scanning microscope (CLSM) using a 63X 1.4 NA HC PL Apo oil immersion objective lens and a pinhole set to 1 Airy unit. EGFP and mCherry probes were excited by 488 nm CW

Argon gas laser and 561 nm CW Helium-Neon gas laser respectively. Emission wavelengths were isolated using an acousto-optical beamsplitter (AOBS) rather than a dichroic mirror, which is tuned to deflect user-selected wavelengths[347, 348], allowing collection of EGFP emission between 500-550 nm and mCherry emission between 600-670 nm. For complete exclusion of the excitation wavelength, a notch filter was also inserted into the light path to block 488 nm or 561 nm wavelengths as required. Emission was detected using a photomultiplier tube (PMT) set to a gain of 600-800 V. The lateral pixel size was restricted to 0.04 μm and the axial pixel size to 0.13 μm as required for Nyquist sampling[300].

3.5.2 Stimulated emission depletion microscopy

Continuous wave gated stimulated emission depletion (CW-gSTED) microscopy was carried out with a 100X 1.4 NA HCX PL Apo oil immersion objective lens on a Leica SP5 SMD CLSM upgraded for STED capability. EGFP was excited using a white light laser tuned to 488 nm and pulsing at 80 MHz. The PSF was reduced by concurrent depletion with a CW 592 nm depletion laser, which was aligned to the excitation beam per experiment. Emission wavelengths were isolated as for standard CLSM and detected with a time-gated Leica HyD hybrid detector synchronised to the excitation pulse. As the efficiency of depletion increases with depletion time[319], time-gated detection was used to ensure peripheral PSF fluorescence has been depleted prior to detection. For EGFP emission, the detector was time-gated such that it switched from the 'off' state to the 'on' state 0.5 ns after each excitation pulse. As the resolution scales with the gated time delay to fluorescence lifetime ratio[373], this value was optimised for EGFP. Due to the narrowed PSF in STED compared to CLSM, a smaller pixel size of 0.015 μm was used to achieve Nyquist sampling[300].

3.5.3 Total internal reflection fluorescence microscopy

TIRFM was carried out with an Olympus Cell Excellence IX81 microscope using a 150X 1.45 NA UAPON oil immersion TIRF objective lens by software adjustment of the angle at which the laser impinges on the coverslip. EGFP and mCherry were imaged using 491 nm and 561 nm diode lasers respectively. In each case, emission was isolated using dual filters encompassing a dichroic mirror with bandpass filters to clean up excitation and emission wavelengths (Chroma, 49002 or 11010V2 for EGFP and mcherry respectively). Emission was detected with a Hamamatsu EMCCD camera resulting in near Nyquist sampling of 0.106 μm when coupling the selected objective with the 16 μm camera pixel.

3.5.4 Structured illumination microscopy

SIM was carried out with a Nikon N-SIM Super-Resolution Microscope System using a 100X 1.49 NA oil immersion objective lens and operating in 3D-SIM mode. EGFP and mCherry were excited by 488 nm and 561 nm lasers respectively and dual filters were employed to separate excitation and emission wavelengths. Emission was detected with an Andor iXon3 DU-897E EMCCD camera resulting in an image pixel size of 0.16 μm. Images were acquired with five structured illumination phase shifts at three different rotations and the super-resolution image was reconstructed using Nikon's NIS-Elements software. Values of high-resolution noise suppression, illumination modulation contrast and out-of-focus blur suppression were optimised iteratively per image to maximise resolution without generating reconstruction artefacts. The ImageJ SIMcheck plugin was used to validate successful reconstruction[374].

3.5.5 Fluorescence lifetime imaging microscopy

TCSPC FLIM-FRET was carried out using a Leica SP5 SMD CLSM microscope upgraded to include a Picoharp 300 TCSPC module and single photon avalanche diode (SPAD) detectors for fluorescence lifetime imaging. Data was acquired and fitted with 32-bit SymPhoTime v5.4.4 (PicoQuant) software, integrating counts at a

maximum rate of 10^5 counts per second for typically 8-12 minutes to achieve a maximum pixel count of approximately 10,000 photons. The pinhole diameter was set to 1 Airy unit and images were acquired with a pixel format of 256x256 using a 63X 1.4 NA HC PL Apo oil immersion objective lens. To reduce the impact of photobleaching by maximising count rates at lower laser powers, a large pixel size of 0.161 μm was used. FRET between EGFP and mCherry was assessed by comparison of EGFP fluorescence lifetimes obtained from an EGFP-only sample or from an EGFP and mCherry sample, both prepared alongside each other. This was accomplished using the analysis routines detailed and validated in section 2.5.2. Further details of the optical paths and TCSPC electronics are also discussed in section 2.5.2.

3.5.6 Image processing

CLSM images were deconvolved with Huygens Professional (Scientific Volume Imaging). A theoretical PSF was used for iterative classic maximum likelihood estimation-based deconvolution to a quality change threshold of 0.01. Deconvolution parameters were adjusted to match the acquisition settings per image.

In some cases, rolling ball background subtraction and signal thresholding may also have been applied to the image. The rolling ball background subtraction subtracts from each pixel the mean intensity value calculated from a pre-defined radius of pixels[375]. This was carried out with the open-source software, Fiji[376], using a radius at least the size of the largest structure as recommended for such analyses[375]; this was typically observed to be 1.2 – 2.0 μm in autophagic cells. Signal thresholding, on the other hand, approaches background subtraction more crudely by highlighting pixels with an intensity value above a user-specified value, allowing pixels with lower signal intensities to be set to zero such that they are excluded from further analyses. This was also carried out with Fiji by visual inspection per image to ensure the exclusion of background signal alone.

3.5.7 Colocalisation analysis

Colocalisation analyses were carried out with the Coloc 2 plugin in Fiji[376, 377]. For Pearson's correlation coefficient[343], images were pre-processed by deconvolution and the manual application of a cell ROI to exclude the influence signal from neighbouring cells. Manders correlation coefficient (MCC)[344], however, is highly biased by background signal towards high correlations[269] with non-processed images observed to consistently report a correlation of 1.0. Images to be analysed by MCC therefore additionally underwent background subtraction and signal thresholding. A negative control colocalisation was also carried out for each image by manually identifying a fluorophore-dense 11 μm x 11 μm region, to which a 90° transformation was applied to the mCherry channel prior to colocalisation. Statistical significance of the reported colocalisation could therefore be determined by direct comparison with a negative control derived from the same image using a paired two-sample t-test.

3.5.8 Puncta concentration analysis

Puncta number per micron can be used to assess autophagic flux[225]. To accomplish this, the Spot Detector plugin[378] within the open source software, Icy 1.8.6.0[379], was used to quantify puncta number using a multiscale analysis algorithm that enhances peak signal and reduces background noise to aid spot characterisation[378]. Prior to spot detection, an ROI was manually drawn around the cell of interest to calculate the area and restrict spot detection to a single cell. The sensitivity settings were adjusted per image to maximise spot detection sensitivity just prior to the point where false positive puncta are detected based on visual inspection.

CHAPTER FOUR:

Confirming the autophagosomal SNARE complex

4.1 Introduction

The mammalian SNARE complex facilitating autophagosome-endolysosome membrane fusion is widely agreed to consist of Stx17, SNAP29 and VAMP8[248]. As a Qbc-SNARE, SNAP29 contributes two SNARE domains to this complex[46], enabling formation of the tetrameric coiled coil that constitutes the assembled SNARE structure in association with the Qa-SNARE domain of Stx17 and the R-SNARE domain of VAMP8. This deviates from *S. cerevisiae* where four SNARE proteins each provide one SNARE domain, namely the Qa-SNARE Vam3, Qb-SNARE Vti1, Qc-SNARE Vam7 and R-SNARE Ykt6[380]. Intriguingly, despite the conservation of these *S. cerevisiae* proteins in higher eukaryotes, their role in autophagy has seemingly been replaced with other family members. The mammalian homolog to yeast Vam3 is syntaxin 12/13, which may play a role in phagophore development[235], raising interesting questions about the evolution of this pathway.

It is noteworthy that the R-SNARE governing autophagosome fusion in *Drosophila melanogaster* has been identified as VAMP7[249]. This deviation from the mammalian complex has been broadly accepted because *D. melanogaster* has no equivalent to VAMP8 and therefore VAMP7 is considered the homolog of both *Homo sapiens* VAMP7 and VAMP8[249], which are themselves 62% similar. However, VAMP8 notably lacks a regulatory longin domain that is encoded by *H. sapiens* VAMP7, *D. melanogaster* VAMP7 and the *S. cerevisiae* autophagosomal R-SNARE Ykt6[381]. The evolutionary conservation of the R-SNARE longin domain from yeast to drosophila suggests it may play an important role in autophagy regulation and highlights VAMP8 as an unexpected R-SNARE to control autophagy completion in mammals. Furthermore, though both VAMP7 and VAMP8 are known to be involved in endosomal trafficking, VAMP8 mediates homotypic endosomal fusion events, whereas VAMP7 mediates heterotypic endosome-lysosome fusions[246], placing it as an arguably more suitable candidate for the heterotypic fusion of the autophagosome and the endolysosome. Indeed, conflicting data that has now largely been excluded from the autophagosome SNARE model, implicated VAMP7 as well as Vti1b in autophagosome clearance due to the accumulation of puncta upon their knockdown[247, 250], directly conflicting with the same work carried out

by Mizushima's group to establish the current model[248]. Moreover, Stx17 immunoprecipitation has been shown to pull-down both VAMP7 and VAMP8[248]. Though the current SNARE model has garnered consensus, these irregularities raise questions as to whether the techniques used to ascertain protein function are sufficient to identify protein interaction *in situ* in this case.

As demonstrated by the endosomal R-SNAREs, a SNARE family member is not restricted to a single membrane fusion event but may instead contribute to others by association with different SNARE partners[246]. Though Stx17 has not been identified as a component of other SNARE complexes to date, interactions with other proteins have implicated it in the modulation of mitochondrial fission[382] and the maintenance of ERGIC and Golgi architecture[383]. SNAP29 on the other hand has been reported to bind syntaxin proteins with high promiscuity[46], resulting in the proposal of diverse roles for it across membrane trafficking. These include the regulation of SNARE disassembly and recycling following synaptic transmission[384], the biogenesis of cilia[385], the maintenance of Golgi complex and endosomal architectures[386], early-stage endocytosis[387] and oligodendrocyte myelination[388]. In addition, studies on VAMP7 and VAMP8 have found both to be required in specialised secretory pathways as well as their aforementioned functions in endocytosis. VAMP8 has demonstrated importance for regulated exocytosis in exocrine tissues[389], such as the secretion of pancreatic zymogen granules[390]; while VAMP7 was first identified as tetanus insensitive VAMP (TI-VAMP), implicated in the transport of vesicles to epithelial cell apical membranes[391]. More recently, VAMP7 has been tied to an unconventional secretory pathway whereby the lysosome itself is secreted[392].

The demonstrated multi-functionality of SNARE proteins presents challenges for distinguishing these varied functions. Additionally, studies of SNAREs in isolated processes can be easily misinterpreted due to the interconnections between various membrane trafficking pathways. Indeed, autophagy converges with both the secretory and endosomal systems, stressing the need for caution when interpreting data. To date, the research that has been carried out to define the autophagosomal SNARE complex has relied on immunoprecipitation, siRNA knockdown and fluorescence colocalisation[248, 249]. Though, independently, each of

these techniques is imperfect for the determination of protein function, it can be assumed that when considered together they may contribute valuable information. However, in the case of SNARE interactions in autophagy, their results may be misleading. Knockdown of syntaxin 5, for example, disrupts autophagic flux due to its requirement for lysosomal biogenesis[393]. This could, however, be misinterpreted as a role for Stx5 in autophagosome-endolysosome biogenesis. More stringent techniques therefore, still need to be employed in order to confirm the autophagosomal SNARE complex.

Immunoprecipitation studies detect protein interactions from cell lysate, thereby abolishing the temporal and spatial control provided by the cell. This is ill-suited to SNARE proteins due to their apparent binding promiscuity[46, 86-88]. RNA knockdowns on the other hand, investigate the phenotypic effect when a specific protein is depleted by inhibition of mRNA translation. However, disruption of one upstream event may have implications further along the pathway that are misinterpreted as evidence of a downstream role for the protein. Given the demonstrated range of functions that have been proposed for the autophagosomal SNAREs and the intersections between autophagy and other membrane trafficking pathways, this could be a likely scenario. Indeed, in addition to Stx17, knockdown of Stx5 also causes autophagosome accumulation due to its requirement for lysosomal biogenesis[393]. In the case of fluorescence colocalisation, the co-occurrence of proteins on the same diffraction-limited structures can be determined, but as with knockdown studies, this may lead to the misinterpretation of upstream events that lead to protein presence on the same membrane, which is often misconstrued as evidence of protein interaction *in situ*.

My research applies appropriately quantified fluorescence colocalisation and FLIM-FRET imaging for the robust detection of protein interactions *in situ*. This approach negates many of the concerns listed above, enabling dissection of the SNARE complex involved in autophagosome-endolysosome fusion.

4.2 Materials and Methods

4.2.1 Buffers for starvation studies

The compositions of all buffers used in section 4.3.1 are outlined in table 4.1. Non-commercial buffers were pH adjusted to 7.4 and osmolarity adjusted to 290 mOsmol/kg.

Table 4.1 Buffers used to assay autophagy

Buffer	Concentration	Reagent
Earle's Balanced Salt Solution (EBSS), Fisher Scientific #11570466		
	5.3 mM	Potassium chloride
	26.2 mM	Sodium bicarbonate
	117.2 mM	Sodium chloride
	1 mM	Sodium phosphate monobasic
	5.6 mM	D-glucose
EBSS-Pyr		
	1X	EBSS
	1 mM	Sodium pyruvate
Hanks' Balanced Salt Solution (HBSS), Fisher Scientific #11530476		
	5.3 mM	Potassium chloride
	4.2 mM	Sodium bicarbonate
	137.9 mM	Sodium chloride
	0.4 mM	Potassium phosphate monobasic
	0.3 mM	Sodium phosphate dibasic anhydrous
	5.6 mM	D-glucose
Dulbecco's Modified Eagle Medium (DMEM), Fisher Scientific #11510416		
	-	Various amino acids and vitamins
	1.8 mM	Calcium chloride
	0.8 mM	Magnesium sulfate
	5.3 mM	Potassium chloride
	44 mM	Sodium bicarbonate
	110.3 mM	Sodium chloride
	0.9 mM	Sodium phosphate monobasic
	0.025 µM	Ferric nitrate
	25 mM	D-glucose
Axe buffer[157]		
	140 mM	Sodium chloride
	1 mM	Calcium chloride
	1 mM	Magnesium chloride
	5 mM	D-glucose
	20 mM	HEPES
Membrane permeant buffer		
	50 mM	Ammonium chloride
	2.8 mM	Potassium chloride
	2 mM	Calcium chloride

	1 mM	Magnesium chloride
	10 mM	D-glucose
	20 mM	HEPES
Non-membrane permeant buffer		
	140 mM	Sodium chloride
	2.8 mM	Potassium chloride
	2 mM	Calcium chloride
	1 mM	Magnesium chloride
	10 mM	D-glucose
	20 mM	HEPES

4.2.2 Sample preparation and microscopy

Unless otherwise specified, all imaging was carried out by confocal laser scanning microscopy (CLSM) on fixed HeLa cells treated with 160 nM rapamycin for 60 minutes immediately prior to fixation. The research presented here exclusively uses EGFP and mCherry probes conjugated to the proteins of interest. Colocalisation experiments acquired multi-channel data sequentially by frame and these were subsequently processed and quantified as outlined in section 3.5.7. Negative control colocalisations were carried out for each image to determine the statistical significance of the reported correlation with a paired two-sample t-test. Negative control colocalisations were performed on a fluorophore-dense 11 µm x 11 µm region of interest with a 90° transformation applied to the mCherry channel only. Quantitation of colocalisation is presented throughout in boxplot or barchart format. The former indicates the median value (line), 25th and 75th quartile values (box) and the maximum and minimum values (whiskers), while the latter reports the mean value and the standard error of the mean (SEM). Statistical significance is presented throughout as 'ns' for non-significant (P values of 0.05 or greater), * for P values between 0.005-0.05, ** for P values between 0.0005-0.005, *** for P values between 0.0001-0.0005 and **** for P values below 0.0001.

FLIM-FRET experiments were performed with a confocal laser scanning microscope equipped with TCSPC electronics and SPAD detection (refer to section 3.5.5 for more information). Fixed HeLa cells treated with 160 nM rapamycin were imaged to acquire up to 10,000 photons per pixel and single pixel analysis was carried out as described in section 2.5.2. Pixels with a total photon count below

1,000 were excluded from analysis based on the decay fitting validation overviewed in figure 2.16. The term 'fluorescence lifetime' refers to the amplitude-weighted average fluorescence lifetime throughout. This information was derived from bi-exponential tail-fits and has been presented as boxplots that report the median value (line), the 25th and 75th quartile value (box) and the 5th and 95th quartile value (whiskers). FRET efficiency was also calculated for donor-acceptor samples based on the median amplitude-weighted average fluorescence lifetime of the equivalent donor-only sample. Statistical significance of changes in FRET efficiency was determined based on the integral of the histogram between 0.1-1.0 (denoted throughout as $\int$) using a one-tailed unpaired two-sample t-test, and presented in the same way as described above for colocalisation. Values below 0.1 are poor indicators of FRET, as determined in section 2.5.2, and were therefore excluded.

The live cell imaging in section 4.3.1 was performed on a widefield TIRF microscope (see section 3.5.3) using HeLa cells pre-treated with 160 nM rapamycin for 60 minutes. The specified imaging buffer was also supplemented with 160 nM rapamycin for continued autophagy induction, and the imaging chamber was maintained at 37°C and 5% CO_2 (v/v).

4.3 Results

4.3.1 Assaying autophagy

Autophagy is carried out by all cells at a basal level for the continuous turnover of cellular material[394]. However, in order to study the pathway, its upregulation is essential and this is achieved widely by either chemical induction or the use of a starvation protocol. LC3 is a useful marker of autophagic activity as it translocates from the cytosol to the autophagic membrane upon autophagy, remaining bound to the vesicle throughout its lifecycle from phagophore to autolysosome[371]. This was demonstrated in figure 4.1a, which shows the LC3-EGFP distribution in both a non-induced and an autophagy-induced HeLa cell. The fold change in LC3 puncta concentration upon induction was therefore used in figure 4.1b to determine the

optimal routine for autophagy induction in HEK293T cells, an easily cultured human cell line. As autophagy is a stress-response pathway, a short induction time of two hours was employed to avoid cytotoxicity from excessive metabolic stress, which is consistent with many published studies[158, 202, 248]. Cells were exposed to different buffer compositions and the resulting LC3 puncta in fixed cells were quantified.

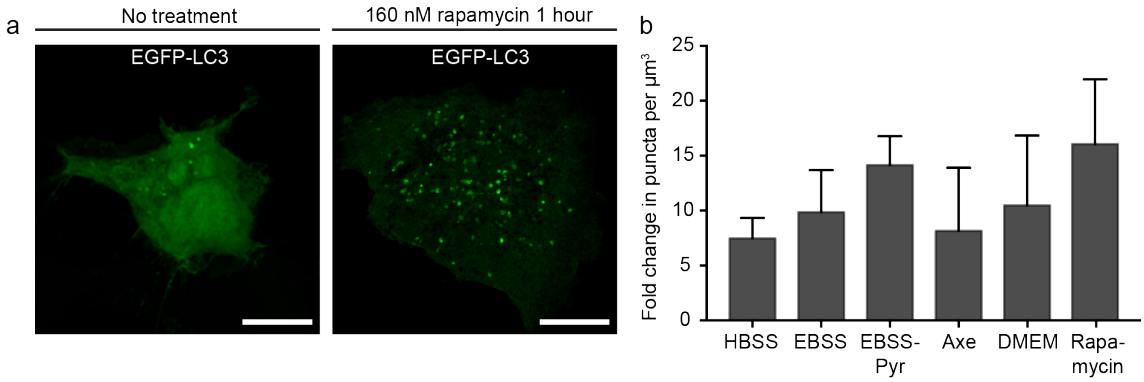

Figure 4.1 Autophagy induction (**a**) Summed projections from 3D stack data of fixed HeLa cells expressing EGFP-LC3 imaged by CLSM, both non-treated (left) and treated with 160 nM rapamycin for one hour (right). Scale bars are 10 µm (**b**) Fold increase in puncta number per µm^3 when culture media is replaced with the starvation buffer indicated for two hours or 100 nM rapamycin for one hour in HEK293T cells, imaged by CLSM [n=3].

Surprisingly, the sodium bicarbonate-based buffers, EBSS and HBSS, produced equivalent induction levels to the sodium bicarbonate buffered non-supplemented DMEM (figure 4.1b). As non-supplemented DMEM imposes serum-starvation only, the cells are deprived of cytokines but not the amino acids contained within DMEM itself. This suggests that there is little gain in amino acid starvation over a short two-hour induction, likely due to the compensatory role of the ubiquitin-proteasome system[395], before the delayed onset of acute autophagy[135]. A published study by Axe *et al.*[157] reported optimal induction of HEK293T cells within 90 minutes when starved of both amino acids and potassium, however no advantage was apparent in my hands when replicating this with 'Axe buffer'. Induction was, however, improved by supplementing the buffer with 1mM sodium pyruvate ('EBSS-Pyr'), which minimises the pro-apoptotic glucose starvation pathway[396].

Chemical induction with 100 nM rapamycin for one hour produced the greatest increase in puncta number and was therefore selected for ongoing work. This was optimised to 160 nM treatment for HeLa cells, which produced more consistent induction than HEK293T cells. Rapamycin is a lipophilic macrolide antibiotic with a long-established capability to induce autophagy by specifically inhibiting mTORC1[186]. As ALR cannot be activated following rapamycin treatment[254], extensive exposure could cause inhibited autophagosome clearance due to enlarged autolysosomes[254] that cannot maintain acidic pH. This was mitigated by the use of a short one hour induction time throughout.

As autophagy is in flux, its inherent variation precludes a direct measurement of autophagic activity. Instead, progress through the pathway is commonly assessed based on the turnover of a known autophagy substrate[225]. This can be achieved by using the different stabilities apparent for LC3-conjugated EGFP and mCherry in the lysosomal environment. As EGFP fluorescence is lost upon formation of the autolysosome, but mCherry is unaffected, a tandem construct of LC3-mCherry-EGFP can be used to differentiate autophagosomes (EGFP and mCherry positive) from autolysosomes (mCherry positive only)[346]. This effect is demonstrated in figure 4.2a, which shows such a tandem construct in rapamycin treated HeLa cells.

EGFP has a high pKa of 6.0[397] compared to mCherry with a pKa below 4.5[398], which would cause selective fluorescence quenching of EGFP in the pH 5 environment of the lysosome[5]. Quenching of intra-luminal EGFP-tagged proteins could be problematic for fluorescence lifetime studies as this would result in a split population of quenched and non-quenched fluorescence lifetimes that may preclude FRET detection. However, studies indicate that EGFP is in fact quenched and hydrolysed, resulting in complete loss of signal[346]. This was confirmed by fluorescence lifetime measurements of EGFP-LC3 in figure 4.2b, where no short lifetime population is evident. Furthermore, EGFP fluorescence lifetimes do not increase when autophagosome-lysosome fusion is inhibited with bafilomycin A_1. Similarly, raising the lysosomal pH by the application of a membrane permeant buffer at pH 7.4 did not result in a significant increase of EGFP puncta in live cells expressing EGFP-LC3 (figure 4.2c).

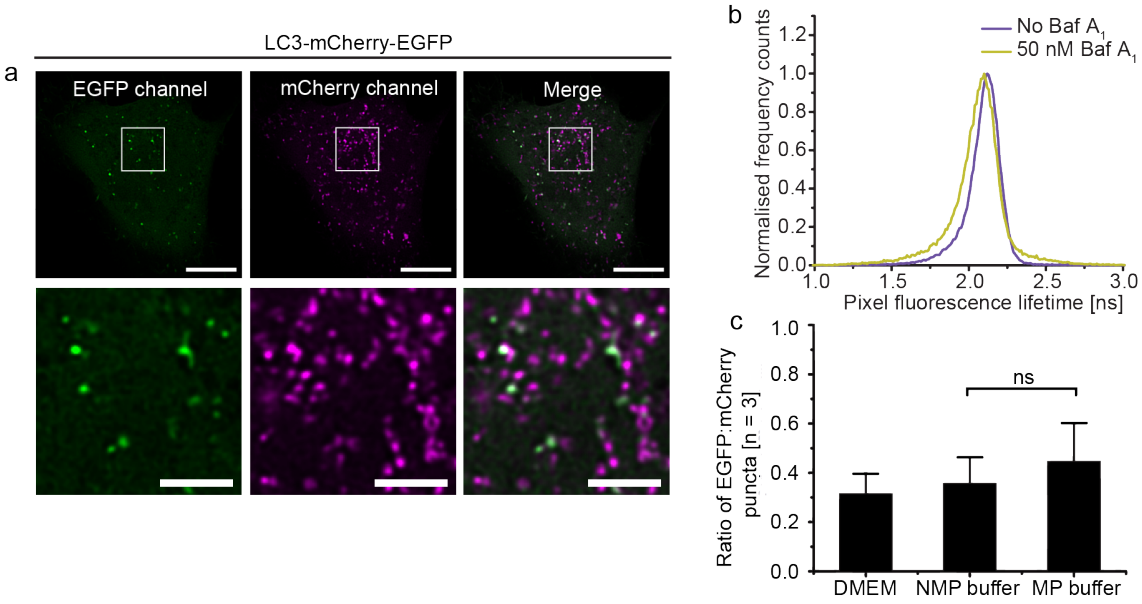

Figure 4.2 Tandem LC3 assay of autophagic flux (**a**) Single channel and merged images of a rapamycin-treated HeLa cell expressing LC3-mCherry-EGFP demonstrating loss of EGFP signal in a population of autophagic vesicles; bottom row is an enlargement of the indicated region. Scale bars are 10 µm (top) and 3 µm (bottom). (**b**) Normalised histogram of single pixel fluorescence lifetimes either from two rapamycin treated cells or from two rapamycin and bafilomycin A_1 treated cells to inhibit autolysosome formation. (**c**) The ratio of EGFP and mCherry puncta in live autophagic HeLa cells imaged by TIRFM in culture medium (DMEM), non-membrane permeant buffer (NMP) or membrane permeant buffer (MP), [n=3]. Statistical significance calculated with an unpaired two-sample t-test.

The use of a dual-colour probe to measure autophagic flux precludes some experimental design options, such as multi-channel colocalisation. An alternative flux assay is to monitor the vesicle accrual that results from blocking progress through the pathway[225]. By inhibiting autophagosome-endolysosome fusion, autophagosomes will accumulate. This provides a useful comparison where an experimental condition is suspected to cause an increase in autophagosome number[225]. Indeed, autophagosome accumulation that does not further increase upon fusion inhibition, indicates decreased autophagosome clearance due to fusion incompetence or non-functional lysosomes, rather than upregulated phagophore nucleation[225]. Bafilomycin A_1 (Baf A_1) can reportedly inhibit fusion with the lysosome as well as de-acidify the compartment[345]. To determine the effectiveness

of this assay, autophagic HeLa cells in figure 4.3 were treated with Baf A_1. The effect on autophagosome-endolysosome fusion was determined by lysosomal turnover of EGFP and the colocalisation of autophagosomal and lysosomal markers, LC3 and LAMP1 respectively. Treatment with 50 nM Baf A_1 for 24 hours prior to fixation both inhibited autophagosome-endolysosome fusion, reported by the reduced colocalisation of LC3 and LAMP1 (figure 4.3a-b), and reduced LC3-conjugated EGFP turnover (figure 4.3c). Baf A_1 needed a long incubation time to take effect, and required a minimum 50 nM treatment to diminish the correlation of LC3 puncta with LAMP1 (figure 4.3d). 24 hour treatment with 50 nM Baf A_1 was therefore employed for all Baf A_1-based assays.

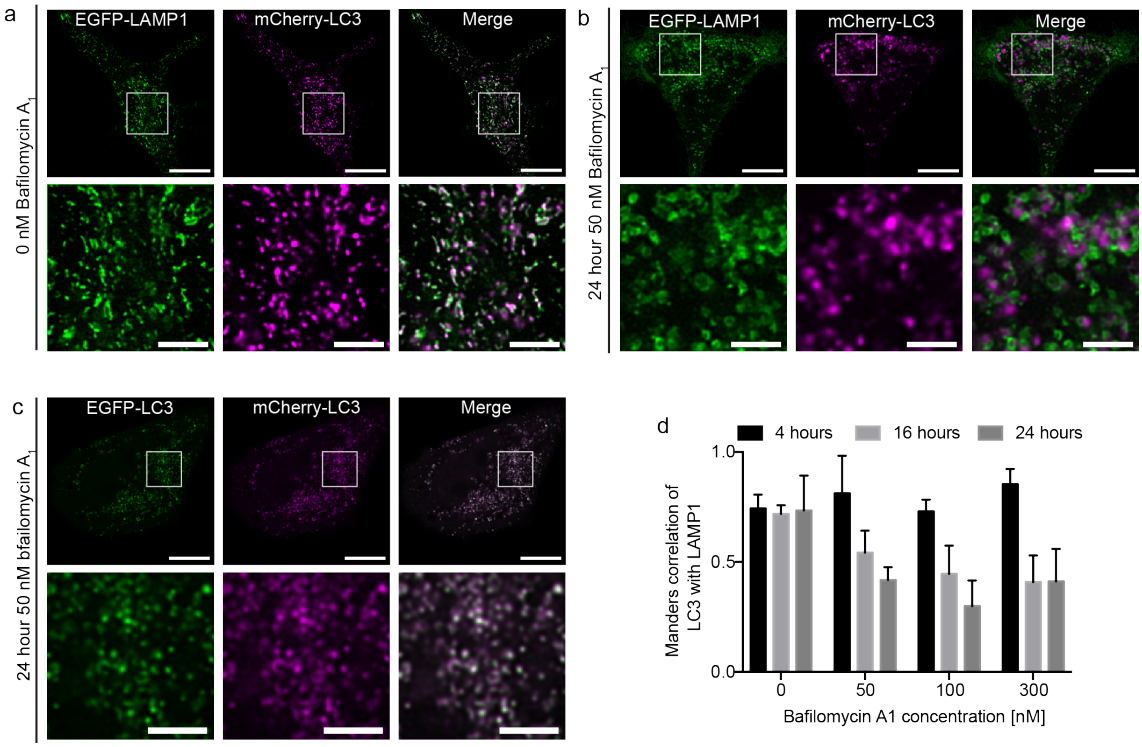

Figure 4.3 Inhibition of autophagosome-endolysosome fusion with Baf A_1 (**a**) Fixed HeLa cells co-expressing EGFP-LAMP1 and mCherry-LC3 treated with 160 nM rapamycin. (**b**) HeLa cells prepared as for (a) but additionally treated with 50 nM Baf A_1 for 24 hours to inhibit fusion of the labelled compartments. (**c**) Fixed HeLa cells expressing LC3-mCherry-EGFP and treated with both 160 nM rapamycin applied 60 minutes prior to fixation and 50 nM baf A_1 applied 24 hours prior. (**d**) Manders correlation coefficient of LC3 puncta colocal with LAMP1 following varied Baf A_1 treatments as indicated, [n=3]. Scale bars throughout are 10 µm for full field and 3 µm for enlarged images of the indicated regions.

4.3.2 SNARE protein targeting in autophagic cells

As a single SNARE protein can contribute to a number of distinct membrane fusion events, its location in a given compartment can stem from a completed upstream function. A comprehensive study was therefore carried out to understand the wider SNARE protein distribution of Stx17, SNAP29, VAMP8 and VAMP7 in autophagic cells, providing a context within which to study their role in autophagy. The SNARE proteins of interest were co-expressed with various organelle markers to ascertain their colocalisation with autophagosomes, early endosomes, late endosomes, lysosomes, the Golgi complex and the ER. As there is no expectation of a stoichiometric relationship between the SNARE proteins and the organelle markers, Manders correlation coefficient was used to quantify colocalisation of labelled compartments in 2D slices following fixed cell imaging.

Shown in figure 4.4 is the Stx17 intracellular targeting study, which shows that Stx17 distribution in autophagic cells correlates significantly with autophagosomes as well as both early and late endosomes. This is consistent with studies that have shown autophagosome fusion with both early and late endosomes[399]. Surprisingly, however, there is no apparent correlation with LAMP1-labelled lysosomal compartments as would be expected for post-fusion autolysosomal *cis*-SNARE complexes. This could perhaps indicate a preference for intermediate amphisome formation and the efficient recycling of the *cis*-SNARE complex. In addition, upon autophagy induction, Stx17 is completely diverted from its well-characterised ER distribution in nutrient replete cells[248], resulting in its enrichment on autophagosomes and endosomes (figure 4.4b), suggestive of an autophagy-dependent redistribution to the endosomal pathway.

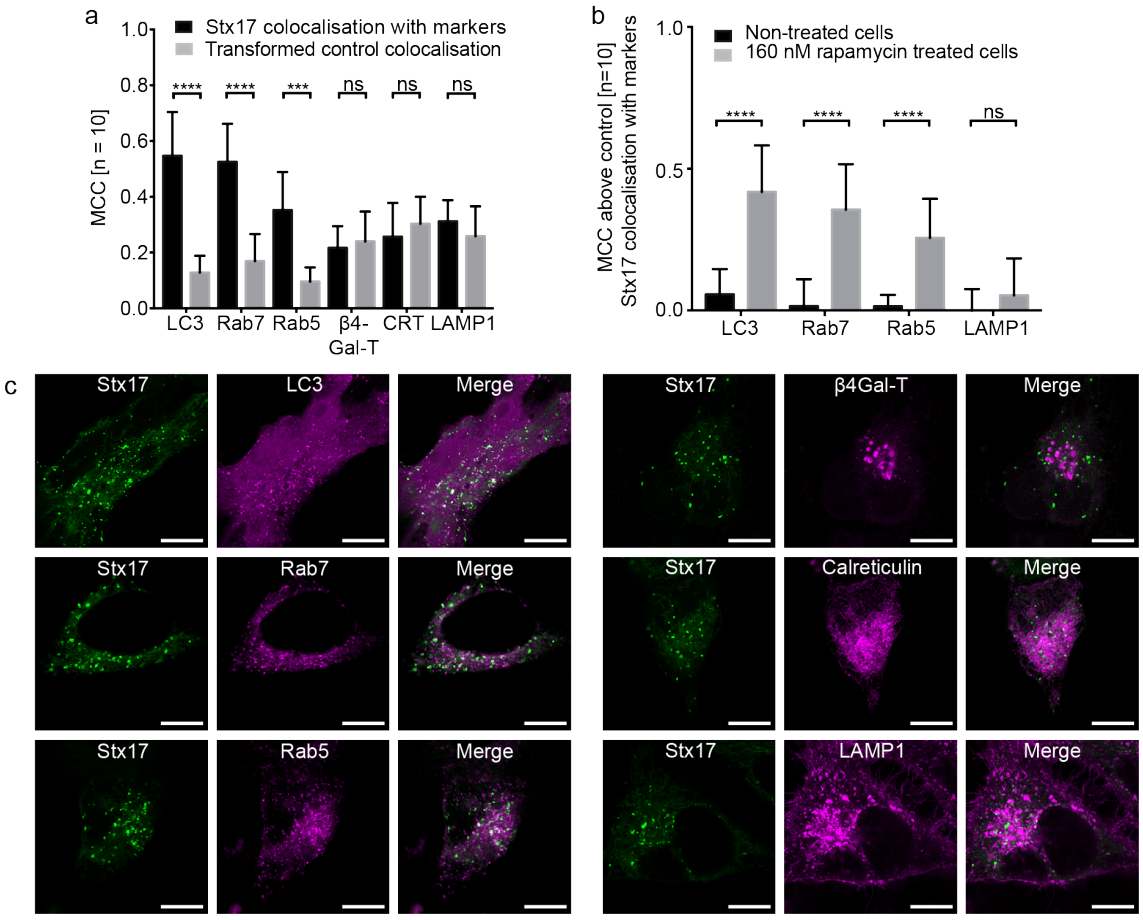

Figure 4.4 Targeting of Stx17 (**a**) Manders correlation coefficient (MCC) of Stx17-EGFP puncta colocal with the indicated mCherry-conjugated organelle markers when co-expressed in autophagic HeLa cells. LC3, Rab7, Rab5, β1,4-galactosyltransferase (β4Gal-T), calreticulin and LAMP1 identify autophagic compartments, late endosomes, early endosomes, Golgi structures, ER and lysosomes respectively. Statistical significance was tested with a paired two-sample t-test, [n=10] (**b**) A barchart of the MCC values reported above the corresponding negative control value to compare colocalisation of Stx17 structures with autophagic and endosomal compartments in non-treated and rapamycin treated HeLa cells. Statistical significance was tested with an unpaired two-sample t-test, [n=10] (**c**) Representative 2D CLSM images of autophagic HeLa cells co-expressing Stx17 and each of the organelle markers. Scale bars are 10 μm.

My research is based on the over-expression of exogenous Stx17, which warrants confirmation that the detected puncta are indeed functional autophagosomes. Super-resolution microscopy was employed to verify that LC3- and Stx17-positive puncta were not simply aggregates of over-expressed protein. Figure 4.5a-b shows gSTED images of Stx17-EGFP, imaged alongside standard confocal microscopy of LC3-mCherry. The gSTED microscopy confirms that Stx17-EGFP is restricted to the

vesicle membrane, indicating specific targeting of the exogenous protein to LC3-positive compartments. Traditional, diffraction-limited imaging does not reveal this detail (figure 4.5a top panels), which is highlighted by the cross-sections shown in figure 4.5b. Additionally, Baf A_1 treatment results in the accumulation of Stx17 and LC3 colocal puncta, confirming that they are fusion-competent autophagosomes (figure 4.5c-e). Indeed, autophagic flux reported by LC3-mCherry-EGFP was unaffected by the over-expression of Stx17 (figure 4.5f-g).

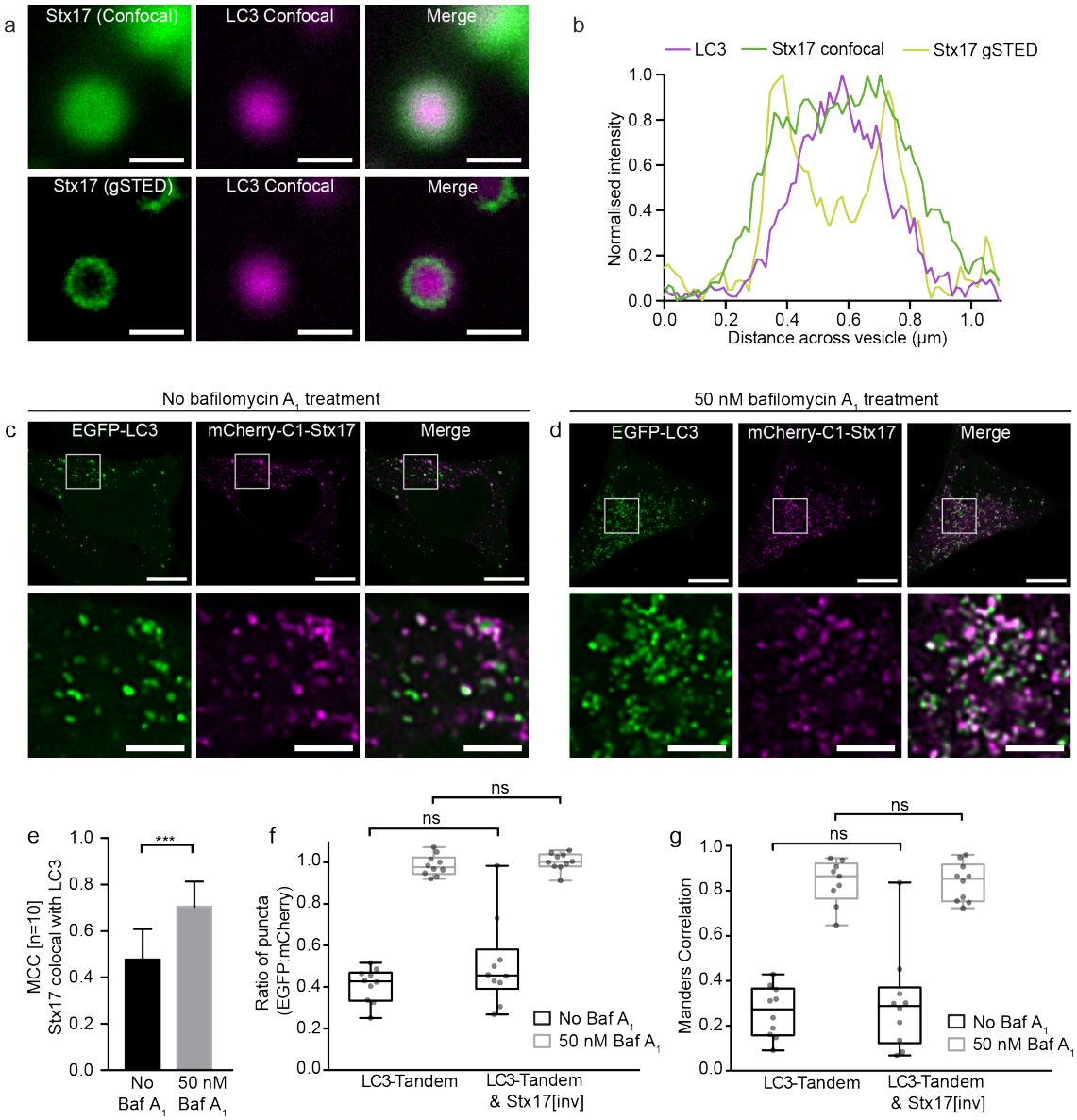

Fig 4.5 Stx17 resides on functional autophagosomes (**a**) A single Stx17-positive punctum imaged by CLSM (top) or gSTED microscopy (bottom), co-expressed with mCherry-LC3 imaged by CLSM. Scale bars are 500 nm. (**b**) Intensity line profile

through the punctum in (a) demonstrating membrane localisation of Stx17 resolved by gSTED alone. (**c**) 2D single channel and merged images of autophagic HeLa cells co-expressing EGFP-LC3 and mCherry-Stx17 in the absence and (**d**) presence of Baf A_1 treatment. Scale bars are 10 μm for full field and 3 μm for enlarged images of the indicated regions. (**e**) Manders correlation coefficient of Stx17 puncta colocal with LC3 to quantify data represented by (c) and (d). (**f**) Ratio of EGFP and mCherry puncta detected in autophagic HeLa cells expressing LC3-mCherry-EGFP (LC3-tandem) in the presence and absence of exogenous non-tagged Stx17 (Stx17[inv]) and (**g**) their colocalisation quantified by Manders correlation coefficient of mCherry puncta colocal with EGFP puncta. Unpaired two-sample t-tests were used throughout for statistical testing, [n=10].

By comparison to Stx17, SNAP29 is widely distributed through the membrane trafficking network, with high variation between cells, including plasma membrane, vesicular, cytosolic and peri-nuclear patterns. As shown in figure 4.6, which presents the SNAP29 intracellular targeting studies, SNAP29 colocalises significantly with all endolysosomal compartments as well as the Golgi complex. SNAP29 is a unique SNARE protein in being a peripheral membrane protein with no means of direct membrane association[46]. Such recruitment of SNAP29 from the cytosol offers the plasticity in distribution noted, which may enable it to fulfil a wide range of roles. Surprisingly, however, figure 4.6 indicates no correlation of signal between SNAP29 and LC3-EGFP as would be required for binary SNARE complex formation with Stx17 on autophagosomes. Furthermore, its strong colocalisation with LAMP1, which is not seen for Stx17, suggests a role for SNAP29 in the endosomal system that is independent of Stx17-mediated autophagosome fusion.

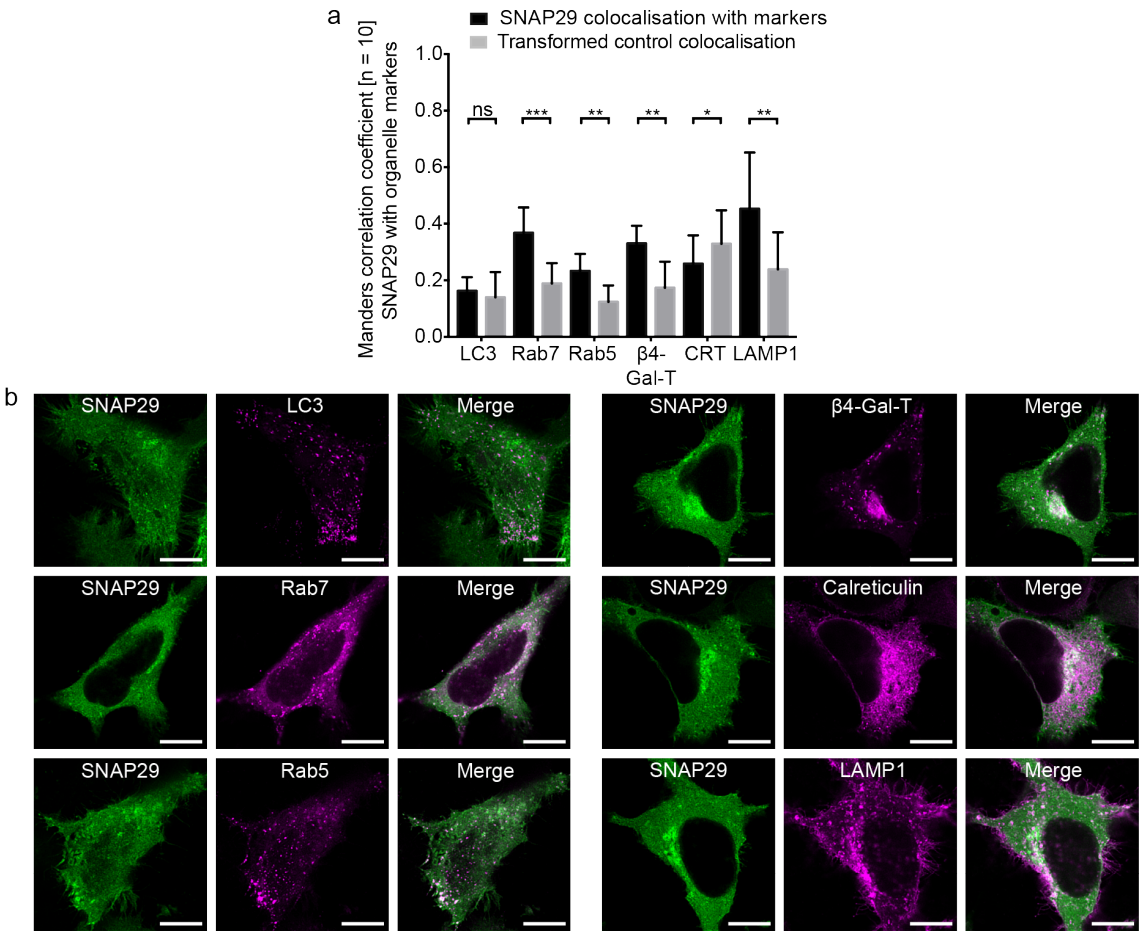

Fig 4.6 Targeting of SNAP29 (**a**) Manders correlation coefficient of SNAP29-EGFP structures colocal with mCherry-conjugated LC3, Rab7, Rab5, β1,4-galactosyltransferase (β4Gal-T), calreticulin or LAMP1 to identify autophagic compartments, late endosomes, early endosomes, Golgi structures, ER and lysosomes respectively. Statistical significance was tested with a paired two-sample t-test, [n=10]. (**b**) Representative 2D CLSM images of autophagic HeLa cells co-expressing SNAP29 and each of the organelle markers. Scale bars are 10 μm.

To determine how SNAP29 distribution is affected by the availability of different SNARE proteins, it was over-expressed in autophagic HeLa cells alone or alongside VAMP7, VAMP8 or Stx17 as shown in figure 4.7. If SNAP29 is co-transfected with a putative SNARE binding partner, its expression pattern notably redistributes to match the co-expressed protein (figure 4.7a-b), perhaps exemplifying the apparent promiscuity of this SNARE protein[46]. Despite the finding that SNAP29 does not target autophagosomes, figure 4.7 suggests that SNAP29 can colocalise in response to exogenously expressed Stx17, which is predominantly autophagosomal (figure 4.4). The aforementioned dependence of SNAP29 on protein association for

membrane targeting, suggests that its localisation is dependent on the availability of SNARE binding partners. The poor recruitment of SNAP29 to autophagosomes in the presence of endogenous levels of Stx17, suggests that a regulatory mechanism may prevent premature binary complex formation, which is saturated by the over-expression of Stx17 in figure 4.7. It is also noteworthy that SNAP29 binding promiscuity may extend to non-syntaxin SNAREs, as shown in figure 4.7 for both VAMP7 and VAMP8. This raises an interesting question as to whether SNAP29 is directly recruited by the R-SNARE itself, presenting a novel SNARE intermediate.

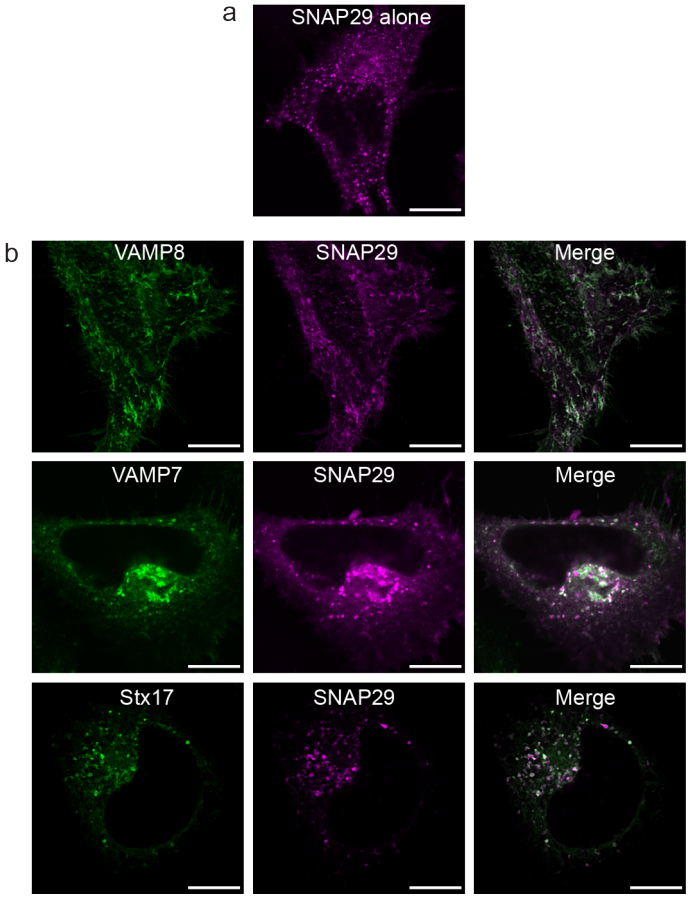

Fig 4.7 SNAP29 targeting promiscuity (**a**) Representative SNAP29-mCherry distribution in an autophagic HeLa cell when expressed alone. (**b**) Representative single channel and merged images of SNAP29-mCherry distribution in autophagic HeLa cells when co-expressed with EGFP-conjugated VAMP8 (top row), VAMP7 (middle row) or Stx17 (bottom row). Scale bars are 10 μm throughout.

The correlation between the various organelle markers and the two R-SNAREs, VAMP7 and VAMP8, is presented in figure 4.8. VAMP8 colocalises significantly with Golgi complex and late endosome markers (figure 4.8a), supporting a role in late endosome homotypic fusion[246]. Other studies have suggested that VAMP8 may be involved in the fusion of recycling endosome-derived vesicles with the plasma membrane[400] and though recycling endosomes were not covered in this study, plasma membrane localisation was indeed observed. Comparatively, VAMP7 has a broader expression profile, with figure 4.8b indicating its presence throughout both the endosomal and secretory pathways. VAMP8 localised strongly with late endosomal compartments consistent with its role in heterotypic endosome-lysosome fusion[246]. The late endosomal distribution of both R-SNAREs is ideally suited to contribute to autophagosomal SNARE complex formation. However, only VAMP7 colocalises significantly with LC3-mCherry, which represents autophagosomes, amphisomes and autolysosomes. To differentiate these vesicles, treatment with Baf A_1 demonstrated that while VAMP8 does not colocalise with LC3 at any stage, VAMP7 colocalises with the autophagosome marker in a fusion-dependent manner (figure 4.8c). This suggests VAMP7 as the most likely R-SNARE candidate for autophagosomal fusion.

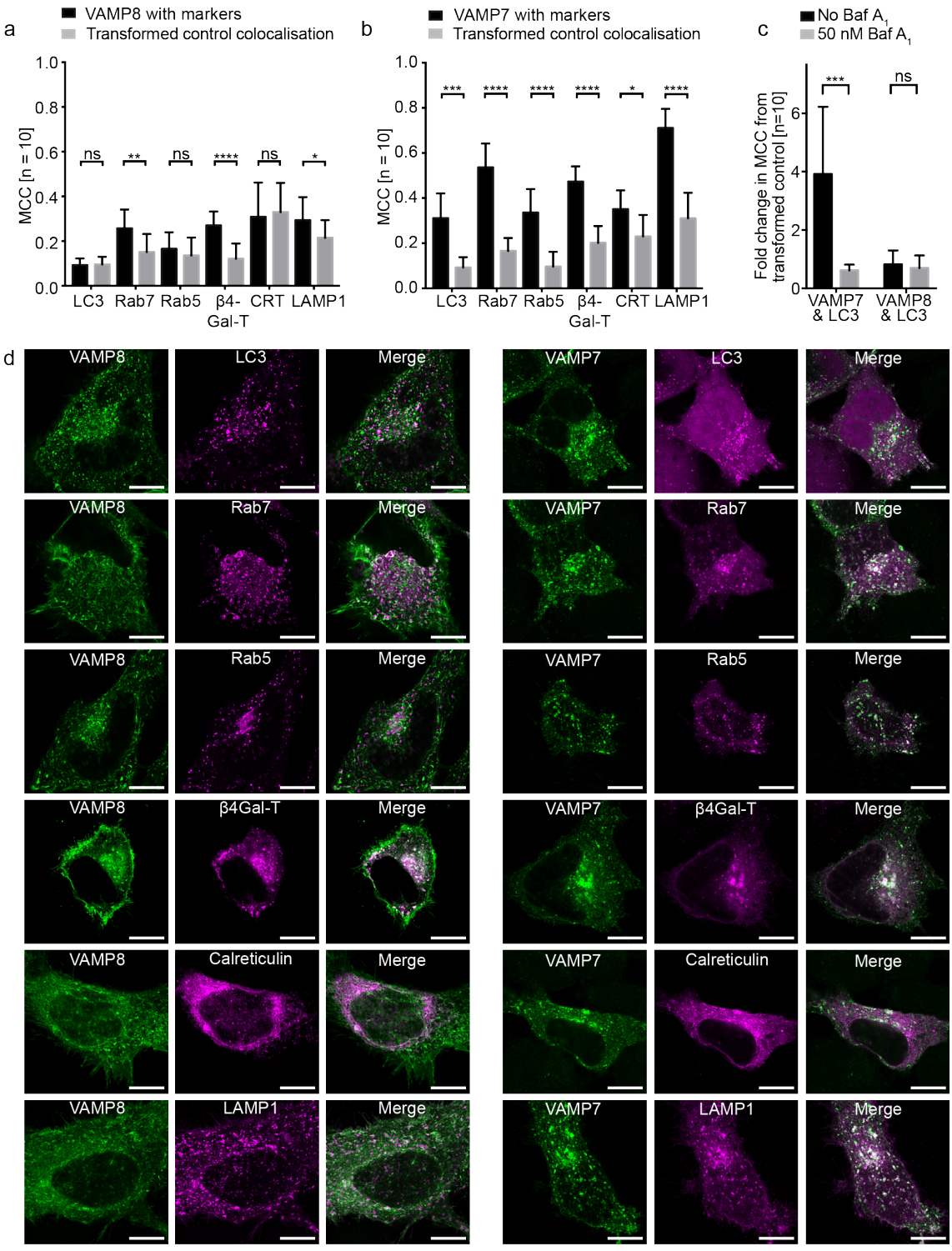

Fig 4.8 Targeting of VAMP7 and VAMP8 (**a**) Manders correlation coefficient of VAMP8-EGFP or (**b**) VAMP7-EGFP structures colocal with mCherry-conjugated LC3, Rab7, Rab5, β1,4-galactosyltransferase (β4Gal-T), calreticulin or LAMP1 to identify autophagic compartments, late endosomes, early endosomes, Golgi structures, ER and lysosomes respectively. Statistical significance was tested with a paired two-sample t-test, [n=10] (**c**) A barchart comparing the fold increase in MCC (from the negative control colocalisation) to quantify the correlation of R-SNARE structures with LC3-mCherry in the presence or absence of Baf A_1. An unpaired

two-sample t-test was used to ascertain statistical significance, [n=10]. (**d**) Single channel and merged representative CLSM images of autophagic HeLa cells co-expressing VAMP8 (left panels) or VAMP7 (right panels) with each of the organelle markers indicated. Scale bars are 10 μm.

4.3.3 The binary autophagosomal SNARE complex

Published studies have identified Stx17 and SNAP29 as the binary autophagosomal SNARE complex based on co-immunoprecipitation and colocalisation work[248, 249]. To confirm this colocalisation in HeLa cells undergoing autophagy, the correlation of SNAP29-EGFP and Stx17-mCherry in autophagic HeLa cells was assessed, shown in figure 4.9. Signal overlap is visually apparent in merged images of the two channels (figure 4.9a), with the signal distribution following a strong linear relationship indicated by the frequency scatter plot in figure 4.9b, suggestive of the 1:1 stoichiometry expected of a binary SNARE complex. As Pearson's correlation coefficient is suited to such stoichiometry (discussed in section 2.5.1), it was therefore used to quantify the signal colocalisation, demonstrating a strong correlation between the two SNARE proteins (figure 4.9c).

As previously discussed, colocalisation is often over-interpreted as evidence of protein interaction *in situ*, however the resolution of both diffraction-limited and super-resolution microscopies are not sufficient to draw such conclusions. In demonstration of this, the characterisation of different imaging modalities in chapter two reported experimentally achievable lateral resolutions of approximately 380 nm, 220 nm, 140 nm and 50 nm, for widefield, confocal laser scanning, structured illumination and stimulated emission depletion microscopy, respectively. Even gSTED resolution is still an order of magnitude larger than the size of a protein. Therefore, to detect *in situ* sub-10 nm proximity between Stx17 and SNAP29, which would indicate a protein interaction, quantitative FLIM-FRET was employed.

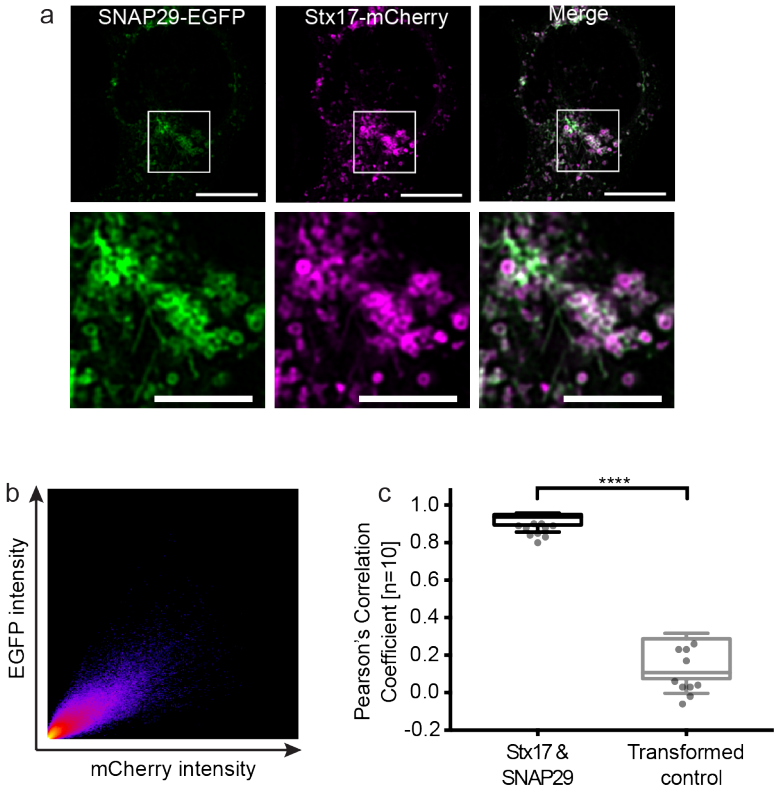

Figure 4.9 Colocalisation of Stx17 and SNAP29 (**a**) Single channel and merged images of autophagic HeLa cells co-expressing EGFP-SNAP29 and mCherry-Stx17 acquired by CLSM. Scale bars are 10 µm for full field and 3 µm for enlarged images of the indicated regions. (**b**) Frequency scatter plot of reported single pixel intensity values in each channel of the image presented in (a), demonstrating a linear relationship. (**c**) A boxplot of the Pearson's correlation coefficient values quantifying the data represented in (a). Significance of colocalisation determined by comparison to transformed negative controls using a paired two-sample t-test, [n=10].

Figure 4.10 shows the results of FLIM-FRET on autophagic HeLa cells expressing SNAP29-EGFP alone and co-expressed with wild-type Stx17. These proteins colocalise as expected (figure 4.10a-b), producing a strong change in donor fluorescence lifetime (figure 4.10a and c). As demonstrated in panel c, the SNAP29-conjugated EGFP donor presented a median fluorescence lifetime of 2.12 ns, which is reduced by 12.3% in the presence of Stx17-mCherry to 1.86 ns. This produced an upward shift in FRET efficiency (figure 4.10d) that is equivalent to the apparent FRET observed for the fused EGFP-mCherry construct characterised in section 2.5.2 (figure 2.15), which has a known separation of 12 amino acids. As discussed in section 2.5.2, integration of the FRET efficiency counts between 0.1-1.0 provides

a suitable metric for sample comparison. The FRET efficiency between SNAP29-EGFP and Stx17-mCherry has an integral of 0.15 (figure 4.10d), which is the same as the FRET efficiency between directly fused fluorescent proteins (figure 2.15). This demonstrates for the first time *in situ*, an interaction between Stx17 and SNAP29, which the fluorescence lifetime maps in figure 4.10a indicate is predominantly localised to punctate structures. This raises the question of how ectopic interactions are inhibited given that soluble intracellular fractions have been observed for both SNAP29 and Stx17[46, 248].

To determine if the apparent FRET-reported proximity between Stx17 and SNAP29 represents a functional SNARE complex, a mutant form of Stx17 was generated that cannot form SNARE interactions. This was achieved by mutating the critical zero-layer glutamine residue of Stx17 to a glycine residue, thereby disrupting formation of the coiled coil. This mutant, termed Stx17[Q196G], could still colocalise with SNAP29 (figure 4.10b), but FRET was strongly diminished as demonstrated by the FRET efficiency histogram in figure 4.10d. SNAP29-EGFP reported a median fluorescence lifetime of 2.03 ns in the presence of Stx17[Q196G]-mCherry. By comparing statistically the FRET efficiency integral above 0.1 for each field of interest, a significant loss of FRET is reported when replacing wild-type Stx17 with the zero-layer mutant. This illustrates the importance of the ionic layer for binary complex formation and confirms that the detected *in situ* proximity between Stx17 and SNAP29 is based on a functional SNARE interaction.

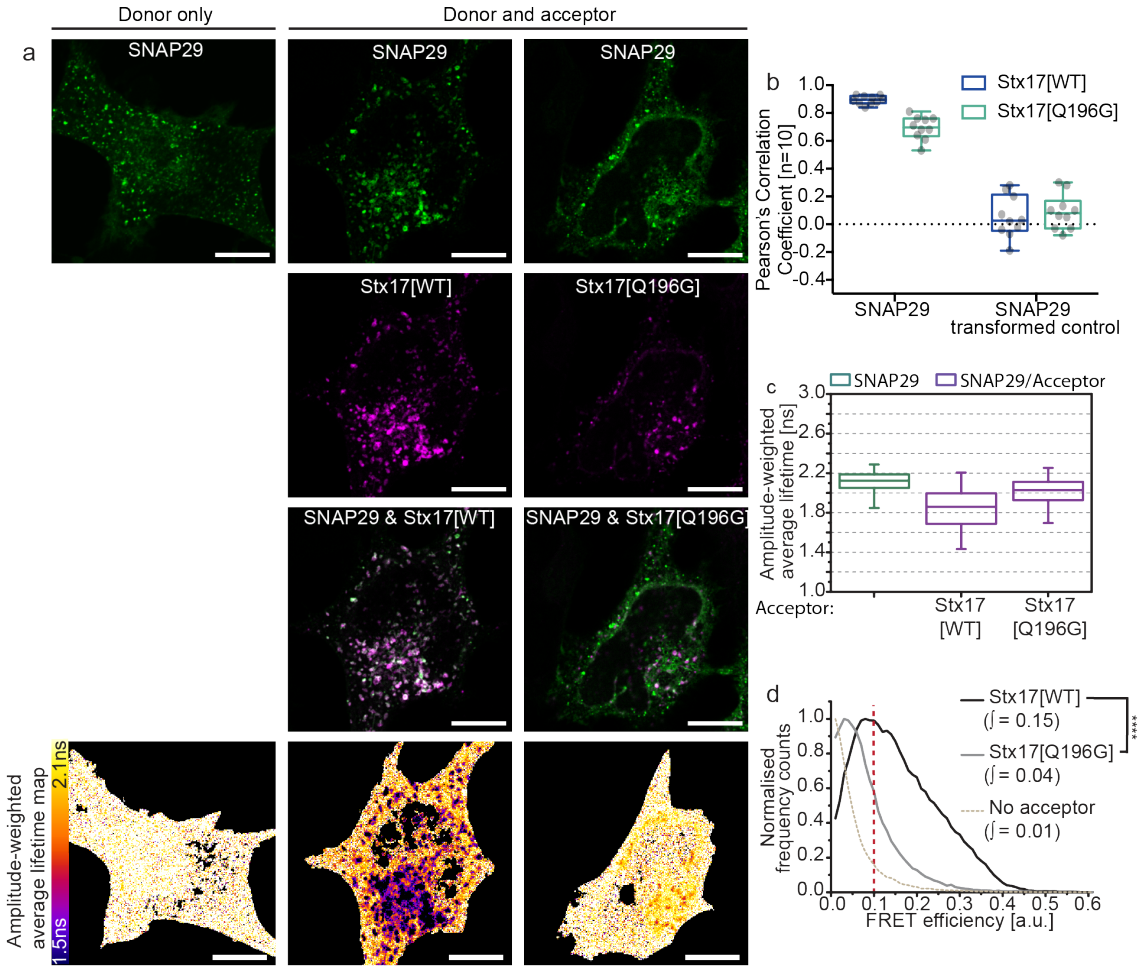

Figure 4.10 Confirming the autophagosomal binary complex by FLIM-FRET (**a**) Autophagic HeLa cells expressing SNAP29-EGFP alone (left) or co-expressed with either wild-type Stx17 (Stx17[WT]; centre), or the zero-layer mutant form of Stx17 (Stx17[Q196G]; right). Intensity maps of the EGFP channel (top row), mCherry channel (second row) and a merge of both channels (third row) are presented in addition to the fluorescence lifetime map (bottom row). (**b**) Boxplots demonstrating SNAP29 colocalisation with both Stx17[WT] and Stx17[Q196G], quantified by Pearson's correlation coefficient, [n=10]. (**c**) Boxplots of all single pixel fluorescence lifetimes accumulated across four cells in each case. Donor alone (SNAP29-EGFP) is green, donor and acceptor (either Stx17[WT] or Stx17[Q196G]) is magenta. (**d**) Histograms of the normalised single pixel FRET efficiency counts from four cells for SNAP29 co-expressed with the acceptor indicated, Integrated values above 0.1 were tested for statistical significance using a one-tailed unpaired two-sample t-test [n=4].

As Stx17 knockdown reportedly blocks autophagosome clearance[248], it can be expected that knockdown of its cognate binary SNARE complex binding partner would have the same effect. This was assessed in figure 4.11 based on the accumulation of mCherry-LC3 or EGFP-LC3 puncta in autophagic HeLa cells

treated with SNAP29 siRNA. As shown by western blot analysis of HeLa cell lysate (figure 4.11a), SNAP29 siRNA transfection efficiently inhibits the translation of SNAP29 in comparison to control siRNA. However, both control and SNAP29 knockdown cells demonstrate normal autophagic flux as indicated by the accumulation of autolysosomal mCherry puncta in comparison to LC3-EGFP expressing cells. This surprising result demonstrates that despite the apparent interaction between Stx17 and SNAP29, SNAP29 may not be essential for autophagosome clearance. This could suggest that SNAP29 plays a functionally redundant role in autophagosome clearance, which may instead be accomplished by another SNARE protein in its absence. However, following siRNA knockdown, residual levels of protein persist as can be seen by the faint bands in figure 4.11a. As residual SNARE proteins can reportedly sustain normal fusion[401], it remains unclear whether SNAP29 is functionally redundant or functional at very low expression levels. The identification of an alternative binary complex component may clarify this.

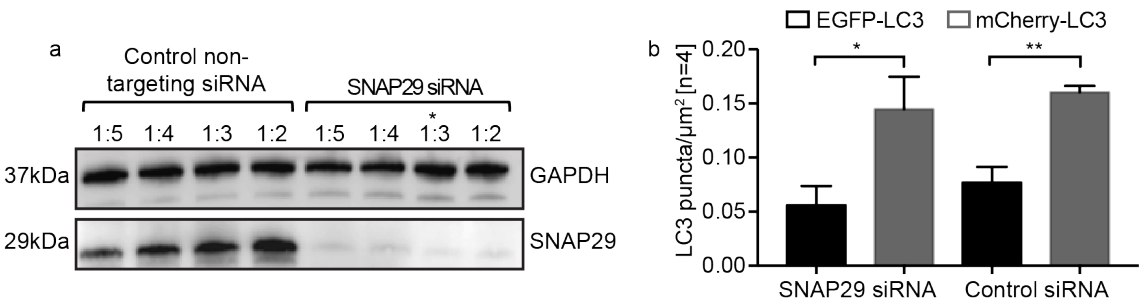

Figure 4.11 SNAP29 knockdown does not inhibit autophagosome clearance (**a**) Western blot reporting successful detection of the housekeeping gene, GAPDH, in all HeLa cell lysates and demonstrating efficiently reduced SNAP29 upon transfection with SNAP29 siRNA (columns 5-8) but not negative control non-targeting siRNA (columns 1-4). The ratio indicates different transfection component volumes in µl (20 µm siRNA:RNAiMax lipofectamine), the ratio 1:3 (starred) was used for further work. (**b**) LC3 puncta number per μm^2 for cells transfected with SNAP29 siRNA or negative control siRNA and expressing either EGFP-LC3 or mCherry-LC3. Statistical testing by an unpaired two-sample t-test demonstrates significantly more mCherry-LC3 puncta in both cases suggestive of functional autophagosome-endolysosome fusion, [n=4].

One candidate that may functionally replace SNAP29 is the Qb-SNARE Vti1b, which has previously been shown to play a role in autophagosome-lysosome fusion[247], though this has now been largely dismissed in favour of the evidence supporting the Stx17, SNAP29 and VAMP8 fusion model[248]. Published work demonstrates that Vti1b can colocalise with LC3-positive xenophagosomes and knockdown of this SNARE protein inhibits both LC3 turnover and the colocalisation of LC3 and LAMP1[247]. To confirm and expand this work, in figure 4.12 the colocalisation of Vti1b with autophagic markers was studied and its FLIM-FRET with Stx17 compared to that of SNAP29. In my hands, the replication of earlier colocalisation studies showed poor correlation between Vti1b and both LC3 and Stx17 (figure 4.12a-b). Reflecting this, the average fluorescence lifetime maps of Stx17-EGFP co-expressed with Vti1b-mCherry show no differentiation (figure 4.12c). Indeed, quantitation indicates that the median fluorescence lifetime of Stx17-EGFP was only reduced by 64 ps, equivalent to 3.2%, in the presence of Vti1b-mCherry, compared to 208 ps, or 10.5%, for SNAP29-mCherry (figure 4.12d). This resulted in a significantly greater FRET efficiency for SNAP29 with Stx17, which reported a FRET efficiency integral of 0.18. Furthermore, the FRET efficiency integral for Vti1b of 0.06, did not differ significantly to the donor-only control distribution. This suggests that Vti1b does not play a dominant role in binary complex formation. It may be that Vti1b is out-competed by SNAP29, an alternative SNARE may be involved or the residual SNAP29 levels following knockdown may be maintaining autophagic flux.

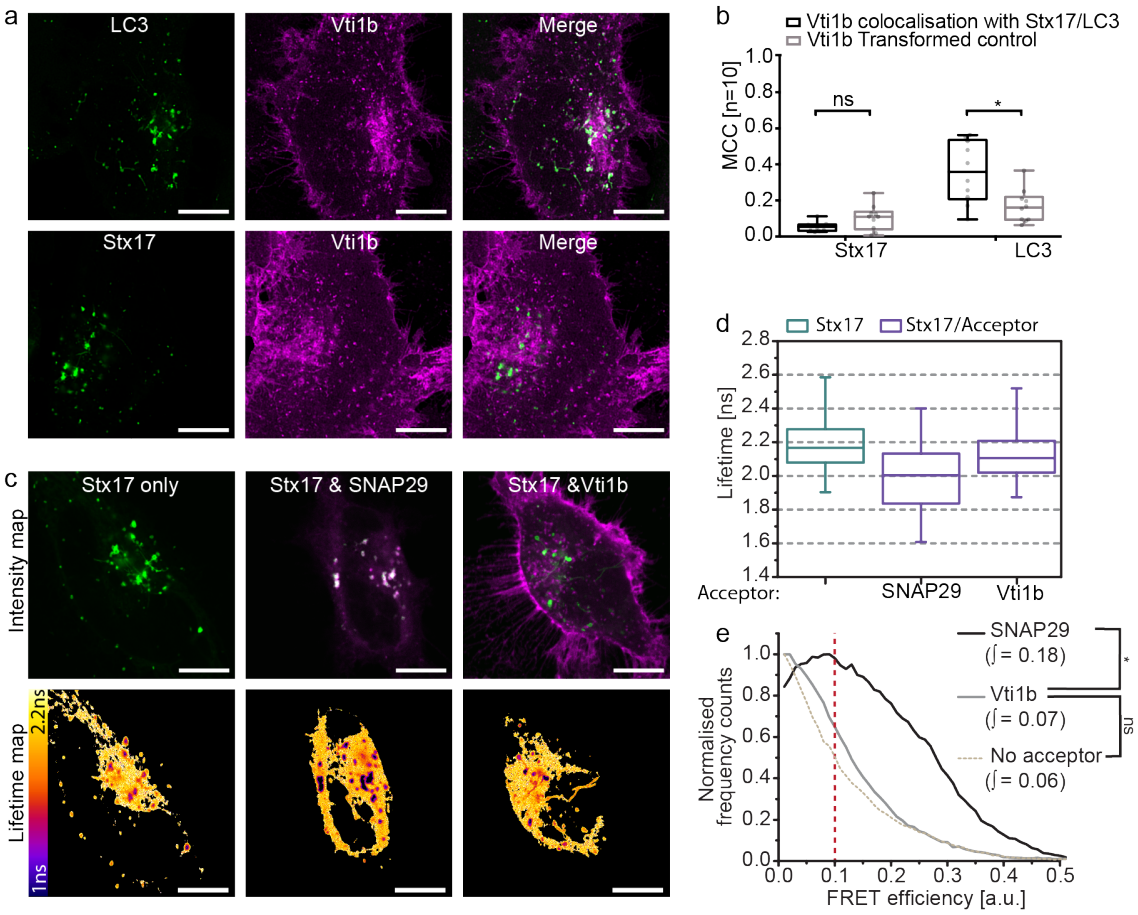

Figure 4.12 Vti1b as an alternative autophagosomal SNARE (**a**) Representative autophagic HeLa cells co-expressing Vti1b-mCherry with either LC3-EGFP (top row) or Stx17-EGFP (bottom row). (**b**) Quantitation of the colocalisation between channels represented in (a) using Manders correlation coefficient (MCC). Statistical significance by comparison to a transformed negative control was ascertained using a paired two-sample t-test, [n=10]. (**c**) Intensity (top row) and fluorescence lifetime (bottom row) maps of Stx17-EGFP expressed alone (left) or in addition to either mCherry-conjugated SNAP29 (centre) or Vti1b (right). (**d**) Boxplots of single pixel fluorescence lifetimes accumulated across four cells for each of the samples represented in (c). (**e**) Histogram of normalised FRET efficiency frequency counts for the acceptor construct indicated, calculated for the values presented in (d). Integrated values above 0.1 were tested for statistical significance using a one-tailed unpaired two-sample t-test [n=4]. Scale bars are 10 μm throughout.

4.3.4 The autophagosomal R-SNARE

As previously noted, the widely agreed autophagosomal SNARE model proposes VAMP8 as the contributing endolysosomal R-SNARE. However, VAMP8 was found to colocalise poorly with LC3 puncta, unlike VAMP7, which colocalised in a fusion-dependent manner (figure 4.8). To investigate this further, colocalisation with

Stx17 was assessed for both VAMP8 and VAMP7 in figure 4.13. As these R-SNAREs are resident on endolysosomal compartments, colocalisation indicates the formation of amphisomes or autolysosomes. Unlike the interaction between Stx17 and SNAP29, only a sub-population of VAMP-positive puncta is therefore expected to correlate with Stx17-positive puncta. Indeed, the merged images in panels a and d show distinct signal distributions in each channel, verified by their non-linear frequency scatter plots comparing single pixel intensity in each channel (figure 4.13b and d). Colocalisation was therefore assessed by Manders correlation coefficient, which is more appropriate for the detection of a sub-population of colocal probes, as discussed in chapter two (section 2.5.1). Figure 4.13c demonstrates that there is no correlation between VAMP8-EGFP and Stx17-mCherry signal. Conversely, in cells co-expressing Stx17 and VAMP7, a population of vesicles are positive for both proteins, resulting in significant colocalisation compared to the transformed negative control data (figure 4.13f). This strongly suggests that VAMP8 is not contributing to the autophagosomal SNARE complex as currently thought and implicates VAMP7 as a possible alternative, further supporting the data in section 4.3.2 (figure 4.8).

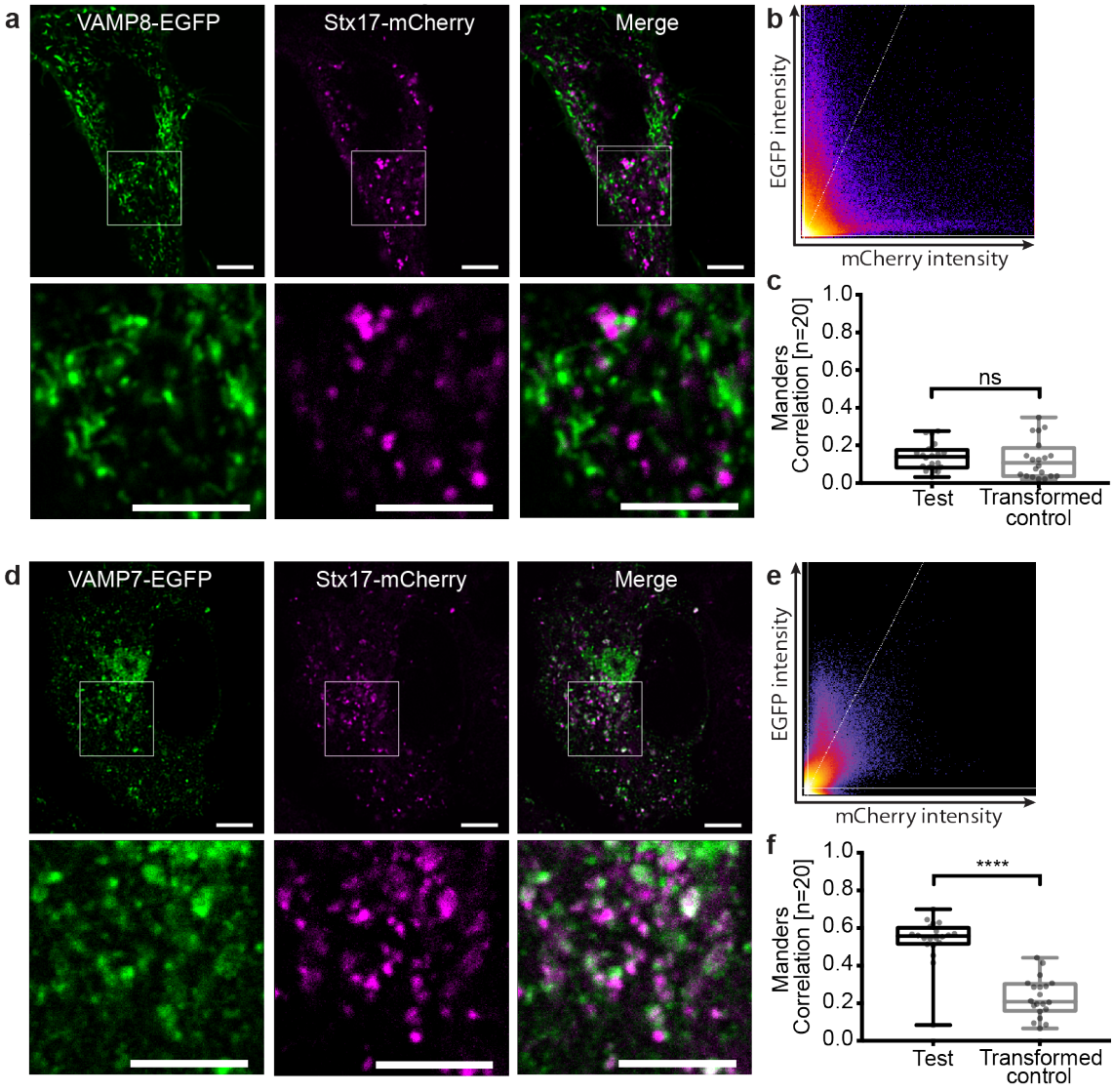

Figure 4.13 Colocalisation of Stx17 with the endosomal R-SNAREs (**a**) Representative autophagic HeLa cells co-expressing VAMP8-EGFP and Stx17-mCherry and (**b**) the resulting frequency scatter plot of the single pixel signal intensities. (**c**) Manders correlation coefficient quantitation of the colocalisation between VAMP8 and Stx17 in comparison to a transformed negative control; statistical significance was determined using a paired two-sample t-test, [n=20]. (**d-f**) Data presented as for (a-c) with autophagic HeLa cells co-expressing VAMP7-EGFP and Stx17-mCherry. Scale bars throughout are 10 µm for full field and 3 µm for enlarged images of the indicated regions.

In order to confirm an interaction between Stx17 and VAMP7, FLIM-FRET analysis was employed. Figure 4.14 compares the quantified FLIM-FRET of Stx17 with each of the R-SNAREs. Though no change in fluorescence lifetime is apparent across the cell for VAMP8 and Stx17, a reduction is observed for VAMP7 (figure 4.14a-b).

Upon quantitation of these data, VAMP7-EGFP demonstrates a 198 ps, or 9.9%, reduction in its median fluorescence lifetime when co-expressed with Stx17-mCherry (figure 4.14c), indicative of high FRET efficiency. Indeed, by comparing to the FRET efficiency distribution of VAMP7-EGFP co-expressed with non-tagged exogenous Stx17, Stx17-mCherry causes a significant shift, with the integral above 0.1 increasing from 0.01 to 0.10 (figure 4.14d). As with the Stx17 and SNAP29 interaction, this shift was significantly diminished (to 0.04) by the replacement of wild-type Stx17 with the zero-layer mutant, Stx17[Q196G], indicating disrupted coiled coil formation between the SNARE domains, evident of a functional interaction. By comparison, VAMP8-EGFP demonstrated a weaker change in median fluorescence lifetime of 77 ps, or 3.7%, resulting in a FRET efficiency distribution integral of 0.04, which is significantly lower than reported for VAMP7. In the context of the findings reported in figures 4.8 and 4.13 this comparison indicates that contrary to the published model[248], VAMP7 appears to be the dominant R-SNARE required for autophagosome clearance.

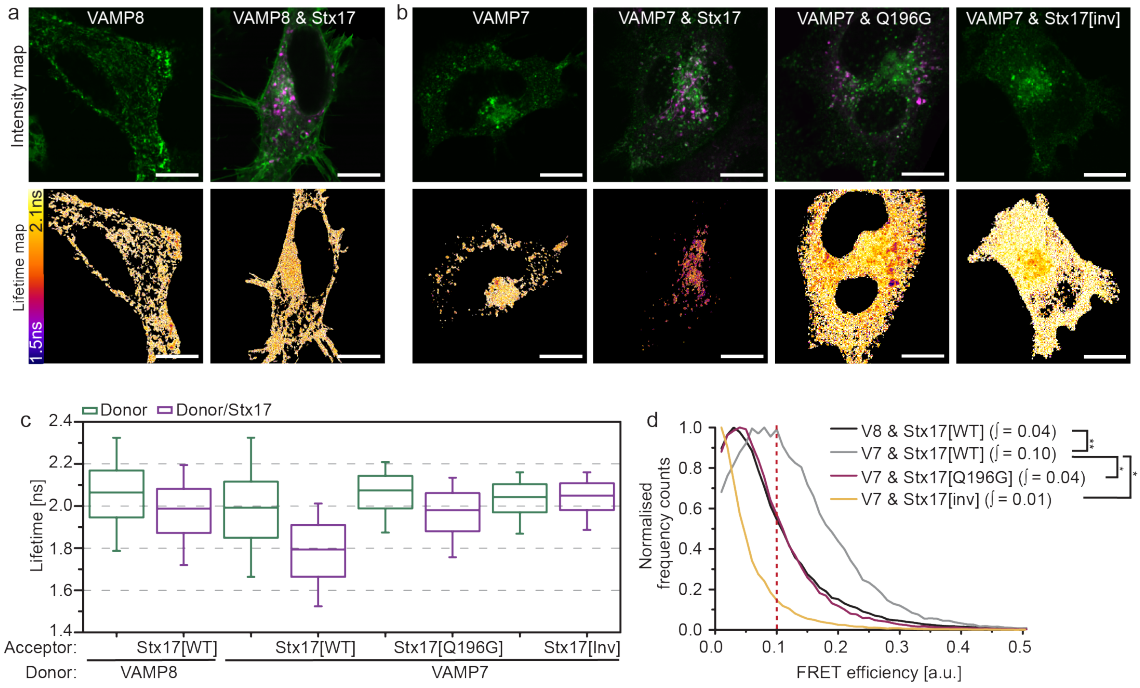

Figure 4.14 FLIM-FRET analysis of Stx17 with the endosomal R-SNAREs (**a**) Intensity (top row) and fluorescence lifetime (bottom row) maps of VAMP8-EGFP alone or co-expressed with Stx17-mCherry. (**b**) Intensity (top row) and fluorescence lifetime (bottom row) maps of VAMP7-EGFP alone or co-expressed with wild-type Stx17-mCherry, Stx17[Q196G]-mCherry or non-tagged Stx17 (Stx17[inv]). (**c**) Boxplots of all single pixel fluorescence lifetimes for each of the samples represented in (a) and (b) accumulated from four cells in each case. (**d**)

Histograms of normalised FRET efficiency frequency counts derived from all fluorescence lifetime values in (c) using the median fluorescence lifetime of VAMP8-EGFP (V8) or VAMP7-EGFP (V7) as appropriate. Integrated values above 0.1 were tested for statistical significance using a one-tailed unpaired two-sample t-test [n=4]. Scale bars throughout are 10 μm.

To confirm the complete ternary complex, FLIM was also used to detect the occurrence of FRET between either VAMP7- or VAMP8-EGFP and SNAP29-mCherry. As figure 4.7 demonstrated, SNAP29 redistributes upon co-expression with both of these SNARE proteins, suggestive of an interaction. Indeed, shown in figure 4.15, which presents the comparative FLIM-FRET between the EGFP-conjugated R-SNAREs in the presence of the SNAP29-mCherry acceptor, both VAMP7 and VAMP8 demonstrate a slight reduction in lifetime (figure 4.15a-b). However, this change is surprisingly small in both cases with no significant shift in the FRET efficiency distribution when compared to the donor-only distributions. The expectation that VAMP7-EGFP would present higher FRET efficiencies than VAMP8-EGFP was not evident, with no significant difference in the integrated FRET efficiency counts above 0.1 (0.05 and 0.06 respectively). Though the basis for this discrepancy remains unclear, it is tempting to speculate that the endogenous levels of Stx17 cannot support ternary complex formation in sufficient numbers for FLIM-FRET detection. Indeed, figure 4.6 presented poor localisation of SNAP29 to autophagosomes, suggesting highly controlled recruitment of this protein that may preclude FLIM-FRET detection of the ternary complex in the absence of exogenous Stx17.

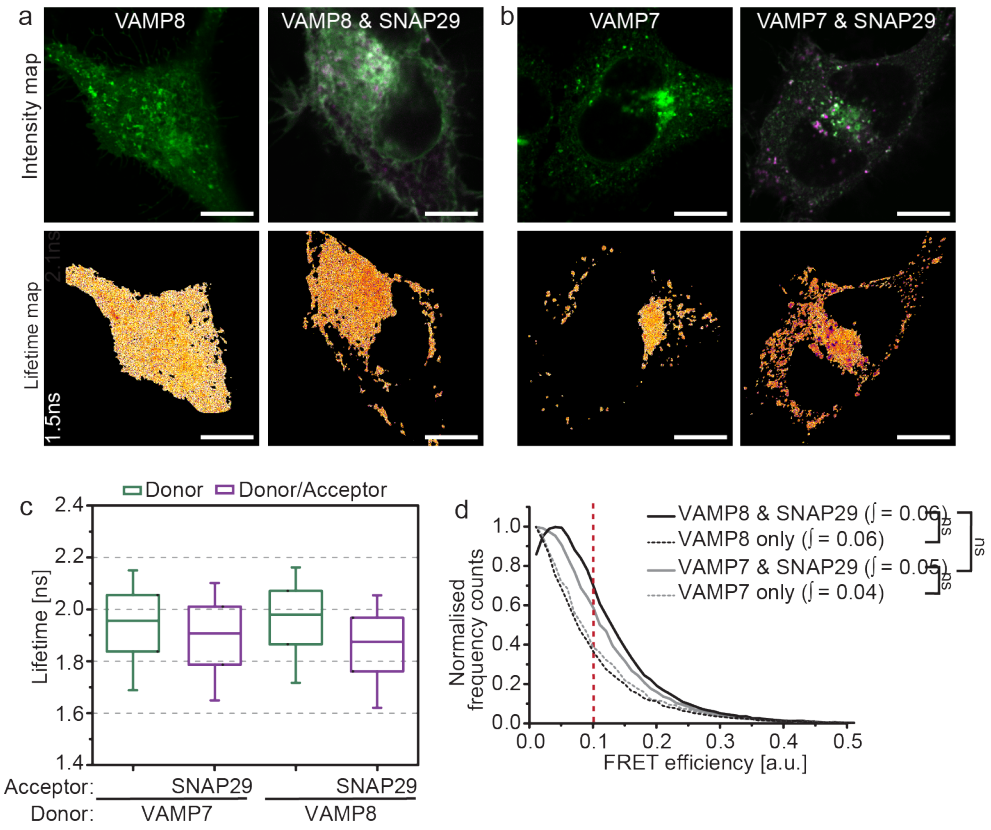

Figure 4.15 FLIM-FRET analysis of SNAP29 with the endosomal R-SNAREs (**a-b**) Intensity (top row) and fluorescence lifetime (bottom row) maps for (a) VAMP8-EGFP or (b) VAMP7-EGFP expressed alone or with SNAP29-mCherry. (**c**) Boxplots of all single pixel fluorescence lifetimes accumulated from four cells for each of the samples represented in (a) and (b). (**d**) Histograms of normalised FRET efficiency frequency counts derived from all fluorescence lifetime values in (c) using the median fluorescence lifetime of VAMP8-EGFP or VAMP7-EGFP as appropriate. Integrated values above 0.1 were tested for statistical significance using a one-tailed unpaired two-sample t-test [n=4]. Scale bars throughout are 10 μm.

4.4 Discussion

My research uses optimised assays combined with imaging techniques to study the SNARE protein interactions underlying autophagosome-endolysosome fusion. In agreement with published studies, gSTED microscopy confirms that Stx17 is recruited to the membrane of fusion-competent LC3-positive autophagosomes (figure 4.5). However, contrary to the agreed model of SNARE-mediated fusion, Stx17 interacts with SNAP29 and VAMP7, not VAMP8, to drive membrane fusion. This is evidenced here by both the availability of the R-SNARE for complex

formation (figures 4.8 and 4.13) and the detection of proximity between Stx17 and the two R-SNAREs *in situ* (figure 4.14).

The work carried out by Mizushima's group to establish the autophagosomal R-SNARE based their model on the greater loss of LC3 turnover in VAMP8 knockdown cells by comparison to VAMP7 knockdown[248]; though both of these should impact endosomal organisation due to their other known roles[59, 246]. Despite their conclusions, their published results do not exclude a role for VAMP7 in the autophagosomal SNARE complex. Indeed, they demonstrate immunoprecipitation of both proteins with Stx17 while finding no colocalisation of either R-SNARE with LC3. To reconcile these conflicts, a means of detecting, robustly, protein interactions *in situ* was required. I achieved this using FLIM-FRET to demonstrate that VAMP7 reports a closer proximity to Stx17 than VAMP8 (figure 4.14). As VAMP7 and VAMP8 are structurally distinct (see figure 4.16), it cannot be discounted that conformational differences may contribute to the disparity in FRET between the two pairings. However, VAMP7 is also a better candidate with respect to the autophagosomal SNARE complex identified in other species as previously discussed in section 4.1 and, unlike VAMP8, VAMP7 alone colocalises with LC3 and Stx17 (figure 4.8 and figure 4.13). It can therefore be credibly concluded that VAMP7 is the dominant autophagosomal R-SNARE.

The fusion-dependent correlation between VAMP7- and LC3-positive puncta contradicts published findings that VAMP7 does not colocalise with LC3[248]. It is unclear why Itakura *et al.* did not detect colocalisation between VAMP7 and LC3[248] as earlier work has indicated a correlation[210]. The method of quantitation of colocalisation was not outlined, and so the limitations on the techniques employed are unknown. As colocalisation can produce different results dependent on the algorithm implemented (as demonstrated in figure 2.12), it is essential that analysis is suited to the data[269] and this discrepancy highlights the need for this methodological information to be presented.

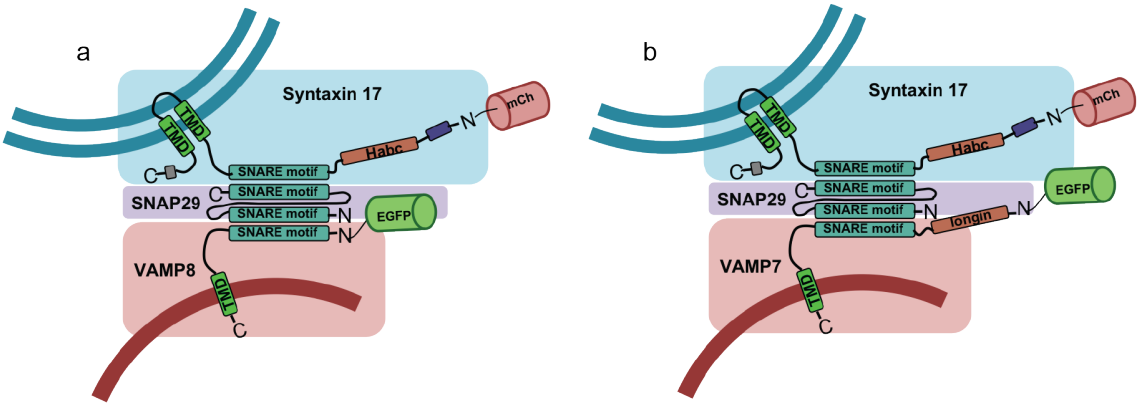

4.16 The endosomal R-SNAREs in complex with Stx17 and SNAP29 Cartoon illustrations of the N-terminal differences between (**a**) VAMP8 and (**b**) VAMP7 that may result in differing configurations of the attached fluorescent proteins upon SNARE assembly with SNAP29 and Stx17. Images are not to scale and no 3D information is included or available.

In addition to identifying the autophagosomal R-SNARE as VAMP7, FLIM-FRET was able to confirm SNAP29 as the cognate Qbc-SNARE (figure 4.10). Furthermore, interaction of Stx17 with both VAMP7 and SNAP29 required the zero-layer glutamine residue for ionic interactions to stabilise the coiled coil. This finding verifies that the detected FRET represents a functional SNARE interaction and presents Stx17[Q196G] as a novel mutant that may be used to dissect SNARE interactions, supplementing SNARE motif deletion mutant studies[248].

The proposed amendment to the autophagosomal SNARE model is of broad importance within the field of autophagy, however, our understanding of autophagosome clearance remains far from complete. Indeed, my research highlights a number of additional questions. Perhaps most outstanding among these is the regulation of the SNARE complex and particularly the binary complex formation. The poor recruitment of SNAP29 to autophagosomes in the presence of endogenous Stx17 (figure 4.6) suggests a tightly regulated association that may modulate the fusion competency of the vesicle and therefore prevent ectopic fusion events. This control mechanism appears to be saturated by the over-expression of Stx17, which causes redistribution of SNAP29 to Stx17-positive structures (figure 4.7). In the case of the exocytic SNARE complex, Syx1A relies on the SM protein, Munc18-1, to prevent ectopic binary complex formation[108]; a

similar mechanism is explored for the autophagosomal SNARE complex in chapter five.

Despite the apparent dependence of SNAP29 on Stx17 for autophagosome recruitment, SNAP29 demonstrated colocalisation with Stx17[Q196G] (figure 4.10). As SNAP29 cannot functionally interact with this Stx17 zero-layer mutant (also demonstrated by the reduction in FRET in figure 4.10), this correlation was very surprising; furthermore, this result demonstrates the importance of not over-interpreting colocalisation data as an 'interaction'. One possible explanation is that an accessory protein, such as an SM protein, provides a scaffold function. This could support weak interaction of SNAP29 and Stx17[Q196G] based on partial zippering of the N-terminal end of the SNARE motif. This hypothesis is consistent with evidence that indicates partially zippered intermediates can be formed[68]. Furthermore, the exocytic model notes binary complex formation prior to R-SNARE engagement[63]. This may explain the poor FRET noted between SNAP29 and VAMP7 (figure 4.15), but raises the question as to why SNAP29 is redistributed when co-expressed with either R-SNARE (figure 4.7). This suggests that its recruitment is linked to their activity, perhaps through a weak non-ternary SNARE complex association and the role of this promiscuity is yet to be determined.

The apparent binary SNARE interaction between Stx17 and SNAP29 suggests that SNAP29 should be essential for fusion. However, figure 4.11 demonstrated that SNAP29 knockdown has no impact on autophagic flux, indicating that residual levels of SNAP29 are sufficient for fusion as observed for other SNARE proteins[401] or that SNAP29 is functionally redundant. Supporting the latter hypothesis, an alternative Qb-SNARE, Vti1b, has previously been suggested to mediate autophagosome clearance. However, only a small shift in Stx17-EGFP fluorescence lifetime was noted upon co-expression with Vti1b-mCherry (figure 4.12). This shift was similar to that observed between VAMP8-EGFP and Stx17-mCherry (figure 4.14) and may indicate the detection of transient non-cognate SNARE pairings, which others have noted both *in vitro* and *in vivo*[86, 87, 401]. As the absence of FRET cannot rule out an interaction that occurs over a range greater than 10 nm, further investigation is still required to rule out a potential role for Vti1b. A means of real-time FLIM-FRET would provide useful insights into the longevity of different

SNARE interactions, perhaps enabling differentiation of cognate and non-cognate interactions. Though no existing technology can yet achieve this, the latest developments are explored with this objective in chapter six.

CHAPTER FIVE:

Regulation of Stx17 dynamics

5.1 Introduction

Precise membrane trafficking requires a regulatory mechanism that can restrict SNARE complex formation to the correct fusion site and prevent the formation of non-cognate SNARE complexes. Indicative of this tight regulation, I demonstrated in chapter four that Stx17 and SNAP29 binary complex formation is restricted to the autophagosome membrane (figure 4.10), despite the apparent promiscuity of SNAP29 (figure 4.7). Moreover, in the presence of endogenous Stx17, SNAP29 localises predominantly with late endolysosomal compartments and poorly with autophagosomes (figure 4.6), consistent with a regulatory mechanism that temporally couples binary complex formation to the fusion event.

Combinatorial SNARE complex formation is not sufficient to designate membrane fusion specificity, as multiple SNAREs may be present at the fusion site[87] and non-cognate SNARE assembly is apparent both *in vivo*[88] and *in vitro*[86, 87]. Fusion specificity is instead theorised to rely on SM proteins, which selectively bind and modulate cognate SNAREs to promote their fusogenic behaviour at the fusion site[95]. As discussed in section 1.2.3, SM proteins can reportedly modulate SNARE function through various mechanisms: stabilisation of the *trans*-SNARE bundle to promote fusion[96, 402-405], enhancement of the fusogenic activity of the complex to facilitate fusion pore formation[406], association with Rab GTPase effectors to recruit SNARE proteins to the fusion site[407] and inhibition of ectopic fusion by stabilising the 'closed' conformation of syntaxin[47-49, 97, 98]. However, not all these binding modes have been detected in all SM-SNARE interactions. Indeed, it has been hypothesised that two functionally divergent classes of SM proteins exist based on their affinities for free and complexed SNARE proteins[404]. As free syntaxin in the open conformation associates with SM proteins using its N-peptide motif[408], the presence of an N-peptide binding pocket has been used to structurally distinguish SM protein class[404]. The N-peptide motif of *N*-(R/K)DRTX(e/q)(L/F)-*C*[409] is proposed to bind to a minor groove on domain 1 of its cognate SM protein[101], requiring two binding pockets that accommodate the arginine side chain and a hydrophobic side chain[409].

The SM proteins Munc18, VPS45 and Sly1 can all reportedly bind the N-peptide of their cognate syntaxin[409] and have been designated class I SM proteins on this basis[404]. The crystal structure has been solved for Munc18-1, Munc18-2, Munc18-3 and Sly1 bound to their cognate syntaxin and indeed demonstrates the expected N-peptide binding cleft[101, 114, 409, 410]. Conversely, yeast Sec1p and Vps33 as well as mammalian VPS33A do not possess the N-peptide-binding patch conserved among class I SM proteins[404, 409], which crystallisation of VPS33A indicates are instead apparently blocked with bulky residues[411]. These SM proteins are therefore categorised as class II for their suspected poor N-peptide binding capability. Yeast Vps33 demonstrated greater affinity for complexed Vam3 than individual Vam3[404], consistent with a lack of N-peptide binding capacity. However, an unexplored possibility remains that class II SM proteins may have a distinct N-peptide binding pocket to interact with an alternative N-peptide motif. Indeed, it could be speculated that variation in the N-peptide motif actually enables specific SM recognition; no two N-peptides are identical among syntaxins[409] and deviation away from the core 'DRT' sequence does not preclude interaction of Stx16 with VPS45[92, 412]. This chapter investigates the divergent N-peptide of syntaxin 17 and explores whether it may associate with its cognate SM protein, VPS33A[177], contrary to its categorisation as a class II SM protein.

Yeast Vps33 and its mammalian homologs, VPS33A and VPS33B, play important roles in vacuolar or endosomal fusion events[413]. VPS33B has a putative function in early endosome fusion and phagocytosis[413], while VPS33A is of particular interest here due to its reported promotion of autophagosome clearance and late endosome-lysosome fusion[177, 414]. VPS33A reportedly promotes SNARE-mediated membrane fusion by stabilising the SNARE complex[404] and enhancing its fusogenic activity[406]. Additionally, VPS33A associates with the multi-subunit tethering complexes (MTCs), HOPS (homotypic fusion and vacuole protein sorting) and CORVET (class C core vacuole/endosome tethering), which aid membrane fusion by recruiting SNARE proteins to the fusion site[413] and proofread to suppress Sec18 disassembly of cognate *trans*-SNARE complexes[415, 416]. VPS33A is considered unique among SM proteins in forming an integral part of MTCs, though other SM proteins have been shown to interact transiently with such complexes[417, 418].

Structural analyses of the HOPS complex indicate that both SNARE binding grooves of VPS33A are exposed when in complex[102, 411, 419], with VPS33A interfacing with HOPS via the outer surface of its domain 3b[411]. Interestingly, the same region in other SM proteins has been implicated in tethering interactions, suggestive of a conserved tethering mechanism[411].

HOPS is an essential component of the minimal fusion machinery required for *in vitro* proteoliposome fusion by the yeast vacuolar SNAREs[420]. Indeed, disruption of any HOPS subunit inhibits vacuolar fusion in yeast[407] and endosomal fusion in mammals[421-423], indicating that the complex has a broader role in fusion than the function of Vps33 alone. The other subunits of HOPS are the vacuolar protein sorting (VPS) proteins VPS11, VPS16, VPS18, VPS39 and VPS41[407, 424], which are arranged in the two-lobe structure[419] depicted in figure 5.1. These enable HOPS to function as both a Rab effector and Rab GEF[407, 425] as well as a multi-subunit tethering complex[407] that can bind SNAREs independent of VPS33A[404]; this latter function has been suggested to tether syntaxin in the absence of an SM N-peptide binding domain[404]. VPS39 and VPS41 have a Rab7-binding activity that recruits HOPS to late endolysosomal structures[407]. These two subunits are replaced in CORVET with VPS3 and the Rab5-binding VPS8 to alternatively direct CORVET to early endosomal compartments[426]. The late endolysosomal targeting of HOPS places it as a probable candidate to assist autophagosome-endolysosome fusion, which indeed has been demonstrated[176]. This function requires VPS33A association with Stx17[177], though the mechanistic details of this regulation are not yet known.

These findings place the HOPS complex as a promoter of membrane fusion and the fundamental importance of VPS33A for this is exemplified in *D. melanogaster* where loss is lethal during larval development[427]. It remains unclear, however, whether the spatial distribution of the HOPS complex is sufficient to suppress ectopic formation of the autophagosomal SNARE complex or if other mechanisms concomitantly inhibit formation elsewhere. The endosomal and autophagosomal syntaxins, 7, 8 and 17 all encode Habc domains[34] that may indicate a capacity to form closed conformations comparable to Syx1A[47-49, 98]. However, no such

conformation has been reported and the presence of this N-terminal domain does not seem to guarantee its formation[92, 99, 100].

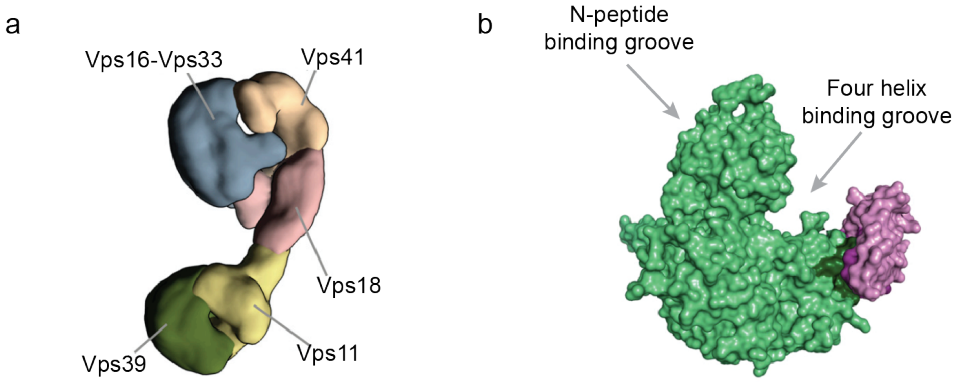

Figure 5.1 VPS33A positioning in the HOPS complex (**a**) A 3D reconstitution of the yeast HOPS complex based on single-particle electron microscopy (taken from Bröcker *et al*., 2012[419]). (**b**) A space-filling model of human VPS33A (green) bound to residues 642-736 of VPS16 (purple), the residues of VPS33A that disrupt interactions with VPS16 are highlighted in dark green. Both the four helix binding groove and the N-peptide binding groove are available when VPS33A is in complex. Image adapted from Graham *et al*., 2013[411].

Other mechanisms have been proposed to regulate autophagosomal SNARE complex formation, notably including Atg14 stabilisation of the binary SNARE complex[253]. As Atg14 reportedly binds exclusively to the Q-SNARE complex to prime it for R-SNARE association[253], it is well placed to inhibit premature complex formation. However, ternary complex associations with Atg14 were ruled out based on poor co-immunoprecipitation of VAMP8[253], which I demonstrated in chapter four is not the dominant R-SNARE for autophagosome clearance. Understanding the role of Atg14 is further complicated by conflicting reports regarding its availability for SNARE binding, with data variously indicating Stx17 recruitment of Atg14 to the phagophore nucleation site[158], Stx17 absence from the phagophore nucleation site[248], Atg14 promotion of autophagosome-endolysosome fusion[253] and Atg14 dissociation from the phagophore upon closure[428]. More clarity is therefore needed to understand the recruitment of Stx17 to the autophagosome, the role of Atg14 in Stx17 dynamics and how this interconnects with HOPS promotion of autophagosome clearance to prevent premature and ectopic fusion events.

5.2 Materials and Methods

5.2.1 Sample preparation and microscopy

All imaging work presented in this chapter was carried out on a Leica SP5 SMD confocal laser scanning microscope (CLSM). With the exception of the live cell calcium imaging in section 5.3.2, all microscopy was performed on fixed samples, prepared as outlined in section 3.4. Immediately prior to fixation or live imaging, transiently transfected HeLa cells were treated with 160 nM rapamycin for 60 minutes. In the case of live cell work, cells were then transferred to Krebs buffer supplemented with 160 nM rapamycin for imaging and maintained at 37°C and 5% (v/v) CO_2. Where indicated, cells were additionally treated with Bafilomycin A_1 (Baf A_1) to inhibit autophagosome-endolysosome fusion by supplementing media with 50 nM Baf A_1 24 hours prior to fixation.

Multi-channel images were acquired sequentially by frame and subsequently processed and quantified to determine colocalisation or puncta concentration as outlined in section 3.5.7. The resulting data is presented throughout in boxplot or barchart format. The former indicates the median value (line), 25th and 75th quartile values (box) and the maximum and minimum values (whiskers), while the latter reports the mean value and the standard error of the mean (SEM). Statistical significance is presented throughout as 'ns' for non-significant (P values of 0.05 or greater), * for P values between 0.005-0.05, ** for P values between 0.0005-0.005, *** for P values between 0.0001-0.0005 and **** for P values below 0.0001.

Consistent with chapter four, all TCSPC FLIM-FRET was carried out on a CLSM, integrating photon counts up to 10,000 photons per pixel. Subsequent single pixel bi-exponential tail fits were performed on all pixels with a minimum of 1,000 photon counts, as discussed in section 2.5.2. Fluorescence lifetime refers to the amplitude-weighted average fluorescence lifetime information, derived from the decay fits, which is presented as boxplots throughout; these report the median value (line), the 25th and 75th quartile value (box) and the 5th and 95th quartile value (whiskers). Single pixel FRET efficiencies were calculated using the median fluorescence lifetime of the control donor-only sample. Statistical significance of changes in FRET efficiency was determined using a one-tailed unpaired two-

sample t-test on the integral of the histogram between values 0.1-1.0 (denoted throughout as ∫), statistical significance is presented in the same way as described above for colocalisation. Values below 0.1 are poor indicators of FRET (refer to section 2.5.2) and were therefore excluded.

5.2.2 Protein sequence and structural analyses

Protein sequence analysis was used to compare the divergence of human syntaxin N-peptide motifs in section 5.3.1. These were performed on sequences obtained from the National Centre for Biotechnology (NCBI) protein database. Sequence alignments used the Geneious (Biomatters Ltd) software alignment tool and kinase consensus sequences were identified using the online NetPhos3.1 phosphorylation site prediction tool[429]. Protein structural analyses were performed in MacPyMOL (Schrödinger LLC) using published atomic coordinate files obtained from the RSCB Protein Data Bank. Surface potential was calculated and visualised using the vacuum electrostatics tool in MacPyMOL.

5.3 Results

5.3.1 The regulation of autophagosomal SNARE assembly

The regulatory SM protein governing autophagosome-endolysosome fusion has been identified as VPS33A based on colocalisation and co-immunoprecipitation studies with Stx17[177]. Notably, VPS33A co-precipitates with Stx17 in complex with all HOPS components and knockdown of VPS33A, VPS16 and VPS39 lead to autophagosome accumulation[177]. However, as autophagosomal SNARE protein interactions have not previously been detected *in situ*, it has not been confirmed that VPS33A knockdown disrupts autophagic flux by reduced *trans*-SNARE complex stability as proposed, nor has any mechanistic insight into the role of VPS33A in the autophagy pathway been elucidated. Indeed, reduced autophagosome clearance could be a secondary affect of disturbed late endosomal fusion events also noted in the same study by Mizushima's laboratory[177].

In my previous chapter, FLIM-FRET successfully detected specific SNARE protein interactions on punctate structures between Stx17 and both SNAP29 and VAMP7 (figure 4.10 and 4.14). Therefore, to confirm the hypothesis that VPS33A stabilises the autophagosomal *trans*-SNARE complex, figure 5.2 presents a similar FLIM-FRET assay carried out in VPS33A and control siRNA knockdown cells to ascertain whether the SNARE complex can form in the absence of VPS33A. As figure 5.2a shows, non-targeting control siRNA treatment presents the expected change in VAMP7-EGFP fluorescence lifetime upon co-expression with mCherry-conjugated SNAP29 or Stx17. No such change is observed, however, upon VPS33A treatment, which produced phenotypically knocked-down cells as indicated by the accumulation of autophagic vesicles[177] in panel b. Indeed, quantitation of single pixel fluorescence lifetimes demonstrates a reduction of 196 ps and 143 ps, or 9.0% and 6.6%, to the median fluorescence lifetime of VAMP7-EGFP in control cells upon co-expression with SNAP29 and Stx17 respectively. This is reduced to a difference of 49 ps and 93 ps, or 2.5% and 4.7%, in VPS33A knockdown cells (figure 5.2b). This equates to a significant difference in FRET efficiency between control and VPS33A knockdown cells for VAMP7 interactions with both Stx17 and SNAP29 (figure 5.2c). These findings therefore confirm that VPS33A knockdown causes autophagosome accumulation due to the loss of the *trans*-SNARE complex.

Based on the conservation of VPS33A structure with other SM protein family members, it is credible that it functions in a similar manner. VPS33A has a large binding cleft between domains 1 and 3a[102, 411] that has been shown to accommodate a four helical structure in other SM proteins[49]. It is therefore likely that VPS33A promotes ternary complex formation by stabilising the four helical SNARE bundle. Consistent with this, VPS33A has been shown to interact with the SNARE domains of the yeast endocytic SNAREs[404]. However, no such studies have been extended to the autophagosomal SNARE complex or carried out in the intracellular environment.

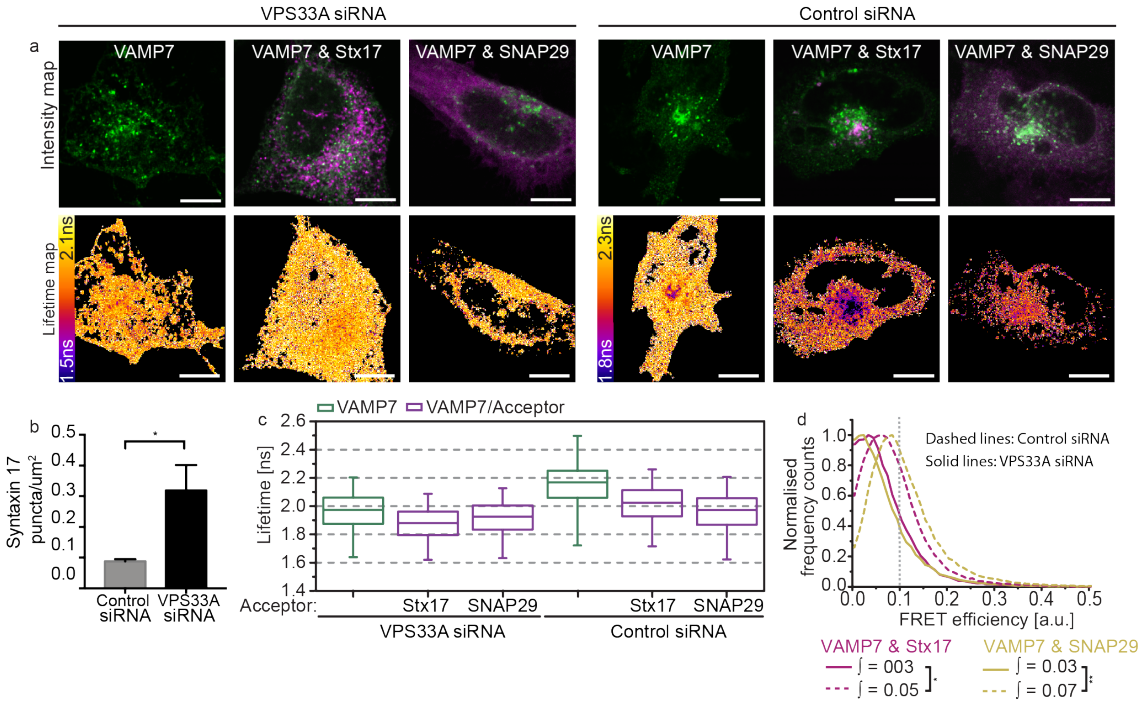

Figure 5.2 VPS33A stabilises the *trans*-SNARE complex (**a**) Intensity (top row) and fluorescence lifetime (bottom row) maps of autophagic HeLa cells treated with non-targeting control siRNA (right panels) or VPS33A siRNA (left panels). Cells express VAMP7-EGFP alone and with Stx17-mCherry or SNAP29-mCherry as indicated. Stx17[inv] was co-expressed with SNAP29-mCherry throughout to aid ternary complex formation. Scale bars are 10 µm. (**b**) A barchart quantifying Stx17-positive puncta concentration per cell to demonstrate the expected accumulation of autophagosomes upon VPS33A knockdown. Significance tested with an unpaired two-sample t-test [n=4]. (**c**) Boxplots of all single pixel fluorescence lifetimes, each represents data accumulated from four cells. (**d**) Histograms of normalised single pixel FRET efficiency frequency counts, each accumulated from four cells. Integrated values above 0.1 were tested for statistical significance using a one-tailed unpaired two-sample t-test [n=4].

FLIM-FRET was performed to verify the interaction between VPS33A and the autophagosomal SNAREs *in situ*. As shown in figure 5.3, which presents the resulting data, co-expression of VPS33A with Stx17, SNAP29 or VAMP7 has little effect on the donor fluorescence lifetime across the cell. The notable exception to this is a localised reduction observed in regions dense in Stx17-positive puncta (figure 5.3a-b). Interestingly, reversing the tag orientation of Stx17-mCherry from the N- to the C-terminus diminishes this change to the donor fluorescence lifetime (figure 5.3b). This provides some insight into the configuration of the VPS33A-Stx17 interaction, indicating that their N-termini may be more closely apposed than their N- and C- termini, respectively. As the change in fluorescence lifetime is

localised to a small number of pixels, quantitation by single pixel analysis across the whole cell poorly represents this change, producing low FRET efficiency integrals of 0.008-0.012, 0.006 and 0.011 for VPS33A paired with Stx17, SNAP29 and VAMP7, respectively (figure 5.3b-c). Furthermore, the FRET efficiency distribution for Stx17 and VPS33A differs significantly from donor-only control values in one experiment but not another (figure 5.3c-d). This discrepancy likely indicates that inclusion of all pixels in quantitation dilutes local changes in fluorescence lifetime. The qualitative trend in puncta-localised fluorescence lifetime reductions when VPS33A is paired with Stx17, is not evident for VAMP7 or SNAP29 (figure 5.3a). This may indicate that VPS33A associates with free Stx17, however, this cannot be reliably concluded based on FRET studies alone, as interactions across large proteins complexes cannot be detected. This is exemplified by the reduction in FRET between VPS33A and Stx17 caused by relocating the fluorescent tag to the opposite terminus of Stx17 (figure 5.3d).

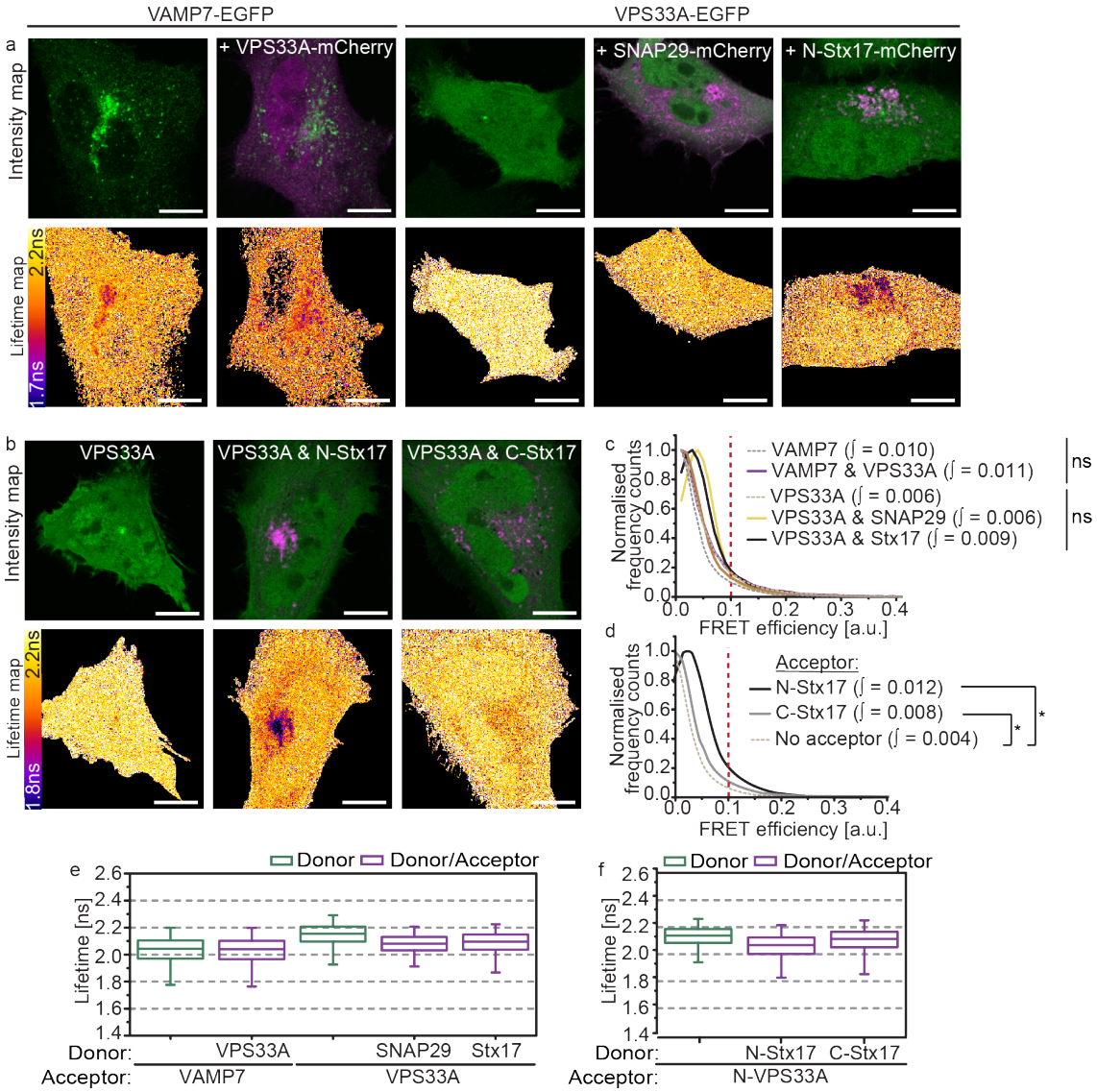

Figure 5.3 VPS33A FLIM-FRET with the autophagosomal SNAREs (a-b) Intensity (top row) and fluorescence lifetime (bottom row) maps of autophagic HeLa cells expressing the constructs indicated. N-Stx17 and C-Stx17 indicates fluorophore conjugation at the amino- or carboxyl-terminal respectively, VPS33A, SNAP29 and VAMP7 were N-terminally labelled throughout. Scale bars are 10 µm. (**c-d**) Histograms of single pixel FRET efficiency counts, accumulated over four cells, for VPS33A co-expressed with each of the autophagosomal SNAREs (c) and VPS33A co-expressed with N-tagged or C-tagged Stx17 (d). Integrated values between 0.1-1.0 are shown and were used to determine statistical significance with a one-tailed unpaired two-sample t-test, [n=4]. (**e-f**) Boxplots of all single pixel fluorescence lifetimes accumulated across four cells for the datasets presented in (a) and (b) respectively.

As a syntaxin family member, Stx17 has an Habc domain[34] that may be able to fold back onto its SNARE domain forming a 'closed' four helical structure that cannot form SNARE associations, similar to Syx1A[49]. VPS33A could theoretically preclude

SNARE complex formation by engaging and stabilising such a closed structure in place of the SNARE bundle[411], by association with its large binding cleft, a conserved region in SM proteins with demonstrated four helix binding[49]. In the case of the exocytic model, such multi-modal regulation relies on an N-peptide association that maintains a connection between Syx1A and Munc18-1 during binding mode transitions[111]. As VPS33A has an atypical N-peptide binding pocket, it has been proposed that it cannot bind a syntaxin N-peptide motif and solely promotes fusion *via* SNARE bundle stabilisation[404, 409]. However, I speculated that as Stx17 has a divergent N-peptide motif, it might encode consensus for the atypical VPS33A N-peptide binding pocket. To explore this possibility, figure 5.4 presents a sequence analysis of Stx17 and a structural analysis of VPS33A in comparison to other family members.

Demonstrated in figure 5.4a, Stx17 has a highly negative N-peptide patch with four consecutive glutamic acid or aspartic acid residues. These are flanked by a putative phosphoserine, determined using the Netphos 3.1 prediction tool[429] (figure 5.4b), which could contribute additional negative charge upon phosphorylation. The Stx17 N-peptide motif matches the consensus sequence for casein kinase II[430], a constitutively active kinase[431] that may therefore result in the constitutive modification of this residue to a phosphoserine. Interestingly, an electrostatic surface charge analysis of VPS33A, shown in figure 5.4c, indicates a remarkably positive surface in the region of VPS33A that corresponds to the N-peptide binding cleft of class I SM family members[432]. VPS33A may therefore encode an alternative N-peptide binding site suited to Stx17. Furthermore, both Stx6 and Stx10 encode similar N-peptide motifs of *N*-MSXED-*C* and have consensus for serine-2 phosphorylation, so this may represent a divergent N-peptide binding mechanism. To explore this hypothesis, a range of mutant Stx17 constructs were designed as outlined in figure 5.4d; these include a charge mutant, a phosphonull mutant and a phosphomimetic mutant, labelled Stx17[ED3-6K], Stx17[S2A] and Stx17[S2E] respectively.

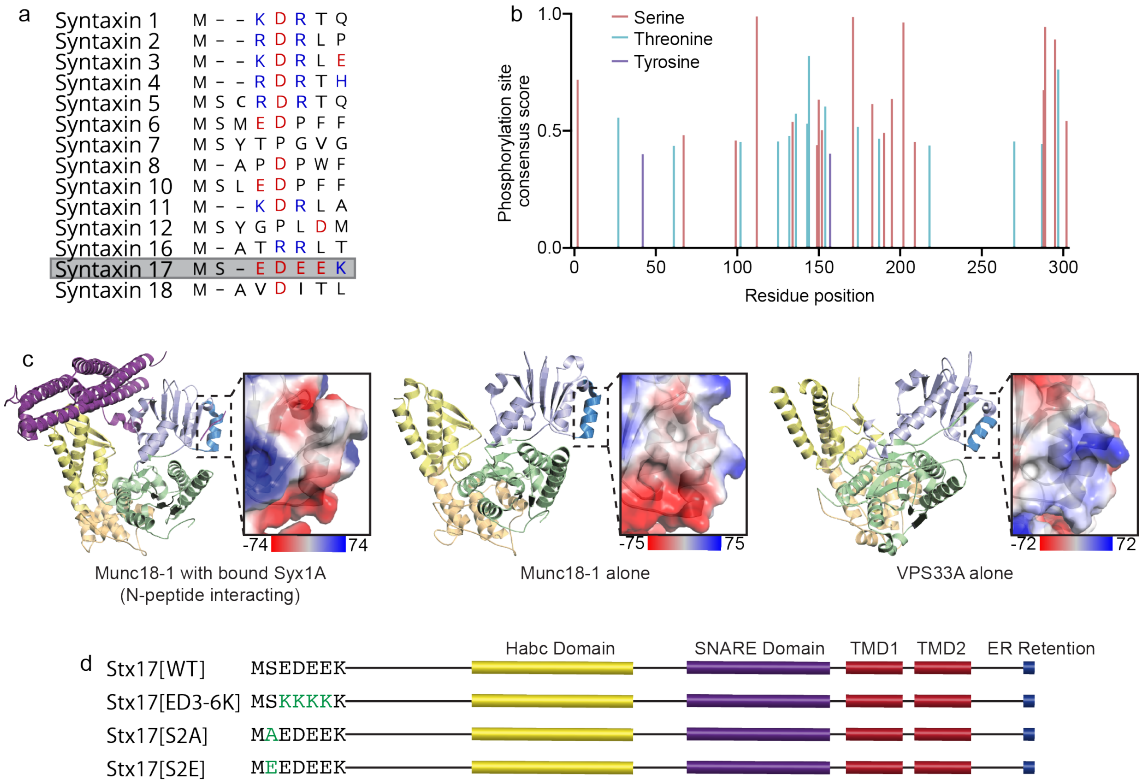

Figure 5.4 The unique Stx17 N-peptide has VPS33A binding compatibility (**a**) An alignment of the N-peptide sequences of human syntaxin family proteins with negatively and positively charged residues highlighted in red and blue respectively. Stx17 demonstrates a highly negative sequence. (**b**) Netphos 3.1[429] phosphorylation site prediction score for each residue of Stx17 indicates probable phosphorylation of the N-peptide at serine-2. (**c**) Cartoon diagrams of the structure of Syx1A-bound Munc18-1[432] (left), Munc18-1 alone[432] and VPS33A alone[411]. SM protein structure is coloured by domain (domain 1 is light blue with dark blue highlighting the N-peptide binding region, domain 2 is green, domain 3a and 3b are yellow and wheat respectively). Magnified panels show the electrostatic surface charge in kT/e_c of the indicated syntaxin N-peptide binding region. (**d**) Structure and sequence of wild-type Stx17, Stx17[WT], (top) with designed N-peptide mutants: Stx17[ED3-6K] charge mutant, Stx17[S2A] phosphonull mutant and Stx17[S2E] phosphomimetic mutant.

The capacity of mutant Stx17 proteins to participate in the autophagosomal SNARE complex was assessed in figure 5.5, using FLIM-FRET to detect associations with SNAP29 and VAMP7. Strikingly, an interaction with SNAP29 or VAMP7 could not be detected for the phosphomimetic mutant, Stx17[S2E]. The expected reduction in fluorescence lifetime of SNAP29-EGFP and VAMP7-EGFP upon co-expression with wild-type Stx17-mCherry is apparent in both the fluorescence lifetime maps and single-pixel boxplots shown in figure 5.5. However, its replacement with the

phosphomimetic variant abolished this, producing significantly reduced FRET efficiencies with integration values of 0.01 for SNAP29 and 0.03 for VAMP7 (figure 5.5c and f), comparable to the donor-only negative control FRET efficiency distributions, which report integrals of 0.01 and 0.02 respectively. Additionally, for both SNAP29 and VAMP7, only the phosphomimetic has a FRET efficiency distribution significantly diminished in comparison to wild-type.

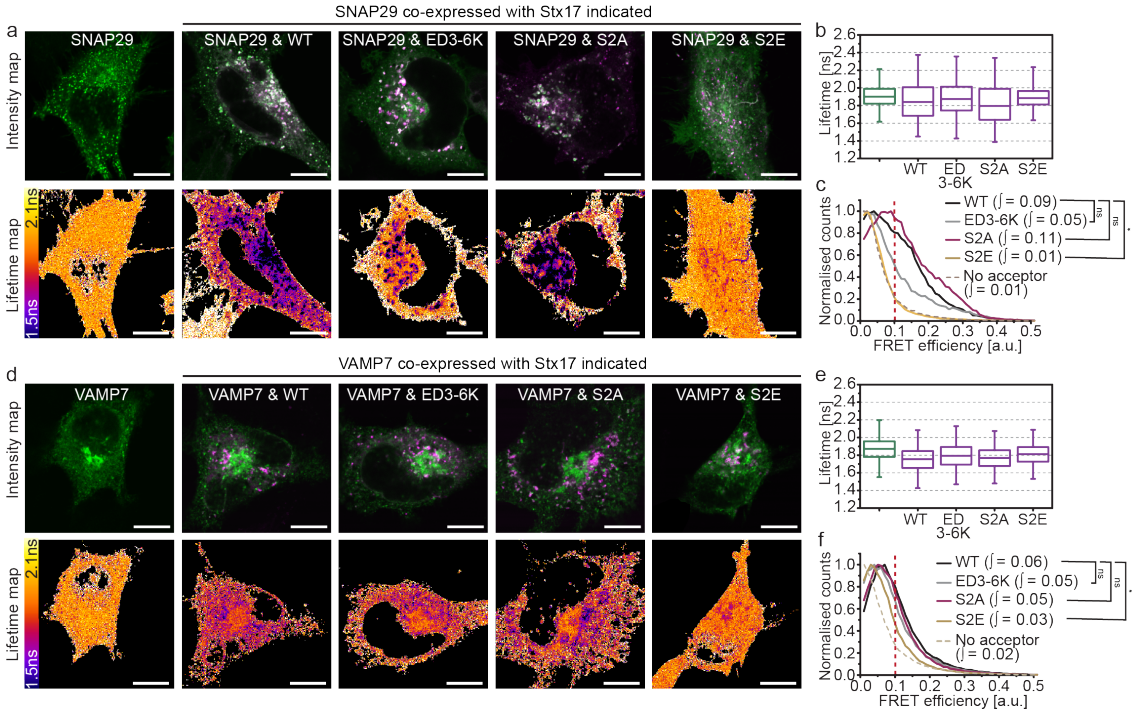

Figure 5.5 Stx17 N-peptide phosphorylation inhibits SNARE assembly (**a and d**) Representative intensity (top row) and fluorescence lifetime (bottom row) maps of autophagic HeLa cells expressing SNAP29-EGFP (a) or VAMP7-EGFP (d) alone and with wild-type or mutant Stx17 as indicated. (**b and e**) Boxplots of all single pixel fluorescence lifetimes across four cells. Boxplots in (b) and (e) quantify the data represented in (a) and (d) respectively. (**c and f**) FRET efficiency histograms calculated using each of the single-pixel fluorescence lifetimes presented in (b) and (e), respectively. Integrated values above 0.1 were tested for statistical significance with a one-tailed unpaired two-sample t-test, n=3 in (d) and n=4 in (f).

In the case of the binary complex, a trend towards an increase in FRET was noted using the phosphonull mutant, though it was not statistically significant (figure 5.5c). This may indicate that incomplete dephosphorylation of wild-type serine-2 limits Stx17 interactions. Conversely, it was observed that the charge mutant, Stx17[ED3-6K], exhibited a slight reduction in FRET efficiency in the binary

complex, suggesting that this motif contributes to the regulation governed by the phosphorylation status of serine-2, perhaps by facilitating regulatory interactions or by aiding kinase recognition. These findings indicate that the N-peptide of Stx17 can negatively regulate SNARE complex formation and that localised dephosphorylation of serine-2 may be a 'master switch' to enable its precise spatiotemporal control.

It is apparent that the Stx17 N-peptide motif has a role in Stx17 reactivity, but it remains unclear how it inhibits SNARE complex formation. Figure 5.4 suggested that electrostatic interactions with VPS33A domain 1 could mediate this, though it is also conceivable that the N-peptide alternatively facilitates self-association of Stx17 into a closed conformation or that the N-peptide drives associations with other regulatory proteins. For example, Atg14 has also been shown to interact with Stx17 in a manner that promotes autophagosome-endolysosome fusion[253]. To assess the role of both regulatory proteins in the inhibition of SNARE complex formation, figure 5.6 presents FLIM-FRET carried out with Atg14 and VPS33A in the presence of the Stx17 N-peptide mutants. As panels a-c show, FLIM-FRET confirms an interaction between Atg14 and Stx17 *in situ*, which is largely restricted to punctate structures. However, this interaction is unaffected by mutations to the N-peptide of Stx17, suggesting that Atg14 is not involved in the negative regulation of SNARE assembly, and further emphasising the specificity of these mutants in dissecting interactions with VPS33A. Conversely, and also in contrast to the reduction in Stx17[S2E] interaction with SNAP29 or VAMP7, FRET between VPS33A and wild-type Stx17 on pre-fusion autophagosomes is *increased* significantly for Stx17[S2E] alone (figure 5.6d-f), with a FRET efficiency integral of 0.030 compared to 0.008 for Stx17[WT]. This increased interaction leads to an increase in the accumulation of VPS33A on punctate structures (figure 5.6d). Together with the structural analysis of VPS33A that indicates a potential binding pocket for the N-peptide of Stx17, these data suggest that VPS33A inhibits Stx17 interactions with its cognate SNAREs *via* association with the Stx17 N-peptide motif.

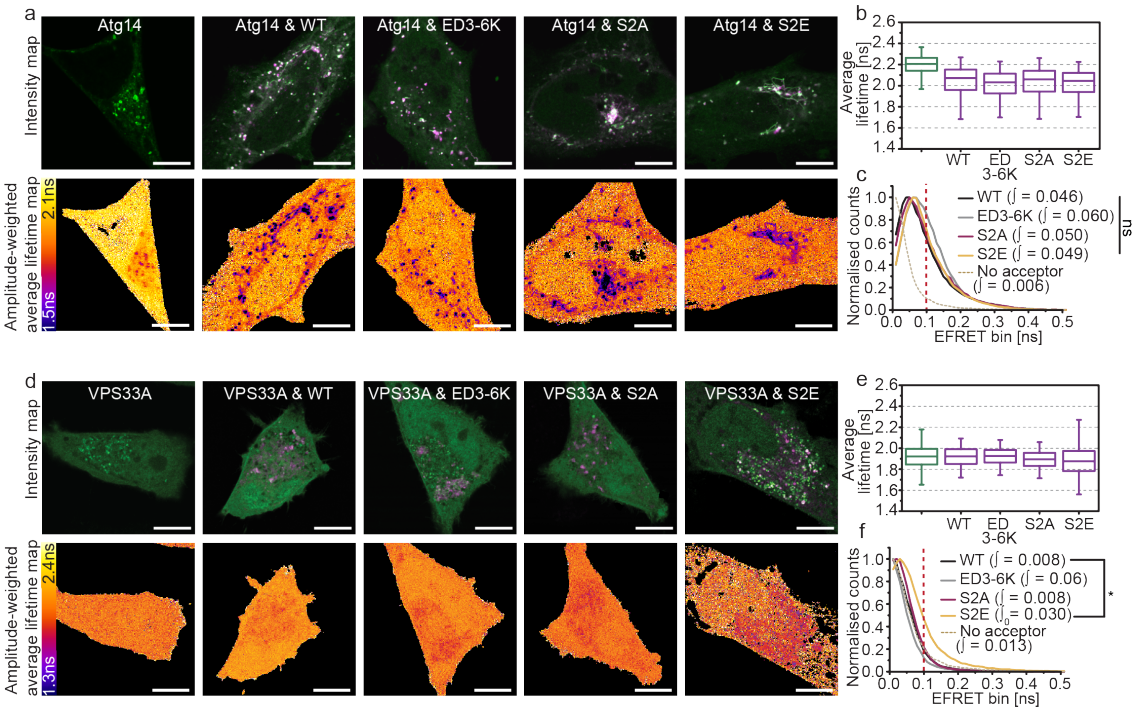

Figure 5.6 VPS33A and Atg14 interactions with Stx17 mutants (**a**) Representative intensity (top row) and fluorescence lifetime (bottom row) maps of autophagic HeLa cells expressing Atg14-EGFP alone or with wild-type or mutant Stx17 as indicated. (**b**) Boxplots of all single pixel fluorescence lifetimes represented in (a), accumulated from four cells. (**c**) FRET efficiency histograms calculated using each of the single pixel fluorescence lifetimes presented in (b). Integrated values above 0.1 were tested for statistical significance using a one-tailed unpaired two-sample t-test [n=4]. (**d**) Representative intensity and fluorescence lifetime maps of autophagic HeLa cells treated with Baf A_1 to isolate pre-fusion autophagosomes. Cells express VPS33A-EGFP alone or with wild-type or mutant Stx17 as indicated. (**e-f**) Equivalent fluorescence lifetime boxplots and FRET efficiency histograms generated as for (b-c) quantifying the data presented in (d). Scale bars are 10 µm throughout.

Cells expressing the phosphomimetic mutant of Stx17 may be expected to exhibit blocked autophagic flux due to the inability of this mutant to assemble into a SNARE complex. Surprisingly however, figure 5.7, which shows colocalisation of LC3-EGFP with each variant of Stx17-mCherry, indicates that this is not apparent. As shown in figure 5.7a-c, cells co-expressing LC3-EGFP and Stx17[S2E]-mCherry reported LC3 puncta densities comparable to cells expressing wild-type Stx17. Moreover, LC3 puncta accumulated upon Baf A_1 treatment, indicating that the fusion event was not previously blocked (figure 5.7d). As these studies were carried out in cells expressing endogenous wild-type Stx17, it may be that endogenous SNAREs enabled normal fusion.

Importantly, I also found that LC3 and Stx17 puncta concentrations did not accumulate to wild-type levels upon Baf A_1 treatment for both Stx17[ED3-6K] and Stx17[S2A] (figure 5.7b-c). This resulted in an unchanged correlation between the probes when fusion is chemically inhibited (figure 5.7d), indicative of disrupted autophagosome clearance in cells over-expressing the non-phosphorylatable N-peptide charge mutants of Stx17. To reconcile this finding with the apparent interaction of these mutants with SNAP29 and VAMP7 (figure 5.5), I hypothesise that N-peptide phosphorylation prevents premature SNARE associations that perturb LC3 delivery to the lysosome. Stx17 may, for example, adopt a phosphorylation-dependent 'closed' conformation equivalent to the structure of monomeric Syx1A[48]. The accumulation of puncta in VPS33A knockdown cells (figure 5.2) may therefore indicate an accumulation of closed-conformation Stx17, suggestive of a role for VPS33A in conversion to the open conformation. As a component of the HOPS tethering complex, it is conceivable that VPS33A is required to draw Stx17 close to the endolysosomal membrane where localised dephosphorylation occurs. The phosphatase involved remains to be determined, but these findings suggest that the endolysosomal membrane may be a suitable location to search.

5.3.2 Stx17 recruitment

In nutrient replete cells, Stx17 is largely localised to the ER membrane due to the ER retention sequence encoded at its C-terminal[248]. It was therefore a surprising observation in the studies that identified Stx17 as the autophagosomal SNARE, that it was being apparently recruited largely from the cytosol to fully-formed autophagosomes[248]. This raises questions as to how Stx17 is solubilised, how it transitions into a membrane-integrated state and how it is targeted. Conflicting studies suggest Stx17 is instead recruited during phagophore nucleation at ER-mitochondrial contact sites upstream of Atg14, an early autophagy protein that targets the PI3K class III complex to the ER[175]. This alternative model suggests that Stx17 is recruited to the phagophore prior to closure and implicates the ER as the recruitment source. The confirmed interaction between Stx17 and Atg14 (figure

5.6) does not clarify when, or how Stx17 is recruited, because Atg14 is proposed to interact with Stx17 both during phagophore nucleation[158] and autophagosome clearance[253].

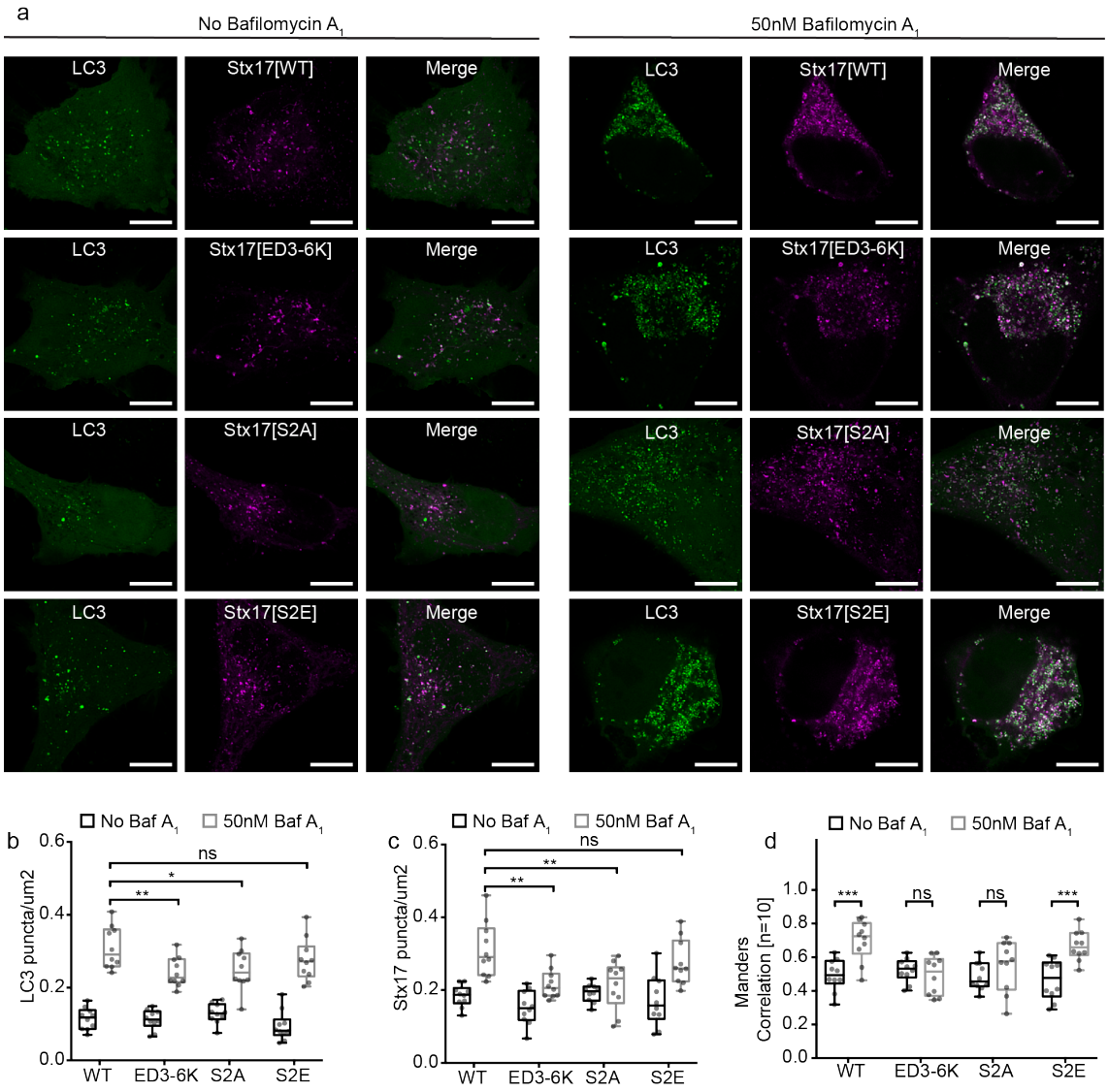

Figure 5.7 Mutant Stx17 colocalisation with LC3 (**a**) Representative single channel and merged images of autophagic HeLa cells expressing LC3-EGFP and the variant of Stx17-mCherry indicated. Both fusion-competent cells (left panel) and Baf A_1 treated cells with inhibited autophagosome-endolysosome fusion (right panel) are displayed. Scale bars are 10 µm. (**b-c**) Boxplots of the LC3-EGFP (c) or Stx17-mCherry (d) puncta concentration per cell in the presence and absence of Baf A_1. (**d**) Boxplots of Manders correlation coefficient to quantify colocalisation between channels in (a). Statistical significance tested with unpaired two-sample t-tests throughout [n=10].

It is possible to investigate the stage of Stx17 recruitment based on the presence of Stx17 in the lumen of the autophagosome. However, this requires knowledge of

how Stx17 integrates into the membrane and which side of the membrane the polypeptide termini reside on. As Stx17 is a SNARE that uniquely encodes two TMDs[46] and autophagosomes are unique vesicles in having two membrane bilayers, it may be hypothesised that Stx17 passes through both membranes. However, published work suggests that the two TMDs instead fold into a hairpin configuration that inserts into one membrane bilayer[248] such that both termini and the soluble bulk of the protein reside on the same side. I established a novel *in situ* FLIM-FRET assay, depicted in figure 5.8a, to verify that the TMDs form a hairpin structure rather than pass through both bilayers. By labelling Stx17 with mCherry at the N-terminus and EGFP at the C-terminus, FRET will be reported if the TMDs hairpin, but not if they pass through both membranes. This dual-labelled probe presented the same punctate distribution as the other Stx17 probes (figure 5.8b). In support of the hairpin model, EGFP from dual-labelled Stx17 reported median fluorescence lifetimes 284 ps and 230 ps, or 14.1% and 11.7%, less than Stx17-EGFP expressed alone or with (separate) Stx17-mCherry respectively (figure 5.8c), the latter indicating that this is not simply a clustering effect of oppositely oriented Stx17. Furthermore, truncation of Stx17 to form the mutant, Stx17[TMD], by removal of the SNARE domain, Habc domain and N-terminal sequence, further enhanced the reduction in fluorescence lifetime by bringing the probes into closer proximity (figure 5.8b-c). The resultant FRET efficiency distributions for dual-labelled Stx17[WT] and Stx17[TMD] reported integrals of 0.14 and 0.22, which are significantly greater than 0.03 reported for Stx17-EGFP co-expressed with Stx17-mCherry (figure 5.8d).

As the data in figure 5.8 confirm that Stx17 'hairpins' into the membrane, recruitment of Stx17 prior to phagophore closure can be assayed by labelling Stx17 on either terminus with a probe sensitive to the luminal environment. Unfortunately, however, little is known about the internal environment of the autophagosome and how it may be differentiated from the cytoplasm. I speculated that as an enclosed compartment, potentially arising from the ER, there is opportunity in the autophagosome for the concentration of calcium ions, which would diffuse quickly and be buffered in the cytoplasm, where the Ca^{2+} concentration is accepted to be approximately 100 nM[433].

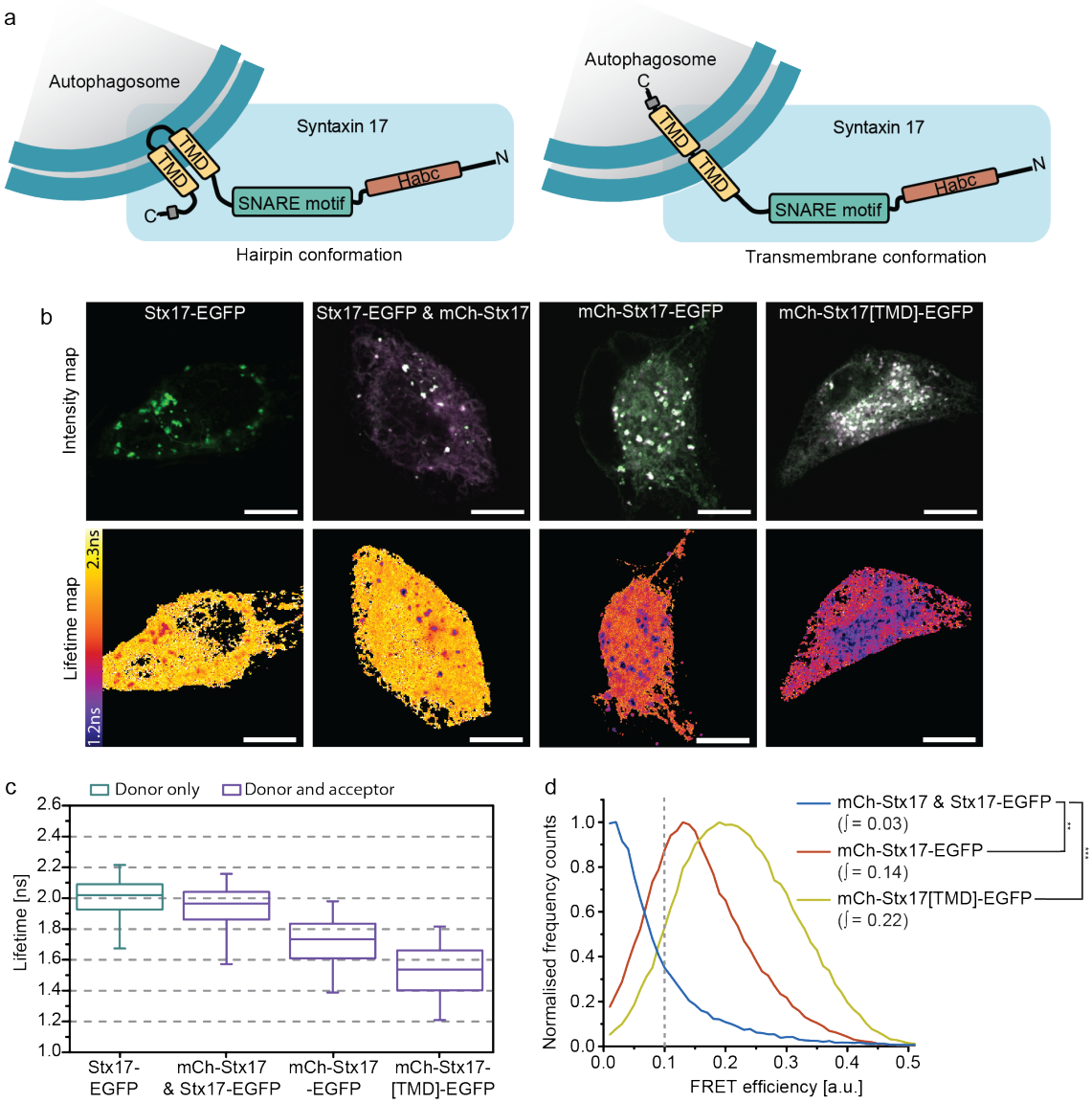

Figure 5.8 Stx17 transmembrane domains form a hairpin configuration (**a**) Cartoon depicting Stx17 with a hairpin conformation (left) or a transmembrane conformation (right); image is not to scale. (**b**) Intensity (top row) and fluorescence lifetime (bottom row) maps of autophagic HeLa cells expressing the construct(s) indicated. Scale bars are 10 µm. (**c**) Boxplots of single pixel fluorescence lifetimes represented in (b) accumulated from four cells. (**d**) FRET efficiency histograms derived from the single-pixel data in (c). Integrated values above 0.1 were tested for statistical significance using a one-tailed unpaired two-sample t-test, [n=4].

To test this hypothesis, cDNA encoding Stx17 was fused to that for the encodable calcium sensors, G-GECO1.1 or R-GECO1, created by Zhao *et al*[434]. These probes have a fluorescence output (the product of their extinction coefficient and quantum yield; see section 2.1.12) of 0.6 and 0.72 mM cm^{-1} in the calcium unbound

state or 15.6 and 10.2 mM cm^{-1} in the calcium bound state, respectively, resulting in a 26-fold and 16-fold increase in fluorescence intensity upon calcium binding[434]. For comparison, EGFP and mCherry have a fluorescence intensity of 34 and 16 mM cm^{-1}, respectively[298]. As both probes have a dissociation constant greater than the sub-nanomolar cytoplasmic Ca^{2+} concentration, of 618 nM for G-GECO1.1 and 482 nM for R-GECO1[434], respectively, there will be low quantum yield if the probes are exclusively localised on the cytosol-facing outer autophagosomal membrane. In figure 5.9, colocalisation analysis was carried out between Stx17-G-GECO1.1 or Stx17-R-GECO1 and LC3. Consistent with a population of probes that are not cytosol-facing, strong punctate signal was detected for both Stx17-G-GECO1.1 and Stx17-R-GECO1, which colocalised significantly with LC3 (figure 5.9). This suggests that some Stx17 is resident on the inner autophagosomal membrane, indicative of recruitment prior to phagophore closure.

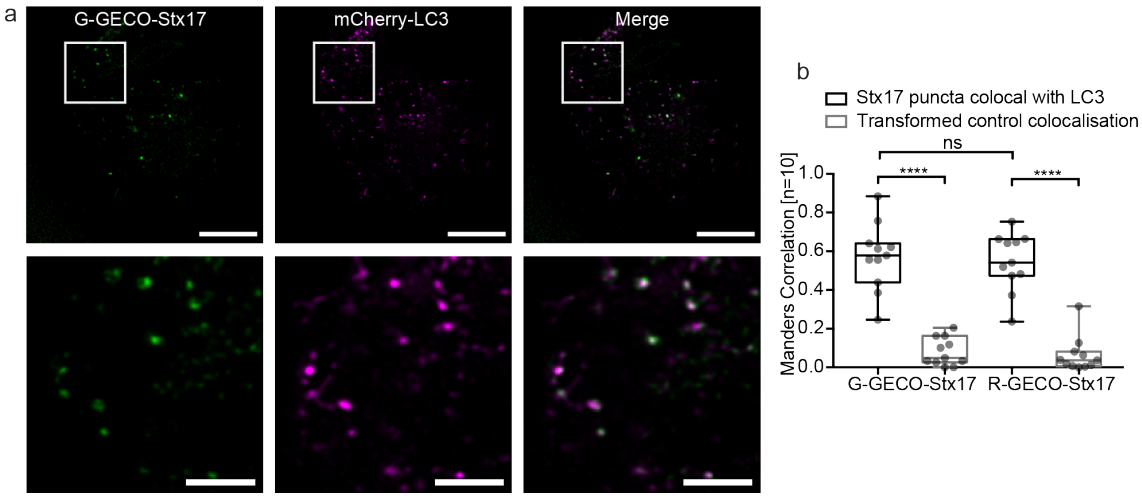

Figure 5.9 Stx17 exists inside a discrete compartment (**a**) Representative single channel and merged images of autophagic HeLa cells co-expressing Stx17-G-GECO and LC3-mCherry. Scale bars are 10 µm for full field (top row) and 3 µm for enlarged indicated region (bottom row). (**b**) Boxplots of Manders correlation coefficients to quantify colocalisation of the dataset represented in (a) in addition to Stx17-R-GECO colocalisation with LC3-EGFP. Statistical significance was determined with a paired two-sample t-test, [n=10]. All data was acquired by live CLSM with a PMT detector (Hamamatsu, R9624) with a gain setting of 750-800 V.

It cannot be discounted that the punctate GECO-Stx17 fluorescence observed is actually from densely packed low quantum yield Stx17-conjugates probes, present on the outer autophagosomal membrane. Therefore, to further explore the

possibility that a population of Stx17 resides on the inner autophagosomal membrane, figure 5.10 presents colocalisation studies carried out on dual-labelled Stx17. As EGFP is known to be sensitive to the lysosomal environment, while mCherry demonstrates resistance[346], luminal mCherry-Stx17-EGFP in pre-fusion autophagosomes will likely report both signals while post-fusion autolysosomes report mCherry signal alone, as overviewed in figure 5.10a. As can be seen in figure 5.10b, mCherry-only puncta were detected in autophagic HeLa cells expressing dual-labelled Stx17. Furthermore, reversing the fusion orientation of the probes had no affect on this result, indicating that a post-translational cleavage event is not the cause. By comparison, mCherry-only puncta were not detected in cells expressing the non-fusogenic mutant, Stx17[TMD]. Colocalisation of the probes to quantify this effect, demonstrates a high correlation in signal for Stx17[TMD] that is significantly reduced for wild-type dual-labelled syntaxin (figure 5.10c). However, unlike dual-labelled LC3 (figure 4.2), the mCherry puncta do not accumulate to numbers significantly greater than for EGFP puncta (figure 5.10d); this likely hints at the different dissociation or recycling kinetics of outer membrane autolysosomal Stx17 and LC3.

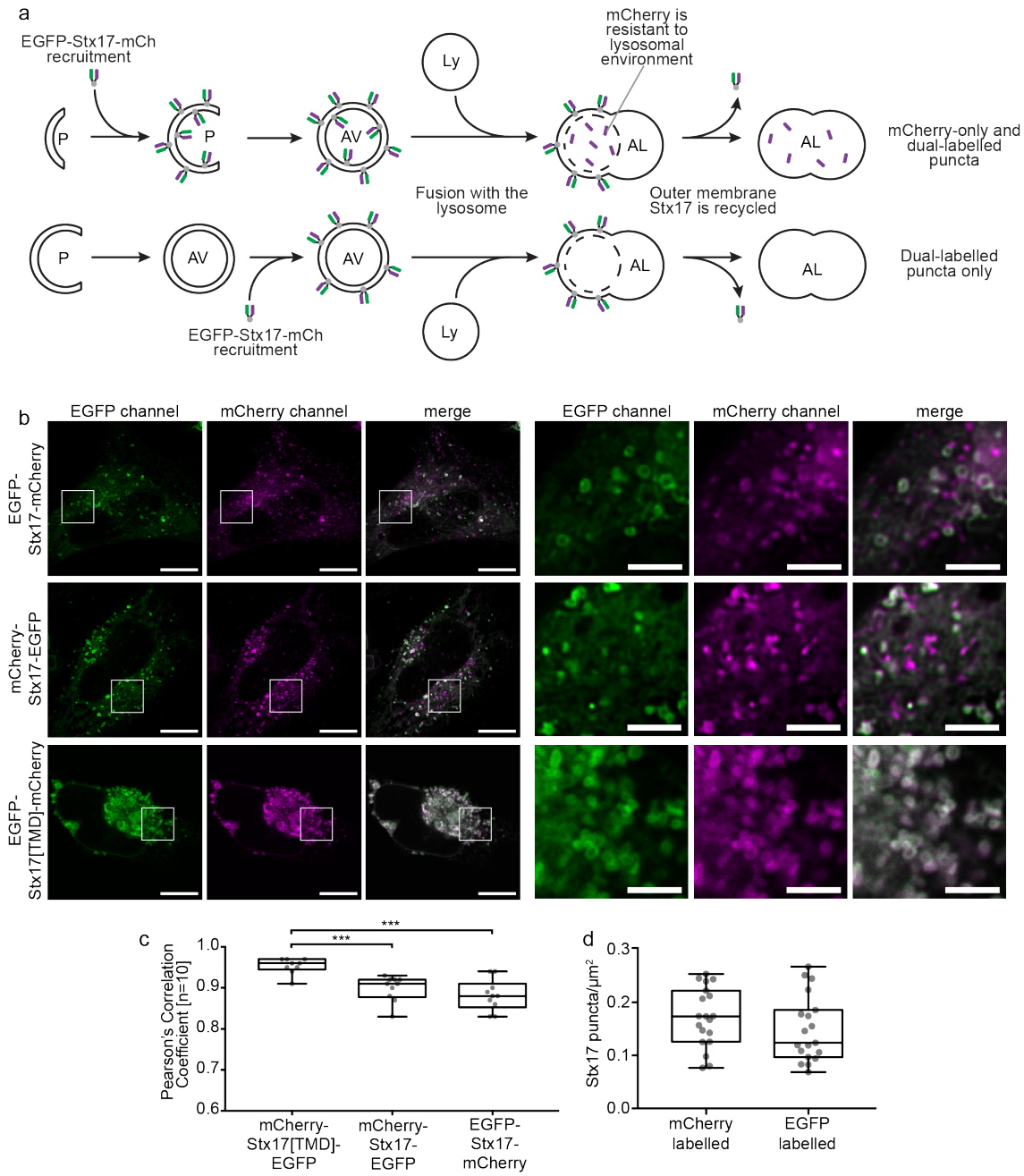

Figure 5.10 mCherry-only puncta present in dual-labelled Stx17 images (**a**) Cartoon illustration of the possible lifecycles of dual-labelled Stx17 on autophagic membranes, both if it is recruited prior to phagophore closure (top row) or following closure (bottom row); membranes indicate a phagophore (P), autophagosome (AV), lysosome (Ly) and autolysosome (AL). (**b**) Representative single channel and merged images of autophagic HeLa cells expressing either EGFP-Stx17-mCherry, mCherry-Stx17-EGFP or EGFP-Stx17[TMD]-EGFP as indicated. Scale bars are 10 μm for full field (left) and 3 μm for enlarged image of indicated region (right). (**c**) Boxplots of Pearson's correlation coefficients to quantify the correlation of signal in the dual-labelled images represented in (a), [n=10]. Statistical significance determined with an unpaired two-sample t-test. (**d**) Boxplots of the syntaxin puncta concentration per cell detected in each channel; data combined from EGFP-Stx17-mCherry and mCherry-Stx17-EGFP [n=20].

Figure 5.10 suggests that luminal inner-membrane Stx17-EGFP is hydrolysed in the autolysosome and outer-membrane Stx17 is recycled. To confirm this is the case, colocalisation studies were carried out, presented in figure 5.11, to determine the correlation between Stx17-EGFP or -mCherry puncta with LC3 and LAMP1 markers of autophagic vesicles and lysosomes respectively. Consistent with the previously presented data, figure 5.11 shows that Stx17-EGFP is recruited to autophagic vesicles but colocalises poorly with the lysosomal marker, LAMP1, suggestive of lysosomal degradation. Stx17-mCherry on the other hand, colocalises well with both markers, indicative of its persistence on the autolysosomal membrane. Taken together, it is apparent from these findings that Stx17 is recruited to the phagophore prior to closure. This early recruitment of Stx17 highlights the importance of the inhibitory regulatory mechanisms identified in section 5.3.1, to prevent ectopic SNARE assembly and premature membrane fusion events.

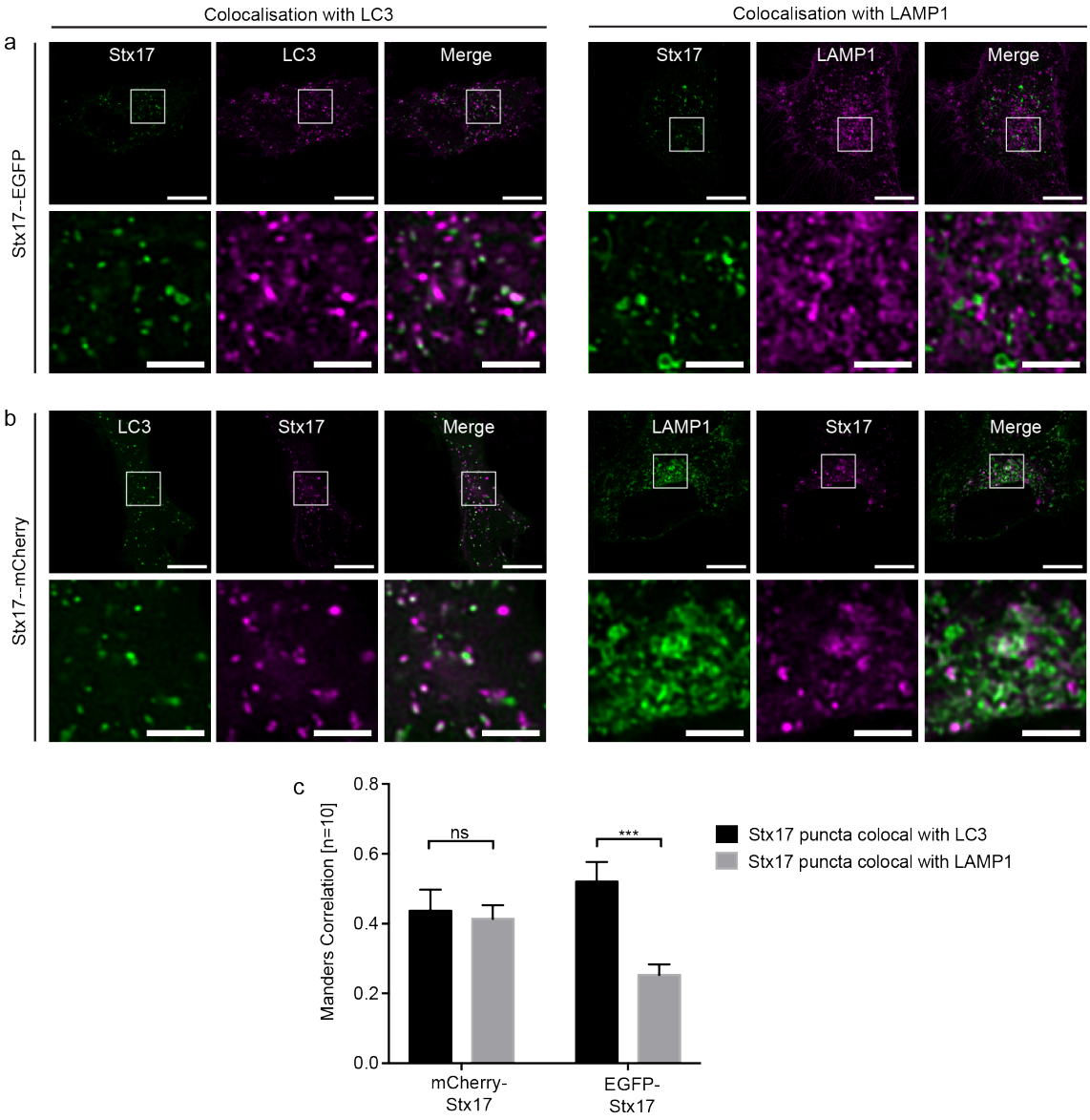

Figure 5.11 Stx17-EGFP colocalises poorly with lysosomes (**a-b**) Representative single channel and merged images of autophagic HeLa cells co-expressing either Stx17-EGFP (a) or Stx17-mCherry (b) with the autophagosomal compartment marker, LC3 (left panels), or the lysosomal compartment marker, LAMP1 (right panels). Scale bars are 10 μm for full field (top row) and 3 μm for enlarged image of indicated region (bottom row). (**c**) Barcharts reporting Manders correlation coefficient values to quantify the colocalisation in datasets represented in (a) and (b). Statistical significance determined using an unpaired two-sample t-test, [n=10].

5.4 Discussion

The HOPS complex reportedly facilitates autophagosome-endolysosome fusion[176] in a manner dependent on the Stx17-binding SM protein VPS33A[177, 414]. Based on our understanding of SM-SNARE interactions (overviewed in section 1.2.3), this is likely achieved by stabilisation of the SNARE core complex. Indeed, VPS33A has a tertiary structure with a conserved binding cleft that may accommodate the four helices of the *trans*-SNARE complex coiled coil[404, 411], consistent with other SM proteins[96, 402, 403, 405]. However, to date, it has not been experimentally demonstrated that VPS33A promotes fusion by facilitating SNARE assembly. This was demonstrated here using FLIM-FRET studies in VPS33A knockdown cells to determine the importance of VPS33A for SNARE complex formation. Consistent with published hypotheses, VPS33A was found to be essential for SNARE assembly (figure 5.2).

Contrary to the role of VPS33A in *facilitating* autophagosome-endolysosome fusion, my *in situ* FLIM-FRET interaction studies presented in figures 5.5 and 5.6 demonstrate that a mutant N-peptide phosphomimetic form of Stx17, which has increased VPS33A interactions, cannot bind its cognate SNAREs, indicative instead of an *inhibitory* role for the SM protein. Similar discrepancies over the regulatory role of the exocytic SM protein, Munc18-1, were reconciled by the finding that Munc18-1 uses multi-modal regulation to both inhibit ectopic SNARE assembly away from the fusion site and to promote SNARE assembly at the fusion site[408]. Importantly, however, VPS33A has been categorised a class II SM protein based on its proposed poor affinity for monomeric syntaxin[404], an interaction that would be required to actively inhibit its association with other SNARE proteins. This classification was based largely on structural comparisons of VPS33A and other SM proteins, which demonstrated that the conserved binding pocket for syntaxin N-peptide 'DRT' motif associations is blocked[411]. However, Stx17 does not have the DRT N-peptide motif conserved by a subset of syntaxin family members[409]. Furthermore, as figure 5.4 shows, VPS33A has a uniquely positive binding surface in the same region, which could enable binding of the highly negative N-peptide of Stx17.

In the case of Syx1A and Munc18-1, the SM protein selectively promotes the fusogenicity of cognate SNAREs in an N-peptide-dependent manner[95]. Conversely, the data presented here suggest that N-peptide binding mediates the inhibitory interaction of VPS33A with Stx17. Reduced associations between Stx17 and its cognate SNAREs were noted for the N-peptide phosphomimetic mutant of Stx17 alongside enhanced VPS33A interactions. As phosphate groups are highly negative[5], the detected increase in Stx17[S2E] association with VPS33A (figure 5.6) is likely mediated by enhanced interaction with the positively charged predicted N-peptide binding surface of VPS33A (figure 5.4). This hypothesis presents an interesting evolutionarily conserved structure-function relationship that diverges within the syntaxin family in the mechanism of its action: for example, the Syx1A N-peptide identifies a specific binding pocket in Munc18-1, whereas the structure-position analogous pocket in VPS33A is blocked, but apparently functions through electrostatic interaction with Stx17. Moreover, expression of the phosphonull mutant of Stx17 abolishes the observed phosphomimetic inhibition of SNARE assembly, identifying phosphorylation of serine-2 as a 'master switch' between the role of VPS33A in facilitating or inhibiting the autophagic SNARE complex formation. Such a switch may also couple autophagosome clearance to intracellular ATP levels, providing a means to swiftly terminate autophagy upon energy replenishment. Interestingly, this may be a conserved mechanism, as casein kinase II phosphorylation of Syx1A serine-14 has also been shown to modulate N-peptide interactions with Munc18-1[435].

As previously noted, the proposed inhibitory interactions of the Stx17 N-peptide with VPS33A diverge from the SNARE-assembly-promoting interactions of 'DRT' encoding syntaxin N-peptide motifs[408, 409]. Interestingly, the Stx17 N-peptide shows some similarity to other syntaxin family members, namely Stx6 and Stx10, which both contain a *N*-MSXED-*C* sequence and consensus for serine-2 phosphorylation (figure 5.4). It could therefore be speculated that there are indeed two divergent classes of SM proteins as previously proposed[404]; however, rather than differing in their N-peptide binding ability, I propose that they differ in their N-peptide binding method and the regulatory outcome of this association. I discuss further, below, the specific implications of this proposed paradigm for autophagy.

Increased FRET efficiency is observed between VPS33A and wild-type Stx17 when both are labelled at the N-terminus, rather than at the N- and C-terminus respectively (figure 5.3). As FRET efficiency is reduced in proportion to the sixth power of the distance between fluorophores[278], it is highly sensitive to probe separation. This configuration dependence of FRET may therefore allude to a close association between the N-terminal peptide of Stx17 and the N-terminal domain 1 N-peptide binding region of VPS33A. The FLIM-FRET observed was highly localised to Stx17 puncta and therefore low FRET efficiency values outwith these regions dominated. Therefore, based on the conflicting inhibitory and facilitative roles of VPS33A for autophagy and the known multi-modal regulation of SM proteins in other fusion events, and notwithstanding the FRET efficiencies noted, I suggest that VPS33A remains associated with Stx17 upon serine-2 dephosphorylation to assist SNARE assembly.

In summary, I propose that as Stx17 has a well-characterised ER localisation in nutrient replete cells[46], the transmembrane domains of Stx17 are most likely integrated into the ER membrane in a hairpin configuration (figure 5.8) upon translation. Stx17 is subsequently phosphorylated, likely by casein kinase II, and maintains an inactive conformation, probably by self-association of its Habc and SNARE domains like other syntaxins. Given the apparent recruitment of Stx17 to the phagophore membrane while it is continuous with the ER membrane (figures 5.9-5.11) and the depletion of ER Stx17 in autophagic cells (figure 4.4), Stx17 likely translocates to ER phagophore nucleation sites where it transfers to the nascent autophagosome prior to closure. The non-reactive, 'closed' (by analogy with other syntaxin-SM protein interaction) conformation of Stx17 precludes ectopic fusion but enables association with VPS33A *via* the N-peptide. The VPS33A-associated HOPS complex tethers autophagosomal Stx17 to the endolysosomal membrane, enabling local dephosphorylation of serine-2 at the fusion site. This weakens both N-peptide association of VPS33A and the closed conformation of Stx17, allowing Stx17 to open and the SNARE complex to form, which is subsequently stabilised by VPS33A binding of the SNARE bundle. Stx17 remains associated with the HOPS complex during SM-SNARE binding mode transitions, perhaps *via* the reported VPS33A-independent association of VPS11 and VPS18 with the newly exposed

Habc domain of Stx17[404]. This proposed mechanism of multi-modal regulation is summarised in figure 5.12.

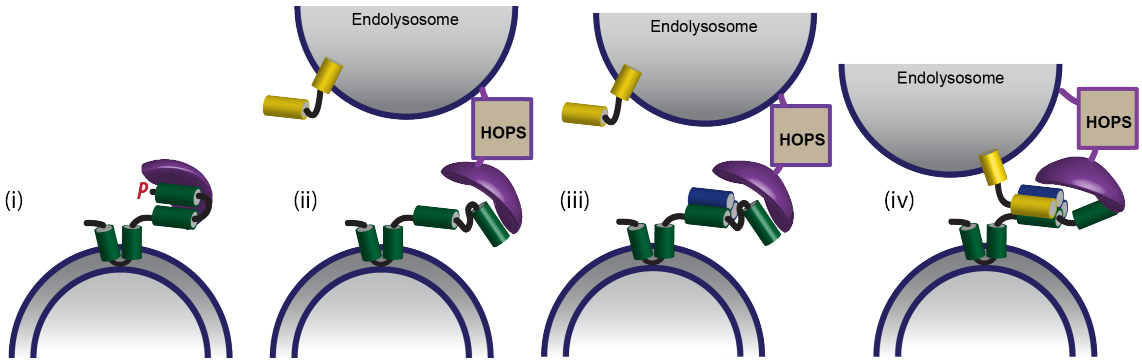

Figure 5.12 Proposed model of VPS33A regulation of autophagosome clearance Syntaxin 17 (green) and VPS33A (purple) interact *via* two distinct binding modes dependent on the phosphorylation status of serine-2 at the N-terminal of Stx17. (i) Phosphorylated Stx17 binds strongly with VPS33A in a closed conformation, precluding SNARE complex formation. (ii) Dephosphorylation of Stx17 at the fusion site weakens VPS33A N-peptide binding and the inhibitory self-association of closed Stx17. This enables step-wise SNARE interactions with Stx17's cognate SNARE proteins. (iii) SNAP29 (blue) interacts to form the binary Q-SNARE complex, followed by (iv) the endolysosome-resident VAMP7 (yellow), which is held in close proximity due to the tethering activity of the VPS33A-associated HOPS complex. The complete *trans*-SNARE ternary complex is then bound by VPS33A, which stabilises the core SNARE bundle to enable fusion to be completed.

It remains to be clarified if and how VPS33A inhibits SNARE assembly outwith the fusion site. As an integral part of the HOPS and CORVET tethering complexes[413], VPS33A is largely reported as residing on endosomal membranes. However, in my hands, the over-expression of VPS33A-EGFP produced a dominant cytosolic population, raising the possibility that VPS33A may function elsewhere in the cell. Surprisingly, VPS33A did not appear to aggregate on punctate structures, except in the presence of Stx17[S2E] over-expression; however, local reductions in fluorescence lifetime indicate interaction between VPS33A and punctate Stx17.

This highlights the advantages of fluorescence lifetime imaging alongside standard microscopy techniques. Despite these advantages, FLIM is infrequently used due to the limitations it imposes on acquisition speed and the complexities of FLIM-FRET

data interpretation. The next chapter therefore explores a new technology to enable faster fluorescence lifetime imaging for the study of dynamic protein interactions.

CHAPTER SIX:

Advancing techniques for real-time FLIM-FRET

6.1. Introduction

Time-domain FLIM offers the most accurate measure of fluorescence lifetime but requires specialist lasers, detectors and electronics to do so[436]. For TCSPC, detectors operating in photon counting mode are coupled with pulsed laser excitation and counting electronics to precisely time single photon arrival following rapidly triggered excitation events[436]. However, the complexity of the detectors restricts commercial TCSPC FLIM platforms to single channel detection, requiring pixel-by-pixel single photon counting[437]. It is therefore an inherently slow process to accumulate the minimum 1,000 photon counts per pixel that was found in section 2.5.2 to be required for accurate bi-exponential decay fitting. This limits TCSPC FLIM-FRET to fixed sample analysis, precluding the investigation of dynamic processes such as the longevity of the autophagosomal SNARE complex. Where faster measurements are required, rapidly time-gated cameras can be used in widefield to sample the intensity profile of the decay, achieving speeds up to 100 Hz but at the significant cost of lifetime accuracy[438]. A new technology is therefore sought to translate TCSPC to a camera-based detection format, which would provide the ideal FLIM camera, incorporating the high speed of time-gated detection with the temporal resolution and single photon sensitivity of single-channel devices.

6.1.1 Single pixel TCSPC FLIM detectors

To generate a fluorescence decay that accurately represents the decay kinetics of the fluorophore, and therefore the fluorescence lifetime, TCSPC detectors must be able to detect single photon events with high temporal resolution. As each component of the detection system requires time to carry out its function, there is a delay between photon arrival and signal output[267]. This would be a trivial problem if the delay were discrete and constant, however timing jitter contributes to variation in the timing delay as described by the transit time spread (TTS)[267]. For any detection system, temporal resolution can be experimentally measured as the FWHM of the instrument response function (IRF) obtained by fluorescence

lifetime measurements of scattered excitation light or emission from ultra-fast lifetime fluorophores[439].

Photomultiplier tubes (PMTs), avalanche photodiodes (APDs) and hybrid detectors, which incorporate a PMT front-end and APD amplification, can all be operated in photon counting mode and achieve single photon sensitivity at high temporal resolution[267]. PMTs use a photocathode to convert a single photon to a photoelectron[440]. This is shuttled to the anode through either a series of dynodes[440] or a microchannel plate (MCP) containing an array of glass capillaries[441] for electron amplification by impact ionisation. As MCPs have narrow capillaries, electrons are more likely to follow the same path, thereby reducing the TTS and improving their time-resolution compared to dynode PMTs[267]. APDs work in a similar way, but are semiconductor based, composed of a positive p-doped region adjacent to a negative n-doped region. At this p-n junction, a neutral depletion layer forms due to the exchange of charge carriers[442]. By applying a reverse biased voltage, current cannot pass through this junction until the reverse breakdown voltage is exceeded by a photon-induced avalanche cascade[443]. A single photon avalanche diode (SPAD) is an APD maintained at a high reverse biased voltage above the breakdown voltage, making it highly sensitive to single photons and useful for TCSPC detection[444].

The single photon sensitivity of both PMTs and SPADs comes at the price of a dead time, a period of insensitivity that follows photodetection prior to reset. This characteristic, which for both detectors typically exceeds the time required for complete fluorescence decay, restricts the useful count rate to below the detector's maximum count rate capabilities to avoid pulse pile up. This therefore further exacerbates the issue of slow-speed acquisition, which is the major limitation of single channel TCSPC detectors. To overcome this, detector multiplexing has been proposed[445, 446], though as yet there are no commercial implementations. An additional limitation unique to photon counting detectors is afterpulsing, where a secondary output pulse to a single photon detection event can contribute to the noise characteristics of the device[447]. However, these spurious pulses are often concealed within the reset time of the detector[447].

SPAD detectors are arguably superior to PMTs for TCSPC and reflecting this, the FLIM-FRET presented in chapters four and five exclusively used a SPAD. For comparison, table 6.1 outlines the specifications of both the PMTs and SPADs on the Leica SP5 SMD CLSM used in my research. In this case, the SPAD detectors were advantaged by higher temporal resolution, higher photon detection efficiency and lower dark count rates (signal output in the absence of a photon) than PMTs. The key disadvantage of a SPAD detector is that to achieve high temporal resolution, the photosensitive area must be small[444]. The SPAD active area diameter is typically on the scale of tens of microns compared to PMTs, which have diameters greater than 10 mm[448]. This requires more complex optical interfacing, but it is in no way a limiting problem. Furthermore, as SPAD electron amplification is not based on electron paths, they are less sensitive to electromagnetic interference and offer a more stable detection device than PMTs[294].

Table 6.1 Comparison of the Hamamatsu R7400U PMT and Micro Photon Devices PDM Series SPAD detectors for the Leica SP5 SMD microscope used for FLIM-FRET studies in the preceding chapters (values provided by the vendor).

Detector	Photon detection efficiency	Time-resolution (FWHM)	Dark count rate	Maximum count rate
PMT	18% at 420 nm	230 ps	>80 Hz	CFD dependent
SPAD	49% at 550 nm	35 ps	5-500 Hz	12 MHz

An alternative and unique approach to TCSPC is offered by streak cameras, which are fully commercialised but typically too expensive for widespread use. Streak cameras spatially deflect photoelectrons in proportion to the time delay relative to the excitation pulse[267]. This technology allows multiple single photon measurements per excitation pulse, extremely high temporal resolution in the order of picoseconds[449] and no dead time for faster scanning regimes[267]. However, they suffer from inherently low detection efficiencies and severely limited temporal detection windows. Fast FLIM has been demonstrated by coupling a streak camera to a multiphoton microscope, producing stacked images with temporal and x,y coordinate information, acquired with a speed of 2 ms per line scan[450]. Alternatively, single pixel scanning can be used to acquire both lifetime and spectral information using a polychromator[451].

6.1.2 Single pixel TCSPC electronics

In addition to the single photon detector, a TCSPC system requires electronics to measure the time delay between the excitation pulse and detector output pulse. A constant fraction discriminator (CFD) is used to identify the output voltage of the detector as a signal pulse event, independent of voltage peak height. A CFD thus provides accurate event discrimination with only 50 ps timing jitter[267]. The first pulse received by the CFD triggers a time-to-amplitude converter (TAC), which begins charging a capacitor linearly over time[452]. The second pulse received by the CFD stops the TAC and the resulting voltage is converted to timing information[452], read out by an analog-to-digital converter (ADC)[267]. The TAC has its own dead time for reset of the capacitor, which can be significantly longer than the desired laser pulse frequency[267]. However, as there are considerably more excitation pulse events than detected photons, time delays caused by TAC reset are commonly avoided by carrying out TCSPC in reverse-mode[453]. In this case, the photon triggers the TAC start signal and the subsequent laser pulse provides the stop signal. Both forward and reverse-mode TCSPC are schematised in figure 6.1 to illustrate these differences.

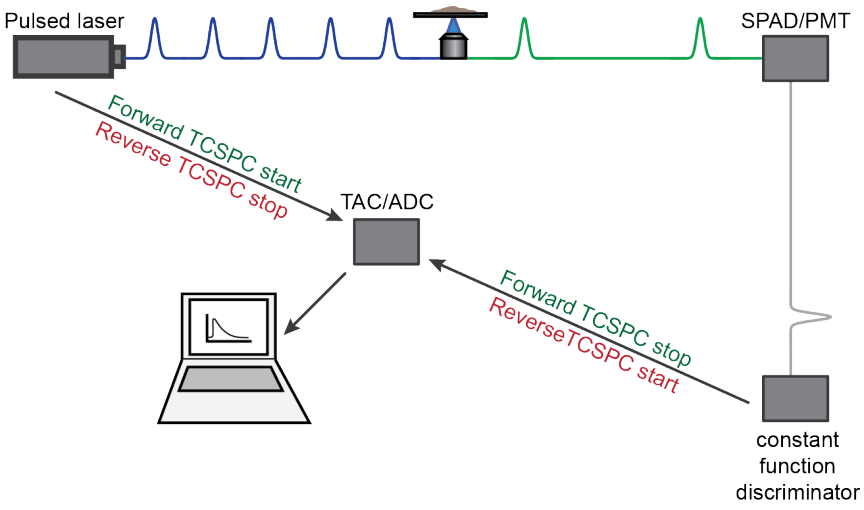

Figure 6.1 Forward and reverse TCSPC A schematic outlining the steps of TCSPC FLIM both in reverse and forward mode. A pulsed laser used to excite the sample additionally signals the time-to-amplitude converter (TAC) to begin timing

(forward mode) or stop timing (reverse mode). A single-channel detector with single photon sensitivity detects the resulting photonic emission and its resulting output pulse is identified with a constant fraction discriminator (CFD). This triggers the TAC timing mechanism (reverse mode) or halts it (forward mode). On the completion of a timing cycle, the amplitude-to-digital converter (ADC) reads out the time-tagged photonic information. Repeated cycles generate a fluorescence decay.

6.1.3 Time gated widefield FLIM

Commercial time-domain widefield FLIM systems are largely restricted to time-gated detection, which typically uses an intensified charged coupled device (ICCD) to sample the intensity of emitted fluorescence at designated time brackets following pulsed excitation[454]. The CCD chip is composed of an array of photodiodes that generate and store electric charge relative to the intensity of incident light during exposure[455]. Photodetection in low light levels is improved in ICCDs by the addition of an image intensifier in front of the CCD chip[454]. Image intensifiers amplify photocathode-generated electrons using two MCPs[456] and convert the amplified signal back into photons *via* a phosphor screen for CCD detection[456]. As the photoelectrons are directed to the capillaries by a negative voltage between the photocathode and the MCP, switching this voltage to positive prevents photoelectron migration, thereby providing a very fast gating switch[454], with commercial detectors typically stating gate widths in the nanosecond range.

Time-gated detection has a number of notable advantages, most prominently are its simplicity, its dependence on standard widefield camera technology, its capacity to record more than one photon per frame and its fast frame rate[436]. Furthermore, it is possible to improve the SNR of time-gated detection by offsetting the detection window approximately 100 ps from the excitation pulse to exclude fast decaying autofluorescence and excitation light scatter[457]. However, the accuracy of the reported fluorescence lifetime is dependent on the gate width in time-gated detection, which typically undersamples the fluorescence decay[436]. Increasing the number of gates improves the temporal resolution[457], but this reduces the photon collection efficiency. Moreover, where time gates are acquired in successive excitation rounds, increased sampling reduces the acquisition speed and increases

photobleaching effects that may skew the data[436]. For these reasons, TCSPC is considered the gold-standard method for time-domain FLIM[436].

6.1.4 Progress towards widefield TCSPC FLIM

A widefield TCSPC FLIM system is not yet commercially available, however a number of recent technological advances have shown promise, including position-sensitive PMTs[458], ultra-fast CMOS imaging[339] and SPAD arrays[338]. Position-sensitive PMTs have an MCP-PMT architecture with a position-sensitive anode to ascertain the coordinates of each detection event[458]. Though these detectors are employed for widefield detection, their architecture restricts them to single photon processing[458]. Different variations of the anode have been proposed[458-460], each providing different spatial resolution and count rates. The delay line anode uses two criss-crossed delay lines to readout position of impact from the time required for the signal to travel through each line[458]. This has produced the fastest count rate at 1 MHz but its poor spatial and temporal resolution of 200 μm and 200 ns respectively[458], preclude its use for live sub-cellular FLIM with common fluorescent proteins.

Ultrafast intensified complementary metal-oxide-semiconductor (CMOS) cameras have accomplished truly widefield TCSPC FLIM[339]. Each CMOS pixel contains its own readout circuitry and therefore the frame rate delays associated with charge transfer-based read out of CCD chips are reduced[339]. By coupling an intensifier with the CMOS camera, single photon counting per pixel can be achieved at high speed following each excitation pulse[339]. The temporal resolution of this detection system is still, however, limited by the frame rate and suited to lifetimes on the microsecond scale[339]. It has been experimentally demonstrated that sub-microsecond time resolution can be achieved by deriving additional information from the phosphor decay of the intensifier[461], but nanosecond timing is not achievable without faster frame rate cameras, precluding the use of ultrafast ICMOS for high-speed FLIM-FRET.

The limitations of other new technologies leave TCSPC SPAD arrays as the most promising new device for widefield TCSPC. These arrays combine the high temporal resolution and high count rates of single channel devices with full-frame detection for rapid imaging[338]. Each pixel of a SPAD array camera contains a single SPAD sensor with integrated timing electronics capable of parallelised time-correlated read out from each independent sensor across the chip[462]. Consequently, this novel technology includes the key characteristics required for widefield TCSPC FLIM-FRET.

6.1.5 The MF32 SPAD array

In this work, a prototype early generation widefield TCSPC SPAD array camera, the MF32, is used to demonstrate the principle of widefield FLIM. The MF32 was developed by Robert Henderson's CMOS Sensors and Systems Group at the University of Edinburgh. It uses a fast gated ring oscillator (GRO) based time-to-digital converter (TDC) for in-pixel TCSPC, which bypasses analog conversion to combine the functions of the TAC and ADC by counting the cycles of a reference clock[462]. This architecture was first proposed in 2009 with a fast 32x16 sub-array test chip[462] that has been extended for the MF32 into a 32x32 pixel array for further characterisation in different applications. The MF32 notably achieves very high frame rates of up to 1 MHz[338]. This fast frame rate is achieved by a split chip architecture whereby each 32x16 sub-array is read out in parallel by sequential row-by-row broadcast to serialiser blocks located at the periphery of the array[338]. Moreover, pixel memory stores one data frame to enable read out simultaneous to acquisition of the next frame[338]. The MF32 has also demonstrated 50 ps temporal resolution, a peak quantum efficiency at 500 nm of 28% and a dark count rate below 50 Hz without cooling[338].

The potential of the MF32 for widefield FLIM has been demonstrated with DNA microarrays excited by TIRFM[463], however, there remain many difficulties to overcome before widespread implementation of SPAD arrays can be achieved. Primarily, the MF32 has a low pixel number with a large 50 μm pitch and a small photosensitive area of 1.1%[462], shown in figure 6.2, providing poor spatial

resolution and photon collection efficiency. Moreover, as each pixel functions as an individual detector, hot pixels and response variation are common across the chip.

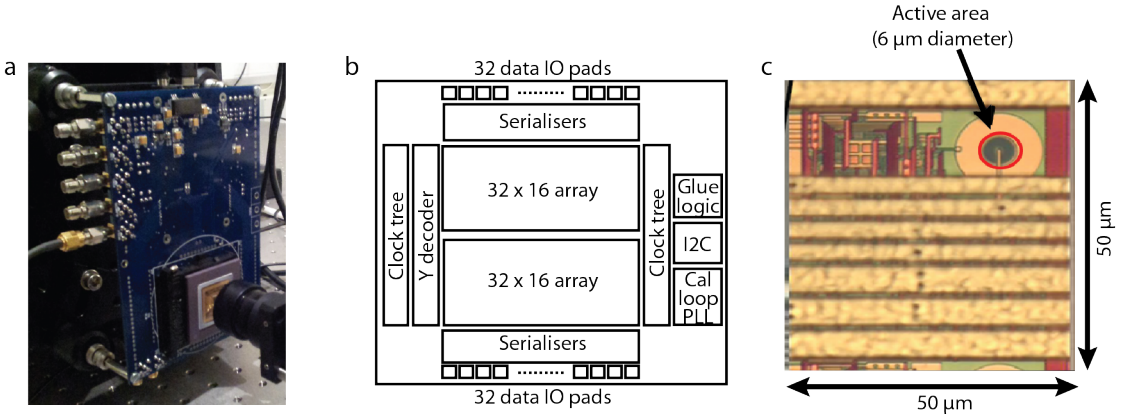

Figure 6.2 MF32 architecture (**a**) Photograph of a microscope coupled MF32 chip on an FPGA board. (**b**) A block diagram of the chip design demonstrating the split read out (diagram by Justin Richardson). (**c**) Micrograph of a single pixel containing SPAD sensor and TDC electronics (taken from Richardson *et al.*, 2009[462]).

Other researchers have previously explored the potential of the MF32 for high-speed FLIM. Most notably, Poland *et al*. have demonstrated fast multiplexed multiphoton TCSPC with an 8 x 8 segment of the MF32[446]. This method uses a diffractive spatial light modulator to generate a focussed beamlet array for multi-beam scanning, achieving frame rates of 10 s with high spatial resolution by using the small active area as a pinhole[446]. Scanned techniques such as this are valuable for live cell imaging and volumetric data acquisition, but require highly advanced optical set ups that are not accessible to a standard biology laboratory. As previously discussed, FLIM-FRET is a largely neglected technique in mainstream biology, possibly due to the requirement for specialist equipment and complexities in data analysis. Simplified set ups using SPAD arrays as plug-and-play cameras for fast widefield fluorescence intensity and lifetime measurements, could therefore facilitate the broader implementation of FLIM-FRET. Additionally, widefield fluorescence lifetime imaging would enable FLIM-FRET measurements in TIRF, with SPIM or at super-resolution with SMLM techniques. The research I present in this chapter therefore aims to investigate the potential of the MF32 for widefield

FLIM-FRET, which to date has not been demonstrated using cells expressing commonly used FLIM-FRET fluorophores. This exploratory work has helped inform the next generation of SPAD array cameras, which are currently under development, funded by the European Research Council's Seventh Framework Programme (grant 339747).

6.2. Materials and Methods

6.2.1. Prism-TIRF build

In this exploratory work, a prism-based TIRF set up was designed to allow prototyping of TIRFM FLIM-FRET using the MF32. Prism-TIRF is analogous in principle to objective TIRF, but does not require a specialised objective lens. The implementation of prism-TIRF on an Olympus iX71 allowed a semi-permanent MF32 set up for extensive characterisation and prototyping work that would not be feasible on the shared and costly commercial objective-based TIRF microscope.

A schematic of the prism-TIRFM design is shown in figure 6.3a, alongside comparative widefield and TIRFM images of QDot 525 nm quantum dots, figure 6.3b-c. As shown in panel a, the light path was directed through a Suprasil prism at an angle no greater than 9.8° from the normal, to achieve an angle of incidence on the slide-mountant interface of 69.9°, as demonstrated by the inset. This angle was calculated to be the critical angle (θ_c) required for TIR by a rearrangement of Snell's law[267],

$$\theta_c = \sin^{-1}\left(\frac{n_r}{n_i}\right) \qquad [6.1]$$

where n_i is the refractive index of the first medium (the quartz slide, 1.544) and n_r is the refractive index of the second medium (Mowiol-488, 1.45). This creates an evanescent field at the interface between the high refractive index quartz slide and the lower refractive index Mowiol-488 mountant[296], as described in section 2.2.2. A pulsed 405 nm laser and a 532 nm continuous wave laser were both included in the TIRF build. The lasers were fibre coupled with single mode fibres using a

power meter (Thorlabs, PM200) to optimise coupling efficiency and the output collimated and aligned. The incident angle was adjusted with a mirror as shown in figure 6.3a. The fluorescent emission was focussed on both the MF32 and a commercial sCMOS (Hamamatsu, C11440-22CU) for reference and comparison using a dichroic mirror to unevenly split the beam such that the MF32 received 90% of the emitted light.

Samples were prepared as described in chapter three on quartz slides or disks so that the cells or quantum dots were at the TIRF interface. The quartz samples were mounted onto coverslips for imaging with a 100x 1.4 NA oil immersion objective lens. As the prism is placed on top of the quartz disk, it was kept on an adjustable arm to move it in and out of the light path with minimal disruption to alignment. The set up was corrected for drift at the start of each experiment. As shown in figure 6.3b, prism TIRF-based illumination successfully excites the test sample, albeit with a restricted field of view and at lower power than the comparative lamp illumination. Based on the following relationship between penetration depth (d) wavelength (λ_{ex}), incident angle (θ_i) and the refractive indices of the first and second media (n_1 and n_2, respectively)[267],

$$d = \frac{\lambda_{ex}}{4\pi}\left(n_1^2 \sin\theta_i - n_2^2\right)^{-1/2} \quad [6.2]$$

a penetration depth of approximately 87 nm using the 405 nm laser or 120 nm using the 561 nm was achieved.

6.2.2 MF32 test set-ups

The MF32 chip was provided on an FPGA board that was connected to the PC via USB 2.0. The MF32 was controlled by a custom-built LabVIEW programme developed by Robert Henderson's group, which provided data output in text file format for further processing. Robert Henderson's group also provided support for FPGA programming throughout the project. The board was mounted with lateral and axial translation mounts to assist optical interfacing. Imaging was carried out either via the aforementioned prism-TIRF microscope or via direct connection of

the single-mode fibre launched laser to the condenser port of the microscope, as no dedicated laser input port was available. Characterisation of the chip was carried out by direct illumination with a defocused beam for near planar coverage unless stated. The laser light was attenuated as required with neutral density filters and the incident power ascertained with a Thorlabs PM800 power meter.

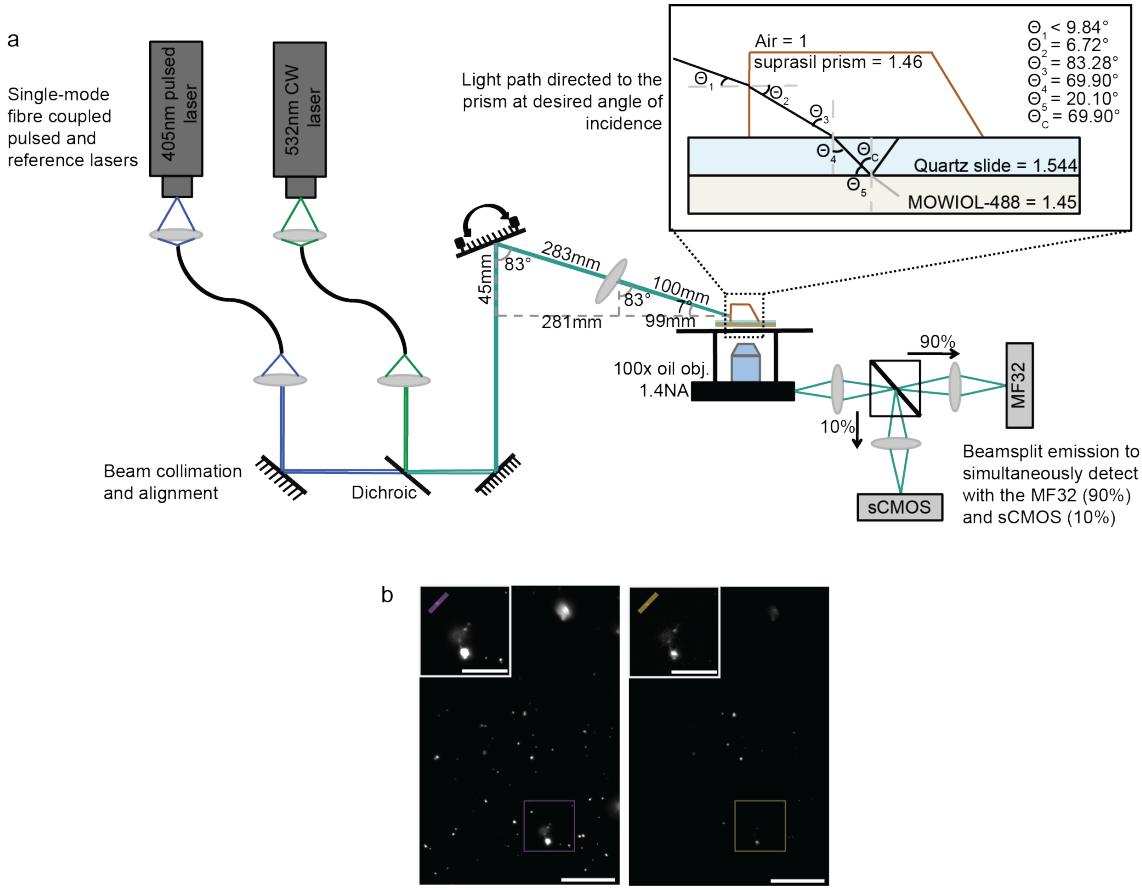

Figure 6.3 Design and characterisation of prism TIRFM (**a**) Schematic of the home-built prism TIRFM set up with calculated light path refraction in the subpanel. (**b**) Comparative images of the same field of quantum dots (525 nm emission maxima) in widefield (left) and TIRF (right). The evanescent field is restricted to a narrow vertical range. The indicated squared region is enlarged in the sub-panel, scale bars are 10 µm at low zoom and 5 µm at high zoom. (**c**) Comparative line profiles through the lines indicated in (b) demonstrating slight improvement in resolution by TIRF.

The MF32 was operated at maximum quench speed to minimise the dead time, which was consequently approximately 100 µs. The breakdown voltage of the detector was set to -14.16 V and the excess bias voltage or the voltage above breakdown was 1.2 V as recommended by Robert Henderson's group. TCSPC was

carried out with a pulsed 405 nm laser (Picoquant, LDH-P-C-405B) driven by a PDL 800-B controller (Picoquant) synchronised to the MF32 via a TTL trigger.

6.3 Results

6.3.1 Characterisation of the MF32 detector in photon counting mode

The MF32 has two imaging modes: photon counting and TCSPC, which allow it to be used as a fluorescence intensity camera or a FLIM camera respectively. Photon counting reports the number of photons accumulated in one pixel per exposure, which must logically have a linear response such that reported photon counts increase in proportion to increases in incident light. This linear response was ascertained for both the MF32 and a commercial CMOS camera (Thorlabs, DCC1545M) for comparison. Each detector was directly illuminated with defocused pulsed 405 nm laser light and counts were captured and averaged across three frames. 1,024 pixel values were integrated and the average pixel value reported as a function of power at various exposures as presented in figure 6.4. For the MF32, signal below 0.01 μW could not be distinguished from background counts (figure 6.4a) indicating its minimum sensitivity. This is notably higher than the minimum sensitivity of the Thorlabs CMOS camera, 0.0001μW (figure 6.4b), which is as expected given the lower photon collection efficiency of the SPAD array due to its 1.1% pixel fill factor and 15-28% quantum efficiency[464]. By comparison, the Thorlabs camera achieves near 100% fill factor and a quantum efficiency of 32-55% across the visible range. The MF32 demonstrates 6-bit saturation (figure 6.4) as expected and the response prior to saturation is largely linear. However, the dynamic range is lower than for the Thorlabs camera and this characterisation study suggests that for photon counting, the detector performs optimally with low exposure at incident power between 0.1-10 μW.

Both shot noise and thermally generated dark counts increase with the square root of the signal or exposure[268]. Therefore, as shown in figure 6.4a, the noise floor increases with exposure, causing a deterioration of the SNR with increased exposure. This promotes the use of a short exposure, accumulating frames where necessary. Based on a 1 s acquisition under dark conditions, the median pixel dark

count rate for the MF32 was calculated as 20 Hz (data collected by Nikola Krstajic, Robert Henderson's group).

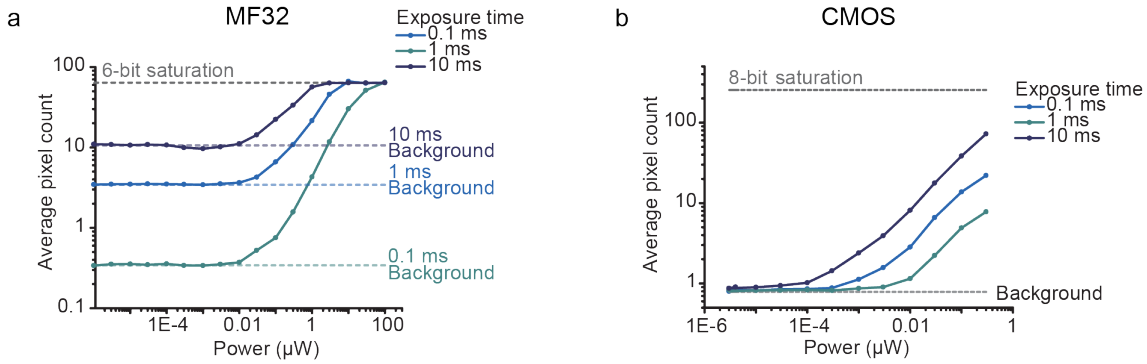

Figure 6.4 Linearity of the MF32 photon counting response Average pixel photon counts over 1,024 pixels directly illuminated with defocused 405 nm pulsed laser illumination for (**a**) the MF32 and (**b**) a commercial CMOS camera (Thorlabs, DCC1545M) as a function of power for three different exposure times.

CMOS cameras contain a number of pixels that either do not respond linearly to light, known as 'hot' pixels, or do not respond at all, 'dead' pixels. These features are common in all commercial CCD and CMOS cameras, but the contribution of these pixels in commercial cameras are often removed by default using median filtering methods. As demonstrated by figure 6.5a-c, which shows the photon counts across the MF32 chip under even illumination with a defocused laser, the pixel response varies notably across the chip. By capturing a long exposure frame with no incident light, it is possible to identify the hot pixels contributing to the fixed pattern noise. This has been done in figure 6.5c, where 4% of the MF32 pixels were identified as hot by defining hot pixels as one standard deviation above the mean signal. This is a high contribution in comparison to the commercial Thorlabs CMOS camera, which is quality controlled to have no more than 0.001% hot pixels[465]. However, the threshold value used for quality control is arbitrary and has not been published for the Thorlabs CMOS camera. Fixed pattern noise can be removed by a background subtraction of an image acquired under the same acquisition parameters but with no incident light. Alternatively, hot pixels can be identified and selectively removed by median filtering. This has been demonstrated in figure 6.5e, where a focussed laser was imaged (image ii) and the hot pixels identified under no illumination (panel d) were selectively median

filtered in ImageJ (iii), producing a similar result to the application of a global median filter (iv).

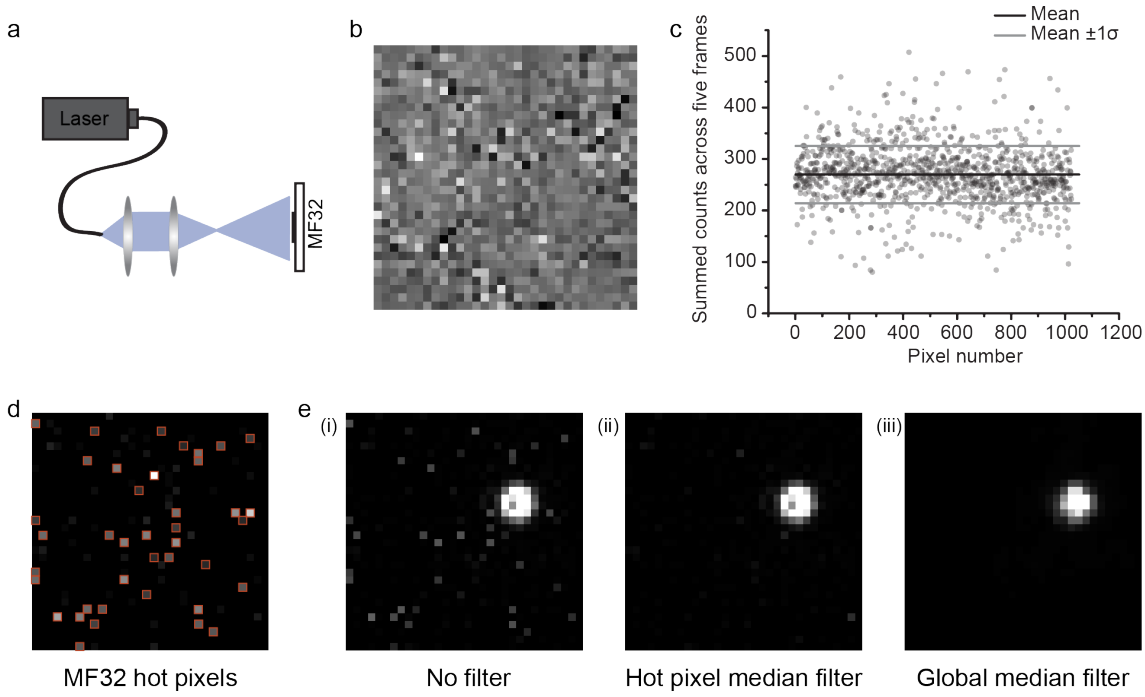

Figure 6.5 MF32 pixel variation in photon counting mode (**a**) A schematic of the experimental set up used to achieve even illumination across the chip by defocusing a collimated 405 nm laser beam by placing a lens with a 30 mm focal distance 200 mm from the detector. (**b**) A photon counting image acquired by 100 µs exposure at 1 µW power with illumination as in (a) demonstrating even illumination but high variation between pixels. (**c**) Scatter plot of the pixel counts from (b). (**d**) MF32 photon counting image taken under dark conditions for 1 ms exposure to highlight hot pixels; the red squares indicate pixels with counts greater than one standard deviation above the mean. (**e**) MF32 photon counting image acquired as for (b) but with the laser focussed onto the detector and the power attenuated to 0.01 µW. This demonstrates the noise caused by hot pixels (i), which was removed by selectively filtering hot pixels (ii) or applying a global median filter with ImageJ (iii).

6.3.2 Characterisation of the MF32 detector in TCSPC mode

In addition to photon counting, the MF32 can be operated in reverse TCSPC mode for single photon time-tagging using 10-bit in-pixel TDCs. The accuracy with which they can report photon arrival establishes the TDC temporal resolution and therefore the minimum temporal bin size used to histogram photon arrival. The average temporal bin size of the TDCs across the camera was determined using a

delay line to measure the shift in IRF peak over a known time delay. This characterisation was carried out by Nikola Krstajic, who used a 2m cable with a known propagation speed of $1.98x10^8$ to introduce a known delay of 10.1 ns. The resulting IRF peak position shifted by 175 time bins indicating a temporal bin size of 57.7 ps. This value differs between pixels due to variations introduced during the fabrication process. It is possible to correct for this variation by determining the accurate temporal bin size per pixel and rationally resampling interpolated decay data to a consistent bin size[446]. However, such corrections were deemed unnecessary for the current test work, as the standard deviation of the temporal bin size for a comparative MF32 array is just 0.7 ps[446].

As with the temporal bin width, the instrumental response function (IRF) also varies between pixels. This variation is experimentally demonstrated in figure 6.6, which shows individual IRFs and their variation across the MF32 chip. These IRFs were recorded using the same experimental set up depicted in figure 6.5a with a defocused pulsed 405 nm laser evenly illuminating the chip at three different intensities within the detector's linear response regime. It is apparent that the IRF broadens with increasing incident power (figure 6.6a), as well as varying from pixel-to-pixel both with respect to its FWHM (figure 6.6b) and its peak location (figure 6.6c). The median reported FWHM was 0.45 ns, 0.59 ns and 1.09 ns when illuminated with 0.1 μW, 0.3 μW or 1 μW respectively (figure 6.6b). This sensitivity of the FWHM to incident power is apparent in the maps presented in panel d, where variation across the field indicates that the illumination was not completely even, as photon counting suggested in figure 6.5b. The IRFs were acquired with a pulsed 405 nm laser using a PDL 800-B controller (Picoquant); the laser was attenuated in all measurements with a 2.0 neutral density filter and power adjustments were made using the laser power dial on the laser driver. As such power adjustments are known to cause the laser pulse width to increase[466], the IRF broadening is likely reporting this, indicating that the system's IRF is limited by the pulse width and not the MF32.

As each pixel has its own unique IRF, lifetime accuracy will vary slightly between pixels and decay fitting based on IRF reconvolution cannot use a global IRF, requiring software that can handle batched analysis of paired decays and IRFs. FLIMfit offers this functionality[467], but is based on a fitting algorithm that

produced a poor tail-fit in direct comparison to commercial software. Decay fits were therefore carried out individually by tail-fitting in OriginPro without reconvolution of the IRF. For this purpose, the decay tail was first obtained by using a VBA script to identify the decay peak and isolate the tail.

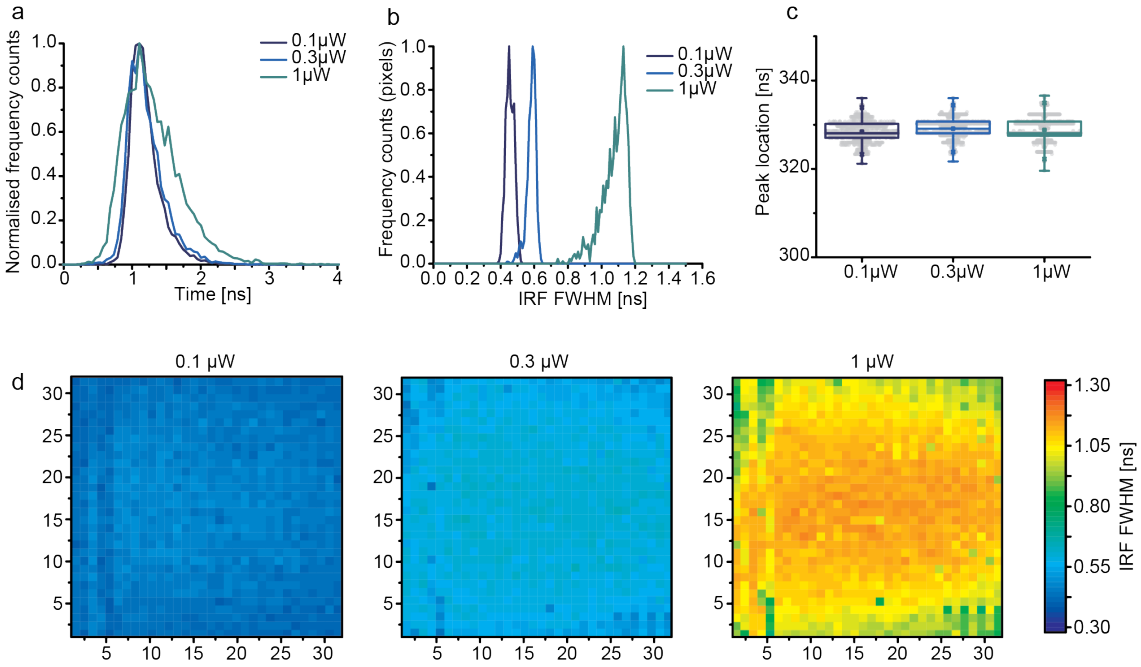

Figure 6.6 MF32 instrumental response functions (**a**) Representative normalised single pixel instrumental response functions (IRF) under direct illumination with a defocussed 405 nm 40 MHz pulsed laser attenuated with a 2 ND filter at increasing laser dial power, acquired by 12 s integration. (**b**) Normalised histograms of single pixel FWHM values from the Gaussian fits of all 1,024 pixel IRFs at each laser power. (**c**) Boxplots demonstrating the IRF peak location of each pixel at various illumination powers; the line represents the median value, the box represents the 25th and 75th quartiles, the dot represents the mean value and the whiskers indicate the minimum and maximum values. (**d**) Pixel maps of the single pixel IRF FWHM at 0.1 µW (left), 0.3 µW (centre) and 1 µW (right).

6.3.3 MF32 imaging capabilities

To characterise the imaging capabilities of the MF32, it was coupled to a microscope for TIRF imaging (depicted in figure 6.3). As shown in figure 6.7, QDot 525 quantum dot samples were imaged in both photon counting mode and TCSPC mode to obtain intensity and fluorescence lifetime maps using single pixel decays. The low spatial resolution of the MF32 is apparent in the intensity map shown in

figure 6.7a by comparison to the raw sCMOS image. This is due to the differences in the pixel sizes, 6.5 μm for the sCMOS and 50 μm for the MF32. Binning the sCMOS to an equivalent pixel size of 50 μm by averaging the pixels, produces a comparable intensity map to the MF32. Single pixel fluorescence decays were simultaneously acquired across the field of view by a 120 s integration with 405 nm excitation pulsing with a repetition rate of 40 MHz. By summing all pixel photon counts into a global fluorescence decay, cyclical variations in time were highlighted by the slow decay kinetics of the quantum dot sample (figure 6.7c). This fixed pattern noise is caused by the design of the TDC, which measures time lapse in eight phases resulting in an eight-step oscillation in the decay. This artefact was removed by averaging every eight time bins to give an effective temporal bin width of 460 ps, smoothing the apparently noisy single pixel decays (figure 6.7d-e). This is, however, an unsatisfactory loss of photon information that will reduce acquisition speed. Methods to correct this clocking effect without information loss by scaling each time bin as required per pixel have been proposed[446] and the next generation SPAD arrays will be designed without this artefact.

Single pixel lifetimes could be obtained by individually tail-fitting each pixel decay in OriginPro with a bi-exponential function. As shown in figure 6.7d, which is a representative corrected single pixel decay taken from a quantum dot cluster, the MF32 reported an amplitude-weighted average fluorescence lifetime of 12.13 ns, which is in good agreement with literature values[468]. Furthermore, conversion of the single pixel fluorescence lifetimes into an image map demonstrates alignment of the long lifetimes with quantum dot clusters (figure 6.7b), which are clearly differentiated from the low background fluorescence lifetimes. This therefore demonstrates that the MF32 has the potential to be used as a plug-and-play TCSPC FLIM camera.

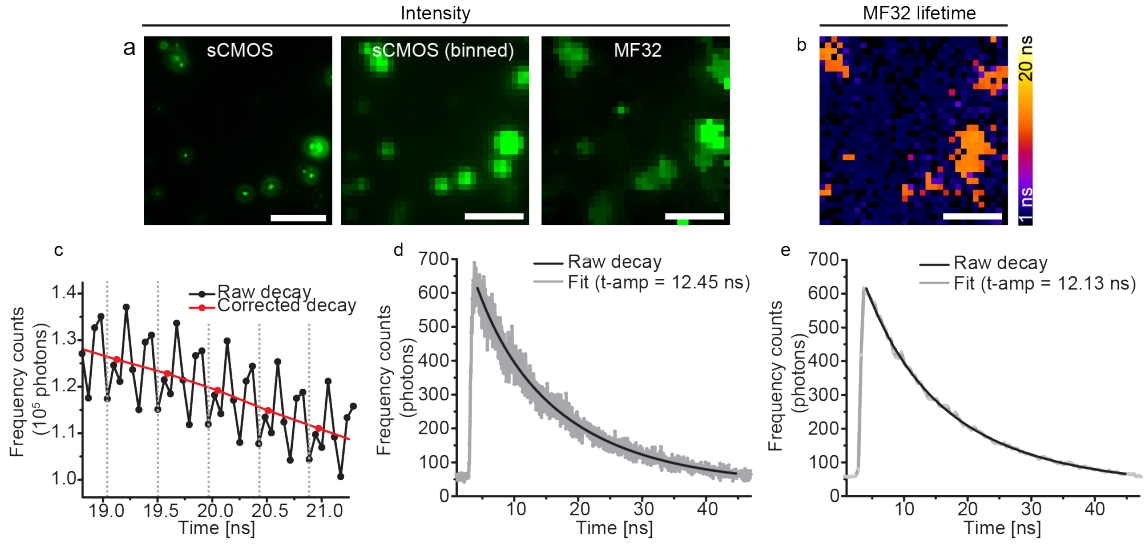

Figure 6.7 MF32 TDC clocking causes oscillations in the fluorescence decay (**a**) Median-filtered intensity images of a quantum dot sample (QDot 525) acquired with the MF32 in photon counting mode by accumulating 10 frames at 500 µs exposure (right) and the sCMOS by 100 ms exposure for comparison, including both the raw sCMOS image (left) and the raw image binned to the same pixel size as the MF32 by pixel averaging (centre). (**b**) Amplitude-weighted average fluorescence lifetime map of the field imaged in (a) generated from single pixel bi-exponential decay tail fits following 120 s TCSPC integration with 405 nm 40 MHz pulsed laser excitation. (**c**) A 2 ns sample of the raw global decay accumulated by summing all pixels. This demonstrates eight-step oscillations that repeat every 460 ps. This can be corrected by averaging every eight time bins (red decay). (**d**) A single pixel raw decay and (**e**) corrected decay. Scale bars 5 µm throughout.

A common use of FLIM is to differentiate spectrally similar fluorophores. This can be less demanding on the detector than FLIM-FRET as fluorophores with vastly different lifetimes can be selected. For this purpose, a sample of EGFP-expressing HeLa cells and quantum dots with peak emission at 525 nm were imaged by the prism TIRF-coupled 405 nm pulsed laser. Figure 6.8 presents the comparative photon counting images acquired with the MF32 and the commercial sCMOS detector in addition to MF32 TCSPC-acquired fluorescence lifetime maps and single pixel decays. The MF32, operating in photon counting mode, closely reproduced the sCMOS intensity image of a HeLa cell beside a brightly emitting fluorophore patch, suspected to be a quantum dot cluster (figure 6.8a). As EGFP has a short fluorescence lifetime, approximately 2-3 ns[469], and the quantum dots (QDot 525) have a reportedly longer lifetime of greater than 10 ns[468], it should be possible to separate these spectrally similar fluorophores through FLIM. Indeed, fluorescence lifetime maps generated by individually tail-fitting each single-pixel

TCSPC-derived fluorescence decay (figure 6.8b), confirmed a high lifetime region (region 1, yellow box) and a low lifetime region (region 2, red box) position-analogous to the bright cluster and the HeLa cell, respectively. Furthermore, representative single pixel fitted decays (figure 6.8c) report a fluorescence lifetime of 11.25 ns for the region 1 quantum dot cluster and 2.35 ns for the region 2 EGFP-expressing HeLa cell, which is in good agreement with the aforementioned literature values[468, 469].

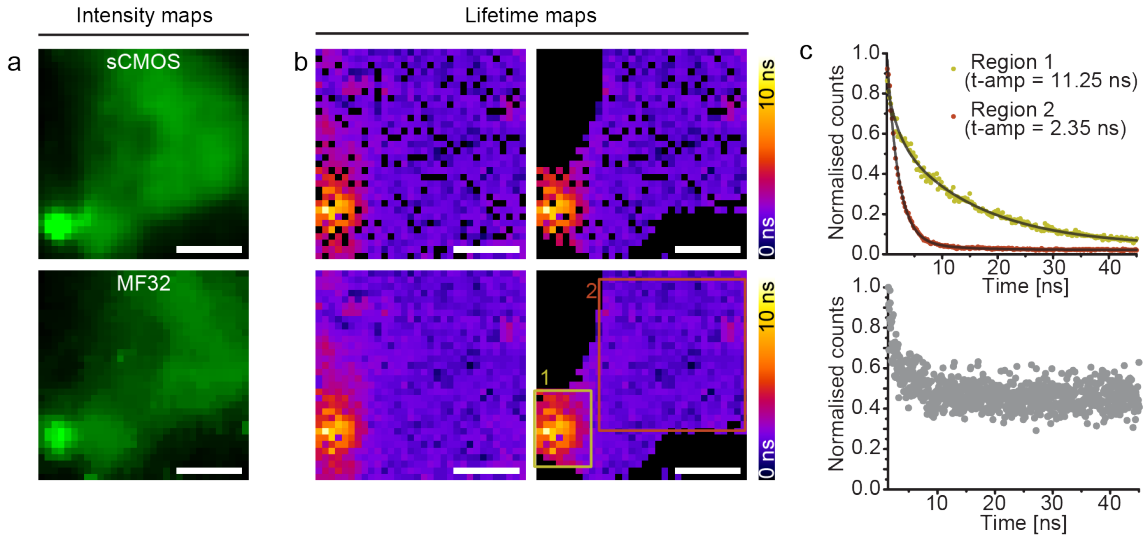

Figure 6.8 TIRF-FLIM of spectrally similar fluorophores with the MF32 (**a**) Comparative sCMOS (top) and MF32 median-filtered photon counting (bottom) intensity images of an EGFP expressing HeLa cell and a spectrally similar QDot 525 quantum dot cluster. Acquired by 500 ms exposure with the sCMOS and accumulated from 20 10 ms exposures with the MF32, excited with a pulsed 405 nm laser coupled by prism-TIRF. (**b**) Amplitude-weighted average lifetime maps of the field in (a) generated from single pixel bi-exponential tail fits of fluorescence decays acquired with the MF32 in TCSPC mode. The fluorophores were excited with a 405 nm TIRF-coupled laser pulsing at 20 MHz and photon counts were integrated over 110 s. The spectrally similar fluorophores are differentiated by fluorescence lifetime in these images: a quantum dot cluster (region 1; yellow box) and an EGFP-expressing HeLa cell (region 2; red box). Images presented are with and without selective median filtering (bottom and top respectively) and low count thresholding (right and left respectively) (**c**) Representative normalised single pixel fitted fluorescence decays corrected for TDC clocking from region 1 and region 2 (top) and a raw hot pixel decay (bottom). Scale bars 5 µm.

A large number of pixels display an improbable lifetime value below the temporal resolution of the detector. These lifetime values are predominantly caused by the pixel having a high dark count rate that precludes detection of the fluorescence

decay as demonstrated in figure 6.8c. Fluorescence lifetimes below the 250 ps average IRF FWHM were therefore identified as unreliable and removed from the fluorescence lifetime map by selective median filtering (figure 6.8b). In addition, an ROI applied to the cell and dot cluster in the photon counting image by intensity thresholding was transferred to the fluorescence lifetime map to exclude background signal (figure 6.8b). This facilitates the direct comparison of the fluorescence lifetime and intensity maps and has been used to visualise data throughout this chapter.

From the data presented in this section, it is apparent that the MF32 can accurately report multidimensional fluorescence decays through fast frame-by-frame TCSPC acquisition. Moreover, the SPAD array can spatially separate distinct fluorophores and demonstrates sufficient sensitivity to image EGFP in TIRF, presenting the first TIRF FLIM image of an intracellular encodable fluorescent protein.

6.3.4 Widefield TCSPC FLIM-FRET with the MF32

The goal of the SPAD array for FLIM applications is to achieve widefield TCSPC FLIM-FRET for fast lifetime imaging of dynamic protein interactions in live cells. However, a change in fluorescence lifetime upon FRET is often in the order of hundreds of picoseconds and therefore requires high temporal resolution for its detection[349]. To explore the capacity of the MF32 for FLIM-FRET, HeLa cells expressing either EGFP alone, co-expressed and separate EGFP and mCherry or an EGFP-mCherry fusion protein (separated by a 12 amino acid linker), were studied. In each case, EGFP was excited using a 405 nm laser pulsing at 20 MHz and photon counts were acquired either in photon counting mode with a 100 µs exposure or in TCSPC mode over a 90 s integration. In this case, the 405 nm laser was coupled to the microscope via the condenser port. This provides higher excitation powers compared to prism TIRF, important due to the low absorption of 405 nm by EGFP.

As shown in figure 6.9, which presents the intensity and fluorescence lifetime maps in addition to representative fitted fluorescence decays, the fluorescence lifetime of EGFP is reduced only when it is maintained in close proximity to mCherry by fusion. This is visually apparent in the false-colour fluorescence lifetime maps (figure 6.9a), where EGFP-only and separately expressed EGFP and

mCherry report similar fluorescence lifetimes (top row and centre row, respectively), however, fused EGFP-mCherry exhibits quenched fluorescence (bottom row). This was quantified with a global fluorescence decay, accumulated by summing all pixel photon counts into a single histogram (figure 6.9e). Tail-fitting the global decays with a bi-exponential function reported fluorescence lifetimes of 2.16 ns, 2.33 ns and 1.42 ns for EGFP only, separate EGFP and mCherry and fused EGFP-mCherry, respectively, evidencing FRET in the latter case alone. Furthermore, these values were consistent with representative single pixel fluorescence lifetimes (figure 6.9b-d), indicating that single pixels can collect sufficient photons to accurately describe the fluorescence decay. The same experiment was carried out on the Leica SP5 SMD commercial FLIM system in section 2.5.2, producing similar fluorescence lifetime values of 2.09 ns, 2.04 ns and 1.73 ns for EGFP only, separate EGFP and mCherry and fused EGFP-mCherry, respectively.

The acquisition time required to acquire a median count of 10,000 photons per pixel was determined for EGFP-expressing HeLa cells for both the MF32 and the commercial confocal laser scanning microscope (CLSM). The MF32 required approximately 24 s integration with pulsed 20 MHz 405 nm excitation, indicating a count rate of 417 photons per second in each pixel. This is notably lower than the maximum count rate of the detector, which is in the order of 100,000 counts per second (calculated based on the measured dead time of 100 μs at maximum quench speed under saturating illumination). The CLSM, on the other hand, requires approximately 30 s to collect the same number of photons over the same area and pixel size under pulsed 40 MHz 488 nm excitation by scanned detection. This equates to a required dwell time of approximately 30 ms per pixel. The relatively slow acquisition speed of the MF32 is due to the poor collection efficiency of the 1.1% photosensitive region of the pixel. Improving the fill factor by 50% by microlensing or improved chip design, could theoretically enable a 500 ms TCSPC 'frame rate'. This speed would likely be compatible with real-time FLIM-FRET studies of the protein dynamics underlying autophagosome clearance. The pixel fill-factor therefore continues to preclude live widefield TCSPC FLIM and is exacerbated here by the poor excitation efficiency of EGFP using a 405 nm laser.

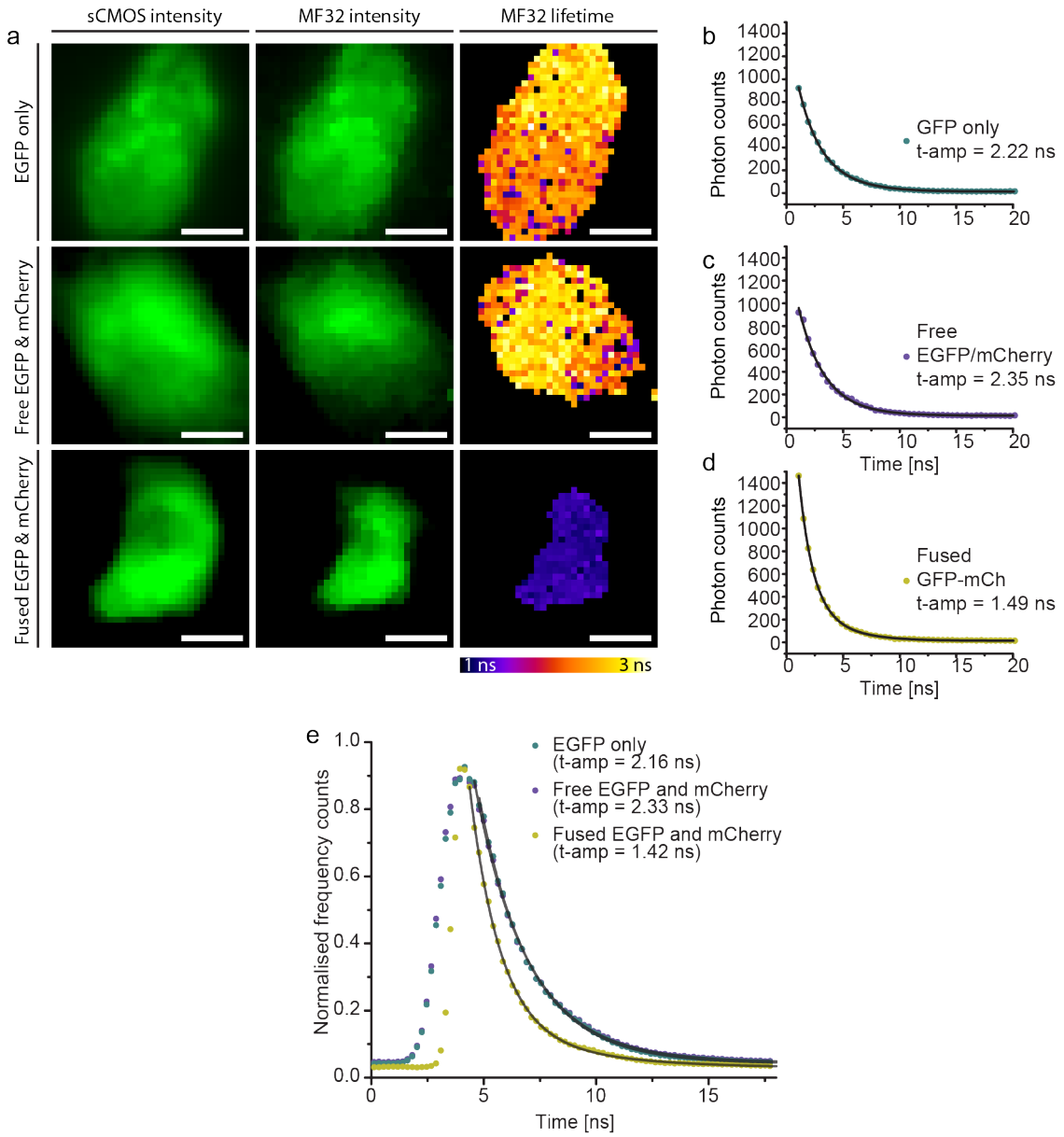

Figure 6.9 Widefield TCSPC FLIM-FRET with the MF32 (**a**) Comparative sCMOS intensity (left), median-filtered MF32 photon counting mode images (centre) and MF32 TCSPC-generated amplitude-weighted average lifetime maps (right), all acquired with a 405 nm 20 MHz pulsed laser coupled to an Olympus iX71 *via* the condenser port. The intensity images for the sCMOS were acquired with a 500 ms exposure and for the MF32 by accumulating 30 frames with a 3 ms exposure time. The MF32 fluorescence decays were integrated over 72 s. Shown are HeLa cells expressing EGFP alone (top row), free EGFP and mCherry (middle row) or EGFP fused to mCherry (bottom row). The reduction in lifetime for the fused construct demonstrates the detection of FRET. Scale bars are 5 µm. (**b-d**) Representative single pixel decays for each fluorescence lifetime map in (a), these were corrected for TDC clocking and fitted with a bi-exponential function. (**e**) Global fluorescence decays accumulated from all pixel photon counts for each of the fluorescence lifetime maps in (a).

6.3.5 Improving the MF32 pixel fill factor by microlensing

The timing jitter of a SPAD increases with the size of the photosensitive pn-junction[444]. This relationship, along with the need to integrate the timing electronics into each pixel, results in a low percentage of the pixel being photosensitive. For the MF32, the circular active area is 6 μm in diameter, making up just 1.1% of the area of each pixel as was shown in figure 6.2. Fluorescence microscopy is challenged by the low quantum yield of many fluorophores and reducing the collection efficiency further with a small fill factor significantly slows the achievable photon count rate. This limitation is overcome in commercial sCMOS cameras by using microlenses fabricated on chip to focus the incident light onto the active region of the pixel[470].

As for commercial detectors, a microlens array could similarly be used to maximise the photon collection efficiency of the MF32 by fabricating and coupling a custom 50 μm pitch array. Other groups have previously tried to fabricate a microlens array directly onto the chip (Simon Ameer-Beg's group, unpublished), however this approach has proven difficult and has been unsuccessful to date. Instead, I explored the possibility of optically coupling a microlens array by introducing it into the optical path *via* a 1-to-1 optical relay. This would allow the fluorescence emission to be focussed into points that if aligned with the photosensitive area of each pixel, will improve the photon detection efficiency of each detector. This principle has been demonstrated in figure 6.10, which shows the signal re-distribution when imaging a test chip using an sCMOS camera, both with and without a commercial 150 μm pitch microlens (Thorlabs, MLA150-7AR) in the optical path.

The microlens array was inserted into the optical path of the Olympus iX71 microscope such that it focussed the output light onto the imaging plane of the microscope. This image was then relayed onto the detector *via* an optical relay as shown in figure 6.10a. A patterned glass and chrome test slide was illuminated with a lamp and the unfiltered transmitted light was detected with an sCMOS camera. In the absence of the microlens array, incident light was evenly transmitted through the glass slide, whereas in the presence of the microlens array, transmitted light was detected in focal points (figure 6.10b). Indeed, single pixel analysis from a focal point indicates high signal gain to saturation (a grey

value of 65535) in the presence of the microlens array when compared to the equivalent pixel without the lens (a grey value of 13755; figure 6.10c). However, this is at the cost of total light, as spaces between the microlenses, shown by the scanning electron micrograph of the microlens array (figure 6.10a), preclude complete transmission. Notably, the focal points appear to be evenly distributed as shown by the consistent peak height and distance between peaks (figure 6.10d-e). This indicates that there is no noticeable tilt in the optics when incorporated by a translation mount, which reduces the complexity of optically coupling a microlens array to lateral and axial adjustments.

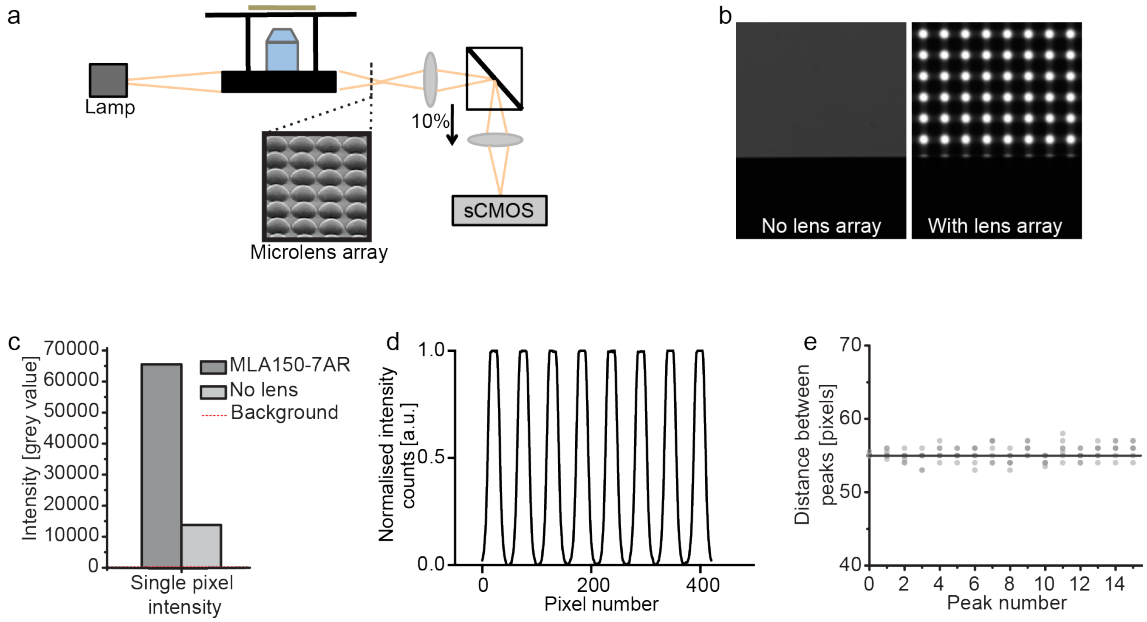

Figure 6.10 sCMOS single pixel signal gain by microlensing (**a**) A schematic of the set up used to optically couple a 150 µm pitch microlens array, Thorlabs MLA150-7AR (dotted line; inset is scanning electron micrograph of the microlens array, provided by Thorlabs) (**b**) A patterned glass and chrome test slide illuminated by lamp light with (right) and without (left) the microlens array focussing the transmitted light onto the microscope's imaging plane. (**c**) Intensity counts for a single pixel within a focal point of the microlens array in (b) demonstrating the high signal gain. (**d**) An x-axis intensity line profile through the focal points of the microlensed image in (b) and (**e**) graphical demonstration that the peak locations are evenly spaced (data presented from three line profiles).

To investigate the feasibility of optically coupling a microlens array with the MF32, a standard objective lens was used to focus a heavily attenuated laser onto the active area of a single pixel in figure 6.11. To achieve this, the objective lens was

mounted with translation controls and used to focus low power attenuated fibre-coupled 405 nm pulsed laser illumination directly onto the MF32, as schematised in figure 6.11a. Incremental translation was provided both by the fine translation control on the lens and the coarser lateral and axial translation controls on the MF32 mount. By this approach, it was possible to align the focal point with the 6 µm diameter active area by using single pixel signal gain as a read out for alignment (figure 6.11b-d). Indeed, by integrating the counts across a 7x7 pixel subarray upon which the focal point is incident, it is apparent that the counts increase from background to near saturation at 50 µm intervals as expected from the 50 µm pixel pitch of the SPAD array (figure 6.11b-c and e).

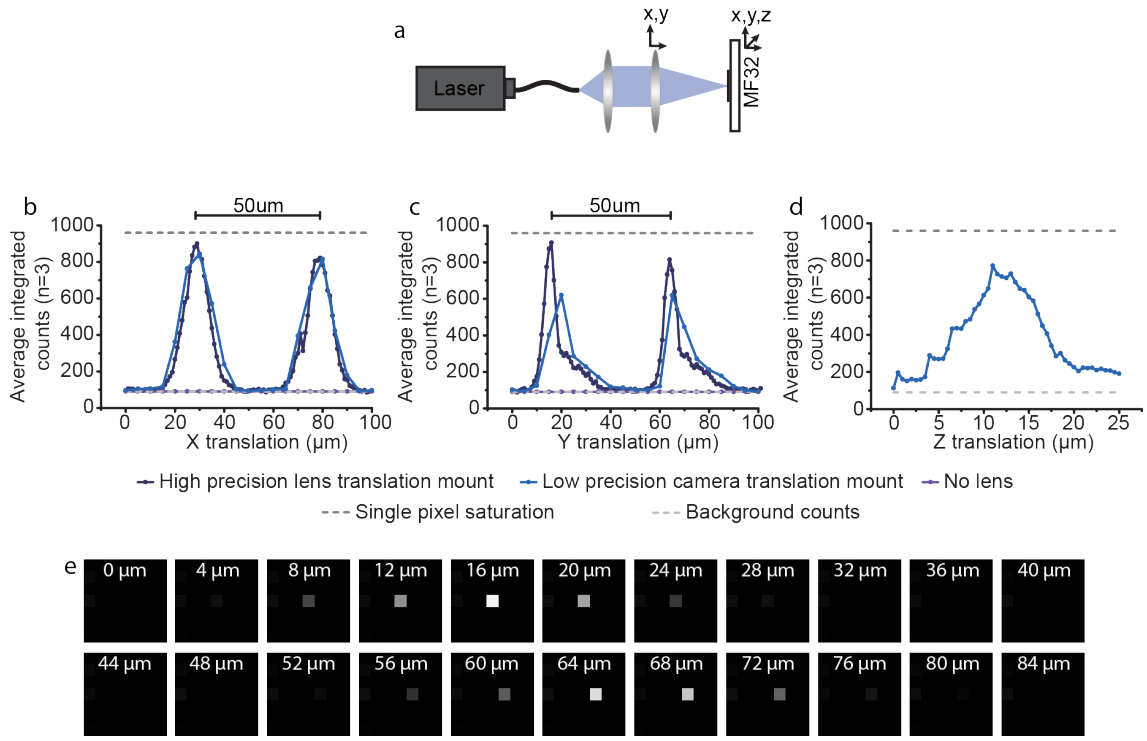

Figure 6.11 Optimising MF32 single pixel collection efficiency (**a**) A fibre-coupled 405 nm pulsed laser was collimated and then focussed with a standard objective lens on an x,y fine precision translation mount onto the MF32, which has x,y,z translation. (**b-d**) Mean integrated counts over a 7x7 pixel sub-array as the focussed laser is translated through (**b**) x, (**c**) y and (**d**) z by fine adjustment with the microlens translation mount (1 µm intervals) or course adjustment with the MF32 mount (5 µm intervals), [n=3]. Incident laser power was 0.001 µW and each image was a frame accumulation of 15 30 µs exposures. (**e**) 4 µm step lateral translations of the focussed light in (a). These demonstrate high signal gain for single MF32 pixels at 50 µm pitch, indicative of alignment with the pixel's active area.

This data demonstrates that it is feasible to optically couple a microlens array, however, the high density of hot pixels and the small active area would make it difficult to couple a full microlens array in practise. It is also unlikely that the microlenses will achieve the focussing power required to restrict all light to the active area, diminishing the achievable signal gain. Furthermore, optical coupling rather than on-chip fabrication suffers from drift, which makes it a higher maintenance set up. Next generation SPAD arrays therefore aim to improve the pixel fill factor through chip design, which as my proof of principle work shows, may then be further improved by microlensing.

6.4 Discussion

The MF32 provides time-resolution comparable to commercial TCSPC detectors with superior frame rate, acquiring time-tagged photon counts across 1,024 channels in parallel[338]. The work presented here has demonstrated the applicability of the MF32 as a plug-and-play detector for widefield TCSPC FLIM, achieving both differentiation of spectrally similar fluorophores and FRET detection (figures 6.8 and 6.9 respectively). This is the first time that FLIM-FRET has been achieved using a widefield application of TCSPC with encodable fluorescent proteins expressed in cells rather than high quantum yield fluorophores poorly suited to live cell work. Through a home-built prism TIRF set up, I have also demonstrated TIRF-FLIM (figure 6.8), which is just one of the advantages of widefield microscopy. The latest developments in lattice light sheet microscopy are enabling widefield optical sectioning for fast volumetric imaging[471], which if paired to fast TCSPC could realise four-dimensional FLIM-FRET. Moreover, super-resolution PALM-FLIM would allow the study of protein interactions alongside single particle tracking.

These techniques are on the horizon, but further development of the SPAD array is needed to accomplish them. The MF32 presented the first viable full TCSPC SPAD array[464] and is therefore a developmental device with known limitations. Nevertheless, the MF32 offered an excellent test bed to investigate the feasibility of widefield TCSPC FLIM-FRET using a plug-and-play camera with parallel capability for fluorescence intensity and lifetime imaging. The key limitations of the MF32 are

the poor spatial resolution due to the large 50 μm pixel size and the low pixel fill factor limiting the photon count rate . However, despite these limitations, FLIM-FRET was demonstrated with modest photon counts in reasonable imaging times, comparable to commercial scanning systems.

During the course of my PhD, prototypes of the next generation of SPAD arrays were designed and manufactured as part of the ERC-funded Total Photon project (grant 339747). Their design was partly informed by the results presented here, namely the need for low dark counts, reasonable temporal resolution and improved fill factor. The new generation detectors propose to both reduce the pixel size to 16 μm and increase the fill factor to approximately 20-50%. This pixel size is well suited to achieve Nyquist sampling for high spatial resolution with a 150x objective lens, progressing from whole cell spatial resolution of the MF32 to sub-cellular resolution.

Despite the anticipated improvements in fill factor, microlensing would still be wise to further improve the photon detection efficiency. To reduce the complexity of the optical set up for users with little technical expertise, the microlens array ideally needs to be fabricated on chip. Additionally, a means to embed correction algorithms within the acquisition software, required for hot pixel management, temporal bin width or IRF peak location (identified in figures 6.5 and 6.6), would make this technology more accessible to a standard biology laboratory by outputting fully corrected data. For widespread implementation, a means of processing the high volume fluorescence lifetime data within a reasonable time frame is also needed. This presents new challenges in data analysis, which presently relies on slow iterative fitting algorithms[268]. Methods of quick processing on FPGA using centre-of-mass methods for real-time FLIM have been proposed[338], though they are less robust than decay fitting analyses. Alternatively, open source software for batch analysis such as those offered by Tri2[472] and FLIMfit[467] hold promise for automated data processing.

Despite the challenges that remain, the work presented here provides proof-of-principle that widefield FLIM-FRET is attainable. With the further improvements anticipated in next-generation SPAD array technology, multidimensional and real-time monitoring of intracellular protein dynamics is becoming a realistic prospect. In the case of SNARE-mediated autophagosome clearance, such capabilities could

enable investigation into the longevity and therefore stability of SNARE complex formation or the temporal changes in VPS33A regulatory interactions. Such advantages offered by widefield TCSPC FLIM-FRET may draw this technique into the mainstream and alleviate conflicts in data that arise from the over-interpretation of methods such as fluorescence colocalisation.

CHAPTER SEVEN:

Discussion

In this research, I set out to use the most appropriate and robust fluorescence microscopy techniques available to investigate the protein dynamics underlying autophagosome clearance *in situ*. In doing so, each technique – CW-gSTED, diffraction-limited fluorescence colocalisation and FLIM-FRET – was validated to assess its limitations and ensure appropriate quantitation and interpretation. Additionally, with knowledge of the limitations of TCSPC FLIM-FRET, most notably the slow acquisition speed that precludes live imaging, I explored the potential of a recent breakthrough camera technology for its applicability to high-speed FLIM.

The core biological questions examined concern the SNARE protein interactions governing autophagosome-endolysosome fusion and therefore the completion of autophagy. The well-established mammalian SNARE complex facilitating this fusion event (Stx17, SNAP29 and VAMP8) has not previously been confirmed by *in situ* studies of protein interaction since it was proposed nearly five years ago[248]. Additionally, though Atg14 and VPS33A have both been implicated in promoting fusion through interactions with Stx17[176, 177, 253], the basis of this regulation is poorly understood.

7.1 Impact of findings and future research

Through the work described in my thesis, a detailed new model has been established of how SNARE-mediated autophagosome clearance is carried out. Briefly, I propose that Stx17 is phosphorylated and remains in an inactive configuration that precludes ectopic complex formation. VPS33A binds this 'closed' conformation at least in part *via* the Stx17 N-peptide, tethering the autophagosome and endolysosome membrane in close apposition through its association with the HOPS complex. This allows local dephosphorylation of Stx17 such that it can open into an active state and form SNARE associations with SNAP29 and VAMP7, which are stabilised by an alternate binding mode of VPS33A to promote fusion. To confirm this model experimentally, confirmation is required for the changing phosphorylation status of endogenous Stx17, for which a phospho-specific antibody would be particularly helpful.

These mechanistic details provide a deeper understanding of the processes and regulation underlying the final stages of autophagy. The apparent inhibitory role of

phosphorylation for autophagosome clearance may couple this process to intracellular energy levels based on ATP availability. If this were indeed the case, it would provide a fast feedback event to prevent the unnecessary degradation of cellular material upon a return to nutrient replete conditions, bypassing the delayed onset of TORC1 reactivation[193].

The finding that VAMP7 and not VAMP8 is the dominant endolysosomal R-SNARE involved has implications on the studies that have been based on the previous model, which must now be revisited. Atg14, for example, has been shown to bind Stx17 and SNAP29 but not VAMP8 and is therefore proposed to specifically stabilise the binary SNARE complex[253]. Additionally, VAMP7 notably differs from VAMP8 in having a regulatory longin domain, consistent with the autophagosomal R-SNAREs identified in *D. melanogaster* and *S. cerevisiae*[381]. This structural conservation may suggest an analogous regulatory mechanism that is as yet unexplored.

The observed interaction between VPS33A and monomeric Stx17 also has implications for the field of SNARE biology. The divergent VPS33A domain 1 N-peptide binding patch previously prompted researchers to propose it cannot bind the partially conserved syntaxin N-peptide[404, 409]. SM proteins have therefore been categorised into two classes, determined by this characteristic[404], which the data presented in chapter five indicate no longer apply. I therefore propose a reclassification: class I SM proteins bind the consensus N-peptide sequence of *N*-(R/K)DRTX(e/q)(L/F)-*C* to associate with open monomeric syntaxin to promote fusion, and class II SM proteins bind a divergent phosphorylated and negatively charged N-peptide consensus sequence to associate with, and perhaps stabilise, inactive monomeric syntaxin. With the N-peptide sequence *N*-MSEDEE-*C*, Stx17's cognate SM, VPS33A, falls into the latter category. I speculate that SM interactions with Stx6 and Stx10, which have the consensus *N*-MSXED-*C*, may follow a similar regulatory mechanism, though further research is required to confirm this.

The proposed model of SNARE-mediated autophagosome clearance prompts a number of new questions for future research. Is casein kinase II responsible for Stx17 phosphorylation as predicted? Is VPS33A required to stabilise inactive Stx17 and is Stx17 inactivated by the same self-association mechanism observed for other syntaxin family members? What is the phosphatase responsible for

activating Stx17? Is Stx17 recruited to the phagophore from an ER source rather than the previously proposed cytosolic population[248]? And can VPS33A interact with Stx17 prior to HOPS complex integration?

A number of regulatory protein interactions have now been identified for Stx17, namely those with VPS33A, Atg14 and HOPS components VPS11 and VPS18[404]. Further research is therefore also needed to understand the interplay between these interactions. This would be an ideal application for live widefield TCSPC FLIM-FRET to ascertain the dynamics of regulatory protein associations through the autophagosome life cycle. The research carried out in chapter six to explore the suitability of prototype SPAD arrays has provided proof-of-concept that they have the required sensitivity and temporal resolution to detect FRET between encodable probes required for live cell FLIM. These studies have helped inform the next generation of SPAD array cameras, which aim to increase photon collection efficiency and reduce pixel size, thus improving both the acquisition speed and the achievable spatial resolution. As autophagosomes persist for approximately 30 minutes[473], changes in protein association may have sufficient temporal separation for live FLIM-FRET detection with the next generation SPAD arrays. Similarly, weak FRET efficiencies were noted between Stx17 and both VAMP8 and Vti1b, which I speculate may be due to a small population of short-lived non-cognate associations. Live FLIM-FRET imaging to ascertain the longevity of SNARE associations may therefore provide insights into cognate and non-cognate pairings.

An emphasis throughout this thesis has been placed on method validation, appropriate data processing and interpretation with consideration of technique limitations. Fluorescence colocalisation is often paired with co-immunoprecipitation to evidence protein interaction *in situ*, however the spatial resolution of existing techniques are not sufficient to support this. This has been exemplified in studies with Stx17[Q196G], a zero-layer mutant, which colocalises significantly with SNAP29 but cannot maintain SNARE associations as reported by diminished FRET efficiencies. This finding highlights the need for the routine implementation of more robust methods to detect protein interactions *in situ*, such as FLIM-FRET.

7.2 Summary

Through the course of this thesis, the process of SNARE-mediated autophagosome clearance has been investigated using carefully validated fluorescence intensity and lifetime microscopy of optimised autophagy assays. These approaches provide a robust determinant of protein interactions to study this mechanism *in situ* for the first time. Consequently, these findings have prompted reconsideration and expansion of the existing autophagosomal SNARE model, which now appears to have been only partially accurate. The cognate SNARE complex, hypothesised to consist of Stx17, SNAP29 and VAMP8, was actually found to contain Stx17, SNAP29 and VAMP7. Furthermore, the regulation of fusion, previously proposed to be dependent on localised VPS33A promotion of fusion, was found to involve a more complex model where VPS33A both inhibits and promotes fusion dependent on Stx17 phosphorylation status. Further investigation is still needed, however, the data presented establish a new model of SNARE-mediated autophagosome clearance; the broad implications of this revised model clarify the final events of autophagy, indicate a novel SNARE-SM functional association and engender reclassification of SM proteins.

BIBLIOGRAPHY:

1. Olkkonen, V.M. & Ikonen, E. When intracellular logistics fails - genetic defects in membrane trafficking. *Journal of Cell Science* **119**, 5031-5045 (2006).
2. Novick, P., Field, C. & Schekman, R. Identification of 23 complementation groups required for post-translational events in the yeast secretory pathway. *Cell* **21**, 205-215 (1980).
3. Wong, E. & Cuervo, A.M. Integration of Clearance Mechanisms: The Proteasome and Autophagy. *Cold Spring Harbor Perspectives in Biology* **2** (2010).
4. Mizushima, N., Levine, B., Cuervo, A.M. & Klionsky, D.J. Autophagy fights disease through cellular self-digestion. *Nature* **451**, 1069-1075 (2008).
5. Alberts, B. *et al. Molecular Biology of the Cell*, Edn. Fourth. (Garland Science, New York; 2002).
6. Palade, G. Intracellular aspects of process of protein-synthesis. *Science* **189**, 347-358 (1975).
7. Budnik, A. & Stephens, D.J. ER exit sites - Localization and control of COPII vesicle formation. *Febs Letters* **583**, 3796-3803 (2009).
8. Carlsson, S.R. & Simonsen, A. Membrane dynamics in autophagosome biogenesis. *Journal of Cell Science* **128**, 193-205 (2015).
9. Kuehn, M.J., Herrmann, J.M. & Schekman, R. COPII-cargo interactions direct protein sorting into ER-derived transport vesicles. *Nature* **391**, 187-190 (1998).
10. Aridor, M., Weissman, J., Bannykh, S., Nuoffer, C. & Balch, W.E. Cargo selection by the COPII budding machinery during export from the ER. *Journal of Cell Biology* **141**, 61-70 (1998).
11. Barlowe, C. *et al.* COPII - A membrane coat formed by Sec proteins that drive vesicle budding from the endoplasmic-reticulum. *Cell* **77**, 895-907 (1994).
12. Letourneur, F. *et al.* Coatomer is essential for retrievl of dilysine-tagged proteins to the endoplasmic-reticulum. *Cell* **79**, 1199-1207 (1994).
13. Pearse, B.M.F. Coated vesicles from pig brain - purification and biochemical characterization. *Journal of Molecular Biology* **97**, 93-& (1975).
14. Altstiel, L. & Branton, D. Fusion of coated vesicles with lysosomes - measurement with a fluorescence assay. *Cell* **32**, 921-929 (1983).
15. Presley, J.F. *et al.* ER-to-Golgi transport visualized in living cells. *Nature* **389**, 81-85 (1997).
16. Chia, P. & Gleeson, P. Membrane tethering. *F1000Prime Reports* **6** (2014).
17. Weber, T. *et al.* SNAREpins: Minimal machinery for membrane fusion. *Cell* **92**, 759-772 (1998).
18. Geumann, U., Barysch, S.V., Hoopmann, P., Jahn, R. & Rizzoli, S.O. SNARE Function Is Not Involved in Early Endosome Docking. *Molecular Biology of the Cell* **19**, 5327-5337 (2008).
19. Heuser, J. & Reese, T. Evidence for recycling of synaptic vesicle membrane during transmitter release at the frog neuromuscular junction. *J Cell Biol.* **57**, 315-344 (1973).
20. Taraska, J.W., Perrais, D., Ohara-Imaizumi, M., Nagamatsu, S. & Almers, W. Secretory granules are recaptured largely intact after stimulated exocytosis in cultured endocrine cells. *Proceedings of the National Academy of Sciences of the United States of America* **100**, 2070-2075 (2003).
21. Ceccarelli, B., Hurlbut, W.P. & Mauro, A. Turnover of transmitter and synaptic vesicles at frog neuromuscular junction. *Journal of Cell Biology* **57**, 499-524 (1973).

22. Fesce, R., Grohovaz, F., Valtorta, F. & Meldolesi, J. Neurotransmitter release: fusion or 'kiss-and-run'? *Trends Cell Biol.* **4**, 1-4 (1994).
23. Sigismund, S. *et al.* Endocytosis and signaling: cell logistics shape the eukaryotic cell plan. *Physiological Reviews* **92**, 273-366 (2012).
24. Saftig, P. & Klumperman, J. Lysosome biogenesis and lysosomal membrane proteins: trafficking meets function. *Nature Reviews Molecular Cell Biology* **10**, 623-635 (2009).
25. Young, A.R.J. *et al.* Starvation and ULK1-dependent cycling of mammalian Atg9 between the TGN and endosomes. *Journal of Cell Science* **119**, 3888-3900 (2006).
26. Ravikumar, B., Moreau, K., Jahreiss, L., Puri, C. & Rubinsztein, D.C. Plasma membrane contributes to the formation of pre-autophagosomal structures. *Nature Cell Biology* **12**, 747-U715 (2010).
27. Puri, C., Renna, M., Bento, C.F., Moreau, K. & Rubinsztein, D.C. Diverse Autophagosome Membrane Sources Coalesce in Recycling Endosomes. *Cell* **154**, 1285-1299 (2013).
28. Kopitz, J., Kisen, G.O., Gordon, P.B., Bohley, P. & Seglen, P.O. Nonselective autophagy of cytosolic enzymes by isolated rat hepatocytes. *Journal of Cell Biology* **111**, 941-953 (1990).
29. Singer, S.J. & Nicolson, G.L. The Fluid Mosaic Model of the Structure of Cell Membranes. *Science* **175**, 720-+ (1972).
30. Lodish, H. *et al. Molecular Cell Biology*, Edn. Fifth. (W.H.Freeman and Co Ltd, Gordonsville; 2003).
31. Di Paolo, G. & De Camilli, P. Phosphoinositides in cell regulation and membrane dynamics. *Nature* **443**, 651-657 (2006).
32. Rameh, L.E. & Cantley, L.C. The role of phosphoinositide 3-kinase lipid products in cell function. *Journal of Biological Chemistry* **274**, 8347-8350 (1999).
33. Bonifacino, J.S. & Glick, B.S. The mechanisms of vesicle budding and fusion. *Cell* **116**, 153-166 (2004).
34. Hong, W.J. & Lev, S. Tethering the assembly of SNARE complexes. *Trends in Cell Biology* **24**, 35-43 (2014).
35. Barr, F.A. Rab GTPases and membrane identity: Causal or inconsequential? *Journal of Cell Biology* **202**, 191-199 (2013).
36. Chavrier, P., Parton, R.G., Hauri, H.P., Simons, K. & Zerial, M. Localization of low-molecular-weight GTP binding-proteins to exocytic and endocytic compartments. *Cell* **62**, 317-329 (1990).
37. Hutagalung, A.H. & Novick, P.J. Role of Rab GTPases in Membrane Traffic and Cell Physiology. *Physiological Reviews* **91**, 119-149 (2011).
38. Leung, K.F., Baron, R. & Seabra, M.C. Geranylgeranylation of Rab GTPases. *Journal of Lipid Research* **47**, 467-475 (2006).
39. Wu, Y.W. *et al.* Membrane targeting mechanism of Rab GTPases elucidated by semisynthetic protein probes. *Nature Chemical Biology* **6**, 534-540 (2010).
40. Blumer, J. *et al.* RabGEFs are a major determinant for specific Rab membrane targeting. *Journal of Cell Biology* **200**, 287-300 (2013).
41. Lodish, H. *et al. Molecular Cell Biology*, Edn. Sixth. (W.H. Freeman and Co Ltd, Gordonsville; 2008).
42. Chernomordik, L.V. & Kozlov, M.M. Protein-lipid interplay in fusion and fission of biological membranes. *Annual Review of Biochemistry* **72**, 175-207 (2003).

43. Wilson, D.W. *et al.* A fusion protein required for vesicle-mediated transport in both mammalian-cells and yeast. *Nature* **339**, 355-359 (1989).
44. Griff, I.C., Schekman, R., Rothman, J.E. & Kaiser, C.A. The yeast Sec17 gene-product is functionally equivalent to mammalian alpha-SNAP protein. *Journal of Biological Chemistry* **267**, 12106-12115 (1992).
45. Sollner, T. *et al.* SNAP receptors implicated in vesicle targeting and fusion. *Nature* **362**, 318-324 (1993).
46. Steegmaier, M. *et al.* Three novel proteins of the syntaxin/SNAP-25 family. *Journal of Biological Chemistry* **273**, 34171-34179 (1998).
47. Dulubova, I. *et al.* A conformational switch in syntaxin during exocytosis: role of munc18. *Embo Journal* **18**, 4372-4382 (1999).
48. Munson, M., Chen, X., Cocina, A.E., Schultz, S.M. & Hughson, F.M. Interactions within the yeast t-SNARE Sso1p that control SNARE complex assembly. *Nature Structural Biology* **7**, 894-902 (2000).
49. Misura, K.M.S., Scheller, R.H. & Weis, W.I. Three-dimensional structure of the neuronal-Sec1-syntaxin 1a complex. *Nature* **404**, 355-362 (2000).
50. Schafer, I.B. *et al.* The binding of Varp to VAMP7 traps VAMP7 in a closed, fusogenically inactive conformation. *Nature Structural & Molecular Biology* **19**, 1300-+ (2012).
51. Weimbs, T. *et al.* A conserved domain is present in different families of vesicular fusion proteins: A new superfamily. *Proceedings of the National Academy of Sciences of the United States of America* **94**, 3046-3051 (1997).
52. Weimbs, T., Mostov, K., Low, S.H. & Hofmann, R. A model for structural similarity between different SNARE complexes based on sequence relationships. *Trends in Cell Biology* **8**, 260-262 (1998).
53. Wesolowski, J. & Paumet, F. Intracellular bacteria encode inhibitory SNARE-like proteins. *Virulence* **1**, 319-324 (2010).
54. Margittai, M., Fasshauer, D., Pabst, S., Jahn, R. & Langen, R. Homo- and heterooligomeric SNARE complexes studied by site-directed spin labeling. *Journal of Biological Chemistry* **276**, 13169-13177 (2001).
55. Hanson, P.I., Roth, R., Morisaki, H., Jahn, R. & Heuser, J.E. Structure and conformational changes in NSF and its membrane receptor complexes visualized by quick-freeze/deep-etch electron microscopy. *Cell* **90**, 523-535 (1997).
56. Fasshauer, D., Otto, H., Eliason, W.K., Jahn, R. & Brunger, A.T. Structural changes are associated with soluble N-ethylmaleimide-sensitive fusion protein attachment protein receptor complex formation. *Journal of Biological Chemistry* **272**, 28036-28041 (1997).
57. Poirier, M.A. *et al.* The synaptic SNARE complex is a parallel four-stranded helical bundle. *Nature Structural Biology* **5**, 765-769 (1998).
58. Sutton, R.B., Fasshauer, D., Jahn, R. & Brunger, A.T. Crystal structure of a SNARE complex involved in synaptic exocytosis at 2.4 angstrom resolution. *Nature* **395**, 347-353 (1998).
59. Antonin, W. *et al.* A SNARE complex mediating fusion of late endosomes defines conserved properties of SNARE structure and function. *Embo Journal* **19**, 6453-6464 (2000).
60. Fasshauer, D., Sutton, R.B., Brunger, A.T. & Jahn, R. Conserved structural features of the synaptic fusion complex: SNARE proteins reclassified as Q- and R-SNAREs. *Proceedings of the National Academy of Sciences of the United States of America* **95**, 15781-15786 (1998).

61. Halemani, N.D., Bethani, I., Rizzoli, S.O. & Lang, T. Structure and Dynamics of a Two-Helix SNARE Complex in Live Cells. *Traffic* **11**, 394-404 (2010).
62. Rickman, C. *et al.* t-SNARE Protein Conformations Patterned by the Lipid Microenvironment. *Journal of Biological Chemistry* **285**, 13535-13541 (2010).
63. Rossi, G., Salminen, A., Rice, L.M., Brunger, A.T. & Brennwald, P. Analysis of a yeast SNARE complex reveals remarkable similarity to the neuronal SNARE complex and a novel function for the C terminus of the SNAP-25 homolog, Sec9. *Journal of Biological Chemistry* **272**, 16610-16617 (1997).
64. Fiebig, K.M., Rice, L.M., Pollock, E. & Brunger, A.T. Folding intermediates of SNARE complex assembly. *Nature Structural Biology* **6**, 117-123 (1999).
65. Li, F. *et al.* Energetics and dynamics of SNAREpin folding across lipid bilayers. *Nature Structural & Molecular Biology* **14**, 890-896 (2007).
66. Hua, Y.Y. & Scheller, R.H. Three SNARE complexes cooperate to mediate membrane fusion. *Proceedings of the National Academy of Sciences of the United States of America* **98**, 8065-8070 (2001).
67. Hernandez, J.M. *et al.* Membrane Fusion Intermediates via Directional and Full Assembly of the SNARE Complex. *Science* **336**, 1581-1584 (2012).
68. Gao, Y. *et al.* Single Reconstituted Neuronal SNARE Complexes Zipper in Three Distinct Stages. *Science* **337**, 1340-1343 (2012).
69. Min, D. *et al.* Mechanical unzipping and rezipping of a single SNARE complex reveals hysteresis as a force-generating mechanism. *Nature Communications* **4** (2013).
70. Lou, X.C. & Shin, Y.K. SNARE zippering. *Bioscience Reports* **36** (2016).
71. Chen, X.C. *et al.* Three-dimensional structure of the complexin/SNARE complex. *Neuron* **33**, 397-409 (2002).
72. Pabst, S. *et al.* Rapid and selective binding to the synaptic SNARE complex suggests a modulatory role of complexins in neuroexocytosis. *Journal of Biological Chemistry* **277**, 7838-7848 (2002).
73. Fernandez, I. *et al.* Three-dimensional structure of an evolutionarily conserved N-terminal domain of syntaxin 1A. *Cell* **94**, 841-849 (1998).
74. Rizo, J. & Sudhof, T.C. SNAREs and Munc18 in synaptic vesicle fusion. *Nature Reviews Neuroscience* **3**, 641-653 (2002).
75. Hayashi, T. *et al.* Synaptic vesicle membrane-fusion complex - action of clostridial neurotoxins on assembly. *Embo Journal* **13**, 5051-5061 (1994).
76. Hayashi, T., Yamasaki, S., Nauenburg, S., Binz, T. & Niemann, H. Disassembly of the reconstituted synaptic vesicle membrane-fusion complex in-vitro. *Embo Journal* **14**, 2317-2325 (1995).
77. Block, M.R., Glick, B.S., Wilcox, C.A., Wieland, F.T. & Rothman, J.E. Purification of an N-ethylmaleimide-sensitive protein catalyzing vesicular transport. *Proceedings of the National Academy of Sciences of the United States of America* **85**, 7852-7856 (1988).
78. Baker, R.W. & Hughson, F.M. Chaperoning SNARE assembly and disassembly. *Nature Reviews Molecular Cell Biology* **17**, 465-479 (2016).
79. Diaz, R., Mayorga, L.S., Weidman, P.J., Rothman, J.E. & Stahl, P.D. Vesicle fusion following receptor-mediated endocytosis requires a protein active in Golgi transport. *Nature* **339**, 398-400 (1989).
80. Beckers, C.J.M., Block, M.R., Glick, B.S., Rothman, J.E. & Balch, W.E. Vesicular transport between the endoplasmic-reticulum and the Golgi stack requires the NEM-sensitive fusion protein. *Nature* **339**, 397-398 (1989).

81. Nagiec, E.E., Bernstein, A. & Whiteheart, S.W. Each domain of the N-ethylmeleimide-sensitive fusion protein contributes to its transport activity. *Journal of Biological Chemistry* **270**, 29182-29188 (1995).
82. Wilson, D.W., Whiteheart, S.W., Wiedmann, M., Brunner, M. & Rothman, J.E. A mutlisubunit particle implicated in membrane-fusion. *Journal of Cell Biology* **117**, 531-538 (1992).
83. Whiteheart, S.W. *et al.* N-ethylmaleimide-sensitive fusion protein - A trimeric ATPase whose hydrolysis of ATP is required for membrane-fusion. *Journal of Cell Biology* **126**, 945-954 (1994).
84. Zhao, M.L. *et al.* Mechanistic insights into the recycling machine of the SNARE complex. *Nature* **518**, 61-+ (2015).
85. Lobingier, B.T., Nickerson, D.P., Lo, S.Y. & Merz, A.J. SM proteins Sly1 and Vps33 co-assemble with Sec17 and SNARE 5 complexes to oppose SNARE disassembly by Sec18. *Elife* **3** (2014).
86. Fasshauer, D., Antonin, W., Margittai, M., Pabst, S. & Jahn, R. Mixed and non-cognate SNARE complexes - Characterization of assembly and biophysical properties. *Journal of Biological Chemistry* **274**, 15440-15446 (1999).
87. Brandhorst, D. *et al.* Homotypic fusion of early endosomes: SNAREs do not determine fusion specificity. *Proceedings of the National Academy of Sciences of the United States of America* **103**, 2701-2706 (2006).
88. Bethani, I. *et al.* The specificity of SNARE pairing in biological membranes is mediated by both proof-reading and spatial segregation. *Embo Journal* **26**, 3981-3992 (2007).
89. Sudhof, T.C. & Rothman, J.E. Membrane Fusion: Grappling with SNARE and SM Proteins. *Science* **323**, 474-477 (2009).
90. Hata, Y., Slaughter, C.A. & Sudhof, T.C. Synaptic vesicle fusion complex contains Unc-18 homolog bound to syntaxin. *Nature* **366**, 347-351 (1993).
91. Peterson, M.R. & Emr, S.D. The class C Vps complex functions at multiple stages of the vacuolar transport pathway. *Traffic* **2**, 476-486 (2001).
92. Dulubova, I. *et al.* How Tlg2p/syntaxin 16 'snares' Vps45. *Embo Journal* **21**, 3620-3631 (2002).
93. Yamaguchi, T. *et al.* Sly1 binds to Golgi and ER syntaxins via a conserved N-terminal peptide motif. *Developmental Cell* **2**, 295-305 (2002).
94. Verhage, M. *et al.* Synaptic assembly of the brain in the absence of neurotransmitter secretion. *Science* **287**, 864-869 (2000).
95. Shen, J.S., Tareste, D.C., Paumet, F., Rothman, J.E. & Melia, T.J. Selective activation of cognate SNAREpins by Sec1/Munc18 proteins. *Cell* **128**, 183-195 (2007).
96. Carr, C.M., Grote, E., Munson, M., Hughson, F.M. & Novick, P.J. Sec1p binds to SNARE complexes and concentrates at sites of secretion. *Journal of Cell Biology* **146**, 333-344 (1999).
97. Nicholson, K.L. *et al.* Regulation of SNARE complex assembly by an N-terminal domain of the t-SNARE Sso1p. *Nature Structural Biology* **5**, 793-802 (1998).
98. Yang, B., Steegmaier, M., Gonzalez, L.C. & Scheller, R.H. nSec1 binds a closed conformation of syntaxin1A. *Journal of Cell Biology* **148**, 247-252 (2000).
99. Christie, M.P. *et al.* Low-resolution solution structures of Munc18:Syntaxin protein complexes indicate an open binding mode driven by the Syntaxin N-peptide. *Proceedings of the National Academy of Sciences of the United States of America* **109**, 9816-9821 (2012).

100. Antonin, W. *et al.* The N-terminal domains of syntaxin 7 and vti1b form three-helix bundles that differ in their ability to regulate SNARE complex assembly. *Journal of Biological Chemistry* **277**, 36449-36456 (2002).
101. Bracher, A. & Weissenhorn, W. Structural basis for the Golgi membrane recruitment of Sly1p by Sed5p. *Embo Journal* **21**, 6114-6124 (2002).
102. Baker, R.W., Jeffrey, P.D. & Hughson, F.M. Crystal Structures of the Sec1/Munc18 (SM) Protein Vps33, Alone and Bound to the Homotypic Fusion and Vacuolar Protein Sorting (HOPS) Subunit Vps16. *Plos One* **8** (2013).
103. Carpp, L.N., Ciufo, L.F., Shanks, S.G., Boyd, A. & Bryant, N.J. The Sec1p/Munc18 protein Vps45p binds its cognate SNARE proteins via two distinct modes. *Journal of Cell Biology* **173**, 927-936 (2006).
104. Margittai, M. *et al.* Single-molecule fluorescence resonance energy transfer reveals a dynamic equilibrium between closed and open conformations of syntaxin 1. *Proceedings of the National Academy of Sciences of the United States of America* **100**, 15516-15521 (2003).
105. Dawidowski, D. & Cafiso, D.S. Allosteric Control of Syntaxin 1a by Munc18-1: Characterization of the Open and Closed Conformations of Syntaxin. *Biophysical Journal* **104**, 1585-1594 (2013).
106. Gerber, S.H. *et al.* Conformational switch of syntaxin-1 controls synaptic vesicle fusion. *Science* **321**, 1507-1510 (2008).
107. Meijer, M. *et al.* Munc18-1 mutations that strongly impair SNARE-complex binding support normal synaptic transmission. *Embo Journal* **31**, 2156-2168 (2012).
108. Medine, C.N., Rickman, C., Chamberlain, L.H. & Duncan, R.R. Munc18-1 prevents the formation of ectopic SNARE complexes in living cells. *Journal of Cell Science* **120**, 4407-4415 (2007).
109. Rodkey, T.L., Liu, S., Barry, M. & McNew, J.A. Munc18a Scaffolds SNARE Assembly to Promote Membrane Fusion. *Molecular Biology of the Cell* **19**, 5422-5434 (2008).
110. Smyth, A.M., Rickman, C. & Duncan, R.R. Vesicle Fusion Probability Is Determined by the Specific Interactions of Munc18. *Journal of Biological Chemistry* **285**, 38141-38148 (2010).
111. Kavanagh, D.M. *et al.* A molecular toggle after exocytosis sequesters the presynaptic syntaxin1a molecules involved in prior vesicle fusion. *Nature Communications* **5** (2014).
112. Zhou, P. *et al.* Syntaxin-1 N-peptide and H-abc-domain perform distinct essential functions in synaptic vesicle fusion. *Embo Journal* **32**, 159-171 (2013).
113. Rathore, S.S. *et al.* Syntaxin N-terminal peptide motif is an initiation factor for the assembly of the SNARE-Sec1/Munc18 membrane fusion complex. *Proceedings of the National Academy of Sciences of the United States of America* **107**, 22399-22406 (2010).
114. Hu, S.H. *et al.* Possible roles for Munc18-1 domain 3a and Syntaxin1 N-peptide and C-terminal anchor in SNARE complex formation. *Proceedings of the National Academy of Sciences of the United States of America* **108**, 1040-1045 (2011).
115. Rickman, C. & Duncan, R.R. Munc18/Syntaxin Interaction Kinetics Control Secretory Vesicle Dynamics. *Journal of Biological Chemistry* **285**, 3965-3972 (2010).

116. Ma, C., Li, W., Xu, Y.B. & Rizo, J. Munc13 mediates the transition from the closed syntaxin-Munc18 complex to the SNARE complex. *Nature Structural & Molecular Biology* **18**, 542-U206 (2011).
117. Hong, W.J. SNARES and traffic. *Biochimica Et Biophysica Acta-Molecular Cell Research* **1744**, 120-144 (2005).
118. Tang, J. *et al.* A complexin/synaptotagmin 1 switch controls fast synaptic vesicle exocytosis. *Cell* **126**, 1175-1187 (2006).
119. Novikoff, A., Beaufay, H. & De Duve, C. Electron microscopy of lysosome-rich fractions from rat liver. *Journal of Biophysical and Biochemical Cytology* **2**, 179-184 (1956).
120. Wilke, S., Krausze, J. & Bussow, K. Crystal structure of the conserved domain of the DC lysosomal associated membrane protein: implications for the lysosomal glycocalyx. *Bmc Biology* **10** (2012).
121. Sleat, D.E. *et al.* The human brain mannose 6-phosphate glycoproteome: A complex mixture composed of multiple isoforms of many soluble lysosomal proteins. *Proteomics* **5**, 1520-1532 (2005).
122. Geuze, H.J., Slot, J.W., Strous, J.A.M., Hasilik, A. & Vonfigura, K. Possible pathways for lysosomal-enzyme delivery. *Journal of Cell Biology* **101**, 2253-2262 (1985).
123. Janvier, K. & Bonifacino, J.S. Role of the endocytic machinery in the sorting of lysosome-associated membrane proteins. *Molecular Biology of the Cell* **16**, 4231-4242 (2005).
124. Mindell, J.A. Lysosomal Acidification Mechanisms. *Annual Review of Physiology, Vol 74* **74**, 69-86 (2012).
125. Thwaites, D.T. & Anderson, C.M.H. The SLC36 family of proton-coupled amino acid transporters and their potential role in drug transport. *British Journal of Pharmacology* **164**, 1802-1816 (2011).
126. Klionsky, D.J. The molecular machinery of autophagy: unanswered questions. *Journal of Cell Science* **118**, 7-18 (2005).
127. Kaushik, S. & Cuervo, A.M. Chaperone-mediated autophagy: a unique way to enter the lysosome world. *Trends in Cell Biology* **22**, 407-417 (2012).
128. Li, W.-w., Li, J. & Bao, J.-k. Microautophagy: lesser-known self-eating. *Cellular and Molecular Life Sciences* **69**, 1125-1136 (2012).
129. Klionsky, D.J. Autophagy: from phenomenology to molecular understanding in less than a decade. *Nature Reviews Molecular Cell Biology* **8**, 931-937 (2007).
130. Ravikumar, B. *et al.* Inhibition of mTOR induces autophagy and reduces toxicity of polyglutamine expansions in fly and mouse models of Huntington disease. *Nature Genetics* **36**, 585-595 (2004).
131. Kim, I., Rodriguez-Enriquez, S. & Lemasters, J.J. Selective degradation of mitochondria by mitophagy. *Archives of Biochemistry and Biophysics* **462**, 245-253 (2007).
132. Sandilands, E. *et al.* Autophagic targeting of Src promotes cancer cell survival following reduced FAK signallin. *Nature Cell Biology* **14**, 51-U76 (2012).
133. Onodera, J. & Ohsumi, Y. Autophagy is required for maintenance of amino acid levels and protein synthesis under nitrogen starvation. *Journal of Biological Chemistry* **280**, 31582-31586 (2005).
134. Matthews, C., van Holde, K. & Ahern, K. *Biochemistry*, Edn. Third. (Prentice Hall, New Jersey; 1999).

135. Kuma, A. *et al.* The role of autophagy during the early neonatal starvation period. *Nature* **432**, 1032-1036 (2004).
136. Lum, J.J. *et al.* Growth factor regulation of autophagy and cell survival in the absence of apoptosis. *Cell* **120**, 237-248 (2005).
137. Kim, J., Kundu, M., Viollet, B. & Guan, K.-L. AMPK and mTOR regulate autophagy through direct phosphorylation of Ulk1. *Nature Cell Biology* **13**, 132-U171 (2011).
138. Djavaheri-Mergny, M. *et al.* NF-kappa B activation represses tumor necrosis factor-alpha-induced autophagy. *Journal of Biological Chemistry* **281**, 30373-30382 (2006).
139. Thurston, T.L.M., Ryzhakov, G., Bloor, S., von Muhlinen, N. & Randow, F. The TBK1 adaptor and autophagy receptor NDP52 restricts the proliferation of ubiquitin-coated bacteria. *Nature Immunology* **10**, 1215-U1103 (2009).
140. Huang, J. & Brumell, J.H. NADPH oxidases contribute to autophagy regulation. *Autophagy* **5**, 887-889 (2009).
141. Pilli, M. *et al.* TBK-1 Promotes Autophagy-Mediated Antimicrobial Defense by Controlling Autophagosome Maturation. *Immunity* **37**, 223-234 (2012).
142. Deretic, V., Saitoh, T. & Akira, S. Autophagy in infection, inflammation and immunity. *Nature Reviews Immunology* **13**, 722-737 (2013).
143. Li, S. *et al.* Sterical Hindrance Promotes Selectivity of the Autophagy Cargo Receptor NDP52 for the Danger Receptor Galectin-8 in Antibacterial Autophagy. *Science Signaling* **6** (2013).
144. Gannage, M. *et al.* Matrix Protein 2 of Influenza A Virus Blocks Autophagosome Fusion with Lysosomes. *Cell Host & Microbe* **6**, 367-380 (2009).
145. Schmid, D., Pypaert, M. & Munz, C. Antigen-loading compartments for major histocompatibility complex class II molecules continuously receive input from autophagosomes. *Immunity* **26**, 79-92 (2007).
146. Trombetta, E.S., Ebersold, M., Garrett, W., Pypaert, M. & Mellman, I. Activation of lysosomal function during dendritic cell maturation. *Science* **299**, 1400-1403 (2003).
147. Furuta, K., Walseng, E. & Roche, P.A. Internalizing MHC class II-peptide complexes are ubiquitinated in early endosomes and targeted for lysosomal degradation. *Proceedings of the National Academy of Sciences of the United States of America* **110**, 20188-20193 (2013).
148. Shoji-Kawata, S. *et al.* Identification of a candidate therapeutic autophagy-inducing peptide. *Nature* **494**, 201-206 (2013).
149. Rabouille, C., Malhotra, V. & Nickel, W. Diversity in unconventional protein secretion. *Journal of Cell Science* **125**, 5251-5255 (2012).
150. Duran, J.M., Anjard, C., Stefan, C., Loomis, W.F. & Malhotra, V. Unconventional secretion of Acb1 is mediated by autophagosomes. *Journal of Cell Biology* **188**, 527-536 (2010).
151. Bruns, C., McCaffery, J.M., Curwin, A.J., Duran, J.M. & Malhotra, V. Biogenesis of a novel compartment for autophagosome-mediated unconventional protein secretion. *Journal of Cell Biology* **195**, 979-992 (2011).
152. Andrei, C. *et al.* The secretory route of the leaderless protein interleukin 1 beta involves exocytosis of endolysosome-related vesicles. *Molecular Biology of the Cell* **10**, 1463-1475 (1999).
153. Tsukada, M. & Ohsumi, Y. Isolation and characterization of autophagy-defective mutants of Saccharomyces-cerevisiae. *Febs Letters* **333**, 169-174 (1993).

154. Feng, Y.C., He, D., Yao, Z.Y. & Klionsky, D.J. The machinery of macroautophagy. *Cell Research* **24**, 24-41 (2014).
155. Suzuki, K. *et al.* The pre-autophagosomal structure organized by concerted functions of APG genes is essential for autophagosome formation. *Embo Journal* **20**, 5971-5981 (2001).
156. Mizushima, N. *et al.* Dissection of autophagosome formation using Apg5-deficient mouse embryonic stem cells. *Journal of Cell Biology* **152**, 657-667 (2001).
157. Axe, E.L. *et al.* Autophagosome formation from membrane compartments enriched in phosphatidylinositol 3-phosphate and dynamically connected to the endoplasmic reticulum. *Journal of Cell Biology* **182**, 685-701 (2008).
158. Hamasaki, M. *et al.* Autophagosomes form at ER-mitochondria contact sites. *Nature* **495**, 389-393 (2013).
159. Koyama-Honda, I., Itakura, E., Fujiwara, T.K. & Mizushima, N. Temporal analysis of recruitment of mammalian ATG proteins to the autophagosome formation site. *Autophagy* **9**, 1491-1499 (2013).
160. Ropolo, A. *et al.* The pancreatitis-induced vacuole membrane protein 1 triggers autophagy in mammalian cells. *Journal of Biological Chemistry* **282**, 37124-37133 (2007).
161. Suzuki, K., Kubota, Y., Sekito, T. & Ohsumi, Y. Hierarchy of Atg proteins in pre-autophagosomal structure organization. *Genes to Cells* **12**, 209-218 (2007).
162. Itakura, E. & Mizushima, N. Characterization of autophagosome formation site by a hierarchical analysis of mammalian Atg proteins. *Autophagy* **6**, 764-776 (2010).
163. Kamada, Y. *et al.* Tor-mediated induction of autophagy via an Apg1 protein kinase complex. *Journal of Cell Biology* **150**, 1507-1513 (2000).
164. Yeh, Y.-Y., Shah, K.H. & Herman, P.K. An Atg13 Protein-mediated Self-association of the Atg1 Protein Kinase Is Important for the Induction of Autophagy. *Journal of Biological Chemistry* **286**, 28931-28939 (2011).
165. Yamamoto, H. *et al.* The Intrinsically Disordered Protein Atg13 Mediates Supramolecular Assembly of Autophagy Initiation Complexes. *Developmental Cell* **38**, 86-99 (2016).
166. Hosokawa, N. *et al.* Nutrient-dependent mTORC1 Association with the ULK1-Atg13-FIP200 Complex Required for Autophagy. *Molecular Biology of the Cell* **20**, 1981-1991 (2009).
167. Mercer, C.A., Kaliappan, A. & Dennis, P.B. A novel, human Atg13 binding protein, Atg101, interacts with ULK1 and is essential for macroautophagy. *Autophagy* **5**, 649-662 (2009).
168. Hara, T. *et al.* FIP200, a ULK-interacting protein, is required for autophagosome formation in mammalian cells. *Journal of Cell Biology* **181**, 497-510 (2008).
169. Di Bartolomeo, S. *et al.* The dynamic interaction of AMBRA1 with the dynein motor complex regulates mammalian autophagy. *Journal of Cell Biology* **191**, 155-168 (2010).
170. Jao, C.C., Ragusa, M.J., Stanley, R.E. & Hurley, J.H. A HORMA domain in Atg13 mediates PI 3-kinase recruitment in autophagy. *Proceedings of the National Academy of Sciences of the United States of America* **110**, 5486-5491 (2013).
171. Marat, A.L. & Haucke, V. Phosphatidylinositol 3-phosphates-at the interface between cell signalling and membrane traffic. *Embo Journal* **35**, 561-579 (2016).

172. Panaretou, C., Domin, J., Cockcroft, S. & Waterfield, M.D. Characterization of p150, an adaptor protein for the human phosphatidylinositol (PtdIns) 5-kinase - Substrate presentation by phosphatedylinositol transfer protein to the p150-PtdIns 3-kinase complex. *Journal of Biological Chemistry* **272**, 2477-2485 (1997).
173. Molejon, M.I., Ropolo, A., Lo Re, A., Boggio, V. & Vaccaro, M.I. The VMP1-Beclin 1 interaction regulates autophagy induction. *Scientific Reports* **3** (2013).
174. Itakura, E., Kishi, C., Inoue, K. & Mizushima, N. Beclin 1 Forms Two Distinct Phosphatidylinositol 3-Kinase Complexes with Mammalian Atg14 and UVRAG. *Molecular Biology of the Cell* **19**, 5360-5372 (2008).
175. Matsunaga, K. *et al.* Autophagy requires endoplasmic reticulum targeting of the PI3-kinase complex via Atg14L. *Journal of Cell Biology* **190**, 511-521 (2010).
176. Liang, C. *et al.* Beclin1-binding UVRAG targets the class C Vps complex to coordinate autophagosome maturation and endocytic trafficking. *Nature Cell Biology* **10**, 776-787 (2008).
177. Jiang, P. *et al.* The HOPS complex mediates autophagosome-lysosome fusion through interaction with syntaxin 17. *Molecular Biology of the Cell* **25**, 1327-1337 (2014).
178. Polson, H.E.J. *et al.* Mammalian Atg18 (WIPI2) localizes to omegasome-anchored phagophores and positively regulates LC3 lipidation. *Autophagy* **6**, 506-522 (2010).
179. Fan, W., Nassiri, A. & Zhong, Q. Autophagosome targeting and membrane curvature sensing by Barkor/Atg14(L). *Proceedings of the National Academy of Sciences of the United States of America* **108**, 7769-7774 (2011).
180. Ragusa, M.J., Stanley, R.E. & Hurley, J.H. Architecture of the Atg17 Complex as a Scaffold for Autophagosome Biogenesis. *Cell* **151**, 1501-1512 (2012).
181. Karanasios, E. *et al.* Dynamic association of the ULK1 complex with omegasomes during autophagy induction. *Journal of Cell Science* **126** (2013).
182. Yla-Anttila, P., Vihinen, H., Jokita, E. & Eskelinen, E.-L. 3D tomography reveals connections between the phagophore and endoplasmic reticulum. *Autophagy* **5**, 1180-1185 (2009).
183. Hayashi-Nishino, M. *et al.* A subdomain of the endoplasmic reticulum forms a cradle for autophagosome formation. *Nature Cell Biology* **11**, 1433-U1102 (2009).
184. Wullschleger, S., Loewith, R. & Hall, M.N. TOR signaling in growth and metabolism. *Cell* **124**, 471-484 (2006).
185. Loewith, R. *et al.* Two TOR complexes, only one of which is rapamycin sensitive, have distinct roles in cell growth control. *Molecular Cell* **10**, 457-468 (2002).
186. Noda, T. & Ohsumi, Y. Tor, a phosphatidylinositol kinase homologue, controls autophagy in yeast. *Journal of Biological Chemistry* **273**, 3963-3966 (1998).
187. Heitman, J., Movva, N.R. & Hall, M.N. Targets for cell-cycle arrest by the immunosuppressant rapamycin in yeast. *Science* **253**, 905-909 (1991).
188. Schmidt, A., Kunz, J. & Hall, M.N. TOR2 is required for organization of the actin cytoskeleton in yeast. *Proceedings of the National Academy of Sciences of the United States of America* **93**, 13780-13785 (1996).

189. Lorenz, M.C. & Heitman, J. TOR mutations confer rapamycin resistance by preventing interaction with FKBP12-rapamycin. *Journal of Biological Chemistry* **270**, 27531-27537 (1995).
190. Yuan, H.X., Russell, R.C. & Guan, K.L. Regulation of PIK3C3/VPS34 complexes by MTOR in nutrient stress-induced autophagy. *Autophagy* **9**, 1983-1995 (2013).
191. Roczniak-Ferguson, A. *et al.* The Transcription Factor TFEB Links mTORC1 Signaling to Transcriptional Control of Lysosome Homeostasis. *Science Signaling* **5** (2012).
192. Settembre, C. *et al.* TFEB Links Autophagy to Lysosomal Biogenesis. *Science* **332**, 1429-1433 (2011).
193. Groenewoud, M.J. & Zwartkruis, F.J.T. Rheb and Rags come together at the lysosome to activate mTORC1. *Biochemical Society Transactions* **41**, 951-955 (2013).
194. Kang, R., Zeh, H.J., Lotze, M.T. & Tang, D. The Beclin 1 network regulates autophagy and apoptosis. *Cell Death and Differentiation* **18**, 571-580 (2011).
195. Liang, X.H. *et al.* Protection against fatal Sindbis virus encephalitis by Beclin, a novel Bcl-2-interacting protein. *Journal of Virology* **72**, 8586-8596 (1998).
196. Maiuri, M.C. *et al.* Functional and physical interaction between Bcl-X-L and a BH3-like domain in Beclin-1. *Embo Journal* **26**, 2527-2539 (2007).
197. Pattingre, S. *et al.* Bcl-2 antiapoptotic proteins inhibit Beclin 1-dependent autophagy. *Cell* **122**, 927-939 (2005).
198. Wang, R.C. *et al.* Akt-Mediated Regulation of Autophagy and Tumorigenesis Through Beclin 1 Phosphorylation. *Science* **338**, 956-959 (2012).
199. Sarbassov, D.D. & Sabatini, D.M. Redox regulation of the nutrient-sensitive raptor-mTOR pathway and complex. *Journal of Biological Chemistry* **280**, 39505-39509 (2005).
200. Chang, N.C., Nguyen, M., Germain, M. & Shore, G.C. Antagonism of Beclin 1-dependent autophagy by BCL-2 at the endoplasmic reticulum requires NAF-1. *Embo Journal* **29**, 606-618 (2010).
201. Biazik, J., Yla-Anttila, P., Vihinen, H., Jokitalo, E. & Eskelinen, E.L. Ultrastructural relationship of the phagophore with surrounding organelles. *Autophagy* **11**, 439-451 (2015).
202. Hailey, D.W. *et al.* Mitochondria Supply Membranes for Autophagosome Biogenesis during Starvation. *Cell* **141**, 656-667 (2010).
203. Zoppino, F.C.M., Militello, R.D., Slavin, I., Alvarez, C. & Colombo, M.I. Autophagosome Formation Depends on the Small GTPase Rab1 and Functional ER Exit Sites. *Traffic* **11**, 1246-1261 (2010).
204. Graef, M., Friedman, J.R., Graham, C., Babu, M. & Nunnari, J. ER exit sites are physical and functional core autophagosome biogenesis components. *Molecular Biology of the Cell* **24**, 2918-2931 (2013).
205. Geng, J.F., Nair, U., Yasumura-Yorimitsu, K. & Klionsky, D.J. Post-Golgi Sec Proteins Are Required for Autophagy in Saccharomyces cerevisiae. *Molecular Biology of the Cell* **21**, 2257-2269 (2010).
206. van der Vaart, A., Griffith, J. & Reggiori, F. Exit from the Golgi Is Required for the Expansion of the Autophagosomal Phagophore in Yeast Saccharomyces cerevisiae. *Molecular Biology of the Cell* **21**, 2270-2284 (2010).
207. Mari, M. *et al.* An Atg9-containing compartment that functions in the early steps of autophagosome biogenesis. *Journal of Cell Biology* **190**, 1005-1022 (2010).

208. Yamamoto, H. *et al.* Atg9 vesicles are an important membrane source during early steps of autophagosome formation. *Journal of Cell Biology* **198**, 219-233 (2012).
209. Nair, U. *et al.* SNARE Proteins Are Required for Macroautophagy. *Cell* **146**, 290-302 (2011).
210. Moreau, K., Ravikumar, B., Renna, M., Puri, C. & Rubinsztein, D.C. Autophagosome Precursor Maturation Requires Homotypic Fusion. *Cell* **146**, 303-317 (2011).
211. Knaevelsrud, H. *et al.* Membrane remodeling by the PX-BAR protein SNX18 promotes autophagosome formation. *Journal of Cell Biology* **202**, 331-349 (2013).
212. Alemu, E.A. *et al.* ATG8 Family Proteins Act as Scaffolds for Assembly of the ULK Complex. *Journal of Biological Chemistry* **287** (2012).
213. Xie, Z., Nair, U. & Klionsky, D.J. Atg8 controls phagophore expansion during autophagosome formation. *Molecular Biology of the Cell* **19**, 3290-3298 (2008).
214. Weidberg, H. *et al.* LC3 and GATE-16/GABARAP subfamilies are both essential yet act differently in autophagosome biogenesis. *Embo Journal* **29**, 1792-1802 (2010).
215. Nath, S. *et al.* Lipidation of the LC3/GABARAP family of autophagy proteins relies on a membrane-curvature-sensing domain in Atg3. *Nature Cell Biology* **16**, 415-U480 (2014).
216. Kaufmann, A., Beier, V., Franquelim, H.G. & Wollert, T. Molecular Mechanism of Autophagic Membrane-Scaffold Assembly and Disassembly. *Cell* **156**, 469-481 (2014).
217. Mi, N. *et al.* CapZ regulates autophagosomal membrane shaping by promoting actin assembly inside the isolation membrane. *Nature Cell Biology* **17** (2015).
218. Coutts, A.S. & La Thangue, N.B. Actin nucleation by WH2 domains at the autophagosome. *Nature Communications* **6** (2015).
219. Aguilera, M.O., Beron, W. & Colombo, M.I. The actin cytoskeleton participates in the early events of autophagosome formation upon starvation induced autophagy. *Autophagy* **8**, 1590-1603 (2012).
220. Ichimura, Y. *et al.* A ubiquitin-like system mediates protein lipidation. *Nature* **408**, 488-492 (2000).
221. Fujita, N. *et al.* The Atg16L complex specifies the site of LC3 lipidation for membrane biogenesis in autophagy. *Molecular Biology of the Cell* **19**, 2092-2100 (2008).
222. Dooley, H.C. *et al.* WIPI2 Links LC3 Conjugation with PI3P, Autophagosome Formation, and Pathogen Clearance by Recruiting Atg12-5-16L1. *Molecular Cell* **55**, 238-252 (2014).
223. Kirisako, T. *et al.* The reversible modification regulates the membrane-binding state of Apg8/Aut7 essential for autophagy and the cytoplasm to vacuole targeting pathway. *Journal of Cell Biology* **151**, 263-275 (2000).
224. Kabeya, Y. *et al.* LC3, GABARAP and GATE16 localize to autophagosomal membrane depending on form-II formation. *Journal of Cell Science* **117**, 2805-2812 (2004).
225. Klionsky, D.J. *et al.* Guidelines for the use and interpretation of assays for monitoring autophagy (3rd edition). *Autophagy* **12**, 1-222 (2016).

226. Priault, M. *et al.* Impairing the bioenergetic status and the biogenesis of mitochondria triggers mitophagy in yeast. *Cell Death and Differentiation* **12**, 1613-1621 (2005).
227. Levine, B. Eating oneself and uninvited guests: Autophagy-related pathways in cellular defense. *Cell* **120**, 159-162 (2005).
228. Pankiv, S. *et al.* p62/SQSTM1 binds directly to Atg8/LC3 to facilitate degradation of ubiquitinated protein aggregates by autophagy. *Journal of Biological Chemistry* **282**, 24131-24145 (2007).
229. Liu, L. *et al.* Mitochondrial outer-membrane protein FUNDC1 mediates hypoxia-induced mitophagy in mammalian cells. *Nature Cell Biology* **14**, 177-185 (2012).
230. Novak, I. *et al.* Nix is a selective autophagy receptor for mitochondrial clearance. *Embo Reports* **11**, 45-51 (2010).
231. Kirkin, V. *et al.* A Role for NBR1 in Autophagosomal Degradation of Ubiquitinated Substrates. *Molecular Cell* **33**, 505-516 (2009).
232. Wild, P. *et al.* Phosphorylation of the Autophagy Receptor Optineurin Restricts Salmonella Growth. *Science* **333**, 228-233 (2011).
233. Ogawa, M. *et al.* A Tecpr1-Dependent Selective Autophagy Pathway Targets Bacterial Pathogens. *Cell Host & Microbe* **9**, 376-389 (2011).
234. Nakatogawa, H., Ichimura, Y. & Ohsumi, Y. Atg8, a ubiquitin-like protein required for autophagosome formation, mediates membrane tethering and hemifusion. *Cell* **130**, 165-178 (2007).
235. Lu, Y., Zhang, Z., Sun, D., Sweeney, S.T. & Gao, F.-B. Syntaxin 13, a Genetic Modifier of Mutant CHMP2B in Frontotemporal Dementia, Is Required for Autophagosome Maturation. *Molecular Cell* **52**, 264-271 (2013).
236. Schmidt, O. & Teis, D. The ESCRT machinery. *Current Biology* **22**, R116-R120 (2012).
237. Rusten, T.E. *et al.* ESCRTs and Fab1 regulate distinct steps of autophagy. *Current Biology* **17**, 1817-1825 (2007).
238. Korolchuk, V.I. *et al.* Lysosomal positioning coordinates cellular nutrient responses. *Nature Cell Biology* **13**, 453-U242 (2011).
239. Kimura, S., Noda, T. & Yoshimori, T. Dynein-dependent Movement of Autophagosomes Mediates Efficient Encounters with Lysosomes. *Cell Structure and Function* **33**, 109-122 (2008).
240. Fass, E., Shvets, E., Degani, I., Hirschberg, K. & Elazar, Z. Microtubules support production of starvation-induced autophagosomes but not their targeting and fusion with lysosomes. *Journal of Biological Chemistry* **281**, 36303-36316 (2006).
241. Gordon, P.B. & Seglen, P.O. Prelysosomal convergence of autophagic and endocytic pathways. *Biochemical and Biophysical Research Communications* **151**, 40-47 (1988).
242. Stromhaug, P.E. & Seglen, P.O. Evidence for acidity of prelysosomal autophagic endocytic vacuoles (amphisomes). *Biochemical Journal* **291**, 115-121 (1993).
243. Futter, C.E., Pearse, A., Hewlett, L.J. & Hopkins, C.R. Multivesicular endosomes containing internalized EGF-EGF receptor complexes mature and then fuse directly with lysosomes. *Journal of Cell Biology* **132**, 1011-1023 (1996).
244. Lawrence, B.P. & Brown, W.J. Autophagic vacuoles rapidly fuse with preexisting lysosomes in cultured-hepatocytes. *Journal of Cell Science* **102**, 515-526 (1992).

245. Tooze, J. *et al.* In exocrine pancreas, the basolateral endocytic pathway converges with the autophagic pathway immediately after the early endosome. *Journal of Cell Biology* **111**, 329-345 (1990).
246. Pryor, P.R. *et al.* Combinatorial SNARE complexes with VAMP7 or VAMP8 define different late endocytic fusion events. *Embo Reports* **5**, 590-595 (2004).
247. Furuta, N., Fujita, N., Noda, T., Yoshimori, T. & Amano, A. Combinational Soluble N-Ethylmaleimide-sensitive Factor Attachment Protein Receptor Proteins VAMP8 and Vti1b Mediate Fusion of Antimicrobial and Canonical Autophagosomes with Lysosomes. *Molecular Biology of the Cell* **21**, 1001-1010 (2010).
248. Itakura, E., Kishi-Itakura, C. & Mizushima, N. The Hairpin-type Tail-Anchored SNARE Syntaxin 17 Targets to Autophagosomes for Fusion with Endosomes/Lysosomes. *Cell* **151**, 1256-1269 (2012).
249. Takats, S. *et al.* Autophagosomal Syntaxin 17-dependent lysosomal degradation maintains neuronal function in Drosophila. *Journal of Cell Biology* **201**, 531-539 (2013).
250. Marcelo Fader, C., German Sanchez, D., Belen Mestre, M. & Colombo, M.I. TI-VAMP/VAMP7 and VAMP3/cellubrevin: two v-SNARE proteins involved in specific steps of the autophagy/multivesicular body pathways. *Biochimica Et Biophysica Acta-Molecular Cell Research* **1793**, 1901-1916 (2009).
251. Jean, S., Cox, S., Nassari, S. & Kiger, A.A. Starvation-induced MTMR13 and RAB21 activity regulates VAMP8 to promote autophagosome-lysosome fusion. *Embo Reports* **16**, 297-311 (2015).
252. Guo, B. *et al.* O-GlcNAc-modification of SNAP-29 regulates autophagosome maturation. *Nature Cell Biology* **16**, 1215-U1202 (2014).
253. Diao, J. *et al.* ATG14 promotes membrane tethering and fusion of autophagosomes to endolysosomes. *Nature* **520** (2015).
254. Yu, L. *et al.* Termination of autophagy and reformation of lysosomes regulated by mTOR. *Nature* **465**, 942-U911 (2010).
255. Hung, Y.-H., Chen, L.M.-W., Yang, J.-Y. & Yang, W.Y. Spatiotemporally controlled induction of autophagy-mediated lysosome turnover. *Nature Communications* **4** (2013).
256. Sancak, Y. *et al.* Ragulator-Rag Complex Targets mTORC1 to the Lysosomal Surface and Is Necessary for Its Activation by Amino Acids. *Cell* **141**, 290-303 (2010).
257. Rong, Y.G. *et al.* Clathrin and phosphatidylinositol-4,5-bisphosphate regulate autophagic lysosome reformation. *Nature Cell Biology* **14** (2012).
258. Munson, M.J. *et al.* mTOR activates the VPS34-UVRAG complex to regulate autolysosomal tubulation and cell survival. *Embo Journal* **34**, 2272-2290 (2015).
259. Puri, C., Renna, M., Bento, C.F., Moreau, K. & Rubinsztein, D.C. ATG16L1 meets ATG9 in recycling endosomes Additional roles for the plasma membrane and endocytosis in autophagosome biogenesis. *Autophagy* **10**, 182-184 (2014).
260. Croft, W.J. *Under the Microscope: A Brief History of Microscopy*. (World Scientific Publishing Co. Pte. Ltd., 2006).
261. Heinrichs, J. Nature Milestones Light Microscopy: Stains and fluorescent dyes (2009). Available at: http://www.nature.com/milestones/milelight/full/milelight2002 (Accessed: 7th January 2017).

262. Zernike, F. Phase contrast, a new method for the microscopic observation of transparent objects Part II. *Physica* **9**, 974-986 (1942).
263. Heimstädt, O. Das Fluoreszenzmikroskop. *Z. Wiss. Mikrosk . Z. Wiss. Mikrosk.* **2828**, 330–337 (1911).
264. Coons, A.H., Creech, H.J. & Jones, R.N. Immunological properties of an antibody containing a fluorescent group. *Proceedings of the Society for Experimental Biology and Medicine* **47**, 200-202 (1941).
265. Chalfie, M., Tu, Y., Euskirchen, G., Ward, W.W. & Prasher, D.C. Green fluorescent protein as a marker for gene-expression. *Science* **263**, 802-805 (1994).
266. Stokes, G. On the Change of Refrangibility of Light. *Philosophical Transactions of the Royal Society of London* **142**, 463–562 (1852).
267. Lakowicz, J. *Principles of Fluorescence Spectroscopy*, Edn. Third. (Springer, US; 2006).
268. Sluder, G. & Wolf, D.E. Methods in Cell Biology: Digital Microscopy, Edn. Fourth (Elsevier Academic Press Inc, San Diego; 2013).
269. Dunn, K.W., Kamocka, M.M. & McDonald, J.H. A practical guide to evaluating colocalization in biological microscopy. *American Journal of Physiology-Cell Physiology* **300**, C723-C742 (2011).
270. Axelrod, D., Koppel, D.E., Schlessinger, J., Elson, E. & Webb, W.W. Mobility measurement by analysis of fluorescence photobleaching recovery kinetics. *Biophysical Journal* **16**, 1055-1069 (1976).
271. Elson, E.L. & Magde, D. Fluorescence correlation spectroscopy 1: Conceptual basis and theory. *Biopolymers* **13**, 1-27 (1974).
272. Magde, D., Elson, E.L. & Webb, W.W. Fluorescence correlation spectroscopy 2: Experimental realization. *Biopolymers* **13**, 29-61 (1974).
273. Hu, C.D., Chinenov, Y. & Kerppola, T.K. Visualization of interactions among bZip and Rel family proteins in living cells using bimolecular fluorescence complementation. *Molecular Cell* **9**, 789-798 (2002).
274. Schwille, P., MeyerAlmes, F.J. & Rigler, R. Dual-color fluorescence cross-correlation spectroscopy for multicomponent diffusional analysis in solution. *Biophysical Journal* **72**, 1878-1886 (1997).
275. Gaviola, E. The abatement period of fluorescence of pigment solutions. *Annalen Der Physik* **81**, 681-710 (1926).
276. Niehorster, T. *et al.* Multi-target spectrally resolved fluorescence lifetime imaging microscopy. *Nature Methods* **13**, 257-+ (2016).
277. Miyawaki, A. *et al.* Fluorescent indicators for Ca2+ based on green fluorescent proteins and calmodulin. *Nature* **388**, 882-887 (1997).
278. Stryer, L. & Haugland, R.P. Energy transfer - a spectroscopic ruler. *Proceedings of the National Academy of Sciences of the United States of America* **58**, 719-& (1967).
279. Lichtman, J.W. & Conchello, J.A. Fluorescence microscopy. *Nature Methods* **2**, 910-919 (2005).
280. Condreay, J.P., Witherspoon, S.M., Clay, W.C. & Kost, T.A. Transient and stable gene expression in mammalian cells transduced with a recombinant baculovirus vector. *Proceedings of the National Academy of Sciences of the United States of America* **96**, 127-132 (1999).
281. Watanabe, N. & Mitchison, T.J. Single-molecule speckle analysis of Aactin filament turnover in lamellipodia. *Science* **295**, 1083-1086 (2002).
282. Cong, L. *et al.* Multiplex Genome Engineering Using CRISPR/Cas Systems. *Science* **339**, 819-823 (2013).

283. Grussmayer, K.S., Kurz, A. & Herten, D.P. Single-Molecule Studies on the Label Number Distribution of Fluorescent Markers. *Chemphyschem* **15**, 734-742 (2014).
284. Abbe, E. On the Estimation of Aperture in the Microscope. *Journal of the Royal Microscopical Society* **1**, 388–423 (1881).
285. Airy, G. On the diffraction of an object-glass with circular aperture. *Transactions of the Cambridge Philosophical Society* **5**, 283–291 (1835).
286. Abbe, E. Beiträge zur Theorie des Mikroskops und der mikroskopischen Wahrnehmung. *Schultze's Archiv für mikroskopische Anatomie* **9**, 413-468 (1873).
287. Rayleigh, J.W.S. On the theory of optical images, with special reference to the microscope. *Philosophical Magazine* **42** (1896).
288. Sparrow, C.M. On spectroscopic resolving power. *Astrophysical Journal* **44**, 76-86 (1916).
289. Keller, H.E. Objective lenses for confocal microscopy. *Handbook of Biological Confocal Microscopy, Revised Edition*, 77-86 (1989).
290. Minsky, M. Microscopy Apparatus. *US Patent Office*, US3013467 A (1961).
291. Pawley, J.B. *Handbook of Biological Confocal Microscopy*, Edn. Third. (Springer US, New York; 2006).
292. Gould, G. Optically pumped laser amplifiers. *US Patent Office*, US4053845 A (1977).
293. Beier, H.T. & Ibey, B.L. Experimental Comparison of the High-Speed Imaging Performance of an EM-CCD and sCMOS Camera in a Dynamic Live-Cell Imaging Test Case. *Plos One* **9** (2014).
294. Donati, S. & Tambosso, T. Single-Photon Detectors: From Traditional PMT to Solid-State SPAD-Based Technology. *Ieee Journal of Selected Topics in Quantum Electronics* **20**, 8 (2014).
295. Axelrod, D. Total internal reflection fluorescence microscopy in cell biology. *Traffic* **2**, 764-774 (2001).
296. Axelrod, D. Cell-substrate contacts illuminated by total internal-reflection fluorescence. *Journal of Cell Biology* **89**, 141-145 (1981).
297. Stout, A.L. & Axelrod, D. Evanescent field excitation of fluorescence by epi-illumination microscopy. *Applied Optics* **28**, 5237-5242 (1989).
298. Shaner, N.C., Steinbach, P.A. & Tsien, R.Y. A guide to choosing fluorescent proteins. *Nature Methods* **2**, 905-909 (2005).
299. Shannon, C.E. Communication in the presence of noise. *Proceedings of the Institute of Radio Engineers* **37**, 10-21 (1949).
300. Scientific Volume Imaging. The Nyquist Rate (2016). Available at: https://svi.nl/NyquistRate (Accessed: 16th November 2016).
301. Wallace, W., Schaefer, L.H. & Swedlow, J.R. A workingperson's guide to deconvolution in light microscopy. *Biotechniques* **31** (2001).
302. Shaw, P.J. & Rawlins, D.J. The point-spread function of a confocal microscope - its measurement and use in deconvolution of 3-D data. *Journal of Microscopy-Oxford* **163**, 151-165 (1991).
303. Schermelleh, L., Heintzmann, R. & Leonhardt, H. A guide to super-resolution fluorescence microscopy. *Journal of Cell Biology* **190**, 165-175 (2010).
304. Betzig, E. *et al.* Imaging intracellular fluorescent proteins at nanometer resolution. *Science* **313**, 1642-1645 (2006).
305. Hess, S.T., Girirajan, T.P.K. & Mason, M.D. Ultra-high resolution imaging by fluorescence photoactivation localization microscopy. *Biophysical Journal* **91**, 4258-4272 (2006).

306. Rust, M.J., Bates, M. & Zhuang, X. Sub-diffraction-limit imaging by stochastic optical reconstruction microscopy (STORM). *Nature Methods* **3**, 793-795 (2006).
307. Thompson, R.E., Larson, D.R. & Webb, W.W. Precise nanometer localization analysis for individual fluorescent probes. *Biophysical Journal* **82**, 2775-2783 (2002).
308. Jia, H., Yang, J.K. & Li, X.J. Minimum variance unbiased subpixel centroid estimation of point image limited by photon shot noise. *Journal of the Optical Society of America a-Optics Image Science and Vision* **27**, 2038-2045 (2010).
309. Small, A. & Stahlheber, S. Fluorophore localization algorithms for super-resolution microscopy. *Nature Methods* **11**, 267-279 (2014).
310. Zanacchi, F.C. *et al.* Live-cell 3D super-resolution imaging in thick biological samples. *Nature Methods* **8** (2011).
311. Wang, S.Y., Moffitt, J.R., Dempsey, G.T., Xie, X.S. & Zhuang, X.W. Characterization and development of photoactivatable fluorescent proteins for single-molecule-based superresolution imaging. *Proceedings of the National Academy of Sciences of the United States of America* **111**, 8452-8457 (2014).
312. Grimm, J.B. *et al.* Bright photoactivatable fluorophores for single-molecule imaging. *Nature Methods* **13** (2016).
313. Manley, S. *et al.* High-density mapping of single-molecule trajectories with photoactivated localization microscopy. *Nature Methods* **5**, 155-157 (2008).
314. Shtengel, G. *et al.* Interferometric fluorescent super-resolution microscopy resolves 3D cellular ultrastructure. *Proceedings of the National Academy of Sciences of the United States of America* **106**, 3125-3130 (2009).
315. Heilemann, M. *et al.* Subdiffraction-resolution fluorescence imaging with conventional fluorescent probes. *Angewandte Chemie-International Edition* **47**, 6172-6176 (2008).
316. Bates, M., Huang, B., Dempsey, G.T. & Zhuang, X.W. Multicolor super-resolution imaging with photo-switchable fluorescent probes. *Science* **317**, 1749-1753 (2007).
317. Huang, B., Wang, W.Q., Bates, M. & Zhuang, X.W. Three-dimensional super-resolution imaging by stochastic optical reconstruction microscopy. *Science* **319**, 810-813 (2008).
318. Folling, J. *et al.* Fluorescence nanoscopy by ground-state depletion and single-molecule return. *Nature Methods* **5**, 943-945 (2008).
319. Hell, S.W. & Wichmann, J. Breaking the diffraction resolution limit by stimulated-emission - stimulated-emission-depletion fluorescence microscopy. *Optics Letters* **19**, 780-782 (1994).
320. Donnert, G. *et al.* Macromolecular-scale resolution in biological fluorescence microscopy. *Proceedings of the National Academy of Sciences of the United States of America* **103**, 11440-11445 (2006).
321. Willig, K.I., Harke, B., Medda, R. & Hell, S.W. STED microscopy with continuous wave beams. *Nature Methods* **4**, 915-918 (2007).
322. Vicidomini, G. *et al.* Sharper low-power STED nanoscopy by time gating. *Nature Methods* **8**, 571-U575 (2011).
323. Wildanger, D., Medda, R., Kastrup, L. & Hell, S.W. A compact STED microscope providing 3D nanoscale resolution. *Journal of Microscopy-Oxford* **236**, 35-43 (2009).

324. Donnert, G. *et al.* Two-color far-field fluorescence nanoscopy. *Biophysical Journal* **92**, L67-L69 (2007).
325. Pellett, P.A. *et al.* Two-color STED microscopy in living cells. *Biomedical Optics Express* **2**, 2364-2371 (2011).
326. Hein, B., Willig, K.I. & Hell, S.W. Stimulated emission depletion (STED) nanoscopy of a fluorescent protein-labeled organelle inside a living cell. *Proceedings of the National Academy of Sciences of the United States of America* **105**, 14271-14276 (2008).
327. Gustafsson, M.G.L. Surpassing the lateral resolution limit by a factor of two using structured illumination microscopy. *Journal of Microscopy-Oxford* **198**, 82-87 (2000).
328. Gustafsson, M.G.L. *et al.* Three-dimensional resolution doubling in wide-field fluorescence microscopy by structured illumination. *Biophysical Journal* **94**, 4957-4970 (2008).
329. Muller, M., Monkemoller, V., Hennig, S., Hubner, W. & Huser, T. Open-source image reconstruction of super-resolution structured illumination microscopy data in ImageJ. *Nature Communications* **7**, 6 (2016).
330. Förster, T. Energiewanderung und Fluoreszenz (Energy transfer and fluorescence). *Naturwissenschaften* **6**, 166-175 (1946).
331. Ishikawa-Ankerhold, H.C., Ankerhold, R. & Drummen, G.P.C. Advanced Fluorescence Microscopy Techniques-FRAP, FLIP, FLAP, FRET and FLIM. *Molecules* **17**, 4047-4132 (2012).
332. Akrap, N., Seidel, T. & Barisas, B.G. Forster distances for fluorescence resonant energy transfer between mCherry and other visible fluorescent proteins. *Analytical Biochemistry* **402**, 105-106 (2010).
333. Dale, R.E., Eisinger, J. & Blumberg, W.E. Orientational freedom of molecular probes - orientation factor in intra-molecular energy-transfer. *Biophysical Journal* **26**, 161-193 (1979).
334. Youvan, D.C. *et al.* Calibration of fluorescence resonance energy transfer in microscopy using genetically engineered GFP derivatives on nickel chelating beads. *Biotechnology* **3**, 1-18 (1997).
335. Bastiaens, P.I.H. & Jovin, T.M. Microspectroscopic imaging tracks the intracellular processing of a signal transduction protein: Fluorescent-labeled protein kinase C beta I. *Proceedings of the National Academy of Sciences of the United States of America* **93**, 8407-8412 (1996).
336. Zeug, A., Woehler, A., Neher, E. & Ponimaskin, E.G. Quantitative Intensity-Based FRET Approaches-A Comparative Snapshot. *Biophysical Journal* **103**, 1821-1827 (2012).
337. Day, R.N. & Davidson, M.W. Fluorescent proteins for FRET microscopy: Monitoring protein interactions in living cells. *Bioessays* **34**, 341-350 (2012).
338. Li, D.D.U. *et al.* Video-rate fluorescence lifetime imaging camera with CMOS single-photon avalanche diode arrays and high-speed imaging algorithm. *Journal of Biomedical Optics* **16** (2011).
339. Hirvonen, L.M., Festy, F. & Suhling, K. Wide-field time-correlated single-photon counting (TCSPC) lifetime microscopy with microsecond time resolution. *Optics Letters* **39**, 5602-5605 (2014).
340. Buurman, E.P. *et al.* Fluorescence lifetime imaging using a confocal laser scanning microscope. *Scanning* **14**, 155-159 (1992).
341. Becker, W. *et al.* Fluorescence lifetime imaging by time-correlated single-photon counting. *Microscopy Research and Technique* **63**, 58-66 (2004).

342. Mizushima, N., Ohsumi, Y. & Yoshimori, T. Autophagosome formation in mammalian cells. *Cell Structure and Function* **27**, 421-429 (2002).
343. Manders, E.M.M., Stap, J., Brakenhoff, G.J., Vandriel, R. & Aten, J.A. Dynamics of 3-Dimensional replication patterns during the S-phase, analyzed by double labeling of DNA and confocal microscopy. *Journal of Cell Science* **103**, 857-862 (1992).
344. Manders, E.M.M., Verbeek, F.J. & Aten, J.A. Measurement of colocalization of objects in dual-color confocal images. *Journal of Microscopy-Oxford* **169**, 375-382 (1993).
345. Mauvezin, C., Nagy, P., Juhasz, G. & Neufeld, T.P. Autophagosome-lysosome fusion is independent of V-ATPase-mediated acidification. *Nature Communications* **6** (2015).
346. Kimura, S., Noda, T. & Yoshimori, T. Dissection of the autophagosome maturation process by a novel reporter protein, tandem fluorescent-tagged LC3. *Autophagy* **3**, 452-460 (2007).
347. Knight, J.C., Birks, T.A., Russell, P.S. & Atkin, D.M. All-silica single-mode optical fiber with photonic crystal cladding. *Optics Letters* **21**, 1547-1549 (1996).
348. Borlinghaus, R., Gugel, H., Albertano, P. & Seyfried, V. in Conference on Three-Dimensional and Multidimensional Microscopy 60900T (Spie-Int Soc Optical Engineering, San Jose; 2006).
349. Becker, W. *Advanced Time-Correlated Single Photon Counting Techniques*. (Springer, Berlin; 2005).
350. Maus, M. *et al.* An experimental comparison of the maximum likelihood estimation and nonlinear least squares fluorescence lifetime analysis of single molecules. *Analytical Chemistry* **73**, 2078-2086 (2001).
351. Gratton, E., Breusegem, S., Sutin, J. & Ruan, Q.Q. Fluorescence lifetime imaging for the two-photon microscope: time-domain and frequency-domain methods. *Journal of Biomedical Optics* **8**, 381-390 (2003).
352. Saiki, R.K. *et al.* Primer-directed enzymatic amplification of DNA with a thermostable SNA-polymerase. *Science* **239**, 487-491 (1988).
353. Sambrook, J. & David, R.W. *Molecular Cloning: A Laboratory Manual*, Edn. Third. (Cold Spring Harbor Laboratory Press, New York; 2001).
354. Cline, J., Braman, J.C. & Hogrefe, H.H. PCR fidelity of Pfu DNA polymerase and other thermostable DNA polymerases. *Nucleic Acids Research* **24**, 3546-3551 (1996).
355. Hemsley, A., Arnheim, N., Toney, M.D., Cortopassi, G. & Galas, D.J. A simple method for site-directed mutagenesis using the polymerase chain-reaction. *Nucleic Acids Research* **17**, 6545-6551 (1989).
356. New England Biolabs. Star Activity. Available at: www.neb.com/tools-and-resources/usage-guidelines/star-activity (Accessed: 7th January 2017).
357. Stratagene. XL10-Gold Ultracompetent Cells. Available at: www.chem-agilent.com/pdf/strata/200314.pdf (Accessed: 7th January 2017).
358. Scherer, W.F., Syverton, J.T. & Gey, G.O. Studies on the propagation invitro of poliomyelitis viruses 4: Viral multiplication in a stable strain of human malignant epithelial cells (strain HeLa) derived from an epidermoid carcinoma of the cervix. *Journal of Experimental Medicine* **97**, 695 (1953).
359. Graham, F.L., Smiley, J., Russell, W.C. & Nairn, R. Characteristics of a human cell line transformed by DNA from human adenovirus type-5. *Journal of General Virology* **36**, 59-72 (1977).

360. Thermo Scientific. Turbofect Transfection Reagent (2011). Available at: https://tools.thermofisher.com/content/sfs/manuals/MAN0011815_TurboFect_Transfection_Reag_UG.pdf (Accessed: 7th January 2017).
361. Lv, H.T., Zhang, S.B., Wang, B., Cui, S.H. & Yan, J. Toxicity of cationic lipids and cationic polymers in gene delivery. *Journal of Controlled Release* **114**, 100-109 (2006).
362. Fire, A. *et al.* Potent and specific genetic interference by double-stranded RNA in Caenorhabditis elegans. *Nature* **391**, 806-811 (1998).
363. Hammond, S.M., Bernstein, E., Beach, D. & Hannon, G.J. An RNA-directed nuclease mediates post-transcriptional gene silencing in Drosophila cells. *Nature* **404**, 293-296 (2000).
364. Bradford, M.M. Rapid and sensitive method for quantitation of microgram quantities of protein utilizing principle of protein-dye binding. *Analytical Biochemistry* **72**, 248-254 (1976).
365. Thermo Scientific. Protein Assay Compatibility Table (2012). Available at: https://tools.thermofisher.com/content/sfs/brochures/TR0068-Protein-assay-compatibility.pdf (Accessed: 6th November 2016).
366. Wilson, K. & Walker, J. *Principles and Techniques of Practical Biochemistry*, Edn. Fifth. (Cambridge University Press, Cambridge; 2000).
367. Ornstein, L. & Davis, B. Disc Electrophoresis (Parts I and II). *Annals of the New York Academy of Sciences* **121**, 321-427 (1964).
368. Jacobson, B.S. & Branton, D. Plasma membrane - Rapid isolation and exposure of cytoplasmic surface by use of positively charged beads. *Science* **195**, 302-304 (1977).
369. Bacallao, R., Sohrab, S. & Phillips, C. *Guiding Principles of Specimen Preservation for Confocal Fluorescence Microscopy*. (Springer US, 2006).
370. Corning. Corning Cell-Tak Cell and Tissue Adhesive. Available at: http://csmedia2.corning.com/LifeSciences/media/pdf/SPC-354240.pdf (Accessed: 27th February 2017).
371. Mizushima, N., Yoshimori, T. & Levine, B. Methods in Mammalian Autophagy Research. *Cell* **140**, 313-326 (2010).
372. Yoshimori, T., Yamamoto, A., Moriyama, Y., Futai, M. & Tashiro, Y. Bafilomycin-A1, a specific inhibitor of vacuolar-type H+-ATPase, inhibits acidification and protein-degradation in lysosomes of cultured-cells. *Journal of Biological Chemistry* **266**, 17707-17712 (1991).
373. Vicidomini, G. *et al.* STED Nanoscopy with Time-Gated Detection: Theoretical and Experimental Aspects. *Plos One* **8**, 12 (2013).
374. Ball, G. *et al.* SIMcheck: a Toolbox for Successful Super-resolution Structured Illumination Microscopy. *Scientific Reports* **5**, 11 (2015).
375. Castle, M. & Keller, J. Rolling Ball Background Subtraction (2007). Available at: http://imagej.net/Rolling_Ball_Background_Subtraction (Accessed: 22nd January 2017).
376. Schindelin, J. *et al.* Fiji: an open-source platform for biological-image analysis. *Nature Methods* **9**, 676-682 (2012).
377. White, D., Kazimiers, T. & Schindelin, J. Coloc 2 - Standardized, modular, pixel intensity modulation over space based colocalization analysis (2015). Available at: http://imagej.net/Coloc_2012 (Accessed: 22nd January 2017).
378. Olivo-Marin, J.C. Extraction of spots in biological images using multiscale products. *Pattern Recognition* **35**, 1989-1996 (2002).

379. de Chaumont, F. *et al.* Icy: an open bioimage informatics platform for extended reproducible research. *Nature Methods* **9**, 690-696 (2012).
380. Dilcher, M., Kohler, B. & von Mollard, G.F. Genetic interactions with the yeast Q-SNARE VTI1 reveal novel functions for the R-SNARE YKT6. *Journal of Biological Chemistry* **276**, 34537-34544 (2001).
381. Rossi, V. *et al.* Longins and their longin domains: regulated SNAREs and multifunctional SNARE regulators. *Trends in Biochemical Sciences* **29**, 682-688 (2004).
382. Arasaki, K. *et al.* A Role for the Ancient SNARE Syntaxin 17 in Regulating Mitochondrial Division. *Developmental Cell* **32**, 304-317 (2015).
383. Muppirala, M., Gupta, V. & Swarup, G. Syntaxin 17 cycles between the ER and ERGIC and is required to maintain the architecture of ERGIC and Golgi. *Biology of the Cell* **103**, 333-350 (2011).
384. Su, Q.N., Mochida, S., Tian, J.H., Mehta, R. & Sheng, Z.H. SNAP-29: A general SNARE protein that inhibits SNARE disassembly and is implicated in synaptic transmission. *Proceedings of the National Academy of Sciences of the United States of America* **98**, 14038-14043 (2001).
385. Lu, Q. *et al.* Early steps in primary cilium assembly require EHD1/EHD3-dependent ciliary vesicle formation. *Nature Cell Biology* **17** (2015).
386. Sato, M. *et al.* Caenorhabditis elegans SNAP-29 is required for organellar integrity of the endomembrane system and general exocytosis in intestinal epithelial cells. *Molecular Biology of the Cell* **22**, 2579-2587 (2011).
387. Rotem-Yehudar, R., Galperin, E. & Horowitz, M. Association of insulin-like growth factor 1 receptor with EHD1 and SNAP29. *Journal of Biological Chemistry* **276**, 33054-33060 (2001).
388. Schardt, A. *et al.* The SNARE Protein SNAP-29 Interacts With the GTPase Rab3A: Implications for Membrane Trafficking in Myelinating Glia. *Journal of Neuroscience Research* **87**, 3465-3479 (2009).
389. Wang, C.C. *et al.* VAMP8/endobrevin as a general vesicular SNARE for regulated exocytosis of the exocrine system. *Molecular Biology of the Cell* **18**, 1056-1063 (2007).
390. Wang, C.C. *et al.* A role of VAMP8/endobrevin in regulated exocytosis of pancreatic acinar cells. *Developmental Cell* **7**, 359-371 (2004).
391. Galli, T. *et al.* A novel tetanus neurotoxin-insensitive vesicle-associated membrane protein in SNARE complexes of the apical plasma membrane of epithelial cells. *Molecular Biology of the Cell* **9**, 1437-1448 (1998).
392. Proux-Gillardeaux, V., Raposo, G., Irinopoullou, T. & Galli, T. Expression of the Longin domain of TI-VAMP impairs lysosomal secretion and epithelial cell migration. *Biology of the Cell* **99**, 261-271 (2007).
393. Renna, M. *et al.* Autophagic substrate clearance requires activity of the syntaxin-5 SNARE complex. *Journal of Cell Science* **124**, 469-482 (2011).
394. Mizushima, N. Autophagy: process and function. *Genes & Development* **21**, 2861-2873 (2007).
395. Vabulas, R.M. & Hartl, F.U. Protein synthesis upon acute nutrient restriction relies on proteasome function. *Science* **310**, 1960-1963 (2005).
396. Ramirez-Peinado, S. *et al.* Glucose-starved Cells Do Not Engage in Prosurvival Autophagy. *Journal of Biological Chemistry* **288**, 30387-30398 (2013).
397. Kneen, M., Farinas, J., Li, Y.X. & Verkman, A.S. Green fluorescent protein as a noninvasive intracellular pH indicator. *Biophysical Journal* **74**, 1591-1599 (1998).

398. Shaner, N.C. *et al.* Improved monomeric red, orange and yellow fluorescent proteins derived from Discosoma sp red fluorescent protein. *Nature Biotechnology* **22**, 1567-1572 (2004).
399. Berg, T.O., Fengsrud, M., Stromhaug, P.E., Berg, T. & Seglen, P.O. Isolation and characterization of rat liver amphisomes - Evidence for fusion of autophagosomes with both early and late endosomes. *Journal of Biological Chemistry* **273**, 21883-21892 (1998).
400. Marshall, M.R. *et al.* VAMP8-dependent fusion of recycling endosomes with the plasma membrane facilitates T lymphocyte cytotoxicity. *Journal of Cell Biology* **210**, 135-151 (2015).
401. Bethani, I. *et al.* Endosomal Fusion upon SNARE Knockdown is Maintained by Residual SNARE Activity and Enhanced Docking. *Traffic* **10**, 1543-1559 (2009).
402. Diao, J.J. *et al.* Single-Vesicle Fusion Assay Reveals Munc18-1 Binding to the SNARE Core Is Sufficient for Stimulating Membrane Fusion. *Acs Chemical Neuroscience* **1**, 168-174 (2010).
403. Dulubova, I. *et al.* Munc18-1 binds directly to the neuronal SNARE complex. *Proceedings of the National Academy of Sciences of the United States of America* **104**, 2697-2702 (2007).
404. Lobingier, B.T. & Merz, A.J. Sec1/Munc18 protein Vps33 binds to SNARE domains and the quaternary SNARE complex. *Molecular Biology of the Cell* **23**, 4611-4622 (2012).
405. Togneri, J., Cheng, Y.S., Munson, M., Hughson, F.M. & Carr, C.M. Specific SNARE complex binding mode of the Sec1/Munc-18 protein, Sec1p. *Proceedings of the National Academy of Sciences of the United States of America* **103**, 17730-17735 (2006).
406. Pieren, M., Schmidt, A. & Mayer, A. The SM protein Vps33 and the t-SNARE H-abc domain promote fusion pore opening. *Nature Structural & Molecular Biology* **17**, 710-U781 (2010).
407. Seals, D.F., Eitzen, G., Margolis, N., Wickner, W.T. & Price, A. A Ypt/Rab effector complex containing the Sec1 homolog Vps33p is required for homotypic vacuole fusion. *Proceedings of the National Academy of Sciences of the United States of America* **97**, 9402-9407 (2000).
408. Rickman, C., Medine, C.N., Bergmann, A. & Duncan, R.R. Functionally and spatially distinct modes of munc18-syntaxin 1 interaction. *Journal of Biological Chemistry* **282**, 12097-12103 (2007).
409. Hu, S.H., Latham, C.F., Gee, C.L., James, D.E. & Martin, J.L. Structure of the Munc18c/Syntaxin4 N-peptide complex defines universal features of the N-peptide binding mode of Sec1/Munc18 proteins. *Proceedings of the National Academy of Sciences of the United States of America* **104**, 8773-8778 (2007).
410. Hackmann, Y. *et al.* Syntaxin binding mechanism and disease-causing mutations in Munc18-2. *Proceedings of the National Academy of Sciences of the United States of America* **110**, E4482-E4491 (2013).
411. Graham, S.C. *et al.* Structural basis of Vps33A recruitment to the human HOPS complex by Vps16. *Proceedings of the National Academy of Sciences of the United States of America* **110**, 13345-13350 (2013).
412. Burkhardt, P., Hattendorf, D.A., Weis, W.I. & Fasshauer, D. Munc18a controls SNARE assembly through its interaction with the syntaxin N-peptid. *Embo Journal* **27**, 923-933 (2008).

413. Balderhaar, H.J.K. & Ungermann, C. CORVET and HOPS tethering complexes - coordinators of endosome and lysosome fusion. *Journal of Cell Science* **126**, 1307-1316 (2013).
414. Wartosch, L., Gunesdogan, U., Graham, S.C. & Luzio, J.P. Recruitment of VPS33A to HOPS by VPS16 Is Required for Lysosome Fusion with Endosomes and Autophagosomes. *Traffic* **16**, 727-742 (2015).
415. Xu, H., Jun, Y., Thompson, J., Yates, J. & Wickner, W. HOPS prevents the disassembly of trans-SNARE complexes by Sec17p/Sec18p during membrane fusion. *Embo Journal* **29**, 1948-1960 (2010).
416. Starai, V.J., Hickey, C.M. & Wickner, W. HOPS proofreads the trans-SNARE complex for yeast vacuole fusion. *Molecular Biology of the Cell* **19**, 2500-2508 (2008).
417. Laufman, O., Kedan, A., Hong, W.J. & Lev, S. Direct interaction between the COG complex and the SM protein, Sly1, is required for Golgi SNARE pairing. *Embo Journal* **28**, 2006-2017 (2009).
418. Morgera, F. *et al.* Regulation of exocytosis by the exocyst subunit Sec6 and the SM protein Sec1. *Molecular Biology of the Cell* **23**, 337-346 (2012).
419. Brocker, C. *et al.* Molecular architecture of the multisubunit homotypic fusion and vacuole protein sorting (HOPS) tethering complex. *Proceedings of the National Academy of Sciences of the United States of America* **109**, 1991-1996 (2012).
420. Mima, J., Hickey, C.M., Xu, H., Jun, Y. & Wickner, W. Reconstituted membrane fusion requires regulatory lipids, SNAREs and synergistic SNARE chaperones. *Embo Journal* **27**, 2031-2042 (2008).
421. Sato, T.K., Rehling, P., Peterson, M.R. & Emr, S.D. Class C Vps protein complex regulates vacuolar SNARE pairing and is required for vesicle docking/fusion. *Molecular Cell* **6**, 661-671 (2000).
422. Rink, J., Ghigo, E., Kalaidzidis, Y. & Zerial, M. Rab conversion as a mechanism of progression from early to late endosomes. *Cell* **122**, 735-749 (2005).
423. Pols, M.S., Brink, C., Gosavi, P., Oorschot, V. & Klumperman, J. The HOPS Proteins hVps41 and hVps39 Are Required for Homotypic and Heterotypic Late Endosome Fusion. *Traffic* **14**, 219-232 (2013).
424. Rieder, S.E. & Emr, S.D. A novel RING finger protein complex essential for a late step in protein transport to the yeast vacuole. *Molecular Biology of the Cell* **8**, 2307-2327 (1997).
425. Wurmser, A.E., Sato, T.K. & Emr, S.D. New component of the vacuolar class C-Vps complex couples nucleotide exchange on the Ypt7 GTPase to SNARE-dependent docking and fusion. *Journal of Cell Biology* **151**, 551-562 (2000).
426. Peplowska, K., Markgraf, D.F., Ostrowicz, C.W., Bange, G. & Ungermann, C. The CORVET tethering complex interacts with the yeast Rab5 homolog Vps21 and is involved in endo-lysosomal biogenesis. *Developmental Cell* **12**, 739-750 (2007).
427. Akbar, M.A., Ray, S. & Kramer, H. The SM Protein Car/Vps33A Regulates SNARE-mediated Trafficking to Lysosomes and Lysosome-related Organelles. *Molecular Biology of the Cell* **20**, 1705-1714 (2009).
428. Cebollero, E. *et al.* Phosphatidylinositol-3-Phosphate Clearance Plays a Key Role in Autophagosome Completion. *Current Biology* **22**, 1545-1553 (2012).
429. Blom, N., Gammeltoft, S. & Brunak, S. Sequence and structure-based prediction of eukaryotic protein phosphorylation sites. *Journal of Molecular Biology* **294**, 1351-1362 (1999).

430. Songyang, Z. *et al.* A structural basis for substrate specificities of protein Ser/Thr kinases: Primary sequence preference of casein kinases I and II, NIMA, phosphorylase kinase, calmodulin-dependent kinase II, CDK5, and Erk1. *Molecular and Cellular Biology* **16**, 6486-6493 (1996).
431. Pinna, L.A. The raison D'Etre of constitutively active protein kinases: The lesson of CK2. *Accounts of Chemical Research* **36**, 378-384 (2003).
432. Colbert, K.N. *et al.* Syntaxin1a variants lacking an N-peptide or bearing the LE mutation bind to Munc18a in a closed conformation. *Proceedings of the National Academy of Sciences of the United States of America* **110**, 12637-12642 (2013).
433. Clapham, D.E. Calcium signaling. *Cell* **131**, 1047-1058 (2007).
434. Zhao, Y. *et al.* An Expanded Palette of Genetically Encoded Ca2+ Indicators. *Science* **333**, 1888-1891 (2011).
435. Colin, R. & R., D.R. Munc18/Syntaxin Interaction Kinetics Control Secretory Vesicle Dynamics. *Journal of Biological Chemistry* **285**, 3965-3972 (2009).
436. Becker, W. Fluorescence lifetime imaging - techniques and applications. *Journal of Microscopy* **247**, 119-136 (2012).
437. Duncan, R.R., Bergmann, A., Cousin, M.A., Apps, D.K. & Shipston, M.J. Multi-dimensional time-correlated single photon counting (TCSPC) fluorescence lifetime imaging microscopy (FLIM) to detect FRET in cells. *Journal of Microscopy-Oxford* **215**, 1-12 (2004).
438. Agronskaia, A.V., Tertoolen, L. & Gerritsen, H.C. High frame rate fluorescence lifetime imaging. *Journal of Physics D-Applied Physics* **36**, 1655-1662 (2003).
439. Becker, W. Application of Modern TCSPC Techniques, in *Advanced Time-Correlated Single Photon Counting Techniques* (Springer, Berlin; 2005).
440. Morton, G.A. Photomultiplier for scintillation counting. *RCA Review* **10**, 525-553 (1949).
441. Yamazaki, I., Tamai, N., Kume, H., Tsuchiya, H. & Oba, K. Microchannel-plate photomultiplier applicability to the time-correlated photon-counting method. *Review of Scientific Instruments* **56**, 1187-1194 (1985).
442. Cova, S., Ghioni, M., Lotito, A., Rech, I. & Zappa, F. Evolution and prospects for single-photon avalanche diodes and quenching circuits. *Journal of Modern Optics* **51**, 1267-1288 (2004).
443. Haitz, R.H. Mechanisms contributing to noise pulse rate of avalanche diodes. *Journal of Applied Physics* **36** (1965).
444. Cova, S., Longoni, A. & Andreoni, A. Towards picosecond resolution with single-photon avalanche diodes. *Review of Scientific Instruments* **52**, 408-412 (1981).
445. Kumar, S. *et al.* Multifocal multiphoton excitation and time correlated single photon counting detection for 3-D fluorescence lifetime imaging. *Optics Express* **15**, 12548-12561 (2007).
446. Poland, S.P. *et al.* A high speed multifocal multiphoton fluorescence lifetime imaging microscope for live-cell FRET imaging. *Biomedical Optics Express* **6**, 277-296 (2015).
447. Gisin, N., Ribordy, G.G., Tittel, W. & Zbinden, H. Quantum cryptography. *Reviews of Modern Physics* **74**, 145-195 (2002).
448. Hadfield, R.H. Single-photon detectors for optical quantum information applications. *Nature Photonics* **3**, 696-705 (2009).
449. Watanabe, M., Koishi, M. & Roehrenbeck, P.W. in Advances in Fluorescence Sensing Technology 155-164 (SPIE, Los Angeles; 1993).

450. Krishnan, R.V., Saitoh, H., Terada, H., Centonze, V.E. & Herman, B. Development of a multiphoton fluorescence lifetime imaging microscopy system using a streak camera. *Review of Scientific Instruments* **74**, 2714-2721 (2003).
451. Biskup, C. *et al.* Multi-dimensional fluorescence lifetime and FRET measurements. *Microscopy Research and Technique* **70**, 442-451 (2007).
452. Rossi, B. & Nereson, N. Experimental arrangement for the measurement of small time intervals between the discharges of Geiger-Mueller counters. *Review of Scientific Instruments* **17**, 65-71 (1946).
453. Haugen, G.R., Wallin, B.W. & Lytle, F.E. Optimization of data-acquisition rates in time-correlated single-photon fluorimetry. *Review of Scientific Instruments* **50**, 64-72 (1979).
454. Dowling, K., Hyde, S.C.W., Dainty, J.C., French, P.M.W. & Hares, J.D. 2-D fluorescence lifetime imaging using a time-gated image intensifier. *Optics Communications* **135**, 27-31 (1997).
455. Boyle, W.S. & Smith, G.E. Charge coupled semiconductor devices. *The Bell System Technical Journal* **49**, 587-593 (1970).
456. McAlister, H.A., Robinson, W.G. & Marcus, S.L. Development of a dual microchannel plate intensified charge-coupled device (CCD) speckle camera. *Proceedings of the Society of Photo-Optical Instrumentation Engineers* **331**, 113-129 (1982).
457. Gerritsen, H.C., Asselbergs, M.A.H., Agronskaia, A.V. & Van Sark, W. Fluorescence lifetime imaging in scanning microscopes: acquisition speed, photon economy and lifetime resolution. *Journal of Microscopy-Oxford* **206**, 218-224 (2002).
458. Becker, W. *et al.* A wide-field TCSPC FLIM system based on an MCP PMT with a delay-line anode. *Review of Scientific Instruments* **87** (2016).
459. Emiliani, V. *et al.* Low-intensity two-dimensional imaging of fluorescence lifetimes in living cells. *Applied Physics Letters* **83**, 2471-2473 (2003).
460. Milnes, J., Lapington, J.S., Jagutzki, O. & Howorth, J. Image charge multi-role and function detectors. *Nuclear Instruments & Methods in Physics Research Section a-Accelerators Spectrometers Detectors and Associated Equipment* **604**, 218-220 (2009).
461. Hirvonen, L.M., Petrasek, Z., Beeby, A. & Suhling, K. Sub-mu s time resolution in wide-field time-correlated single photon counting microscopy obtained from the photon event phosphor decay. *New Journal of Physics* **17**, 14 (2015).
462. Richardson, J. *et al.* in IEEE Custom Integrated Circuits Conference 77-80 (IEEE, San Jose, CA; 2009).
463. Giraud, G. *et al.* Fluorescence lifetime biosensing with DNA microarrays and a CMOS-SPAD imager. *Biomedical Optics Express* **1**, 1302-1308 (2010).
464. Richardson, J.A., Grant, L.A. & Henderson, R.K. Low Dark Count Single-Photon Avalanche Diode Structure Compatible With Standard Nanometer Scale CMOS Technology. *Ieee Photonics Technology Letters* **21**, 1020-1022 (2009).
465. Thorlabs. DCx camera functional description and SDK manual. Available at: https://www.thorlabs.de/newgrouppage9.cfm?objectgroup_id=4024&pn=DCC1545M (Accessed: 20th November 2016).
466. Picoquant. Picosecond Pulsed Sources. Available at: https://www.picoquant.com/products/category/picosecond-pulsed-

sources/ldh-series-picosecond-pulsed-diode-laser-heads (Accessed: 27th February 2017).
467. Warren, S.C. *et al.* Rapid Global Fitting of Large Fluorescence Lifetime Imaging Microscopy Datasets. *Plos One* **8** (2013).
468. Wu, Y., Lopez, G.P., Sklar, L.A. & Buranda, T. Spectroscopic characterization of streptavidin functionalized quantum dots. *Analytical Biochemistry* **364**, 193-203 (2007).
469. Hess, S.T., Sheets, E.D., Wagenknecht-Wiesner, A. & Heikal, A.A. Quantitative analysis of the fluorescence properties of intrinsically fluorescent proteins in living cells. *Biophysical Journal* **85**, 2566-2580 (2003).
470. Bigas, M., Cabruja, E., Forest, J. & Salvi, J. Review of CMOS image sensors. *Microelectronics Journal* **37**, 433-451 (2006).
471. Chen, B.C. *et al.* Lattice light-sheet microscopy: Imaging molecules to embryos at high spatiotemporal resolution. *Science* **346** (2014).
472. Barber, P.R. *et al.* Multiphoton time-domain fluorescence lifetime imaging microscopy: practical application to protein-protein interactions using global analysis. *Journal of the Royal Society Interface* **6**, S93-S105 (2009).
473. Ganley, I.G., Wong, P.M., Gammoh, N. & Jiang, X.J. Distinct Autophagosomal-Lysosomal Fusion Mechanism Revealed by Thapsigargin-Induced Autophagy Arrest. *Molecular Cell* **42**, 731-743 (2011).